THE MINISTRY OF SCIENCE AND HIGHER EDUCATION OF THE RUSSIAN FEDERATION

ST. PETERSBURG STATE POLYTECHNICAL UNIVERSITY

JOURNAL

Physics and Mathematics

VOLUME 12, No.1, 2019

Peter the Great St. Petersburg
Polytechnic University
2019

ST. PETERSBURG STATE POLYTECHNICAL UNIVERSITY JOURNAL.
PHYSICS AND MATHEMATICS

The journal is included in the List of leading peer-reviewed scientific journals and other editions to publish major findings of theses for the research degrees of Doctor of Sciences and Candidate of Sciences.

The publications are presented in the VINITI RAS Abstract Journal and Ulrich's Periodical Directory International Database.

The journal is published since 2008 as part of the periodical edition 'Nauchno-tekhnicheskie vedomosti SPb-GPU'.

The journal is registered with the Federal Service for Supervision in the Sphere of Telecom, Information Technologies and Mass Communications (ROSKOMNADZOR). Certificate ПИ № ФС77-52144 issued December 11, 2012.

The journal is distributed through the CIS countries catalogue, the «Press of Russia» joint catalogue and the «Press by subscription» Internet catalogue. The subscription index is **71823.**

The journal is in the **Web of Science** (Emerging Sources Citation Index) and the **Russian Science Citation Index** (RSCI) databases.

Address: 195251 Politekhnicheskaya St. 29, St. Petersburg, Russia.

Phone: (812) 294-22-85.

http://ntv.spbstu.ru/physics

МИНИСТЕРСТВО НАУКИ И ВЫСШЕГО ОБРАЗОВАНИЯ РОССИЙСКОЙ ФЕДЕРАЦИИ

НАУЧНО-ТЕХНИЧЕСКИЕ ВЕДОМОСТИ

САНКТ-ПЕТЕРБУРГСКОГО ГОСУДАРСТВЕННОГО ПОЛИТЕХНИЧЕСКОГО УНИВЕРСИТЕТА

Физико-математические науки

ТОМ 12, №1

2019

Санкт-Петербургский политехнический
университет Петра Великого
2019

НАУЧНО-ТЕХНИЧЕСКИЕ ВЕДОМОСТИ САНКТ-ПЕТЕРБУРГСКОГО ГОСУДАРСТВЕННОГО ПОЛИТЕХНИЧЕСКОГО УНИВЕРСИТЕТА. ФИЗИКО-МАТЕМАТИЧЕСКИЕ НАУКИ

Журнал с 2002 г. входит в Перечень ведущих рецензируемых научных журналов и изданий, в которых должны быть опубликованы основные результаты диссертаций на соискание ученых степеней доктора и кандидата наук.

Сведения о публикациях представлены в Реферативном журнале ВИНИТИ РАН, в международной справочной системе «Ulrich's Periodical Directory».

С 2008 года выпускается в составе сериального периодического издания «Научно-технические ведомости СПбГПУ».

Журнал зарегистрирован Федеральной службой по надзору в сфере информационных технологий и массовых коммуникаций (Роскомнадзор). Свидетельство о регистрации ПИ № ФС77-52144 от 11 декабря 2012 г.

Распространяется по Каталогу стран СНГ, Объединенному каталогу «Пресса России» и по Интернет-каталогу «Пресса по подписке». Подписной индекс **71823**.

Журнал индексируется в базе данных **Web of Science** (Emerging Sources Citation Index), а также включен в базу данных **«Российский индекс научного цитирования»** (РИНЦ), размещенную на платформе Научной электронной библиотеки на сайте

http://www.elibrary.ru

Адрес редакции и издательства:

Россия, 195251, Санкт-Петербург, ул. Политехническая, д. 29.

Тел. редакции (812) 294-22-85.

http://ntv.spbstu.ru/physics

Contents

Atmosphere physics

Mathematics

Mechanics

Содержание

Физика конденсированного состояния

Математическое моделирование физических процессов

Приборы и техника физического эксперимента

Физическая электроника

Физическое материаловедение

Физика атмосферы

Математика

Механика

DOI: 10.18721/JPM.12101
УДК 535.37

THE APPLICATION OF BARIUM FLUORIDE LUMINESCENCE: CHALLENGES AND PROSPECTS

P.A. Rodnyi[1], E.A. Garibin[2], I.D. Venevtsev[1], Yu.I. Davydov[3]

[1] Peter the Great St. Petersburg Polytechnic University, St. Petersburg, Russian Federation;

[2] CJS "INCROM", St. Petersburg, Russian Federation;

[3] Joint Institute for Nuclear Research, Dubna, Russian Federation

The problem of obtaining BaF_2 crystals with a predominant sub-nanosecond luminescence component has been considered. A detailed analysis of methods for suppressing the slow component of the crystal luminescence was carried out. It was shown that the introduction of a number of dopants led to the suppression of the slow component, but, as a rule, the intensity of the sub-nanosecond component decreased, and the transparency and radiation hardness of the crystal also deteriorated. The results of spectral and kinetic measurements of BaF_2:Tm and BaF_2:Sc luminescence were presented. It was shown that the solution of the problem can be achieved by using an undoped BaF_2 crystal in combination with a filter suppressing the slow luminescence component.

Keywords: barium fluoride, core-valence luminescence, ultrafast scintillators, optical filters

Citation: P.A. Rodnyi, E.A. Garibin, I.D. Venevtsev, Yu.I. Davydov, The application of barium fluoride luminescence: challenges and prospects, St. Petersburg Polytechnical State University Journal. Physics and Mathematics. 12 (1) (2019) 9–24. DOI: 10.18721/JPM.12101

ПРОБЛЕМЫ И ПЕРСПЕКТИВЫ ПРИМЕНЕНИЯ ЛЮМИНЕСЦЕНЦИИ ФТОРИДА БАРИЯ

П.А. Родный[1], Е.А. Гарибин[2], И.Д. Веневцев[1], Ю.И. Давыдов[3]

[1] Санкт-Петербургский политехнический университет Петра Великого,

Санкт-Петербург, Российская Федерация;

[2] ЗАО «ИНКРОМ», Санкт-Петербург, Российская Федерация;

[3] Объединенный институт ядерных исследований, г. Дубна, Российская Федерация

Рассмотрена проблема получения кристаллов BaF_2 с преобладающим субнаносекундным компонентом рентгенолюминесценции. Проведен подробный анализ методов подавления медленного компонента указанной люминесценции данного соединения. Показано, что введение ряда примесей приводит к подавлению медленного компонента, однако, как правило, интенсивность субнаносекундного компонента также снижается, при этом ухудшаются прозрачность и радиационная стойкость кристалла. Приведены результаты измерения спектрально-кинетических характеристик кристаллов BaF_2:Tm и BaF_2:Sc. Показано, что проблему можно решить путем использования нелегированного кристалла BaF_2 в сочетании с фильтром, подавляющим медленный компонент люминесценции.

Ключевые слова: фторид бария, остовно-валентная люминесценция, сверхбыстрый сцинтиллятор, оптический фильтр

Ссылка при цитировании: Родный П.А., Гарибин Е.А., Веневцев И.Д., Давыдов Ю.И. Проблемы и перспективы применения люминесценции фторида бария // Научно-технические ведомости СПбГПУ. Физико-математические науки. 2019. Т. 12. № 1. С. 9–24. DOI: 10.18721/JPM.12101

Introduction

Barium fluoride (BaF_2) has been the focus of extensive research spanning several decades, ever since subnanosecond (0.7–0.8 ns) luminescence in the range between ultraviolet (UV) and vacuum ultraviolet (VUV) spectral regions [1, 2] has been discovered in this compound in the early 1980s. Radiative electronic transitions between the top core (5*p*, Ba) and valence (2*p*, F) levels of the crystal were later confirmed to be responsible for this luminescence [3]. The phenomenon was termed core-valence luminescence (CVL) [4], or cross-luminescence [5]. BaF_2 has a short decay time, making it a promising option for use in medical diagnostic systems, experimental nuclear physics and astrophysics as a fast scintillator. A wide luminescence band with a maximum of 310 nm (in addition to CVL) is another known problem with barium fluoride. Self-trapped excitons (STE) are responsible for this luminescence, which has a decay time $\tau = 630$ ns. Numerous studies have been dedicated to suppression of this long (and often undesirable) component of luminescence [6–9]; this problem is also considered in our study.

Another issue is related to the spectral position of CVL bands: two emission peaks are located at wavelengths of 220 and 196 nm (UV and VUV ranges). Very few types of photodetectors can effectively operate in this spectral region; solar-blind photomultipliers with CsTe photocathodes making it possible to reduce the output signal from the slow component by 9 times have long been used for this purpose; however, the signal from the fast component also decreased by 1.84 times [7].

Solar-blind photodetectors with a response time of 15 ps and a quantum efficiency of about 12% have been developed [10]; a quantum efficiency of 17% at 220 nm was recently obtained for an avalanche photodiode (APD) [11].

Moreover, interest in the characteristics of barium fluoride has been renewed because this compound is considered as a working material for a new calorimeter, aimed at observing muon-to-electron conversion (the Mu2e experiment at Fermilab [11, 12]). Effort is currently underway to improve the luminescent characteristics of barium fluoride by introducing impurities, changing the conditions of growth and annealing of crystals, using such materials as nanoparticles, composites and ceramics.

In our study, we have carried out generalization and analysis of the most important results on improving the luminescence and scintillation characteristics of barium fluoride, giving the experimental data for BaF_2:Tm and BaF_2:Sc crystals.

BaF_2:Tm samples have been chosen because thulium (Tm) is one of the best dopants among rare-earth ions for suppressing the slow luminescence component [5, 6]. As for the second dopant, scandium (Sc) is the least studied "suppressive" dopant among the ions with a filled outer shell.

Suppression of slow component of luminescence in barium fluoride by introducing dopants

Ions with a filled outer shell. Numerous studies considered "suppression" of the slow luminescence component (310 nm band), which is undesirable for fast scintillators. Ions with a filled outer electron shell, such as La^{3+}, Y^{3+}, Lu^{3+}, Sc^{3+} and Cd^{2+} are the best dopants for this purpose since they do not generate additional emission bands. The first experiments showed that substantial suppression of slow luminescence is always accompanied by a slight decrease in CVL [5, 6]. For example, the slow component in BaF_2:La(0.2%) decreases by 1.72 times, while the fast one decreases by 1.09 times [13]; the slow and the fast components in BaF_2:La(0.5%) decrease, respectively, by 3.6 and 1.6 times. According to [8], suppression of the slow component in crystalline BaF_2:La starts when the lanthanum content exceeds 1% (Fig. 1). The concentration dependence of slow X-ray luminescence (XRL) in BaF_2:Y is similar to that for BaF_2:La (Fig. 1). A BaF_2:Y(1 at.%) crystal whose slow component was suppressed by 6 times, and the CVL intensity was the same as in pure BaF_2 was synthesized recently [14].

Introducing cadmium considerably suppresses the slow XRL component of BaF_2:Cd (curve *3* in Fig. 1). With the cadmium content of 0.35 mol.%, the intensity of this component is less than 10% compared to that for an undoped crystal, while the intensity of the fast component practically does not change. Unfortunately, Cd^+ ions form in a BaF2:Cd crystal irradiated with X-rays, generating absorption bands in the visible and UV spectral regions [8].

Lutetium (Lu) reduces the intensity of the slow component in BaF_2 by 4 times, but the fast component also decreases considerably [15]. Aside from that, introducing lutetium resulted in deteriorated radiation hardness of such a crystal. According to [6], the CVL decay time for BaF_2:Lu(1.0 mol.%) is 0.4 ns;

this means that a small loss in CVL intensity is compensated by a nearly twofold decrease in the luminescence decay constant.

The spectral and kinetic characteristics of BaF_2 crystals with scandium contents of 0.5, 1.0, and 2.0 mol.% were studied in [16], where the intensity of the slow component for the BaF_2:Sc(1.0%) decreased by 2.4 times.

Since the RbF crystal has CVL [4], it was proposed to increase the intensity of the fast component by introducing rubidium fluoride into barium fluoride. The experiment with a BaF_2:Rb crystal revealed no CVL and a slight decrease in the slow XRL component [17].

Rare-earth ions. A large number of studies have been dedicated to suppression of the slow luminescence component (310 nm band), which is undesirable for fast scintillators. Trivalent rare-earth (RE^{3+}) ions were introduced into barium fluoride crystals as dopants for this purpose. It was established that any rare-earth dopant reduces the intensity of the slow scintillation component [5, 6]. The presence of interstitial fluorine ions F^- serving as charge compensators for trivalent dopants was traditionally believed to be the reason for suppression of the slow component of scintillation by RE^{3+} ions. It was assumed that because these interstitial ions generate energy levels near the top of the crystal's valence band (in the bandgap), they can trap holes from the valence band [8]. This trapping is a competing process between formation of V_k centers and self-trapped excitons, or $(V_k e^-)$*-centers, resulting in decreased STE luminescence intensity. While this model is certainly attractive, it does not explain suppression of the slow component in BaF_2 crystals doped with divalent Cd^{2+}, Mg^{2+} and Sr^{2+} ions [18]. Comparing the dependences of XRL intensity in BaF_2:La and BaF_2:K crystals, the authors of [8] concluded that interstitial F^- ions are only partially responsible for the suppression effect. It was also established that diffusion of excitons to the centers of their nonradiative annihilation makes the main contribution to this effect [8].

Suppression of slow luminescence component of barium fluoride by thermal quenching

CVL intensity is characterized by high thermal stability (tested up to 500°C [18]); this property can be used to eliminate the slow component. The intensity and decay time of the slow XRL component considerably decrease at higher temperatures ranging from room temperature. For example, if the oper-

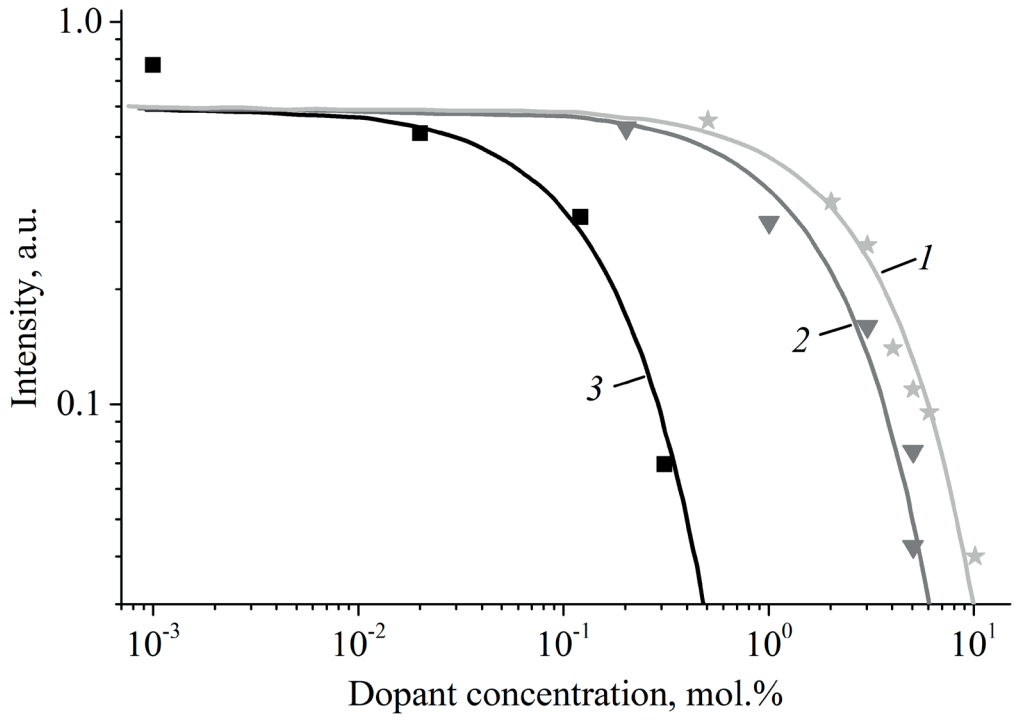

Fig. 1. Concentration dependences of slow XRL luminescence intensity for BaF_2:La (*1*), BaF_2:Y ($_1$) and BaF_2:Cd (*3*) crystals (based on data given in [8])

ating temperature of the device is chosen to be 120°C, the intensity of the slow component is lower than that of the fast component, and the decay time of STE luminescence is approximately 40 ns. This mode of operation of the scintillator can be established in an individual physical experiment, but it is hardly suitable for technical devices. It was found in [19] that the slow XRL component of barium fluoride is completely suppressed at 220°C, and the light yield of the subnanosecond component is 1000 photons/MeV.

Conversion of exciton emission to faster activator luminescence

The main idea of these experiments is to transform emission of self-trapped excitons into faster activator luminescence rather than suppress it. The elements at the beginning of the lanthanide series (Ce, Pr, Nd) are known to possess the most effective allowed (i.e., fast) $5d \rightarrow 4f$ transitions. The heavier rare-earth elements tend to have slow UV luminescence governed by high-spin (HS) $5d \rightarrow 4f$ transitions, forbidden by the spin selection rule. Additionally, a large number of $4f$ levels in some ions (Nd, Eu, Tb, Dy) leads to slow (undesirable) luminescence due to forbidden $4f \rightarrow 4f$ transitions. Therefore, light rare-earth ions Ce^{3+}, Pr^{3+}, Nd^{3+}, as well as ions with a relatively small number of $4f$ levels (Gd^{3+} and Tm^{3+}) are the best candidates for barium fluoride activators.

BaF_2:Ce compound. Cerium serves as an activator in many modern phosphors and scintillators; for this reason, introducing Ce^{3+} ions into barium fluoride was expected to increase the light yield of the crystal and obtain scintillation decay times of several tens of nanoseconds. Early experiments revealed that the light yield of BaF_2:Ce at the optimal concentration (about 0.2 mol.%) of Ce^{3+} ions (the optimal concentration is the one with the maximum luminescence intensity) was slightly lower compared to pure BaF_2 [20, 21]. It was suggested that either Ce aggregates or (Ce^{3+}–O^{2-}) centers form in the crystal if the content of Ce^{3+} ions exceeds 0.2 mol.% [21]. A later study [22] reported on a slight increase in the light yield for a BaF_2:Ce crystal, finding that self-trapped holes in the form of V_k and H centers participate in the recombination process.

Subsequent studies managed to increase the light yield of BaF_2:Ce by 2.5 times compared with pure barium fluoride, but the kinetic characteristics of XRL could not be significantly improved [23]. The BaF_2:Ce crystal exhibits some unusual properties: the XRL spectrum corresponds to emission of Ce^{3+} ions (308 and 322 nm bands), and the kinetics to emission of self-trapped excitons (the main decay constant is equal to 250 ns). A luminescence decay constant of 31 ns is detected in the BaF_2crystal upon direct UV excitation of Ce^{3+} ions [22]. This behavior of BaF_2:Ce is due to superposition of the absorption band of Ce^{3+} ions on the emission band of self-trapped excitons in the region of 280–300 nm, resulting in energy transfer from excitons to Ce ions (STE → Ce^{3+}).

Introducing a lutetium dopant into BaF_2:Ce leads to a decrease in the intensity of the two main Ce^{3+} emission bands and to a new wide XRL band appearing, with a peak at 355 nm [15]. The XLR band at 355 nm in BaF_2:Ce, Lu is believed to be associated with interstitial fluorine ions.

BaF_2:Pr compound. Trivalent praseodymium has a shorter decay time ($5d \rightarrow 4f$ transitions) and a slightly lower XLR intensity in different crystals, compared with those parameters for the Ce^{3+} dopant. The BaF_2:Pr^{3+} crystal has the main decay constant of 28 ns, and a faster component with a duration of 7–8 ns appears as the Pr^{3+} content exceeds 1%. However, the $5d \rightarrow 4f$ emission band overlaps with the core-valence luminescence band; as a result, energy transfer from CVL transitions to Pr^{3+} ions occurs (CVL is not detected). Another drawback of the crystals containing Pr^{3+} is the presence of $f \rightarrow f$ transitions with slow emission.

BaF_2:Nd compound. The first experiments showed a very weak (below the CVL level) ($5d \rightarrow 4f$) luminescence of Nd^{3+} in BaF_2 (slightly higher than the XLR intensity in BaY_2F_8:Nd) [25]. It was subsequently proved for crystals with a higher quality that BaF_2:Nd(1%) samples emit in the UV spectral region (175–200 nm), with the main decay constant of 12 ns [26]. The light yield of the crystal was only 7% lower than that of BaF_2. Adding lanthanum improves the characteristics: the $(La_{0.9},Ba_{0.1})F_{2.9}$:Nd crystal has a narrow (12 nm) luminescence band with a maximum at 175 nm and a short decay time, $\tau = 6.1$ ns [27].

BaF_2:Tm compound. Interconfiguration $5d \rightarrow 4f$ transitions of Tm^{3+}ions in BaF_2 are manifested as a luminescence band with a maximum at 178 nm and a decay time of 5–6 ns [28]. The intensity of this luminescence is lower than the CVL intensity. As the Tm^{3+} concentration increases from 0.1 to 10%, the intensity of the STE band decreases substantially (the same as

for other rare-earth ions), but the yield of the subnanosecond component also decreases with a thulium concentration $C_{Tm} > 0.1\%$.

Ref. [29] investigated the ($5d \rightarrow 4f$) luminescence of Nd^{3+}, Sm^{3+}, Ho^{3+}, Er^{3+}, Tm^{3+} ions in barium fluoride and other alkaline earth fluorides. It was established that the exciton mechanism of energy transfer to $5d$ states of these ions is inefficient in fluorides.

Suppression of slow luminescence component in barium fluoride by double doping

BaF_2:Gd,Ce compound. It was proposed in [30] to introduce 10% of Gd^{3+} into barium fluoride with the addition of the Ce^{3+} co-activator not only as a means of suppressing the slow emission component but also to improve other characteristics of the material. The synthesized $Ba_{0.9}Gd_{0.1}F_{2.1}$ crystal had a high density equal to 5.11 g/cm^3 (4.89 g/cm^3 for undoped BaF_2), and a higher mechanical strength of 240 kg/mm^2 (80 kg/mm^2 for BaF_2). As Ce^{3+} ions were introduced into the compound, the peak of the luminescence band of self-trapped excitons shifted to the long-wavelength region to a value of 350 nm. The $Gd_{0.1}Ba_{0.9}F_{2.1:}Ce$(0.1 mol.%) crystal had a 46% light yield compared to pure barium fluoride and a luminescence decay constant of 30–40 ns. Notably, the decay constant characteristic for the Ce^{3+} ion is manifested in the spectrum due to a shift of the luminescence band to the long-wavelength region. The slow XRL component the crystal was almost completely suppressed. The optimal (before the quenching started) concentration of Ce^{3+} ions in a $Ba_{0.9}Gd_{0.1}F_{2.1}$ is 0.2–0.3 mol.% [30]. Unfortunately, the radiation hardness of a $Ba_{0.9}Gd_{0.1}F_{2.1}$:Ce(0.1 mol.%) crystal is lower than that for pure barium fluoride.

BaF_2:La,Er compound. As noted above, the ions of the second half of the lanthanide series have slow ($5d \rightarrow 4f$) luminescence from the HS $5d$ state. In particular, slow emission of $5d$(HS) $\rightarrow 4f$ transitions is prevalent in the BaF_2:Er^{3+} crystal , which has a high intensity due to presence of a $^2F_{5/2}$ energy level between LS (low-spin) states and HS (high-spin) $5d$ states. This level promotes nonradiative energy transfer to the $5d$(HS) $\rightarrow 4f$ luminescence component, prohibited by the spin selection rule. A red shift of $5d$ excitation bands of Er^{3+} was obtained by introducing 30% of LaF_3 into barium fluoride ($BaLaF_2$:Er^{3+} crystal), and the $^2F_{5/2}$ level was located higher than the $5d$(LS) and $5d$ (HS) levels [31]. As a result, $5d$(LS) $\rightarrow 4f$ transitions, allowed by the selection rules and generating two emission bands in the 140–150 and 152–160 nm regions with a luminescence decay time of 35 ns, were prevalent in the crystal obtained by the authors [31].

BaF_2:La,Ce compound. Since lanthanum usually serves as a "suppressor" of the slow XRL component, and cerium is the best activator, it was of interest to introduce these ions in barium fluoride together. The experiment in [32] established that the decay constant in the BaF_2:La,Ce compound is 76 ns, the slower component is substantially suppressed, and the light yield is lower than in pure barium fluoride.

Radiation hardness of doped BaF_2 crystals

Crystals intended for collider experiments should have a high radiation hardness [5], and high-purity barium fluoride crystals [33, 34] fully satisfy this requirement. *F* centers induced by radiation are formed in the crystal, generating a broad optical absorption band with a peak at 570 nm. This absorption does not affect the position and intensity of the core-valence luminescence bands. Introducing dopants (RE^{3+}, Me^{2+}, etc.) typically reduces the radiation hardness of barium fluoride [34]. The crystals doped with La^{3+} acquire a red color upon irradiation with X-rays, which is due to interstitial fluorine ions forming. A monovalent metal is introduced into the BaF_2:La crystal in the same concentration as the concentration of lanthanum ions in order to increase radiation hardness (reducing the number of interstitial fluorine ions). For example, it was demonstrated that a BaF_2:La(0.3%)K(0.3%) crystal has a higher radiation hardness but a lower suppressive effect than a potassium-free crystal, BaF_2:La(0.3%) [8]. Alkali-containing crystals acquire a blue color upon irradiation with X-rays, which is associated with *F*-aggregates forming due to the presence of fluorine vacancies [8].

The optical absorption level near 500 nm is higher in the irradiated BaF_2:La crystal than in pure barium fluoride, but the absorption intensity becomes comparable for these crystals in the UV region of the spectrum [13]. Radiation resistance of the BaF_2 crystal (absorption bands in the range of 200–800 nm) deteriorates upon doping with Tm, Nd, Gd, Eu. Notably, lead is the most dangerous residual dopant that suppresses CVL, with the maximum of the absorption band located at 205 nm [13].

Other methods for reducing the intensity of slow luminescence component

Using nanoparticles. Nanoparticles are known for their high surface/volume ratios and therefore have different properties than the corresponding single crystals [35, 36]. Luminescence intensity can be increased and luminescence decay time can be decreased by decreasing the size of nanoparticles. These effects are well studied for excitons in semiconductor nanoparticles. Studies into high-band-gap dielectric materials with small-radius excitons are currently in their initial stages. Another advantage of nanoparticles over ordinary particles is that higher activator concentrations can be introduced for them to increase luminescence intensity.

The behavior of luminescence in barium fluoride nanoparticles ranging in size from 20 to 100 nm was studied in [35]. The intensity of the CVL band with decreasing size of nanoparticles from 80 to 30 nm practically does not differ from the CVL intensity for a single-crystal sample of BaF_2, and it is only for samples with the size of 20 nm that it does decrease by 1.5 times. The luminescence intensity of self-trapped excitons decreases by an order of magnitude when nanoparticles 20 nm in size are used instead of a single crystal. The sizes of the given nanoparticles (20–100 nm) substantially exceed the diffusion length of the core hole (about 1.5 nm), which explains the relative stability of CVL intensity. The luminescence intensity of STE decreases starting from a nanoparticle size of 80 nm. The critical size of barium fluoride nanoparticles, for which the luminescence intensity of STE decreases sharply, is about 50 nm. This size is comparable with the thermalization length of photoelectrons (30–100 nm) in fluorides [35].

BaF_2:Ce nanoparticles were obtained and studied in a number of works [37, 38]. The BaF_2:Ce nanoparticles obtained in [37] with a size of 18±3 nm had a cerium luminescence band with a maximum at 370 nm; in this case, the core-valence and exciton luminescence bands were absent. The luminescent characteristics of BaF_2:Ce nanoparticles ranging in size from 1 to 30 nm were considered in [38]. The samples had a wide luminescence band with a maximum at 355 nm. The maximum luminescence intensity was achieved for cerium content of about 15%. The optimal concentration of Ce^{3+} ions in the nanopowders was higher compared to single crystals, which the authors attributed to the decrease in the number of defects (traps) with decreasing nanoparticle size of nanoparticles.

Using composites. Nanoparticles with good scintillation properties are difficult to use as radiation detectors. Composites consisting of heavy inorganic micro- and nanoparticles and ultrafast organic phosphors are used to synthesize bulk scintillators. The inorganic ("heavy") particles in a composite scintillator efficiently absorb ionizing radiation, while part of the absorbed energy is transferred to organic molecules in contact with the particles, with nanosecond scintillation pulses then induced in the molecules. A polymer based on polystyrene activated with PPO (2,5-diphenyloxazole) and POPOP (1,4-bis(5-phenyloxazol-2-yl) benzene) scintillators is usually chosen as an organic binder, since it has fast (less than 2 ns) scintillations.

Barium fluoride has a low refractive index $n = 1.478$ at a wavelength of 500 nm, which is convenient for combining it with a polymer matrix. BaF_2:Ce nanocomposites were prepared in [38] using epoxy resins. The light yield of the BaF_2:15%Ce composite was approximately 5 times higher than that of the BaF_2:2%Ce crystal.

Zinc oxide is known as an effective scintillator with a subnanosecond luminescence time (like BaF_2). Bound excitons are responsible for its luminescence [39]. Zinc oxide (ZnO) nanoparticles 7.5–30 nm in size were successfully embedded into a barium fluoride film in [40]. Radiofrequency magnetron sputtering with subsequent thermal annealing of the samples was used for this purpose. Barium fluoride has a low refractive index compared with zinc oxide (whose refractive index is $n \approx 2.4$), contributing, it is believed, to formation of optical waveguides in the crystal. It was established that the intensity of the subnanosecond ZnO luminescence component in BaF_2 increases significantly with annealing temperature increasing from 400 to 800°C [40].

Synthesizing ceramics. Attempts have been made in the recent years to improve kinetic and other characteristics of barium fluoride by creating ceramics, including nanoceramics [23, 41]. Notably, ceramics have a number of advantages over single crystals, in particular, high mechanical and thermal strength.

Optical ceramics of barium fluoride was prepared by hot-pressing and thermoforming using the K-2718 system (INKROM CJSC) [23, 41]. Maximum transparency of ceramics in a wide optical range was achieved by varying

two main parameters: temperature and degree of deformation. To increase the intensity of the fast component and reduce the decay constant of the slower component, the ceramics was annealed in gaseous carbon tetrafluoride CF_4 for 24 hours at a temperature of about 1180°C. As a result, the transparency of the ceramics obtained was comparable to the transparency of the corresponding single crystal in the visible spectral region and slightly lower than that in the short-wave region ($\lambda < 250$ nm).

Using filters and other devices. Subnanosecond luminescence of barium fluoride can be induced with a suitable UV filter, however, as a rule, the filter reduces the luminescence intensity. A special short-wave filter has been developed recently, suppressing the slow luminescence component of barium fluoride to 1% [42].

The so-called shifters, i.e., organic substances that shift the UV luminescence to a longer wavelength region are used to make the "fast" UV luminescence of barium fluoride more acceptable for photomultipliers that are sensitive in the visible region of the spectrum. Defenyl-anthracene, perylene, and other shifters were tested in [43]; using them helped increase the time constant to 2.5–7 ns, and decrease the light yield.

Since the decay times of the fast and slow components differ by almost 3 decimal orders, these components can be separated at the output of the photodetector using electronic devices. A schematic for such a device was proposed in [44].

Experimental procedure

The given crystals were grown by the Stepanov–Stockbarger method at INKROM. The obtained samples were classified as VUV crystals, i.e., as materials with high transparency in the short-wave region of the spectrum. Polished samples of single crystals prepared in the form of parallelepipeds 5 Ч 10 Ч 15 mm in size were used for spectral measurements. The optical transmission spectra of the samples were recorded from the longitudinal size of the sample (15 mm) using a VMR-2 spectrophotometer. The luminescence spectra were captured with continuous X-ray excitation (40 kV, 14 mA). The detecting part of the setup contained an MDR-2 monochromator and a Hamamatsu H8259-01 photon counting system. Thermally stimulated luminescence (TSL) curves were measured in samples 1 mm thick. Before the measurements, the samples were irradiated with an X-ray beam at a temperature of 80 K, and then heated at a rate of 0.3 K/min.

An X-ray source with the following parameters was used to measure the luminescence kinetics: 30 kV, 500 mA, pulse duration of 1 ns, and pulse repetition rate of 12 kHz [45]. The detecting part of the device was assembled by the standard start/stop scheme; the time resolution of the system was no worse than 50 ps. The luminescence spectra and kinetics were measured in reflection geometry: the angle between the direction of X-ray radiation and the photodetector was 90°.The measurements were taken at room temperature.

Experimental results and discussion

X-ray luminescence (XRL) spectra of BaF_2 and BaF_2:Tm crystals are shown in Fig. 2. The spectra exhibit an intense exciton band with a peak at 310 nm and a core-valent luminescence (CVL) band with peaks at 196 and 220 nm; the spectra were not corrected for sensitivity of the setup, which means that the intensity of the CVL bands is actually higher. The low-intensity bands with peaks at 347, 360, and 450 nm (curves *2* and *3*, Fig. 2) are responsible for the $f \rightarrow f$ electronic transitions in the thulium ion Tm3+ [28]. Evidently, the intensity of the exciton band decreases by 6 times when the thulium content is 0.5%, but the CVL intensity also slightly decreases. Introducing 2.0% of thulium leads to a decrease in the exciton band by 7 times, and CVL decreases by 1.6 times. Thus, the necessary (by more than 10 times) suppression of the exciton band cannot be achieved without a significant decrease in CVL for the BaF2:Tm crystal.

Inset to Fig. 2 shows the XRL decay curves recorded in BaF_2 and BaF_2: Tm(0.5%) crystals. It can be seen that the intensity of the slow XRL component of the doped compound is slightly lower than that of pure barium fluoride. The decay time constant of the slow component for thulium-doped sample is noticeably lower and is about 400 ns (while for pure barium fluoride it is 630 ns). As follows from the XRL spectra and kinetics, the effect of suppression of the slow component in BaF_2:Tm begins with a thulium content of 0.5%.

The total optical transmission spectra of the crystals are shown in Fig. 3. The BaF_2:Tm (0.5%) spectrum contains a minimum at 260 nm, for which the $^3H_6 \rightarrow {}^5P_2$ electronic transition in the Tm^{3+} ion is responsible, as well as

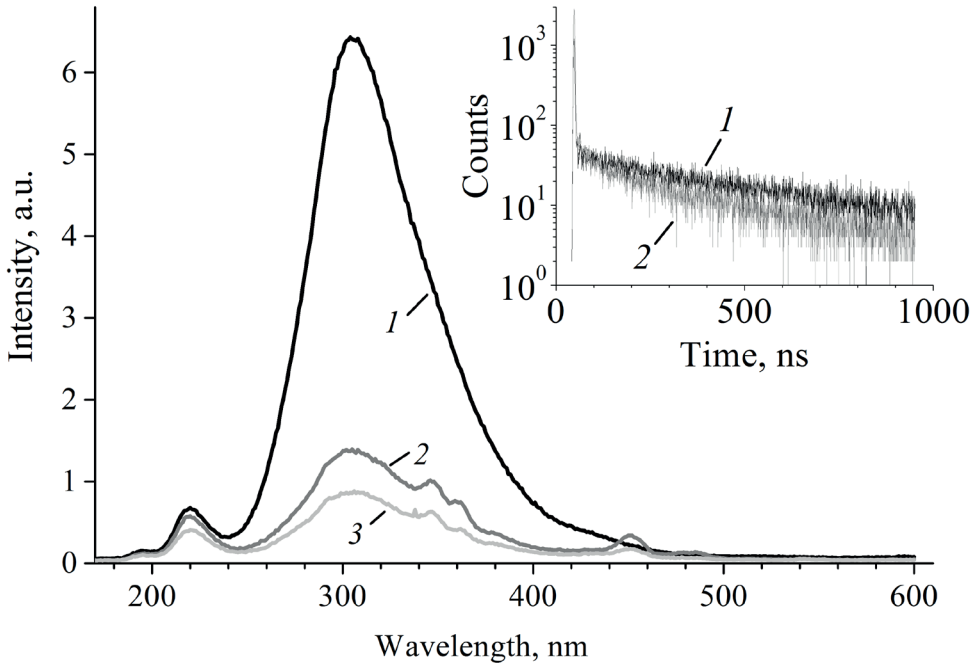

Fig. 2. X-ray luminescence spectra and kinetics
of BaF_2 (*1*), BaF_2:Tm(0.5%) (*2*) and BaF_2:Tm (2.0%) (*3*) crystals

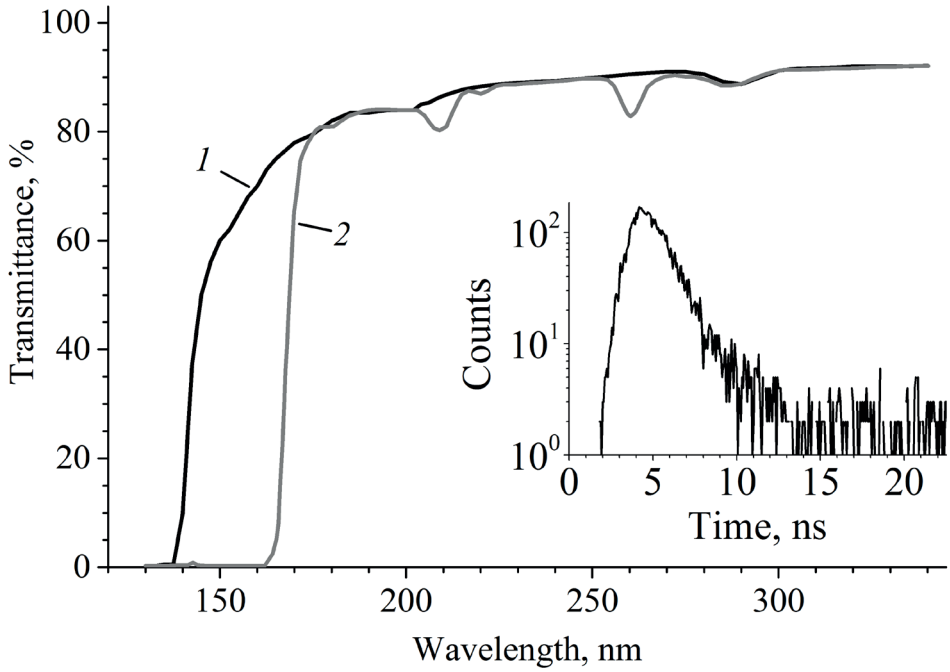

Fig. 3. Optical transmittance spectra for BaF_2 (*1*) and BaF_2:Tm(0.5%) (*2*) crystals;
samples were 5 mm thick.
Inset shows XRL kinetics of the BaF_2Tm(0.5%) crystal, measured in a short time interval

a minimum of unknown origin at 208 nm. The BaF_2:Tm(0.5%) crystal 5 mm thick has rather high (more than 80%) transparency in the CVL region (175–260 nm), however it is lower than in pure barium fluoride (see Fig. 1). Therefore, introducing Tm^{3+} ions into BaF_2 worsens the conditions for fast luminescence (CVL) from the crystal, which is particularly important for large samples. Inset to Fig. 3 shows, as an example, the XRL kinetics curve of a BaF_2:Tm(0.5%) crystal, measured in a short time interval. The decay time of the fast component of the compound was 0.8±0.1 ns.

It is known that radiation hardness of a material can be assessed by the intensity of thermally stimulated luminescence (TSL) peaks. Fig. 4 shows the TSL curves for BaF_2 and BaF_2:Tm(1.0%) crystals, measured after the crystals were irradiated with X-rays (40 kV) for 2 minutes. It can be seen that the non-activated crystal has an intense thermal peak with a maximum at 114 K. Such low-temperature peaks are characteristic for crystals of the fluorite group, reflecting the delocalization of V_k-centers. The low-temperature peak in the BaF_2:Tm(1.0%) crystal is located at 138 K, and thermal peaks are recorded in the region from 200 to 300 K, for which V_{kA} centers and aggregates of Tm^{2+} ions and interstitial fluorine ions are responsible [46]. Additionally, a high-temperature peak is recorded at 453 K in BaF_2:Tm(1.0%), induced by deep traps. These traps may be involved in afterglow luminescence, impairing the scintillation properties of the crystal. The data obtained indicate that doping barium fluoride with Tm_{3+} ions worsens the radiation hardness of the crystal; the same conclusion was reached in [5].

Introducing Sc^{3+} ions into a BaF_2 crystal leads to significant suppression of the slow component; the corresponding XRL spectra have the form similar to that shown in Fig. 2. Fig. 5 shows the total transmittance spectra of the BaF_2 and BaF_2:Sc(1.0%) crystals. BaF2:Sc(1.0%) exhibits a characteristic reduction in the transmission near 290 nm. We also recorded an absorption band at 290 nm in a BaF_2:Cd crystal (not shown). Interestingly, this band is also observed when La^{3+} [5] and Y^{3+} ions are introduced into BaF_2 [14]. The nature of this band remains unknown; it can be argued only that substituting barium with an ion with a filled outer shell leads to a defect appearing in BaF_2, producing absorption at 290 nm.

Inset to Fig. 5 shows the X-ray decay curves of BaF_2 and BaF_2:Sc(1.0%) crystals. A noticeable decrease in the integral intensity of the slow XRL component was registered in a

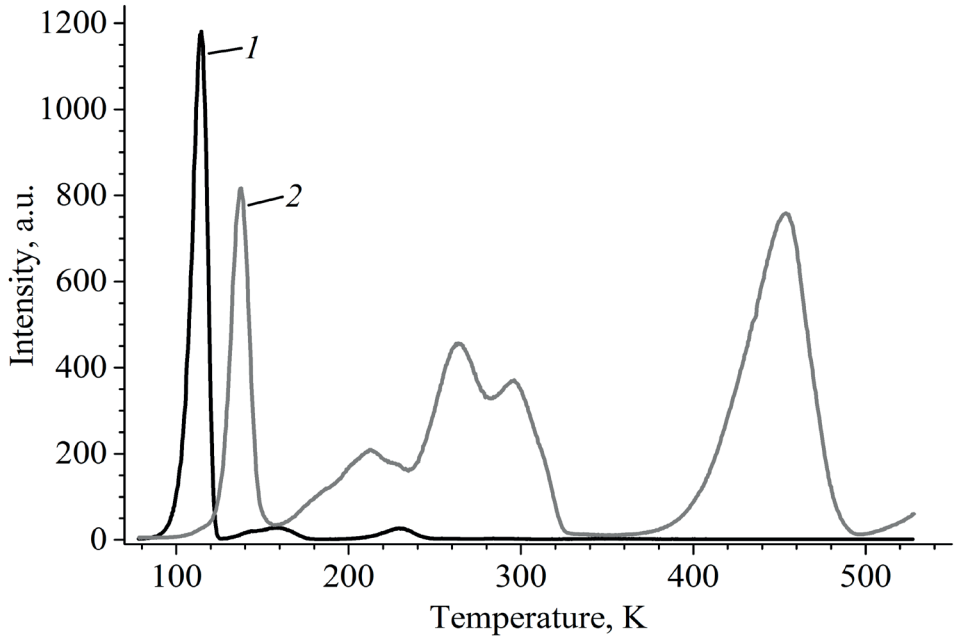

Fig. 4. Thermally stimulated luminescence curves for BaF_2 (*1*) and BaF_2:Tm (2.0 %) (*2*) crystals. Sample heating rate was 0.3 K/min

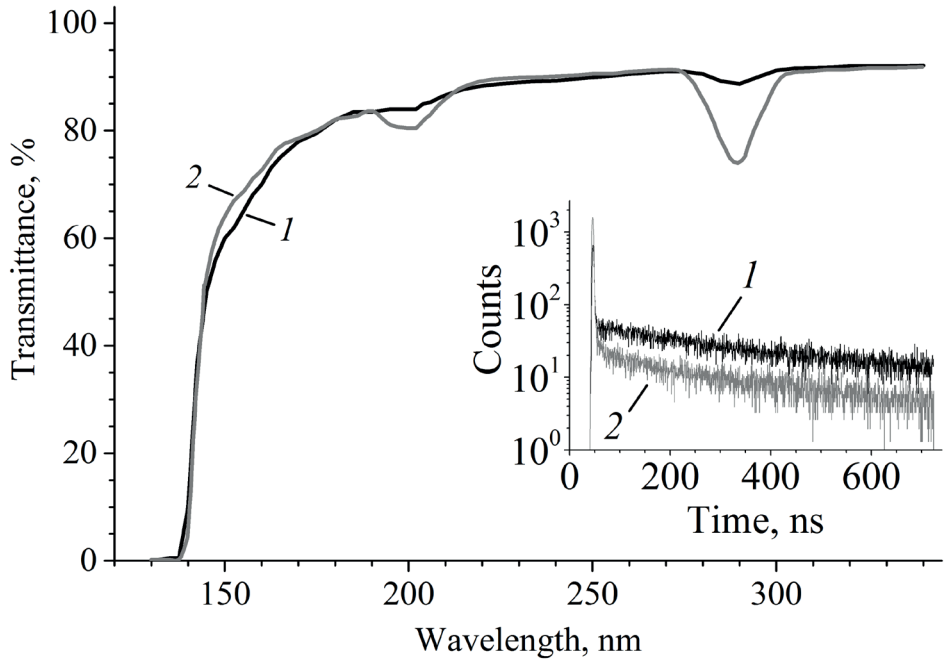

Fig. 5. Optical transmittance spectra and XRL kinetics (inset)
of BaF2(1) and BaF2:Sc(1.0%) (2) crystals;
spectra were collected for 5 mm thick samples

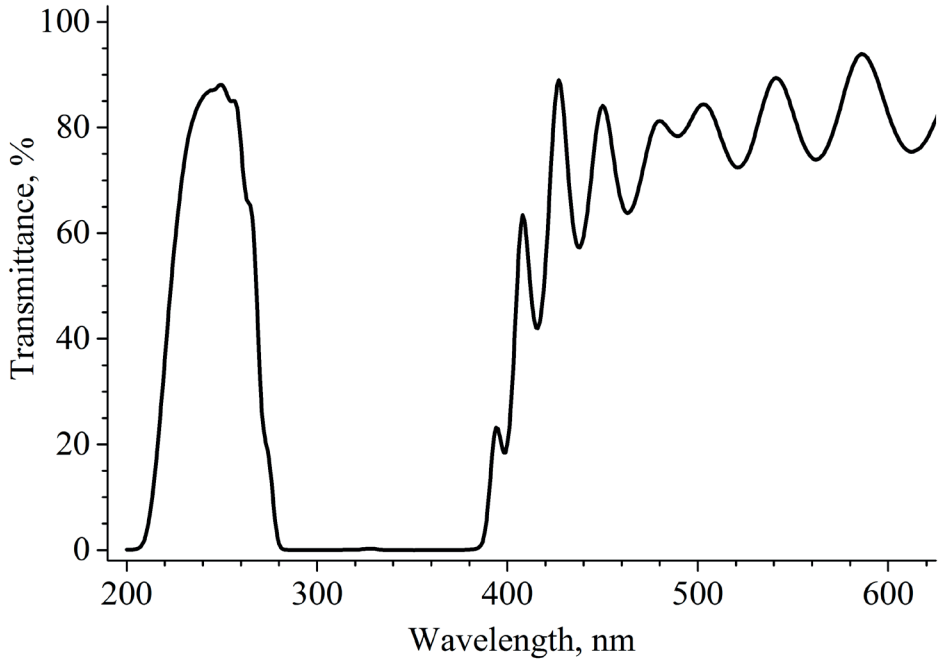

Fig. 6. Optical transmittance spectrum of multilayer filter
sprayed on quartz glass

BaF2:Sc(1.0%) crystal, as compared with pure barium fluoride. The time decay constant of the slow component of the sample doped with scandium is less than that of pure BaF_2 and is about 240 ns.

Another way to suppress the slow luminescence component is to use a filter that is transparent in the spectral region of CVL and opaque in the region of exciton radiation of BaF_2. Fig. 6 shows the transmission spectrum for a filter of this type, obtained by layer-by-layer sputtering of rare-earth oxides on a quartz substrate. Apparently, the transparency of the filter in the region of the main OVL peak (220 nm) is 50%, and is close to zero near the exciton luminescence peak (310 nm).

Conclusion

We have conducted a series of experiments and analyzed the data given in literature, concluding that suppressing the slow component of X-ray luminescence in barium fluoride by introducing a dopant seems insufficiently effective. Introducing trivalent ions leads to defects forming, in particular in interstitial fluorine ions. The crystal structure of divalent ions is typically distorted. Suppressing the slow component of luminescence by introducing dopants into BaF_2 has the following disadvantages:

required decrease in the intensity of the slow component (by more than 10 times) is accompanied by a substantial decrease in CVL;

doped crystal is generally less transparent than a pure one;

radiation hardness of barium fluoride typically deteriorates as dopants are introduced;

it is fairly difficult to uniformly distribute dopants in large crystals (the required length of BaF_2 samples for the new collider is more than 20 cm).

Studies of nanoparticles, nanoparticle-based composites and ceramics aimed at obtaining the optimal ratio of intensities of the fast and slow luminescence components of BaF_2 have not yielded satisfactory results either.

We have found that using a filter that is transparent in the spectral region of CVL and opaque in the region of exciton luminescence of BaF_2 is the most effective method to suppress the slow component of luminescence. Such a filter can be sprayed directly onto the surface of the output window of the BaF_2 sample.

We plan to assemble and test a system that includes a BaF_2 scintillator with a filter and a solid-state photodetector.

REFERENCES

[1] **N.N. Ershov, N.G. Zakharov, P.A. Rodnyi,** Spektralno-kineticheskoye issledovaniye kharakteristik sobstvennoy lyuminestsentsii kristallov tipa flyuorita [Studies in spectra and kinetics of intrinsic luminescence of fluorite-type crystals] Optics and Spectroscopy. 53 (1) (1982) 51–54.

[2] **M. Laval, M. Moszynski, R. Allemand, et al.,** Barium fluoride inorganic scintillator for subnanosecond timing, Nuclear Instruments and Methods in Physics Research. 206 (1-2) (1983) 168–176.

[3] **Yu.M. Aleksandrov, V.N. Makhov, P.A. Rodnyi, et al.,** Sobstvennaya lyuminestsentsiya BaF_2 pri impulsnom vozbuzhdenii sinkhrotronnym izlucheniyem [Intrinsic luminescence under pulse excitation by synchrotron radiation], Soviet Physics, Solid State, 26 (9) (1984) 265–286.

[4] **P.A. Rodnyi,** Ostovno-valentnyye perekhody v shirokozonnykh ionnykh kristallakh [Core-valence transitions in the high-bandgap ion crystals], Physics of the Solid State. 34 (7) (1992) 1975–1998.

[5] **C.L. Woody, P.W. Levy, J.A. Kierstead,** Slow component suppression and radiation damage in doped BaF_2 crystals, IEEE Transactions on Nuclear Science. 36 (1) (1989) 536–542.

[6] **B.P. Sobolev, E.A. Krivandina, S.E. Derenzo, et al.,** Suppression of BaF_2 slow component of X-ray luminescence in non-stoichiometric $Ba_{0.9}R_{0.1}F_{2.1}$ crystals (R = rare earth element), Proceedings of The Material Research Society: Scintillator and Phosphor Materials (M.J. Weber, ed.), (1994) 277–283.

[7] **A. Nepomnyashchikh, E.A. Radzhabov, A.V. Egranov, V.F. Ivashechkin,** Luminescence of BaF_2-LaF_3, Radiation Measurements. 33 (2001) 759–762.

[8] **E. Radzhabov, A. Istomin, A. Nepomnyashikh, et al.,** Exciton interaction with impurity in barium fluoride crystals, Nuclear Instruments and Methods in Physics Research. A. 537 No. 1–2. (2005) 71–75.

[9] **S. Diehl, R.W. Novotny, B. Wohlfahrt, R. Beck,** Readout concepts for the suppression of the slow component of BaF_2 for the upgrade of the TAPS spectrometer at ELSA, Journal of Physics: Conference Series. 587 (2015) 012044.

[10] **Ch.K. Najeeb, J.-H. Lee, J. Chang, et al.,** Ultrafast UV-photo detector based on single-walled carbon nanotube/PEDOT-

PSS composites, Journal of Nanoscience and Nanotechnology. 9 (2009) 6928–6933.

[11] **D. Hitlin, J.H. Kim, J. Trevor, et al.,** An APD for the detection of the fast scintillation component of BaF_2, IEEE Transactions on Nuclear Science. 63 (2) (2016) 513–515.

[12] **R.-Y. Zhu,** The next generation of crystal detectors, Journal of Physics: Conference Series. 587 (2015) 012055.

[13] **P. Schotanus, P. Dorenbos, C.W.E. van Eijk, R.W. Hollander,** Recent developments in scintillator research, IEEE Transactions on Nuclear Science. 36 (1) (1989) 132–136.

[14] **J. Chen, F. Yang, L. Zhang, et al.,** Slow scintillation suppression in yttrium doped BaF_2 crystals, IEEE Transactions on Nuclear Science. 65 (8) (2018) 2147–2151.

[15] **V. Nesterkina, N. Shiran, A. Gektin, et al.,** The Lu-doping effect on the emission and the coloration of pure and Ce-doped $LiLuF_4$ crystals, Radiation Measurements. 42 (2007) 819–822.

[16] **D.M. Seliverstov, A.A. Demidenko, E.A. Garibin, et al.,** New fast scintillators on the base of BaF_2 crystals with increased light yield of 0.9 ns luminescence for TOF PET, Nuclear Instruments and Methods in Physics Research, A. 695 (2012) 369–372.

[17] **P. Dorenbos, R.W. Visser, C.W.E. van Eijk, et al.,** Photon yields and decay times of cross luminescence in ionic crystals, IEEE Transactions on Nuclear Science. 39 (4) (1992) 506–510.

[18] **A.V. Golovin, N.G. Zakharov, P.A. Rodnyi,** Mekhanizm korotkovolnovoy lyuminestsentsii ftorida bariya [A shortwave luminescent mechanism of barium fluoride], Optics and Spectroscopy. 65 (1) (1988) 176–180.

[19] **M. Biasini, D.B. Cassidy, S.H.M. Deng, et al.,** Suppression of the slow component of scintillation light in BaF_2, Nuclear Instruments and Methods in Physics Research, A. 553 (3) (2005) 550–558.

[20] **P. Dorenbos, R. Visser, R.W. Hollander, et al.,** The effects of La^{3+} and Ce^{3+} dopants on the scintillation properties of BaF_2 crystals, Radiation Effects and Defects in Solids. 119–121 (1) (1991) 87–92.

[21] **C.W.E. Van Eijk,** Inorganic-scintillator development, Nuclear Instruments and Methods in Physics Research, A. 460 (1) (2001) 1–14.

[22] **A.J. Wojtowicz, P. Szupryczynski, J. Glodo, et al.,** Radioluminescence and recombination processes in BaF_2:Ce, Journal of Physics: Condensed Matter. 12 (2000) 4097–4124.

[23] **P.A. Rodnyy, Gain S.D., I.A. Mironov, et al.,** Spectral-kinetic characteristics of crystals and nanoceramics based on BaF_2 and BaF_2:Ce, Physics of the Solid State. 52 (9) (2010) 1910–1914.

[24] **E. Radzhabov, V. Nagirnyi,** Excitation of Pr^{3+} ions in alkaline-earth fluorides, IOP Conference Series: Materials Science and Engineering. 15 (2010) 012029

[25] **R. Visser, P. Dorenbos, C.W.E. Van Eijk, et al.,** The scintillation intensity and decay from Nd^{3+} $4f^2$ $5d$ and $4f^3$ excited states in several fluoride crystals, Journal of Physics: Condensed Matter. 5 (44) (1993) 8437 – 8460.

[26] **M. Kirm, A. Lushchik, Ch. Lushchik, et al.,** VUV luminescence of BaF_2, BaF_2:Nd and BaY_2F_8 crystals under inner-shell excitation, Nuclear Instruments and Methods in Physics Research, A. 486 (1–2) (2002) 422–425.

[27] **M. Cadatal, Y. Furukawa, Y.-S. Seo, et al.,** Vacuum ultraviolet optical properties of a micro-pulling-down-method grown Nd^{3+}:$(La_{0.9}, Ba_{0.1})F_{2.9}$, Journal of the Optical Society of America, B. 25 (7) (2008) B27–B31.

[28] **N. Abe, Y. Yokota, T. Yanagida, et al.,** Evaluation of Gamma-Ray Response of Tm:BaF_2 Single Crystals, IEEE Transactions on Nuclear Science, 57 (3) (2010) 1304–1307.

[29] **E. Radzhabov, V. Nagirnyi, M. Kirm, E. Prosekina,** $5d - 4f$ emission of Nd^{3+}, Sm^{3+}, Ho^{3+}, Er^{3+}, Tm^{3+} ions in alkaline earth fluorides, IEEE Transactions on Nuclear Science. 59 (5) (2012) 2074–2078.

[30] **M. Kobayashi, M. Ishii, B.P. Sobolev, et al.,** Scintillation characteristics of nonstoichiometric phases formed in MF_2–GdF_3–CeF_3 system, Part I. (M = Ba), scintillation of $Ba_{0.9}Gd_{0.1-x}Ce_xF_{2.1}$ ($0 < x < 0.1$) fluorite-type crystals, Nuclear Instruments and Methods in Physics Research, A. 421 (1–2) (1999) 180–190.

[31] **A.J. Wojtowicz, S. Janus, D. Piatkowski,** Fast and efficient VUV/UV emissions from (Ba, La)F_2:Er crystals, Journal of Luminescence. 129 (2009) 1594–1597.

[32] **Sh. Kurosawa, T. Yanagida, Yu. Yokota, A. Yoshikawa,** Crystal growth and scintillation properties of fluoride scintillators, IEEE Transactions on Nuclear Science. 59 (5) (2012) 2173–2176.

[33] **V.V. Yanovsky, V.M. Reiterov, P.A. Rodnyi,** Effect of gamma-radiation on optical characteristics of barium fluoride scintillation crystals, Nuclear Physics, B. (Proceedings. Supplements). 23A (1991) 347–351.

[34] **R.-Y. Zhu,** On quality requirements to the barium fluoride crystals, Nuclear Instruments and Methods in Physics Research, A. 340 (3) (1994) 442–457.

[35] **V.V. Vistovskyy, A.V. Zhyshkovych, Ya.M.**

Chornodolskyy, **et al.,** Self-trapped exciton and core-valence luminescence in BaF_2 nanoparticles, Journal of Applied Physics. 114 (2013)194306.

[36] **Z. Kang, M. Barta, J. Nadler, et al.,** Synthesis of BaF_2:Ce nanophosphor and epoxy encapsulated transparent nanocomposite, Journal of Luminescence. 131 (10) (2011) 2140–2143.

[37] **L.G. Jacobsohn, K.B. Sprinkle, S.A. Roberts, et al.,** Fluoride Nanoscintillators, Journal of Nanomaterials. 2011 (2011) 523638.

[38] **L.G. Jacobsohn, C.J. Kucera, T.L. James, et al.,** Preparation and characterization of rare earth doped fluoride nanoparticles, Materials. 3 (2010) 2053–2068.

[39] **P.J. Simpson, R. Tjossem, A.W. Hunt, et al.,** Superfast timing performance from ZnO scintillators, Nuclear Instruments and Methods in Physics Research, A. 505 (1–2) (2003) 82–84.

[40] **C.H. Zang, Y.C. Liu, R. Mu, et al.,** Optical properties of ZnO nanocrystals embedded in BaF_2 film fabricated by magnetron sputtering, Journal of Physics D: Applied Physics. 40 (2007) 5598–5601.

[41] **S.Kh. Batygov, L.S. Bolyasnikova, E.A. Garibin, et al.,** BaF_2:Ce^{3+} scintillation ceramics, Doklady Akademii Nauk. 422 (2) (2008) 179–181.

[42] **H. Han, Z. Zhang, X. Weng, et al.,** Development of a fast radiation detector based on barium fluoride scintillation crystal, The Review of Scientific Instruments. 84 (2013) 073503.

[43] **T.A. De Vol, D.K. Wehe, G.F Knol,** Evaluation of wavelength shifters for spectral separation of barium fluoride emissions, Nuclear Instruments and Methods in Physics Research Section, A. 348 (1) (1994) 156–162.

[44] **C. Boiano, R. Bassini, A. Pullia, et al.,** A fast-stretcher for an easy acquisition of the fast component of BaF_2 detectors signals, IEEE Nuclear Science Symposium Conference Record. 3 (2004) 1349–1351.

[45] **P.A. Rodnyi, S.B. Mikhrin, A.N. Mishin, A.V. Sidorenko,** Small-size pulsed X-ray source for measurements of scintillator decay time constants, IEEE Nuclear Science Symposium, Conference Record. 48 (6) (2001) 2340–2343.

[46] **J.H. Beaumont, W. Hayes, D.L. Kirk, G.P. Summers,** An investigation of trapped holes and trapped excitons in alkaline earth fluorides, Proceedings of the Royal Society of London, Ser. A. 315 (1520) (1970) 69–97.

Received 28.01.2019, accepted 14.02.2019.

THE AUTHORS

RODNYI Piotr A.
Peter the Great St. Petersburg Polytechnic University
29 Politechnicheskaya St., St. Petersburg, 195251, Russian Federation
rodnyi@physics.spbstu.ru

GARIBIN Evgeniy A.
CJS «INCROM»
36-1 Babushkina St., St. Petersburg, 193171, Russian Federation
e.garibin@incrom.ru

VENEVTSEV Ivan D.
Peter the Great St. Petersburg Polytechnic University
29 Politechnicheskaya St., St. Petersburg, 195251, Russian Federation
Venevtsev.Ivan@gmail.com

DAVYDOV Yuriy I.
Joint Institute for Nuclear Research
6 Joliot-Curie St., Dubna, Moscow region, 141980, Russian Federation
Davydov@jinr.ru

СПИСОК ЛИТЕРАТУРЫ

1. **Ершов Н.Н., Захаров Н.Г., Родный П.А.** Спектрально-кинетическое исследование характеристик собственной люминесценции кристаллов типа флюорита // Оптика и спектроскопия 1982. Т. 1 № .53. С. 89–93.

2. **Laval M., Moszyncki M., Allemand R., Cormoreche E., Guinet P., Odru R., Vacher J.** Barium fluoride – inorganic scintillator for subnanosecond timing // Nuclear Instruments and Methods in Physics Research. 1983. Vol. 206. No. 1–2. Pp. 168–176.

3. Александров Ю.М., Махов В.Н., Родный П.А., Сырейщикова Т.И., Якименко М.Н. Собственная люминесценция BaF_2 при импульсном возбуждении синхротронным излучением // Физика твердого тела. 1984. Т. 26. № 9. С. 265–286.

4. Родный П.А. Остовно-валентные перев ходы в широкозонных ионных кристаллах // Физика твердого тела. 1992. Т. 7 № .34. С. 1975–1998.

5. **Woody C.L., Levy P.W., Kierstead J.A.** Slow component suppression and radiation damage in doped BaF_2 crystals // IEEE Transactions on Nuclear Science. 1989. Vol. 36. No. 1. Pp. 536–542.

6. **Sobolev B.P., Krivandina E.A., Derenzo S.E., Moses W.W., West A.C.** Suppression of BaF_2 slow component of X-ray luminescence in non-stoichiometric $Ba_{0.9}R_{0.1}F_{2.1}$ crystals (R = rare earth element) // Proceedings of the Material Research Society: Scintillator and Phosphor Materials; M.J. Weber (Ed.). Cambridge, Cambridge University Press, 1994. Pp. 277–283.

7. **Nepomnyashchikh A., Radzhabov E.A., Egranov A.V., Ivashechkin V.F.** Luminescence of BaF_2–LaF_3 // Radiation Measurements. 2001. Vol. 33. No. 5. Pp. 759–762.

8. **Radzhabov E., Istomin A., Nepomnyashikh A., Egranov A., Ivashechkin V.** Exciton interaction with impurity in barium fluoride crystals // Nuclear Instruments and Methods in Physics Research. A. 2005. Vol. 537. No. 1–2. Pp. 71–75.

9. **Diehl S., Novotny R.W., Wohlfahrt B., Beck R.** Readout concepts for the suppression of the slow component of BaF_2 for the upgrade of the TAPS spectrometer at ELSA //Journal of Physics: Conference Series. 2015. Vol. 587. P. 012044.

10. **Najeeb Ch.K., Lee J.-H., Chang J., Kang W.-S., Kim J.H.** Ultra fast UV-photo detector based on single-walled carbon nanotube/PEDOT-PSS composites // Journal of Nanoscience and Nanotechnology. 2009. Vol. 9. No. 12. Pp. 6928–6933.

11. **Hitlin D., Kim J.H., Trevor J., HennessyJ., Hoenk M., Jewell A., R. Farrell R., McClish M.** An APD for the detection of the fast scintillation component of BaF_2 // IEEE Transactions on Nuclear Science. 2016. Vol. 63. No. 2. Pp. 513–515.

12. **Zhu R.-Y.** The next generation of crystal detectors // Journal of Physics: Conference Series. 2015. Vol. 587. P. 012055.

13. **Schotanus P., Dorenbos P., Van Eijk C.W.E., Hollander R.W.** Recent developments in scintillator research // IEEE Transactions on Nuclear Science. 1989. Vol. 36. No. 1. Pp. 132–136.

14. **Chen J., Yang F., Zhang L., Zhu R.-Y., Du Y., Wang S., Sun S., Li X.** Slow scintillation suppression in yttrium doped BaF_2 crystals // IEEE Transactions on Nuclear Science. 2018. Vol. 65. No. 8. Pp. 2147–2151.

15. **Nesterkina V., Shiran N., Gektin A., Shimamura K., Villora E.** The Lu-doping effect on the emission and the coloration of pure and Ce-doped $LiLuF_4$ crystals // Radiation Measurements. 2007. Vol. 42. No. 4–5. Pp. 819–822.

16. **Seliverstov D.M., Demidenko A.A., Garibin E.A., Gain S.D., Gusev, P.P. Fedorov Yu.I., Kosyanenko S.V., Mironov I.A., Osiko V.V., Rodnyi P.A., Smirnov A.N., Suvorov V.M.** New fast scintillators on the base of BaF_2 crystals with increased light yield of 0.9 ns luminescence for TOF PET // Nuclear Instruments and Methods in Physics Research. A. 2012. Vol. 695. Pp. 369–372.

17. **Dorenbos P., Visser R.W., van Eijk C.W.E, Valbis J., Khaidukov N.M.** Photon yields and decay times of cross luminescence in ionic crystals // IEEE Transactions on Nuclear Science. 1992. Vol. 39. No. 4. Pp. 506–510.

18. Головин А.В., Захаров Н.Г., Родный П.А. Механизм коротковолновой люминеси ценции фторида бария // Оптика и спектроскопия. 1988. Т. 65. № 1. С. 176–180.

19. **Biasini M., Cassidy D.B., Deng S.H.M., Tanaka H.K.M., Mills A.P. Jr.** Suppression of the slow component of scintillation light in BaF_2 // Nuclear Instruments and Methods in Physics Research. A. 2005. Vol. 553. No. 3. Pp. 550–558.

20. **Dorenbos P., Visser R., Hollander R.W., Van Eijk C.W.E., Den Hartog H.W.** The effects of La^{3+} and Ce^{3+} dopants on the scintillation properties of BaF_2 crystals // Radiation Effects and Defects in Solids. 1991. Vol. 119–121. No. 1. Pp. 87–92.

21. **Van Eijk C.W.E.** Inorganic-scintillator development // Nuclear Instruments and Methods in Physics Research. A. 2001. Vol. 460. No. 1. Pp. 1 – 14.

22. **Wojtowicz A.J., Szupryczynski P., Glodo**

J., Drozdowski W., Wisniewski D. Radioluminescence and recombination processes in BaF_2:Ce // Journal of Physics: Condensed Matter. 2000. Vol. 12. No. 17. Pp. 4097–4124.

23. Родный П.А., Гаин С.Д., Миронов И.А., Гарибин Е.А., Демиденко А.А., Селиверстов Д.М., Гусев Ю.И., Федоров П.П., Кузнецов С.В. Спектрально-кинетические характеристики кристаллов и нанокерамик на основе BaF_2 и BaF_2:Ce // Физика твердого тела 2010. Т. 9 № .52. С. 1784–1780.

24. **Radzhabov E., Nagirnyi V.** Excitation of Pr^{3+} ions in alkaline-earth fluorides // IOP Conference Series: Materials Science and Engineering. 2010. Vol. 15. No. 1. P. 012029.

25. **Visser R., Dorenbos P., Van Eijk C.W.E., Meijerink A., Den Hartog H.W.** The scintillation intensity and decay from Nd^{3+} $4f^25d$ and $4f^3$ excited states in several fluoride crystals //Journal of Physics: Condensed Matter. 1993. Vol. 5. No. 44. Pp. 8437–8460.

26. **Kirm M., Lushchik A., Lushchik Ch., Makhov V., Negodin E., Vielhauer S., Zimmerer G.** VUV luminescence of BaF_2, BaF_2:Nd and BaY_2F_8 crystals under inner-shell excitation // Nuclear Instruments and Methods in Physics Research. A. 2002. Vol. 486. No. 1–2. Pp. 422–425.

27. **Cadatal M., Furukawa Y., Seo Y.-S., Ono S., Estacio E., Murakami H., Fujimoto Y., Sarukura N., Nakatsuka M., Fukuda K., Simura R., Suyama T., Yoshikawa A., Saito F.** Vacuum ultraviolet optical properties of a micro-pulling-down-method grown Nd^{3+}:$(La_{0.9}, Ba_{0.1})F_{2.9}$ // Journal of the Optical Society of America. B. 2008. Vol. 25. No. 7. Pp. B27–B31.

28. **Abe N., Yokota Y., Yanagida T., Kawaguchi N., Pejchal J., Yoshikawa A.** Evaluation of gamma-ray response of Tm:BaF_2 single crystals // IEEE Transactions on Nuclear Science. 2010. Vol. 57. No. 3. Pp. 1304–1307.

29. **Radzhabov E., Nagirnyi V., Kirm M., Prosekina E.** $5d$–$4f$ emission of Nd^{3+}, Sm^{3+}, Ho^{3+}, Er^{3+}, Tm^{3+} ions in alkaline earth fluorides // IEEE Transactions on Nuclear Science. 2012. Vol. 59. No. 5. Pp. 2074–2078.

30. **Kobayashi M., Ishii M., Sobolev B.P., Zhmurova Z.I., Krivandina E.A.** Scintillation characteristics of nonstoichiometric phases formed in MF_2-GdF_3-CeF_3 system. Part I. (M = Ba), scintillation of $Ba_{0.9}Gd_{0.1-x}Ce_xF_{2.1}$ ($0 < x < 0.1$) fluorite-type crystals // Nuclear Instruments and Methods in Physics Research. A. 1999. Vol. 421. No. 1–2. Pp. 180–190.

31. **Wojtowicz A.J., Janus S., Piatkowski D.** Fast and efficient VUV/UV emissions from (Ba,-La)F_2:Er crystals // Journal of Luminescence. 2009. Vol. 129. No. 12. Pp. 1594–1597.

32. **Kurosawa Sh., Yanagida T., Yokota Yu., Yoshikawa A.** Crystal growth and scintillation properties of fluoride scintillators //IEEE Transactions on Nuclear Science. 2012. Vol. 59. No. 5. Pp. 2173 – 2176.

33. **Yanovsky V.V., Reiterov V.M., Rodnyi P.A.** Effect of gamma-radiation on optical characteristics of barium fluoride scintillation crystals // Nuclear Physics B. (Proceedings. Supplements). 1991. Vol. 23A. No. 1. Pp. 347–351.

34. **Zhu R.-Y.** On quality requirements to the barium fluoride crystals // Nuclear Instruments and Methods in Physics Research. A. 1994. Vol. 340. No. 3. Pp. 442–457.

35. **Vistovskyy V.V., Zhyshkovych A.V., Chornodolskyy Ya.M., Myagkota O.S., Gloskovskii A., Gektin A.V., Vasil'ev A.N., Rodnyi P.A., Voloshinovskii A.S.** Self-trapped exciton and core-valence luminescence in BaF_2 nanoparticles // Journal of Applied Physics. 2013. Vol. 114. No. 19. P. 194306.

36. **Jacobsohn L.G., Kucera C.J., James T.L., Sprinkle K.B., di Maio J.R., Kokuoz B., Yazgan-Kukouz B., de Vol T.A., Ballato J.** Preparation and characterization of rare earth doped fluoride nanoparticles // Materials. 2010. Vol. 3. No. 3. Pp. 2053–2068.

37. **Jacobsohn L.G., Sprinkle K.B., Roberts S.A., Kucera C.J., James T.L., Yukihara E.G., de Vol T.A., Ballato J.** Fluoride nanoscintillators //Journal of Nanomaterials. 2011. Vol. 2011. P. 523638.

38. **Kang Z., Barta M., Nadler J., Wagner B., Rosson R., Kahn B.** Synthesis of BaF_2:Ce nanophosphor and epoxy encapsulated transparent nanocomposite // Journal of Luminescence. 2011. Vol. 131. No. 10. Pp. 2140–2143.

39. **Simpson P.J., Tjossem R., Hunt A.W., Lynn K.G., Munne V.** Superfast timing performance from ZnO scintillators // Nuclear Instruments and Methods in Physics Research. A. 2003. Vol. 505. No. 1–2. Pp. 82–84.

40. **Zang C.H., Liu Y.C., Mu R., Zhao D.X., Ma J.G., Zhang J.Y., Shen D.Z., Fan X.W.** Optical properties of ZnO nanocrystals embedded in BaF_2 film fabricated by magnetron sputtering // Journal of Physics D: Applied Physics. 2007. Vol. 40. No. 18. Pp. 5598–5601.

41. Батыгов С.Х., Болясникова Л.С., Гарибин Е.А., Демиденко В.А., Дорошенко М.Е., Дукельский К.В., Лугинина А.А., Миронов И.А., Осико В.В., Федоров П.П. Сцинтилляционная керамика BaF_2:Ce^{3+} // Доклады Академии наук. 2008. Т. 422. № 2. С.

179 –181.

42. **Han H., Zhang Z., Weng X., Liu J., Guan X., Zhang K., Li G.** Development of a fast radiation detector based on barium fluoride scintillation crystal // The Review of Scientific Instruments. 2013. Vol. 84. No. 7. P. 073503.

43. **de Vol T.A., Wehe D.K., Knol G.F.** Evaluation of wavelength shifters for spectral separation of barium fluoride emissions // Nuclear Instruments and Methods in Physics Research Section. A. 1994. Vol. 348. No. 1. Pp. 156–162.

44. **Boiano C., Bassini R., Pullia A., Camera F., Benzoni G., Bracco A., Brambilla S., Million B., Wieland O.** A fast-stretcher for an easy acquisition of the fast component of BaF_2 detectors signals // IEEE Nuclear Science Symposium Conference Record. 2004. Vol. 3. Pp. 1349–1351.

45. **Rodnyi P.A., Mikhrin S.B., Mishin A.N., Sidorenko A.V.** Small-size pulsed X-ray source for measurements of scintillator decay time constants //IEEE Nuclear Science Symposium. Conference Record. 2001. Vol. 48. No. 6. Pp. 2340–2343.

46. **Beaumont J.H., Hayes W., Kirk D.L., Summers G.P.** An investigation of trapped holes and trapped excitons in alkaline earth fluorides // Proceedings of the Royal Society of London. Ser. A. 1970. Vol. 315. No. 1520. Pp. 69–97.

Статья поступила в редакцию 28.01.2019, принята к публикации 14.02.2019.

СВЕДЕНИЯ ОБ АВТОРАХ

РОДНЫЙ Пётр Александрович – *доктор физико-математических наук, профессор Института физики, нанотехнологий и телекоммуникаций Санкт-Петербургского политехнического университета Петра Великого.*
195251, Российская Федерация, г. Санкт-Петербург, Политехническая ул., 29
rodnyi@physics.spbstu.ru

ГАРИБИН Евгений Андреевич – *директор ЗАО «ИНКРОМ».*
193171, Российская Федерация, г. Санкт-Петербург, ул. Бабушкина, 36.
e.garibin@incrom.ru

ВЕНЕВЦЕВ Иван Дмитриевич – *ассистент Института физики, нанотехнологий и телекоммуникаций Санкт-Петербургского политехнического университета Петра Великого.*
195251, Российская Федерация, г. Санкт-Петербург, Политехническая ул., 29
Venevtsev.Ivan@gmail.com

ДАВЫДОВ Юрий Иванович – р*уководитель отдела Объединенного института ядерных исследований.*
141980, Российская Федерация, г. Дубна Московской обл., ул. Жолио-Кюри, 6
Davydov@jinr.ru

DOI: 10.18721/JPM.12102
УДК 537.622: 539.378:620.186

HIGH-MAGNETOSTRICTION LAVES-PHASE ALLOY OF THE SAMARIUM-IRON SYSTEM: THE STRUCTURE AND PHASE TRANSFORMATIONS

G.A. Politova[1,2], A.Yu. Karpenkov[3], T.P. Kaminskaya[4], M.A. Ganin[1], Ravi Kumar[5], A.V. Filimonov[2]

[1]Baikov Institute of Metallurgy and Materials Science, RAS, Moscow, Russian Federation;

[2] Peter the Great St. Petersburg Polytechnic University, St. Petersburg, Russian Federation;

[3]Tver State University, Tver, Russian Federation;

[4]Lomonosov Moscow State University, Moscow, Russian Federation;

[5]Indian Institute of Technology Madras, Chennai, India

In this study, the $SmFe_2$ alloy in a high-purity single-phase state has been prepared by the induction melting technique. The surface features of the alloy at room temperature were investigated using the atomic-force and magnetic-force microscopy. The forming of heterogeneous granular structure was revealed, the main structural elements were determined. The presence of the complex domain structure was shown, its description was presented and the domain sizes were found. The results of X-ray structural studies over the temperature range from 100 to 300 K were presented. The experimental data on the temperature dependences of magnetostriction in magnetic fields up to 1.2 T were obtained and analyzed in the region of the spin-reorientational phase transition. The existence of the "angular" phase was indirectly confirmed, its temperature boundaries were refined.

Keywords: rare-earth Laves phase, phase transition, magnetostriction, atomic force microscopy, structure

Citation: G.A. Politova, A.Yu. Karpenkov, T.P. Kaminskaya, M.A. Ganin, Ravi Kumar, A.V. Filimonov, High-magnetostriction Laves-phase alloy of the samarium-iron system: the structure and phase transformations, St. Petersburg Polytechnical State University Journal. Physics and Mathematics. 12 (1) (2019) 25–34. DOI: 10.18721/JPM.12102

СТРУКТУРА И ФАЗОВЫЕ ПРЕВРАЩЕНИЯ ВЫСОКОМАГНИТОСТРИКЦИОННОГО СПЛАВА СИСТЕМЫ САМАРИЙ-ЖЕЛЕЗО СО СТРУКТУРОЙ ФАЗ ЛАВЕСА

Г.А. Политова[1,2], А.Ю. Карпенков[3], Т.П. Каминская[4], М.А. Ганин[1], Рави Кумар[5], А.В. Филимонов[2]

[1] Институт металлургии и материаловедения им. А.А. Байкова РАН, Москва, Российская Федерация;

[2] Санкт-Петербургский политехнический университет Петра Великого, Санкт-Петербург, Российская Федерация;

[3] Тверской государственный университет, г. Тверь, Российская Федерация;

[4] Московский государственный университет им. М.В. Ломоносова, Москва, Российская Федерация;

[5] Индийский технологический институт Мадраса, г. Ченнаи, Индия

В работе методом индукционной плавки получен сплав $SmFe_2$ в высокочистом однофазном состоянии. Методами атомно-силовой и магнитно-силовой микроскопии исследованы особенности поверхности сплава при комнатной температуре. Выявлено наличие неоднородной зернистой структуры, определены основные структурные элементы. Показано наличие сложной доменной структуры, проведено ее описание, определены размеры доменов. Представлены результаты рентгеноструктурных исследований

в интервале температур 100 – 300 K. Получены и проанализированы экспериментальные данные по температурным зависимостям магнитострикции в магнитных полях до 1,2 Тл в области спин-переориентационного фазового перехода. Косвенно подтверждено существование «угловой» фазы, уточнены ее температурные границы.

Ключевые слова: редкоземельная фаза Лавеса, фазовый переход, магнитострикция, атомно-силовая микроскопия, магнитно-силовая микроскопия

Ссылка при цитировании: Политова Г.А., Карпенков А.Ю., Каминская Т.П., Ганин М.А., Кумар Рави, Филимонов А.В. Структура и фазовые превращения высокомагнитострикционного сплава системы самарий-железо со структурой фаз Лавеса // Научно-технические ведомости СПбГПУ. Физико-математические науки. 2019. Т. 12. № 1. С. 25–34. DOI: 10.18721/JPM.12102

Introduction

Recent years have seen a renewed interest in study of RFe_2 Laves-phase alloys (where R is a rare-earth metal) [1–3]. Compounds of rare-earth and 3*d* transition metals with the Laves phase structure are an important family of magnetic materials exhibiting high values of anisotropic magnetostriction (of the order of 10^{-3}) in relatively low magnetic fields (less than 1 T) below the Curie temperature. It is known [4–6] that highly magnetostrictive compounds can convert electrical energy into mechanical energy and are used in such devices as drives and sensors operating in various environments and in a wide temperature range. Some Laves phases demonstrate both high values of magnetostriction and large magnetocaloric effects around the Curie temperature, which can also find practical application [7, 8]. While the physical mechanism responsible for high values of magnetostriction in these compounds is well known [9, 10], comprehensive studies on the structure, magnetic properties and anomalies in the phase transition region were only carried out by different techniques for individual samples.

RFe_2 intermetallic compounds crystallize into a cubic structure of the $MgCu_2$ type (*Fd*3*m* space group). According to theory, giant spontaneous magnetostriction is most likely to occur along the easy <111> axis of magnetization as a result of magnetic ordering. Special symmetry of cubic *C*15 Laves phase leads to large rhombohedral distortion in the <111> direction. The best-known Laves phase compounds with giant saturation magnetostriction at room temperature are $TbFe_2$ and $SmFe_2$ ($+1.7\cdot10^{-3}$ and $-1.5\cdot10^{-3}$, respectively) [11–15]. These alloys have close magnitostriction values (differing in sign) at room temperature. Both of these alloys undergo rhombohedral distortions upon transition to a magnetically ordered state; however, while the cubic lattice in $TbFe_2$ compound stretches along the <111> direction, it is slightly compressed in $SmFe_2$. These compounds also differ by type of magnetic ordering. It is known that magnetic moments of the R and Fe sublattices are parallel, with the total magnetic moments of the sublattices co-directional for light REM and antiparallel for heavy REM. Because of this, $TbFe_2$ is a ferrimagnet, and $SmFe_2$ is a ferromagnet.

Unlike $TbFe_2$, the crystal structure of $SmFe_2$, as well as the direction of its magnetic moment change with decreasing temperature. Mцssbauer and XRD studies [15–18] found that the spontaneous magnetic moment of the $SmFe_2$ compound at room temperature is oriented along the <111> crystal direction. It was previously believed that a spin-reorientational phase transition (SRPT) is observed with a temperature decrease in the region $T = 180–200$ K, with magnetic moments oriented along the <110> direction. However, detailed analysis of the diffraction spectra obtained at low temperatures revealed [17, 18] that the structure of the alloy remains rhombohedral with a decrease in temperature to about 200 K, while the distortions increase in absolute value. An “angular” magnetic phase appears in the alloy with a further decrease in temperature (in the range of 140–240 or 106–180 K but different sources cite different ranges): the vector of spontaneous magnetic moment is in the (110) plane and does not coincide in direction with either <111> or <110>. The character that transformation of the X-ray diffraction spectrum bears at low temperatures indicates orthorhombic distortions of the crystal lattice, and the magnetic moment is directed along the <110> axis. Anomalies in the SRPT region are also manifested in the temperature dependences of magnetization [15].

The goal of this study has been to analyze the changes in the crystal structure and

magnetostrictive properties of the $SmFe_2$ alloy in the temperature range from 100 to 320 K, and also to consider the peculiarities of its surface at room temperature using atomic-force and magnetic-force microscopy.

In view of this goal, we needed to obtain a high-purity single-phase alloy of $SmFe_2$.

Experimental procedure

Sample preparation. The $SmFe_2$ alloy was synthesized by high-frequency induction melting (Donets-1 furnace) in an alundum crucible in ultra-pure argon (moisture content less than 0.02 $g \cdot m^{-3}$, nitrogen content 0.0005%, oxygen content 0.001%) at 1.1–1.2 atm. High-purity metals were taken as the initial components. We experimentally selected mixtures with higher REM contents (by 10%), which allowed to obtain single-phase compounds upon subsequent homogenizing annealing. The cooling rate of the alloys was rather slow (about 1–2 K/s), which contributed to achieving a near-steady state. The prepared samples were placed in quartz tubes pumped to high vacuum. Melted alloys were subjected to heat treatment in a specially selected mode using a Carbolite TZF 15/610 3-zone high-temperature tube furnace: the samples in tubes were heated to a temperature of 720°C at a rate of 7 K/min. Next, the samples were kept at this temperature for 72 hours and then quenched in water.

Recording the X-ray diffraction spectra. The spectra were recorded for powder samples using CuK_α radiation (λ = 0.1540598 nm) at room temperature with a DRON-7 X-ray diffractometer modified with a rapid-response system based on a Mythen 1K linear position-sensitive strip detector (Dectris Ltd, Switzerland). The unit cell parameters were calculated from reflections in the angle range 2θ = 15–105°. The phase composition of the sample was studied by Rietveld refinement in the Powder Cell 2.4 program. Temperature measurements of the XRD patterns were carried out in the temperature range of 110–250 K with a Supernova X-ray diffractometer (Agilent) using filtered MoK_α radiation. The sample temperature was controlled by its contact with nitrogen gas stream of a given temperature, maintained by a Cobra PLus Cryosystem (Oxford Cryosystems).

Microscopy. The microstructure of the samples was studied with a Neophot-30 metallographic microscope. The samples were observed and photographed under a xenon lamp in either bright field or polarized light modes. Microstructure patterns were fed through the optical channel of the microscope to a Levenhuk M800 Plus high-resolution digital camera; a Smena-A scanning probe microscope (Solver platform, NT-MDT, Russia) was used.

Analysis of surface morphology. The morphology was studied by atomic force microscopy (AFM) of Laves phases in the samples in both tapping and contact modes at room temperature using standard HA_NC Etalon silicon cantilevers. Thin sections of the samples were etched in a 5% solution of nitric acid in alcohol to reveal the nanostructural features of the surface. Magnetic force microscopy (MFM) studies were carried out with fully demagnetized thin sections of the samples using special magnetic cantilevers MFM01 with a cobalt chromium coating, at a resonant frequency of about 70 kHz and a force constant of 1–5 N/m. MFM in non-contact vibration mode yields greater sensitivity, allowing to collect high-quality MFM images of the sample surface via a two-pass quasistatic technique (the maximum sensitivity of the method is achieved when the cantilever excitation frequency coincides with the resonant frequency of the system comprising the probe and the sample).

Deformation measurements. Deformation of the polycrystalline sample made of $SmFe_2$ alloy was studied by the strain-gauge method in the temperature range from 100 to 320 K and in magnetic fields up to 1.2 T, with measurements carried out both along the direction of the magnetic field (longitudinal magnetostriction) and perpendicular to it (transverse magnetostriction).

Experimental results and discussion

$SmFe_2$ samples were synthesized by high-frequency induction melting. The problem with synthesizing RFe_2 compounds is that the eutectic points of RFe_2 and RFe_3 are close and, as a result, it is the 1:3 phase that crystallizes in the alloy if there is insufficient REM content in the mixture or if the perictetic reaction does not go to completion, since it takes fewer REM atoms for this phase to form. Analysis of the XRD data obtained at room temperature (Fig. 1) established that the alloy is single-phase and the atomic and crystal structure is isotypic to the structure of the cubic Laves phase *C*15 ($MgCu_2$). The lattice parameter found was 7.4239 E.

The temperature dependences of the lattice parameters (Fig. *2, a*) were obtained by fitting the XRD spectra to the cubic lattice model. Evidently, the slope of the temperature

dependence of the lattice parameter changes in the temperature range of 180–190 K; this indicates a change in the crystal lattice associated with the spin-reorientational phase transition. The results obtained are in good agreement with the data given in literature [15–18], describing a structural transition from the high-temperature rhombohedral phase to the angular phase, which is then transformed into the low-temperature rhombic phase, in this temperature range. Temperature dependences of the lattice parameters *a b c*, obtained by fitting the XRD spectra in accordance with the models of rhombohedral (above 190 K) and rhombic (orthorhombic) (below 180 K) crystal lattices are shown in Fig. 2, *b*. For easy comparison in a single graph, the parameters were transformed (factors $\sqrt{2}$, $\sqrt{3}$) and reduced to a pseudocubic cell.

Analysis of the microstructure by the optical method revealed the second phase in the samples, which was not detected by the X-ray method. Quantitative analysis of the micrographs was carried out with a computer program calculating the relative content of the phases by pixel shades, confirming that the volume content of the secondary phases did not exceed 1–2%, suggesting that the synthesized compounds are almost single-phase.

Atomic-force and magnetic-force microscopy are getting increasingly popular in materials science, providing additional data on homogeneity of phase composition, graininess of synthesized phases, size and morphology of individual grains, domain structure [19–21]. The studies were carried out for micron (scan size of 90 × 90 μm, see Fig. 3, *d*), nanometer (scan size of 4 × 4 μm, see Fig. 3, *a, b*) and smaller scales. It was established by analysis of AFM images of the surface topology that the cells) ranging from 500 to 700 nm in one direction and up to 1 μm in the perpendicular direction. The cells were filled with small grains (these are other structural elements) with an average size of 80 nm, which can be clearly seen in Fig. 3, *a*.

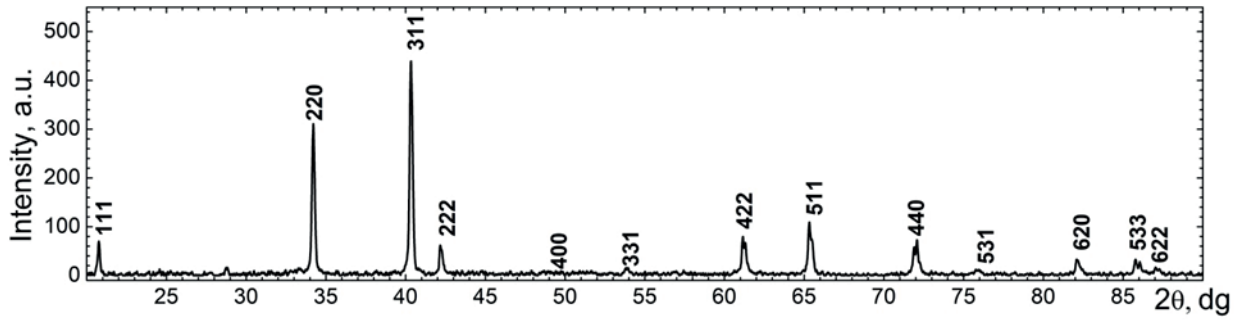

Fig. 1. Experimental XRD pattern of $SmFe_2$ alloy;
numbers above the peaks correspond to the indices hkl; the data are for room temperature

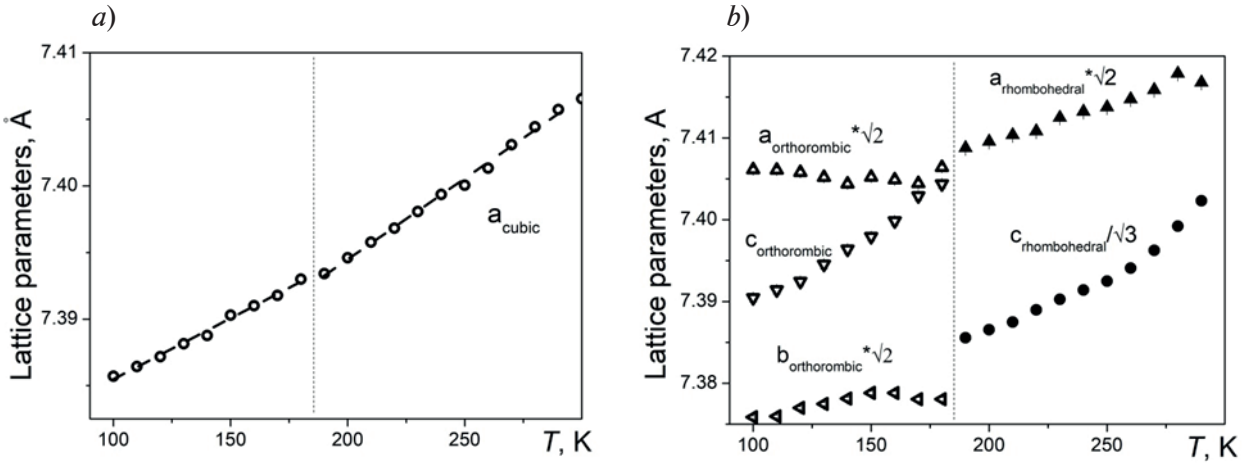

Fig. 2. Temperature dependences of $SmFe_2$ unit cell parameters:
obtained by fitting XRD spectra within models for cubic (*a*), rhombic (< 180 K)
and rhombohedral (> 190 K) (*b*) lattices

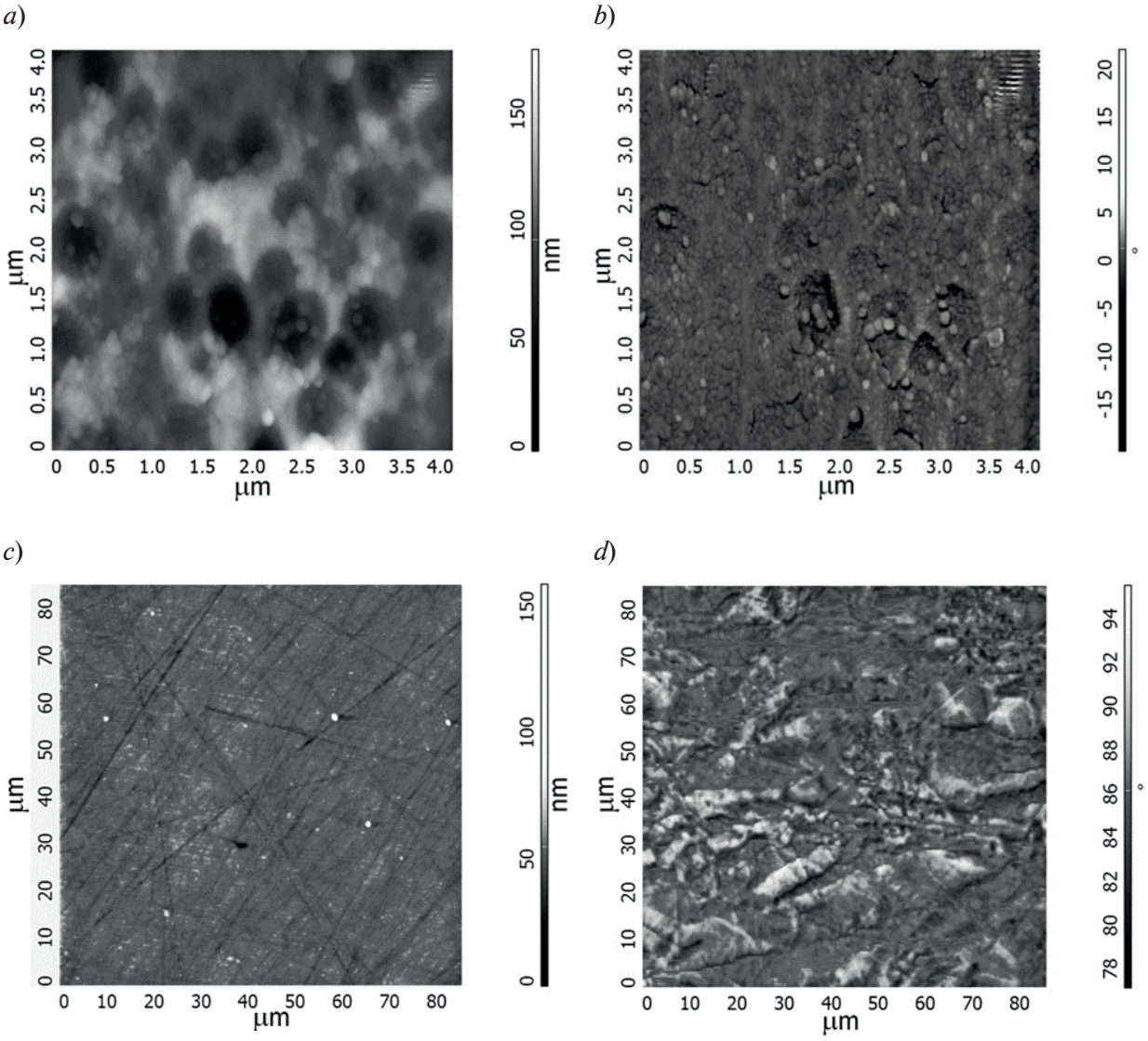

Fig. 3. AFM (*a*, *b*, *c*) and MFM (*d*) images of SmFe2 alloy surface, obtained with scan sizes of 4 × 4 μm (*a*, *b*) and 90 × 90 μm (*c*, *d*); phase contrast method was used in *b*

Surface studies of the polished thin section of $SmFe_2$ by magnetic force microscopy (Fig, 3, *d)* revealed a pronounced and rather complicated domain structure consisting of islands with the sizes from 6 to 12 μm and strips with the widths from 3 to 5 μm. The smallest domains are 0.8–1.0 μm wide. There may be different reasons for such a complex domain structure on the sample surface, for example, scattering fields (associated with stresses in the sample), as well as microinclusions of another phase. The presence of stresses is most likely due to high magnetostrictive properties of the $SmFe_2$ compound.

We studied linear deformation of $SmFe_2$ samples under the action of an external magnetic field depending on temperature (thermal expansion). Fig. 4 shows the temperature dependences of elongation at break and the coefficient of thermal expansion of the sample. Two anomalies can be observed at temperatures of 126 and 188 K, associated with phase transitions: a transition from the rhombohedral to the "angular" phase occurs at $T_2 = 188$ K, and a transition from the "angular" to the rhombic phase at $T_2 = 126$ K. These assertions are supported by the data found in literature [11, 12], as well as by the results of our own XRD studies. Notably, while there are only slight differences in the data given in literature for the value of the temperature T_2, the values cited for T_1 differ greatly. Thus, we have refined the values of the given temperature points by measuring the thermal expansion coefficient of $SmFe_2$ samples as a function of temperature.

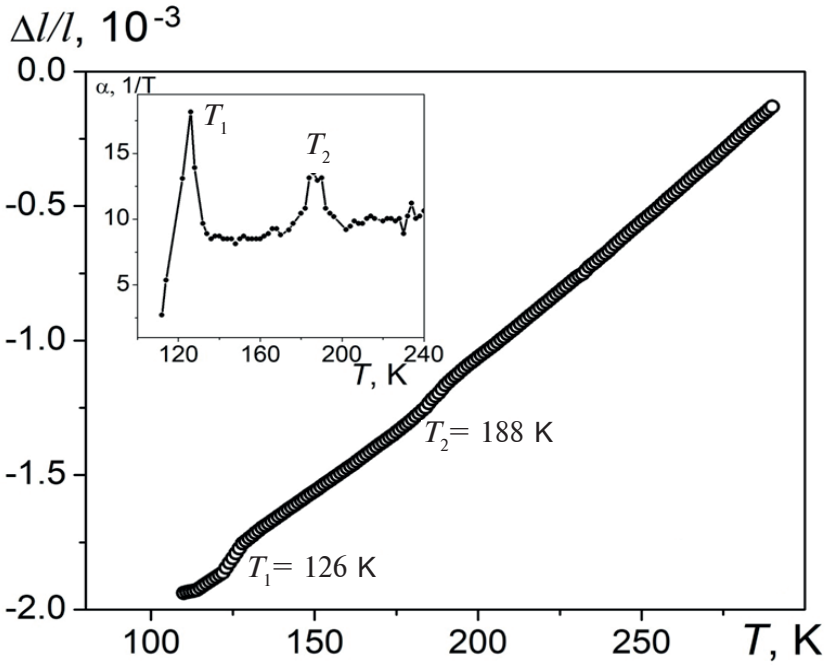

Fig. 4. Temperature dependences of elongation at break in $SmFe_2$ sample (thermal expansion) and its coefficient of thermal expansion (inset);
T_1, T_2 correspond to phase transition points

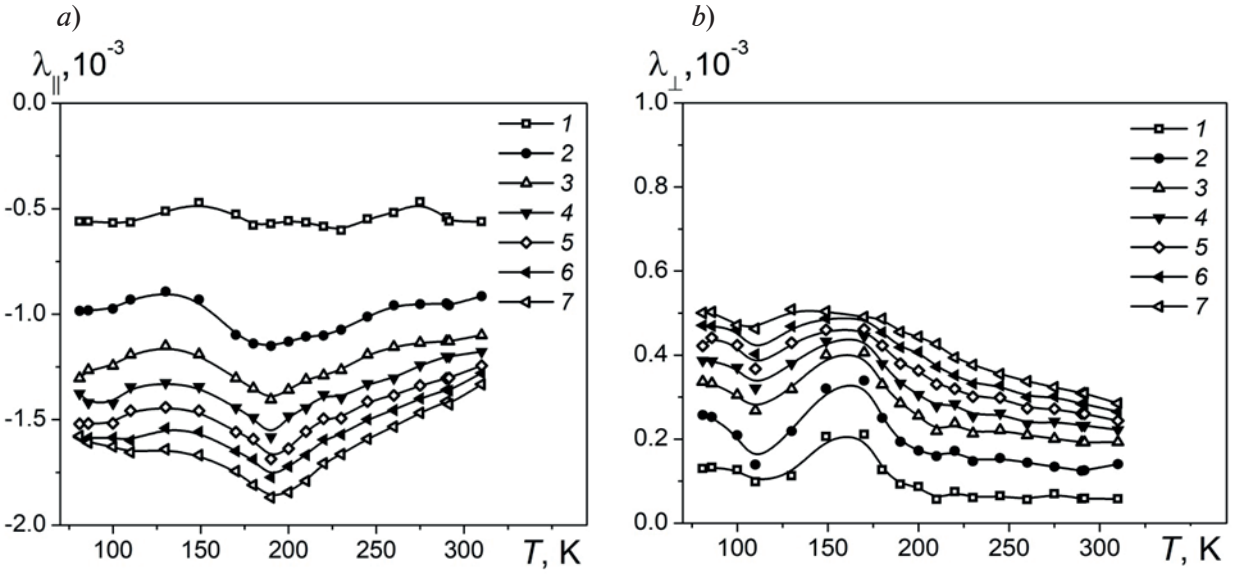

Fig. 5. Temperature dependence of longitudinal (*a*) and transverse (*b*) magnetostriction in $SmFe_2$ with magnetic field strengths, T:
0.15 (*1*), 0.35 (*2*), 0.50 (*3*), 0.70 (*4*) 0.80 (*5*), 1.0 (*6*), 1.2 (*7*)

Magnetostrictive deformations turn out to be even more sensitive to magnetic and structural changes in the sample; therefore, it is convenient to use magnetostriction measurements as a method for detecting magnetic and structural phase transitions. Fig. 5 shows the temperature dependences of magnetostriction in the given alloy. Both longitudinal (Fig. 5, *a),* and transverse (Fig. 5, b) magnetostriction anomalies are observed at temperatures of 126 and 188 K for all values of the applied external field, expressed in terms of minimum and maximum absolute magnetostriction, respectively. Longitudinal magnetostriction in $SmFe_2$ has a negative sign and the maximum absolute value of $-1.9\cdot10^{-3}$, while transverse magnetostriction is positive and takes a maximum value of $+0.5\cdot10^{-3}$. The absolute values of magnetostriction decrease at room temperature, with the values of the longitudinal and transverse components amounting, respectively, to $-1.4\cdot10^{-3}$ and $+0.3\cdot10^{-3}$.

Conclusion

We have used induction melting to synthesize a $SmFe_2$ alloy; comprehensive study of the alloy included optical metallography and X-ray diffraction analysis to confirm that the alloy was homogeneous and single-phase. In addition, we have specifically established that a phase with 1:3 stoichiometry (most frequently observed in these compounds) was absent in our case.

We have used atomic force and magnetic force microscopy to verify that the sample surface had a heterogeneous cellular microstructure and a complex domain pattern. We have determined the sizes of the main structural elements.

We have found the specific temperature range where the angular phase exists during transition from rhombohedral to rhombic phase. We have considered the behavior of magnetostriction in the region of these anomalies.

The study was carried out with the financial support of the Russian Foundation for Basic Research, projects no. 18-03-00798-a, n. 16-52-48016 ИНД_оми (R. Kumar and A.V. Filimonov), and within the framework of State Task of the Ministry of Education and Science of the Russian Federation, project 11.5861.2017/БЧ (Peter the Great St. Petersburg Polytechnic University) and State Task no. 075-00746-19-00 (Baikov Institute of Metallurgy and Materials Science).

REFERENCES

[1] **N.J. Wang, Y. Liu, H.W. Zhang, et al.,** Fabrication, magnetostriction properties and applications of Tb-Dy-Fe alloys: a review, China Foundry. 13 (2) (2016) 75–84.

[2] **W.J. Ren, Z.D. Zhang,** Progress in bulk $MgCu_2$-type rare-earth iron magnetostrictive compounds, Chin. Phys. B. 22 (7) (2013) 077507.

[3] **Y. Wang, T.Y. Ma, C. Wu, et al.,** Correlation between magnetostriction and magnetic structure in pseudobinary compounds $Tb(Co_{1-x}Fe_x)_2$, AIP Advances. 7 (7) (2017) 075311.

[4] **Z.Q. Chu, M.J. Pourhosseini-Asl, S.X. Dong,** Review of multi-layered magnetoelectric composite materials and devices applications, J. Phys. D: Appl. Phys. 51 (24) (2018) 243001(21).

[5] **A.V. Kalgin., S.A. Gridnev, I.I. Popov,** Magnetoelectric effect in two-layered self-biased composites $Tb_{0.12}Dy_{0.2}Fe_{0.68}$/epoxy $PbZr_{0.53}Ti_{0.47}O_3$, Phys. Status Solidi, C. 14 (3–4) (2017) 1600231.

[6] **S.A. Nikitin, I.S. Tereshina, V.N. Verbetsky, et al.,** Magnetostriction and magnetic anisotropy in $TbFe_{11}TiH_x$ single crystal, J. Alloys and Compounds. 322 (1–2) (2001) 42–44.

[7] **V.B. Chzhan, I.S. Tereshina, A.Y. Karpenkov, E.A. Tereshina-Chitrova,** Persistent values of magnetocaloric effect in the multicomponent Laves phase compounds with varied composition, Acta Materialia. 154 (2018) 303–310.

[8] **I. Tereshina, J. Cwik, E. Tereshina, et al.,** Multifunctional phenomena in rare-earth intermetallic compounds with a Laves phase structure: Giant magnetostriction and magnetocaloric effect, IEEE Trans. Mag. 50 (11) (2014) 2504604.

[9] **K.P. Belov,** Magnitostriktsionniye yavleniya i ikh technicheskiye prilozheniya [Magnetostriction phenomena and their technical applications], Nauka, Moscow, 1987.

[10] **I. Tereshina, S. Nikitin, A. Tulyakov, et al.,** Rare earth compounds with compensated magnetic anisotropy and giant magnetostriction, J. Alloys Comp. 451 (1–2) (2008) 481–483.

[11] **H. Samata, N. Fujiwara, Y. Nagata, et al.,** Magnetic anisotropy and magnetostriction of $SmFe_2$ crystal, J. Magn. Magn. Mater. 195 (2) (1999) 376–383.

[12] **R. Grössinger, R.S. Turtelli, N. Mehmood,** Materials with high magnetostriction, IOP Conf. Series: Materials Science and Engineering. 60

(2014) 012002.

[13] **Y.J. Tang, H.L. Luo, N.F. Gao, et al.,** Magnetic properties and magnetostriction in $TbFe_2$ compound with the addition of manganese or gallium, Appl. Phys. Lett. 66 (3) (1995) 388–390.

[14] **Y.M. Tang, L.Y. Chen, L. Zhang, et al.,** Temperature dependence of the magnetostriction in polycrystalline $PrFe_{1.9}$ and $TbFe_2$ alloys: experiment and theory, Journal of Applied Physics. 115 (17) (2014) 173902.

[15] **X.N. Liu, K. Lin, Q.L. Gao, et al.,** Structure and phase transformation in the giant magnetostriction Laves-phase $SmFe_2$, Inorganic Chemistry. 57 (2) (2018) 689–694.

[16] **U. Atzmony, M.P. Dariel,** Nonmajor cubic axes of easy magnetization in rare-earth-iron Laves compounds, Phys. Rev. B. 13 (9) (1976) 4006–4014.

[17] **V.S. Gaviko, A.V. Korolyov, N.V. Mushnikov,** X-ray diffraction investigation of spin reorientation in $SmFe_2$, J. Magn. Magn. Mater. 157–158 (May) (1996) 659–660.

[18] **A.C. Ilyushin, E.V. Solodov, Z.S. Umkhayeva,** Structural and spin-orientation phase transitions in pseudobinary $(Sm_{1-x}Tb_x)Fe_2$ system, Journal Perspektivnye materialy. (11) (2013) 42–47.

[19] **V.I. Mironov,** Osnovy skaniruyushchey zondovoy mikroskopii [Principles of scanning probe microscopy], Institute for Physics of Microstructures of the RAN, Nizhni Novgorod, 2004.

[20] **G.A. Politova, G.S. Burkhanov, I.S. Tereshina, et al.,** The effect of adding aluminum and iron to Tb-Dy-Ho-Co multialloys on their structure, magnetic and magnetocaloric properties, Technical Physics. 62 (4) (2017) 577–582.

[21] **N.V. Andreeva, A.V. Filimonov, A.I. Rudskoi, et al.,** A study of nanostructure magnetosolid Nd-Ho-Fe-Co-B materials via atomic force microscopy and magnetic force microscopy, Physics of the Solid State. 58 (9) (2016) 1862–1869.

Received 01.02.2019, accepted 05.02.2019.

THE AUTHORS

POLITOVA Galina A.
Baikov Institute of Metallurgy and Materials Science, RAS
49 Leninskiy Ave., Moscow, 119334, Russian Federation
gpolitova@gmail.com

KARPENKOV Aleksey Yu.
Tver State University
35 Sadovaya, 170002, Tver, Russian Federation
karpenkov_alex@mail.ru

KAMINSKAYA Tatiana P.
Lomonosov Moscow State University
GSP-1, Leninskie Gory, Moscow, 119991, Russian Federation
ktp53@mail.ru

GANIN Maksim A.
Baikov Institute of Metallurgy and Materials Science, RAS
49 Leninskiy Ave., Moscow, 119334, Russian Federation
ganmax_90@mail.ru

KUMAR RAVI
Indian Institute of Technology Madras
Chennai (Madras), 600036, India
nvrk@iitm.ac.in

FILIMONOV Alexey V.
Peter the Great St. Petersburg Polytechnic University
29 Politechnicheskaya St., St. Petersburg, 195251, Russian Federation
filimonov@rphf.spbstu.ru

СПИСОК ЛИТЕРАТУРЫ

1. **Wang N.J., Liu Y., Zhang H.W., Chen X., Li Y.X.** Fabrication, magnetostriction properties and applications of Tb-Dy-Fe alloys: a review // China Foundry. 2016. Vol. 13. No. 2. Pp. 75–84.

2. **Ren W.J., Zhang Z.D.** Progress in bulk $MgCu_2$-type rare-earth iron magnetostrictive compounds // Chin. Phys. B. 2013. Vol. 22. No. 7. P. 077507.

3. **Wang Y., Ma T.Y., Wu C., et al.** Correlation between magnetostriction and magnetic structure in pseudobinary compounds $Tb(Co_{1-x}Fe_x)_2$ // AIP Advances. 2017. Vol. 7. No. 7. P. 075311.

4. **Chu Z.Q., Pourhosseini-Asl M.J., Dong S.X.** Review of multi-layered magnetoelectric composite materials and devices applications // J. Phys. D: Appl. Phys. 2018. Vol. 51. No. 24. P. 243001(21).

5. **Kalgin A.V., Gridnev S.A., Popov I.I.** Magnetoelectric effect in two-layered self-biased composites $Tb_{0.12}Dy_{0.2}Fe_{0.68}$/epoxy $PbZr_{0.53}Ti_{0.47}O_3$ // Phys. Status Solidi. C. 2017. Vol. 14. No. 3–4. P. 1600231.

6. **Nikitin S.A., Tereshina I.S., Verbetsky V.N., Salamova A.A., Skokov K.P., Pankratov N.Yu., Skourski Yu.V., Tristan N.V., Zubenko V.V., Telegina I.V.** Magnetostriction and magnetic anisotropy in $TbFe_{11}TiH_x$ single crystal // J. Alloys and Compounds. 2001. Vol. 322. No. 1–2. Pp. 42–44.

7. **Chzhan V.B., Tereshina I.S, Karpenkov A.Y., Tereshina-Chitrova E.A.** Persistent values of magnetocaloric effect in the multicomponent Laves phase compounds with varied composition // Acta Materialia. 2018. Vol. 154. Pp. 303–310.

8. **Tereshina I., Cwik J., Tereshina E., Politova G., Burkhanov G., Chzhan V., Ilyushin A., Miller M., Zaleski A., Nenkov K., Schultz L.** Multifunctional phenomena in rare-earth intermetallic compounds with a Laves phase structure: Giant magnetostriction and magnetocaloric effect // IEEE Trans. Mag. 2014. Vol. 50. No. 11. P. 2504604.

9. **Белов К.П.** Магнитострикционные явления и их технические приложения. М.: Наука, 1987. 159 с.

Статья поступила в редакцию 01.02.2019, принята к публикации 05.02.2019.

СВЕДЕНИЯ ОБ АВТОРАХ

ПОЛИТОВА Галина Александровна – *кандидат физико-математических наук, старший научный сотрудник Института металлургии и материаловедения им. А.А. Байкова РАН, Москва, Российская Федерация.*

119334 Российская Федерация, г. Москва, Ленинский пр., 49
gpolitova@gmail.com

КАРПЕНКОВ Алексей Юрьевич – *кандидат физико-математических наук, доцент кафедры физики конденсированного состояния Тверского государственного университета, г.Тверь, Российская Федерация.*

170002 Российская Федерация, г. Тверь, Садовый пер., 35
karpenkov_alex@mail.ru

КАМИНСКАЯ Татьяна Петровна – *кандидат технических наук, доцент, научный сотрудник кафедры общей физики Московского государственного университета им. М.В. Ломоносова, Москва, Российская Федерация.*

119999 Российская Федерация, г. Москва, Ленинские горы, 1
ktp53@mail.ru

ГАНИН Максим Алексеевич – *младший научный сотрудник Института металлургии и материаловедения им. А.А. Байкова РАН, Москва, Российская Федерация.*

119334 Российская Федерация, г. Москва, Ленинский пр., 49
ganmax_90@mail.ru

КУМАР РАВИ – *доктор естественных наук, профессор Лаборатории машиностроительной керамики Индийского технологического института Мадраса, г. Ченнаи, Индия.*
Chennai (Madras), 600036, India
nvrk@iitm.ac.in

ФИЛИМОНОВ Алексей Владимирович – *доктор физико-математических наук, заведующий кафедрой физической электроники Санкт-Петербургского политехнического университета Петра Великого, Санкт-Петербург, Российская Федерация.*
195251, Российская Федерация, г. Санкт-Петербург, Политехническая ул., 29
filimonov@rphf.spbstu.ru

DOI: 10.18721/JPM.12103
УДК 532.517.4:536.24

METHOD OF CALCULATION OF TURBULENT PRANDTL NUMBER FOR THE SST TURBULENCE MODEL

D.K. Zaitsev, E.M. Smirnov

Peter the Great St. Petersburg Polytechnic University, St. Petersburg, Russian Federation

We present a new model for turbulent Prandtl number that provides an improvement of prediction capabilities of the SST turbulence model in application to wall heat transfer problems. The model was calibrated using Kader's empirical correlation for near-wall temperature profile. To get an initial assessment of the model we performed computations of the fully developed flow in a round tube and a flat channel with Prandtl number varying from 0.004 to 95; the simulation results were validated against benchmark DNS data and empirical correlations for the Nusselt number. According to the tests, applying the new model resulted in considerable reduction of the Nusselt number prediction error (by factor two and more) in the whole range of Prandtl number considered; the most pronounced effect was observed at Prandtl number values below 0.1.

Keywords: turbulent flow, wall heat transfer, numerical simulation, turbulent Prandtl number

Citation: D.K. Zaitsev, E.M. Smirnov, Method of calculation of turbulent Prandtl number for the SST turbulence model, St. Petersburg Polytechnical State University Journal. Physics and Mathematics. 12 (1) (2019) 35–44. DOI: 10.18721/JPM.12103

МЕТОД РАСЧЕТА ТУРБУЛЕНТНОГО ЧИСЛА ПРАНДТЛЯ ДЛЯ SST-МОДЕЛИ ТУРБУЛЕНТНОСТИ

Д.К. Зайцев, Е.М. Смирнов

Санкт-Петербургский политехнический университет Петра Великого,

Санкт-Петербург, Российская Федерация

В работе представлена новая модель для турбулентного числа Прандтля, обеспечивающая улучшение предсказательных возможностей популярной полуэмпирической модели турбулентности SST (Shear Stress Transport – модель переноса сдвиговых напряжений) при ее использовании для расчетов пристенного теплообмена. Начальное тестирование разработанной модели проведено на задачах установившегося течения и теплообмена в круглой трубе и плоскопараллельном канале при варьировании числа Прандтля в широких пределах: от 0,004 до 95. По результатам тестов погрешность расчета теплоотдачи во всем диапазоне значений числа Прандтля снизилась в два раза и более. Наибольший положительный эффект от использования разработанной модели наблюдается при числах Прандтля, меньших 0,1.

Ключевые слова: турбулентное течение, пристенный теплообмен, численное моделирование, турбулентное число Прандтля

Ссылка при цитировании: Зайцев Д.К., Смирнов Е.М. Метод расчета турбулентного числа Прандтля для SST-модели турбулентности // Научно-технические ведомости СПбГПУ. Физико-математические науки. Т. 12. № 1. С. 35–44. DOI: 10.18721/JPM.12103

Introduction

Numerical simulation of turbulent heat transfer based on Reynolds-averaged Navier–Stokes (RANS) equations commonly involves some sort of semi-empirical model of turbulent viscosity [1, 2] for most practical applications, with the relationship between the coefficients of turbulent heat transfer λ_t and turbulent viscosity μ_t given by the turbulent Prandtl number $\mathrm{Pr}_t = \mu_t C_p/\lambda_t$. Models which entail solving additional differential equations to determine the coefficient of turbulent heat transfer (for example, the transfer equations for the "energy" of temperature fluctuations and dissipation rate [3]) are often seen as overly complex and have not as yet gained wide acceptance.

Heat transfer models using the turbulent Prandtl number typically take it for a constant value (as a rule, $\mathrm{Pr}_t = 0.85$ or 0.90, depending on the turbulence model used), which does not actually happen in most cases. The general understanding of the mechanism of turbulent heat transfer, supported by many computational and experimental studies (see, for example, reviews [4–6]) is that the turbulent Prandtl number varies depending on the contribution of molecular conduction to the scale of turbulent fluctuations. Specifically, if molecular conduction can be neglected (at a distance from the walls bounding the flow with sufficiently high Reynolds numbers), the turbulent Prandtl number should have a certain boundary value $\mathrm{Pr}_{t\infty} < 1$; as the relative role of molecular conduction increases (for example, upon approaching a wall, or with decreasing Reynolds number and/or Prandtl molecular number $\mathrm{Pr} = \mu C_p/\lambda$), Pr_t should increase.

Numerous models have been proposed in literature for turbulent Prandtl number, aimed to gain better agreement between the computed and experimental data on heat transfer for some classes of flows than that obtained using the "standard" value $\mathrm{Pr}_t \approx 0.85$. We can mention, for example, the following formulations from [7, 4, 8, 9, 5], respectively:

$$\mathrm{Pr}_t = \Gamma\Big/\left(1-e^{-\Gamma}\right),\quad \Gamma = \left(0.014\,\mathrm{Re}^{0.45}\,\mathrm{Pr}^{0.2}\right)^{-1}; \tag{1}$$

$$\mathrm{Pr}_t = \left(1+\frac{100}{\sqrt{\mathrm{Re}\,\mathrm{Pr}}}\right)\times\left(\frac{1}{1+120/\sqrt{\mathrm{Re}}}-0.15\right); \tag{2}$$

$$\mathrm{Pr}_t = 1.855 - \mathrm{th}\left(0.2y^+ - 1.5\right);\quad y^+ = \frac{\sqrt{\rho\tau_w}\,d}{\mu}; \tag{3}$$

$$\frac{1}{\mathrm{Pr}_t} = \frac{0.5}{\mathrm{Pr}_{t,\infty}} + \frac{\alpha\,\mathrm{Pe}_t}{\mathrm{Pr}_{t,\infty}^{0.5}} - \left(\alpha\,\mathrm{Pe}_t\right)^2\left[1-\exp\left(\frac{-1}{\alpha\,\mathrm{Pe}_t\,\mathrm{Pr}_{t,\infty}^{0.5}}\right)\right]; \tag{4}$$

$$\mathrm{Pr}_t = 0.85 + \frac{f}{\mathrm{Pe}_t};\quad \mathrm{Pe}_t = \mathrm{Pr}\cdot\frac{\mu_t}{\mu}. \tag{5}$$

Models (1) and (2) were constructed for specific cases of fully developed flow in cylindrical tubes. The turbulent Prandtl number is assumed constant over the cross-section of the tube in these models but its value depends on the global regime parameter, the Reynolds number Re. For this reason, even though the temperature profile is not predicted completely correctly, the computation gives the correct value of the heat transfer coefficient.

Models (3)–(5), where the value of Pr_t varies in space, increasing as it approaches the wall, seem more physically justified. In particular, the distance to the wall d is explicitly included in the definition of the universal near-wall coordinate y^+ in formulation (3). On the other hand, however, model (3) is very inconvenient from the standpoint of modern hydrodynamic CFD (Computational Fluid Dynamics) codes, since the argument y^+ used in expression (3) is not a purely local variable: the shear stress τ_w on the wall, at a point closest to the given point of the flow, has to be found to compute it.

It follows then that models without any non-local computations are more attractive. In particular, the argument in formulations (4) and (5) with the parameters $\mathrm{Pr}_{t\infty} = 0.85$, $\alpha = 0.3$, $f = 2$ is the purely local parameter Pe_t, often called the turbulent Peclet number.

Notice that "non-local" modifications (of little use for general-purpose CFD codes) were proposed in literature for both formulations. In particular, it was pointed out in [5] that it would be practical to "switch" from correlation (5) to a fixed value $\mathrm{Pr}_t = 1.07$ for $y^+ < 10$; it was proposed in [10] to compute the boundary value of $\mathrm{Pr}_{t,\infty}$ in expression (4) with the Reynolds number taken into account to achieve better agreement with experimental data on heat transfer in tubes with small Prandtl numbers (liquid metals)

$$\mathrm{Pr}_{t,\infty} = 0.85 + 100\mathrm{Pr}^{-1}\mathrm{Re}^{-0.888}.$$

Additionally, it should be borne in mind that the effect from applying a particular method for computing the turbulent Prandtl number may depend on the turbulence model used, since different models predict different distributions of turbulent viscosity. We can mention [11] as an example, where the accuracy of k–ε [12] (realizable) and k–ω SST (Shear Stress Transport) [13] models was assessed as applied to heat transfer computations; the assessment was carried out for the problem of liquid metal flow (Pr = 0.025) in a flat channel. The computations in [11] indicate that correlation (2) yielded the best agreement with the data of reference computations [14], performed by direct numerical simulation (DNS) in case of the k–ε model, while in case of the SST model, formulation (5) with the parameter $f = 0.7$ produced the best results.

Thus, the model for the turbulent Prandtl number should be constructed for a specific semi-empirical turbulence model.

In this study, we have proposed a new method for computing the turbulent Prandtl number, aimed primarily at simulation of near-wall heat transfer at low and moderate Prandtl numbers using the popular k–ω SST turbulence model [13].

We have introduced the concept of the calibration method, presenting its final mathematical formulation and providing the results of initial testing.

The computations were carried out using the SINF/Flag-S in-house CFD code, focused on numerically solving hydrodynamics and heat transfer problems with structured and unstructured computational grids embedded in the flow. Some applications of the code and the details of the numerical schemes used in it are given in [15–19].

Mathematical model

The standard formulation of the SST turbulence model [13] assumes the value of the turbulent Prandtl number to be $\mathrm{Pr}_t = 0.85$, which usually provides acceptable accuracy for simulation of turbulent heat transfer for media with the Prandtl number of the order of unity. However, in case of liquid metals whose Prandtl number is smaller by two orders of magnitude, the computations with the "standard" Pr_t value significantly overestimate heat transfer on the wall because, as already noted, the turbulent Prandtl number should increase as the relative role of molecular conduction increases; this is especially important near the wall with low Prandtl numbers.

Considering the relations given in literature for computing the turbulent Prandtl number, we have chosen formulation (5) [5] as a basis for refining the model of near-wall heat transfer, as it is simple and satisfies the above general requirements. We should also emphasize that the turbulent Prandtl number far from the wall (where $\mu_t >> \mu$ and, respectively, $\mathrm{Pe}_t >> 1$) tends to the "standard" value $\mathrm{Pr}_t = 0.85$ within this formulation, which is why the model of turbulent heat transfer has to be adjusted only in the near-wall region, without changing the properties of the standard model for the rest of the flow.

The proposed model was tailored for the turbulent Prandtl number on the problem of fully developed plane flow of incompressible fluid in the gap between differentially heated walls, one of which moved in the axial direction (Couette flow). The Reynolds number Re, constructed from the height of the channel and the velocity of the wall, was taken to be 10^7; the Prandtl numbers Pr ranged from 0.001 to 95.

Although this problem is essentially one-dimensional, the computations were carried out in a fully three-dimensional formulation, with periodic (i.e., in fact, homogeneous) conditions imposed in the axial direction. The computational grid across the channel was taken fine enough to obtain a grid-independent solution (the value of the normalized near-wall coordinate in the computational point closest to the wall was $y^+ < 0.03$). A series of computations was carried out for each selected Prandtl number with different values of the coefficient f in expression (5) (the total number of variants was 15). The results of the computations were used to determine the "optimal" value of the coefficient f providing the closest match between the computed temperature profile $T^+(y^+)$ and the following approximation

$$\begin{aligned} T^+ &= e^{-G}\,\mathrm{Pr}\,y^+ + e^{-1/G}T^+_{log};\\ G &= \frac{0.01\left(\mathrm{Pr}\;y^+\right)^4}{1+5\,\mathrm{Pr}^3\,y^+};\\ T^+_{log} &= 2.12\ln\left(\mathrm{Pr}\left(1+y^+\right)\right)+\\ &+\max\left(0;\,3.85\,\mathrm{Pr}^{1/3}-1.3\right)^2, \end{aligned} \qquad (6)$$

where, as usual,

$$T^+ = \frac{(T - T_w)\rho C_p u_\tau}{q_w};$$

$$u_\tau = \sqrt{\frac{\tau_w}{\rho}};\ y^+ = \frac{\rho d u_\tau}{\mu}.$$

This approximation is based on Kader's well-known semi-empirical correlation [20], which successfully approximates extensive experimental data with Prandtl numbers ranging from 0.025 to 95 and, therefore, can serve as their fairly reliable analytical "equivalent". Since the Reynolds number used was rather, we removed the corrections taking into account the influence of the channel height from the original Kader correlation [20]. Additionally, a limiter was introduced in approximation (6), eliminating non-monotonicity with respect to the Prandtl number in the region of its very low values (the second term in the expression for T^+_{log}).

Aside from selecting the coefficient f, we introduced some modifications to relations (5) in order to obtain the best agreement of the computed temperature profile with approximation (6). In particular, we tested different limiters preventing unbounded growth of Pr_t with $\mathrm{Pe}_t \to 0$. The final formulation of the developed model for the turbulent Prandtl number is described by the following relations:

$$\begin{gathered}
\mathrm{Pr}_t = 0.85 \cdot \begin{cases} \left(1 + f^*/\mathrm{Pe}_t^*\right), & f^* > 0 \\ \left(1 - f^*/\mathrm{Pe}_t^*\right)^{-1}, & f^* < 0 \end{cases}; \\
\mathrm{Pe}_t^* = \sqrt{0.01 + \left(\mathrm{Pr}\,\mu_t/\mu\right)^2}; \\
f^*(\mathrm{Pr}) = (\psi_1 - 1)\cdot\left(\psi_2^2 + \psi_3^2\right)^{1/2}; \\
\psi_1 = \left[\left(0.68\ln\left(1 + 50/\mathrm{Pr}\right) + 0.46\right)^{-4} + 2.2^{-4}\right]^{-1/4}; \\
\psi_2 = 0.25 + \frac{0.75}{1 + 500\,\mathrm{Pr}^2}; \\
\psi_3 = 0.11 + \frac{0.89}{1 + 5\,\mathrm{Pr}^{-2}}.
\end{gathered} \tag{7}$$

Here the function $f^*(\mathrm{Pr})$ is given by the expressions obtained as a result of approximating discrete "optimal" values of the coefficient f^*. The quality of this approximation is illustrated in Fig. 1.

Fig. 2 compares the near-wall temperature profiles for Couette flow, computed with Pr = 0.7 and 0.025, with the corresponding experimental data given in [20]. It can be seen that using the developed model (7) provided a much better agreement between the computed and measured temperature profiles, as compared with the case of the standard value Prt = 0.85. This means that we can also expect the prediction for the heat transfer coefficient to be more accurate.

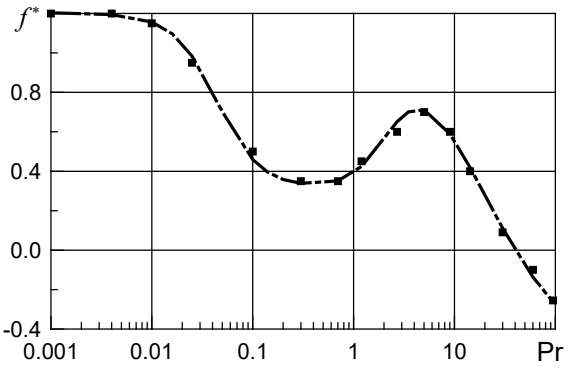

Fig. 1. Form of function $f^*(\mathrm{Pr})$ in relations (7); discrete "optimal" values of f^*(symbols) and approximating function (line) are shown

Test simulations

The above configuration of the heat transfer model (7) was carried out for the Couette model problem with a rather large Reynolds number (uncommon for practical applications), which was dictated by the desire to minimize the influence of channel height on the near-wall flow and obtain a pronounced "logarithmic" segment in the temperature profile. The predictive capabilities of the developed model in the conditions closer to real configurations were assessed by running RANS computations for fluid flow in a round tube and in a flat channel with moderate Reynolds numbers (about 10^4–10^5). We considered fully developed flow (under the action of a given pressure difference) with a volumetric heat source in both cases. The same as for the Couette flow, the problem was solved in a three-dimensional statement with periodic conditions imposed in the axial direction; the computational grid was sufficiently fine ($y^+ < 0.03$) to obtain a grid-independent solution.

Let us consider the problem of flow in a round tube in more detail. Within the adopted formulation, motion is given by superposition of the axial pressure gradient dp/dx (equivalent body force), and the mean flow rate U is found from the computation results. The pressure gradient is related to the shear stress τ_w on the wall and the diameter D of the tube by the balance ratio

$$\frac{dp}{dx} = -\frac{4\tau_w}{D}.$$

If we introduce dimensionless quantities, we can formulate the expression, relating the Reynolds number Re, the "dynamic" Reynolds number Re_τ and the friction factor ξ:

$$\frac{\mathrm{Re}_\tau}{\mathrm{Re}} = \frac{u_\tau}{U} = \sqrt{\frac{\xi}{8}},$$

where the dimensionless parameters are defined as follows:

$$\mathrm{Re} = \frac{\rho U D}{\mu};$$
$$\mathrm{Re}_\tau = \frac{\rho u_\tau D}{\mu}; \qquad (8)$$
$$\xi = \left|\frac{dp}{dx}\right| \cdot \frac{2D}{\rho U^2}.$$

Thus, the parameter set in the problem is actually the "dynamic" Reynolds number Re_τ, and the values of Re and ξ are found by computing the velocity profile.

The fluid is heated relative to a fixed wall temperature T_w by a uniform volumetric heat source Q, which actually sets the heat flux q_w on the wall: $q_w = QD/4$. This model formulation of the problem with a volumetric heat source approximately corresponds to the conditions of physical experiments with a constant heat flux on the wall. The bulk temperature $\bar{T}$ and the dimensionless heat transfer coefficient corresponding to it, that is, the Nusselt number are determined from the computed fields of flow velocity and temperature:

$$\mathrm{Nu} = \frac{q_w D}{\left(\bar{T} - T_w\right)\lambda}. \qquad (9)$$

The computations were carried out using the k–ω SST turbulence model [13] for two values of the "dynamic" Reynolds number: $\mathrm{Re}_\tau = 10^3$ and $5 \cdot 10^3$; the values obtained for Re and for the friction factor ξ (8) were, respectively, $\mathrm{Re} = 1.671 \cdot 10^4$and $1.045 \cdot 10^5$, $\xi = 0.0286$ and 0.01883. Notably, the deviation of the computed friction factors from the values given by the well-known Blasius formula [21]

$$\xi = \frac{0.3164}{\mathrm{Re}^{0.25}}$$

does not exceed 4%.

The computations were performed with the Prandtl numbers varying from 0.004 to 95. Along with the developed model (7), we also used the standard approach setting a fixed value of the turbulent Prandtl number $\mathrm{Pr}_t = 0.85$.

Fig. 3 shows the summary results of test computations, namely, comparison of the computed Nusselt numbers (points) with known empirical correlations for smooth tubes (lines):

$$\mathrm{Nu} = \frac{(\xi/8)\,\mathrm{Pr}\,\mathrm{Re}}{1.07 + 12.7\sqrt{\xi/8}\left(\mathrm{Pr}^{2/3} - 1\right)}; \qquad (10)$$

$$\mathrm{Nu} = 6.3 + 0.0167\,\mathrm{Re}^{0.85}\,\mathrm{Pr}^{0.93}. \qquad (11)$$

Correlation (10) [22, 23] for moderate Prandtl numbers ($0.5 < \mathrm{Pr} < 200$) relates the Nusselt number to the friction factor ξ (see formula (8)); the error of this correlation in the range of Reynolds numbers $10^4 < \mathrm{Re} < 5 \cdot 10^6$ does not exceed 6%.

Correlation (11) [24] is considered to be one of the best for liquid metals in the range of Reynolds numbers $10^4 < \mathrm{Re} < 10^6$.

It can be seen from Fig. 3 that the deviation of the computed Nusselt numbers from empirical correlation (10) does not exceed 10%

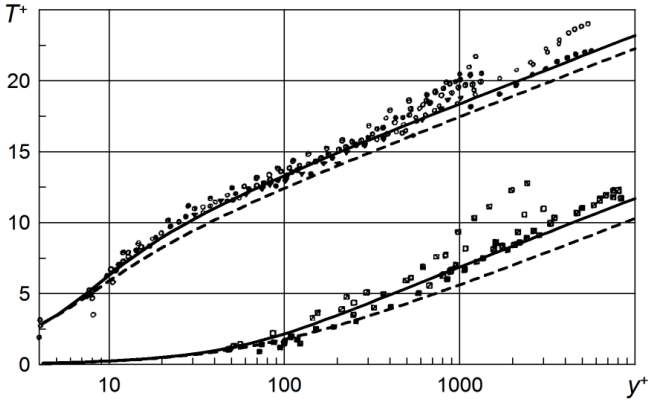

Fig. 2. Computed (lines) and measured (symbols) temperature profiles in near-wall region of quasi-steady turbulent flow for Prandtl numbers Pr = 0.7 and 0.025 (upper and lower profiles, respectively); the figure shows the results computed by model (7) (solid lines) and with $\mathrm{Pr}_t = 0.85$ (dashed lines) are given; symbols correspond to the experimental data obtained by different authors cited in [20]

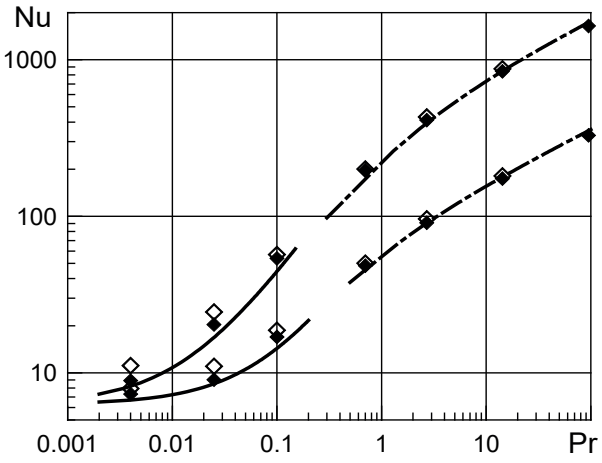

Fig. 3. Comparison of computed (symbols) and experimental (lines) data for heat transfer in round tube with "dynamic" Reynolds numbers $Re_\tau = 10^3$ and $5 \cdot 10^3$ (lower and upper curve, respectively); the figure shows the results computed by model (7), with $Pr_t = 0.85$ (shaded and empty symbols, respectively), and empirical correlations using formulae (10) and (11) (solid and dashed lines, respectively)

for Prandtl numbers $Pr \geq 0.7$, and the positive effect from using model (7) is relatively small, that is, less than 5%. In case of low Prandtl numbers ($Pr \leq 0.1$), the computation with the "standard" value $Pr_t = 0.85$ gives a significantly overestimated heat transfer rate (by almost one and a half times at the maximum); using model (7) significantly improves the situation, as the deviation from correlation (11) does not exceed 20%. In general, considering the wide scatter of experimental data on heat transfer for liquid metals, we can assume that these computations using model (7) have fairly satisfactory accuracy.

We used the open database of DNS computations [25] carried out at Prandtl numbers from 0.025 to 10 for the second test verifying the performance of the proposed model (flow in a flat channel). The statement of the problem is completely identical to the one considered above for the case of a round tube.

First, following the conditions of numerical experiments [25], we carried out computations for flow in the channel with "dynamic" Reynolds numbers $Re_\tau = 360$ and 790 (the height D of the channel was taken as the length scale). However, the obtained values of Re (8) turned out to be 4% lower than the corresponding values given in [25]; this is equivalent to overestimation of the friction factor by about 7%. Since the Nusselt number is customarily related to the Reynolds number Re (and not to Re_τ) in thermohydraulic analysis, further computations were performed with the corrected values $Re_\tau = 373$ and 814. In this case, the deviation of the obtained values $Re = 5.70 \cdot 10^3$ and $1.41 \cdot 10^4$ from the "reference" values given in [25] did not exceed 0.5%.

The main source of error in determining the friction factor in our computations is obviously the SST model itself, as it is not particularly accurate at predicting turbulent viscosity values in near-wall flow. In particular, as seen in Fig. 4, the value obtained for turbulent viscosity at the boundary of the viscous sublayer ($y^+ \approx 10$) with $Re = 1.41 \cdot 10^4$, computed according to the given model, is overestimated by a factor of 1.5, which noticeably distorts the flow velocity profile $u^+ = u/u_\tau$. Naturally, this also affects the

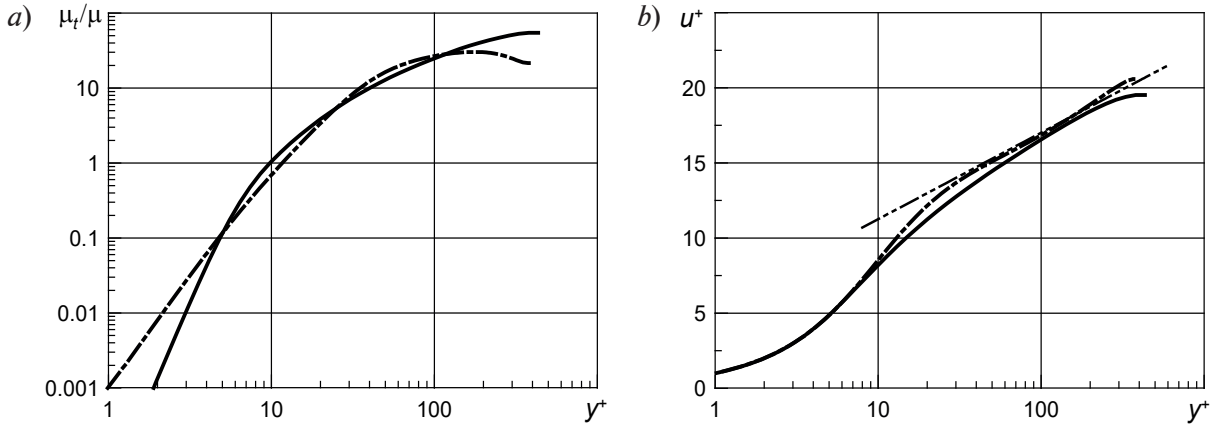

Fig. 4. Normalized profiles of turbulent viscosity (*a*) and velocity (*b*) in flat channel with $Re = 1.41 \cdot 10^4$; the figure shows the results computed by the SST model (solid lines), by DNS [25] (dash-dotted lines), and analytical solution (12) (double dash-dotted lines)

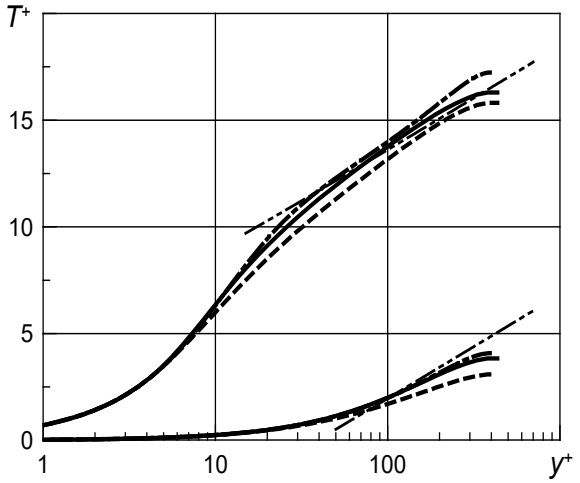

Fig. 5. Profiles of temperature T+(y+) in flat channel with Re = $1.41 \cdot 10^4$ for Pr = 0.71 and 0.025 (upper and lower family of curves, respectively); figure shows the results computed by model (7) (solid lines), with $Pr_t = 0.85$ (dashed lines), by DNS [25] (dash-dotted lines), and "logarithmic" profiles T^+_{log} (6) (double dash-dotted lines)

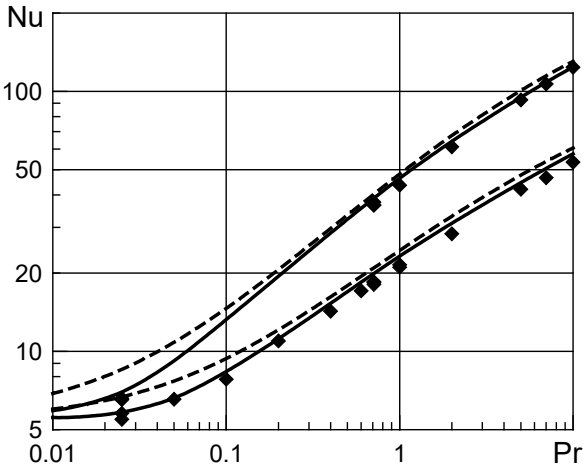

Fig. 6. Computed heat transfer in flat channel with Re = $5.7 \cdot 10^3$ and $1.41 \cdot 10^4$ (lower and upper family of curves, respectively); figure shows the results computed by model (7) (solid lines), with $Pr_t = 0.85$ (dotted lines), by DNS[25] (symbols)

magnitude of shear stress on the wall.

Fig. 4, *b* also shows the well-known analytical solution

$$u^+_{log} = 2.5 \ln\left(y^+\right) + 5.5 \qquad (12)$$

for the velocity distribution in the equilibrium "logarithmic" region of near-wall flow (see, for example, [21]). Experience of computations by the SST turbulence model indicates that the "logarithmic" region in the near-wall velocity profile tends to start with a delay in this model. It can be seen from Fig. 4, *b* that DNS computations reveal a fairly extended "logarithmic" region in the near-wall velocity profile, while the corresponding region is virtually absent in the SST model.

Fig. 5 shows the normalized temperature profiles $T^+(y^+)$ obtained in this study and by reference DNS computations [25] with the Prandtl numbers Pr = 0.71 and 0.025. Evidently, the same as in Fig. 2, using model (7) yields much better agreement of the computed temperature profiles with the reference data.

Fig. 6 shows summary results of thermal computations, namely, comparison of the Nusselt numbers (9) obtained in this study (lines) and in DNS computations [25] (points). Similar to the previous test (see Fig. 3), using the developed model (7) significantly improves the accuracy of heat transfer computations for all values of the Prandtl number. The maximum deviation of the Nusselt number from the reference values [25] decreased from 15 to 8% in the region with Pr ≥ 0.2, and from 24 to 6% for Pr ≤ 0.1.

We should also note that the final error in computing heat transfer is of the same order of magnitude as the error in computing friction (about 7%). This leads us to conclude that the reason for both errors is that the k–ω SST turbulence model is not quite accurate at predicting the behavior of turbulent viscosity.

Conclusion

We have obtained the following main results.

We have developed a new model for computing the local turbulent Prandtl number, with improved prediction of heat transfer characteristics in fluid flows with small and moderate Prandtl numbers as applied to the popular k–ω SST turbulence model.

We have carried out initial testing of the developed model for problems of fully developed flow and heat transfer in a round tube and a flat channel by varying the Prandtl number from 0.004 to 95. We have confirmed that using the proposed model helps substantially decrease the error in computing heat transfer (by about two or more times).The greatest positive effect is achieved with the Prandtl numbers less than 1/10.

The study was carried out with the financial support of the grant of the Russian National Fund No. 18-19-00082.

REFERENCES

[1] **D.C. Wilcox,** Turbulence modelling for CFD, DCW Industries Inc., 1993.

[2] **M. Leschziner,** Statistical turbulence modeling for fluid dynamics, demystified, Imperial College Press, London, 2016.

[3] **Y. Nagano, M. Shimada,** Development of a two-equation heat transfer model based on direct simulations of turbulent flows with different Prandtl numbers, Physics of Fluids. 8(12) (1996) 3379–3402.

[4] **A.J. Reynolds,** The prediction of turbulent Prandtl and Schmidt numbers, International Journal of Heat and Mass Transfer. 18 (9) (1975) 1055–1069.

[5] **W.M. Kays,** Turbulent Prandtl number – Where are we? ASME Journal of Heat Transfer. 116 (2) (1994) 284–295.

[6] **F. Chen, X. Huai, J. Cai, et al.,** Investigation on the applicability of turbulent Prandtl number models for liquid lead-bismuth eutectic, Nuclear Engineering and Design. 257 (April) (2013) 128–133.

[7] **S. Aoki,** A consideration on the heat transfer in liquid metal, Bulletin of the Tokyo Institute of Technology, Ser. B. 54 (1963) 63–73.

[8] **D.K. Hollingsworth, W.M. Kays, R.J. Moffat,** Measurement and prediction of the turbulent thermal boundary layer in water on flat and concave surface, Report HMT-41 (1989). Dept. Mech. Engineering, Stanford University.

[9] **W.M. Kays, M.E. Crawford,** Convective heat and mass transfer, McGraw-Hill, New York, 1980.

[10] **B. Weigand, J.R. Ferguson, M.E. Crawford,** An extended Kays and Crawford turbulent Prandtl number model, International Journal of Heat Mass Transfer. 40 (17) (1997) 4191–4196.

[11] **S. Vodret, D.V. di Maio, G. Caruso,** Numerical simulation of turbulent forced convection in liquid metals, Journal of Physics: Conference Series. 547 (2014) 012033, 1–10.

[12] **T.H. Shih, W.W. Liou, A. Shabbir, et al.,** A new k–e eddy-viscosity model for high Reynolds number turbulent flows – Model development and validation, Computers & Fluids. 24(3) (1995) 227–238.

[13] **F.R. Menter, M. Kuntz, R. Langtry,** Ten years of industrial experience with the SST turbulence model, Turbulence, Heat and Mass Transfer 4, Begell House, (2003) 625–632.

[14] **H. Kawamura, H. Abe, Y. Matsuo,** DNS of turbulent heat transfer in channel flow with respect to Reynolds and Prandtl number effect, International Journal of Heat and Fluid Flow. 20(3) (1999) 196–207.

[15] **E.M. Smirnov, D.K. Zaitsev,** Finite volume method as applied to hydro- and gas dynamics and heat transfer problems in complex geometry domains, St. Petersburg State Polytechnical University Journal. (2(36)) (2004) 70–81.

[16] **A.G. Abramov, G.A. Kovalev, E.M. Smirnov,** Numerical simulation of circulation of steam-air mixture and film condensation on series of vertical tubes, St. Petersburg Polytechnical University Journal. Physics and Mathematics. (3 (177)) (2013) 69–79.

[17] **A.A. Pozhilov, D.K. Zaitsev, E.M. Smirnov, A.A. Smirnovsky,** Numerical simulation of heat and mass transfer in a 3D model of a loop heat pipe evaporator, St. Petersburg Polytechnical University Journal. Physics and Mathematics. 3(3) (2017) 210–217.

[18] **S.I. Smirnov, E.M. Smirnov, A.A. Smirnovsky,** Endwall heat transfer effects on the turbulent mercury convection in a rotating cylinder, St. Petersburg Polytechnical University Journal. Physics and Mathematics. 3(2) (2017) 83–94.

[19] **E.M. Smirnov, A.A. Smirnovsky, N.A. Schur, et al.,** A comparison of RANS and IDDES solutions for turbulent flow and heat transfer past a backward-facing step, Heat and Mass Transfer. 54(8) (2018) 2231–2241.

[20] **B.A. Kader,** Temperature and concentration profiles in fully turbulent boundary layers, International Journal of Heat and Mass Transfer. 24 (9) (1981) 1541–1544.

[21] **H. Schlichting,** Boundary layer theory, McGraw-Hill, New York, 1979.

[22] **B.S. Petukhov, V.V. Kirillov,** K voprosu o teploobmene pri turbulentnom techenii zhidkosti v trubah [On heat exchange in the turbulent fluid flow in tubes], Thermal Engineering. 4 (1958) 63–68.

[23] **B.S. Petukhov,** Heat transfer and friction in turbulent pipe flow with variable physical properties, Advances in Heat Transfer. 6 (1970) 504–564.

[24] **C.A. Sleicher, A.S. Awad, R.H. Notter,** Temperature and eddy diffusivity profiles in NaK, International Journal of Heat and Mass Transfer. 16(8) (1973) 1565–1575.

[25] **H. Kawamura,** DNS database of wall turbulence and heat transfer, https://www.rs.tus.ac.jp/~t2lab/db/index.html, accessed Jan. 11, 2019.

Received 16.01.2019, accepted 31.01.2019.

THE AUTHORS

ZAITSEV Dmitri K.
Peter the Great St. Petersburg Polytechnic University
29 Politechnicheskaya St., St. Petersburg, 195251, Russian Federation
zaitsev_dk@spbstu.ru

SMIRNOV Evgueni M.
Peter the Great St. Petersburg Polytechnic University
29 Politechnicheskaya St., St. Petersburg, 195251, Russian Federation
smirnov_em@spbstu.ru

СПИСОК ЛИТЕРАТУРЫ

1. **Wilcox D.C.** Turbulence modelling for CFD. La Canada: DCW Industries Inc., 1993. 460 p.

2. **Leschziner M.** Statistical turbulence modelling for fluid dynamics, demystified. London: Imperial College Press, 2016. 424 p.

3. **Nagano Y., Shimada M.** Development of a two-equation heat transfer model based on direct simulations of turbulent flows with different Prandtl numbers // Physics of Fluids. 1996. Vol. 8. No. 12. Pp. 3379–3402.

4. **Reynolds A.J.** The prediction of turbulent Prandtl and Schmidt numbers // International Journal of Heat and Mass Transfer. 1975. Vol. 18. No. 9. Pp. 1055–1069.

5. **Kays W.M.** Turbulent Prandtl number – Where are we? // ASME Journal of Heat Transfer. 1994. Vol. 116. No. 2. Pp. 284–295.

6. **Chen F., Huai X., Cai J., Li X., Meng R.** Investigation on the applicability of turbulent Prandtl number models for liquid lead-bismuth eutectic // Nuclear Engineering and Design. 2013. Vol. 257. April. Pp. 128–133.

7. **Aoki S.** A consideration on the heat transfer in liquid metal // Bulletin of the Tokyo Institute of Technology. Ser. B. 1963. Vol. 54. Pp. 63–73.

8. **Hollingsworth D.K., Kays W.M., Moffat R.J.** Measurement and prediction of the turbulent thermal boundary layer in water on flat and concave surface // Report HMT-41. Dept. Mech. Engineering, Stanford University, 1989.

9. **Kays W.M., Crawford M.E.** Convective heat and mass transfer. New York: McGraw-Hill, 1980. 387 p.

10. **Weigand B., Ferguson J.R., Crawford M.E.** An extended Kays and Crawford turbulent Prandtl number model // International Journal of Heat and Mass Transfer. 1997. Vol. 40. No. 17. Pp. 4191–4196.

11. **Vodret S., di Maio D.V., Caruso G.** Numerical simulation of turbulent forced convection in liquid metals // Journal of Physics: Conference Series. 2014. Vol. 547. P. 012033. Pp. 1–10.

12. **Shih T.H., Liou W.W., Shabbir A., Yang Z., Zhu J.** A new $k - e$ eddy-viscosity model for high Reynolds number turbulent flows – model development and validation // Computers & Fluids. 1995. Vol. 24. No. 3. Pp. 227–238.

13. **Menter F.R., Kuntz M., Langtry R.** Ten years of industrial experience with the SST turbulence model // Turbulence, Heat and Mass Transfer 4. Begell House. 2003. Pp. 625–632.

14. **Kawamura H., Abe H., Matsuo Y.** DNS of turbulent heat transfer in channel flow with respect to Reynolds and Prandtl number effect // International Journal of Heat and Fluid Flow. 1999. Vol. 20. No. 3. Pp. 196–207.

15. **Смирнов Е.М., Зайцев Д.К.** Метод конечных объемов в приложении к задачам гидрогазодинамики и теплообмена в областях сложной геометрии // Научно-технические ведомости. 2004. № 2 (36). С. 70–81.

16. **Абрамов А.Г., Ковалев Г.А., Смирнов Е.М.** Численное моделирование циркуляции паровоздушной среды и сопутствующей конденсации на ряде вертикальных трубок // Научно-технические ведомости СПбГПУ. Физико-математические науки. 2013. № 3 (177). С. 69–79.

17. **Пожилов А.А., Зайцев Д.К., Смирнов Е.М., Смирновский А.А.** Численное моделирование тепломассопереноса в трехмерной модели испарителя контурной тепловой трубы // Научно-технические ведомости СПбГПУ. Физико-математические науки. 2017. Т. 10. № 3. С. 52–63.

18. **Смирнов С.И., Смирнов Е.М., Смирновский А.А.** Влияние теплопереноса в торцевых стенках на турбулентную конвекцию ртути во вращающемся цилиндре // Научно-технические ведомости СПбГПУ. Физико-математические науки. 2017. Т. 10, № 1. С. 31–46.

19. **Smirnov E.M., Smirnovsky A.A., Schur N.A., Zaitsev D.K., Smirnov P.E.** Comparison

of RANS and IDDES solutions for turbulent flow and heat transfer past a backward-facing step // Heat and Mass Transfer. 2018. Vol. 54. No. 8. Pp. 2231–2241.

20. **Kader B.A.** Temperature and concentration profiles in fully turbulent boundary layers // International Journal of Heat and Mass Transfer. 1981. Vol. 24. No. 9. Pp. 1541–1544.

21. **Шлихтинг Г.** Теория пограничного слоя. М.: Наука, 1974. 712 с.

22. **Петухов Б.С., Кириллов В.В.** К вопросу о теплообмене при турбулентном течении жидкости в трубах // Теплоэнергетика. 1958. № 4. С. 63–68.

23. **Petukhov B.S.** Heat transfer and friction in turbulent pipe flow with variable physical properties // Advances in Heat Transfer. 1970. Vol. 6. Pp. 504–564.

24. **Sleicher C.A., Awad A.S., Notter R.H.** Temperature and eddy diffusivity profiles in NaK // International Journal of Heat Mass Transfer. 1973. Vol. 16. No. 8. Pp. 1565–1575.

25. **Kawamura H.** DNS database of wall turbulence and heat transfer. URL: https://www.rs.tus.ac.jp/~t2lab/db/index.html (Accessed date: 11.01. 2019).

Статья поступила в редакцию 16.01.2019, принята к публикации 31.01.2019.

СВЕДЕНИЯ ОБ АВТОРАХ

ЗАЙЦЕВ Дмитрий Кириллович – *доктор физико-математических наук, профессор кафедры* «Гидроаэродинамика, горение и теплообмен» Санкт-Петербургского политехнического университета Петра Великого, Санкт-Петербург, Российская Федерация.

195251, Российская Федерация, г. Санкт-Петербург, Политехническая ул., 29

zaitsev_dk@spbstu.ru

СМИРНОВ Евгений Михайлович – *доктор физико-математических наук, заведующий кафедрой* «Гидроаэродинамика, горение и теплообмен» Санкт-Петербургского политехнического университета Петра Великого, Санкт-Петербург, Российская Федерация.

195251, Российская Федерация, г. Санкт-Петербург, Политехническая ул., 29

smirnov_em@spbstu.ru

DOI: 10.18721/JPM.12104
УДК 517.946

SEMI-BOUNDED STRING'S VIBRATIONS INITIATED BY THE BOUNDARY REGIME

D.S. Anikonov, D.S. Konovalova

Sobolev Institute of Mathematics, Novosibirsk, Russian Federation

Transverse vibrations of a semi-bounded string consisting of different materials are considered. The homogeneous wave equation with piecewise constant coefficients stand duty as a mathematical model. As a first step, we have investigated the solution of this equation with zero Cauchy data. The existence and uniqueness of the generalized solution of the problem were proved and the properties of the solution were analyzed. The specificity of the obtained conclusions was discussed, in particular, the zones of oscillations' propagation and of their absence were demonstrated. The obtained results are of a constructive character and can serve as a basis for the creation of a numerical algorithm. The importance of such problems is caused by their use in the theory of sensing inhomogeneous media by physical signals.

Keywords: differential equation, discontinuous coefficient, sounding of unknown media, wave process

Citation: D.S. Anikonov, D.S. Konovalova, Semi-bounded string's vibrations initiated by the boundary regime, St. Petersburg Polytechnical State University Journal. Physics and MatheS matics. 12 (1) (2019) 45–54. DOI: 10.18721/JPM.12104

КОЛЕБАНИЯ ПОЛУОГРАНИЧЕННОЙ СТРУНЫ, ИНИЦИИРОВАННЫЕ ГРАНИЧНЫМ РЕЖИМОМ

Д.С. Аниконов, Д.С. Коновалова

Институт математики им. С.Л. Соболева СО РАН,

г. Новосибирск, Российская Федерация

Рассматриваются поперечные колебания полуограниченной струны, состоящей из различных материалов. Математической моделью служит однородное волновое уравнение с кусочно-постоянными коэффициентами. В качестве первого этапа исследуется решение этого уравнения с нулевыми данными Коши. Доказывается существование и единственность обобщенного решения поставленной задачи, и анализируются его свойства. Отмечается специфичность полученных выводов, в частности, указываются зоны распространения колебаний и их отсутствия. Полученные результаты имеют конструктивный характер и могут служить основой создания численного алгоритма. Актуальность подобных задач вызвана их использованием в теории зондирования неоднородных сред физическими сигналами.

Ключевые слова: дифференциальное уравнение, разрывный коэффициент, зондирование неизвестных сред, волновой процесс

Ссылка при цитировании: Аниконов Д.С., Коновалова Д.С. Колебания полуограниченной струны, инициированные граничным режимом // Научно-технические ведомости СПбГПУ. Физико-математические науки. 2019. Т. 12. № 1. С. 50–60. DOI: 10.18721/JPM.12104

Introduction

In this study, we have considered solutions of differential equations with discontinuous coefficients for higher derivatives. This field of research is still in its infancy, with no consistent results available. All the same, a number of studies of this type have been carried out [1–13]; the findings in [8–10] are perhaps closest to our own.

The essence of this problem is as follows. Considering a plane of variables (x,t) in the

first quadrant

$$\mathbb{R}_2^{++}=((x,t), x>0, t>0)$$

we take the equation

$$\alpha(x)\frac{\partial^2 u(x,t)}{\partial t^2}-\beta(x)\frac{\partial^2 u(x,t)}{\partial x^2}=0, \quad (x,t)\in\mathbb{R}_2^{++}, \alpha(x), \beta(x)>0 \qquad (1)$$

and additional conditions

$$u(0,t)=\mu(t),\ u(x,0)=0,\ u_t(x,0)=0 \qquad (2)$$

It is assumed that the function $\mu(t)$ has continuous derivatives up to and including the second order and the consistency conditions are satisfied:

$$\mu(0)=\mu'(0)=\mu''(0)=0, \qquad (3)$$

These conditions coincide with the traditional requirements formulated in monograph [11].

For convenience, we assume that the function $\mu(t)$ is extended by zero at $t < 0$. Problem (1), (2) consists in finding the function $u(x,t)$ with the given functions $\alpha(x)$, $\beta(x)$, $\mu(t)$. Equations for solving this problem with constant α, β are well known and are given, for example, in monograph [11].

The case we are considering has not been studied previously: it is when the functions $\alpha(x)$, $\beta(x)$ are piecewise-constant:

$$\alpha(x)=\alpha_1,\ 0\le x\le x_0,\ \alpha(x)=\alpha_2,\ x>x_0;$$

$$\beta(x)=\beta_1,\ 0\le x\le x_0,\ \beta(x)=\beta_2,\ x>x_0,$$

where x_0, α_1, α_2, β_1, β_2 are positive constant numbers.

Equalities (1), (2), in particular, are a mathematical model for the process of transverse vibrations of a semi-bounded string. The vibrations are caused in this case only by the behavior of the boundary point ($x = 0$). According to our initial assessment, studying a more general problem with a nonzero right-hand side of Eq. (1) and nonzero Cauchy data $(u(x,0),u_t(x,0))$ would be incredibly cumbersome; we plan to tackle this task step-by-step in the future.

We should also note that the given problem (1), (2) is rather peculiar both because a relatively simple method can be used to solve it and because of the conclusions. In particular, we are going to find the zone of propagation of vibrations and the zone with no vibrations. The structure of these zones depends on the values of discontinuous coefficients of Eq. (1) and differs from the classical case.

Notations and definitions adopted

Aside from traditional notations, we are also going to use $\partial_1\chi(x,t)$, $\partial_2\chi(x,t)$ for the first derivatives of an arbitrary function $\chi(x,t)$, differentiable with respect to x and t.

Let us introduce the following unit vectors with characteristic directions:

$$\omega_1^+=\left(\frac{\sqrt{\beta_1}}{\sqrt{\alpha_1+\beta_1}},\frac{\sqrt{\alpha_1}}{\alpha_1+\beta_1}\right),$$

$$\omega_1^-=\left(\frac{-\sqrt{\beta_1}}{\sqrt{\alpha_1+\beta_1}},\frac{\sqrt{\alpha_1}}{\sqrt{\alpha_1+\beta_1}}\right),$$

$$\omega_2^+=\left(\frac{\sqrt{\beta_2}}{\sqrt{\alpha_2+\beta_2}},\frac{\sqrt{\alpha_2}}{\sqrt{\alpha_2+\beta_2}}\right),$$

$$\omega_2^-=\left(\frac{-\sqrt{\beta_2}}{\sqrt{\alpha_2+\beta_2}},\frac{\sqrt{\alpha_2}}{\sqrt{\alpha_2+\beta_2}}\right).$$

Let us denote

$$\gamma_1=\sqrt{\alpha_1\beta_1},\gamma_2=\sqrt{\alpha_2\beta_2},$$

$$a_1=\sqrt{\beta_1}/\sqrt{\alpha_1},$$

$$a_2=\sqrt{\beta_2}/\sqrt{\alpha_2}.$$

The following sets are taken in the quadrant $\mathbb{R}_2^{++}$:

$$G_1=\{(x,t): 0<x<x_0,\ t>0\}$$

$$G_2=\{(x,t): x>x_0,\ t>0$$

$$G_0=G_1\cup G_2$$

Line integrals of the second kind are widely used in our study. The notation (PQ) is used for a curve starting at point $P=(p_1, p_2)$ and ending at point $Q=(q_1, q_2)$. If the curve is the boundary of a simply-connected bounded domain, the orientation adopted is such that the domain is located on the left for a point moving along the curve. We have assumed that the points P and Q belong to the curve (PQ).

A generalized solution is sought in the class of functions $u(x,t)$ satisfying conditions (2) and Eq. (1) in the domains G_1 and G_2. In general, $u(x,t)$ is assumed to be continuous for $x\ge 0$, $t\ge 0$ and have partial derivatives in the domains G_1 and G_2, which are uniformly continuous in any bounded subdomain in G_1 and G_2. It is

additionally assumed that the below coupling conditions are satisfied on the ray (x_0,t), $t > 0$:

$$\lim_{x\to x_0-0}\partial_2 u(x,t)=\lim_{x\to x_0+0}\partial_2 u(x,t), \quad (4)$$

$$\lim_{x\to x_0-0}\beta_1\partial_1 u(x,t)=\lim_{x\to x_0+0}\beta_2\partial_1 u(x,t), \quad (5)$$

which are consequences of Hooke's law and the law of conservation of momentum.

Monograph [11] considered a problem with the same sense as the problem (1), (2) that we have formulated, but under different restrictions, namely, with an integro-differential equation with respect to the function $u(x,t)$ studied instead of Eq. (1):

$$J(G)=\int_{\partial G}\alpha(\xi)\partial_2 u(\xi,\tau)d\xi+ \\ +\beta(\xi)\partial_1 u(\xi,\tau)d\tau=0. \quad (6)$$

The argument G in equality (6) is an arbitrary simply-connected domain in $\overline{\mathbb{R}}_2^{++}$ and its boundary ∂G is a piecewise smooth line of class C^1. The function $u(x,t)$ *is* continuous in $\overline{\mathbb{R}}_2^{++}$ and its partial derivatives $\partial_1 u(x,t)$, $\partial_2 u(x,t)$ are piecewise continuous with possible discontinuities of the first kind on certain lines. In this case, discontinuities of $\partial_1 u(x,t)$, $\partial_2 u(x,t)$ are allowed within G and it is also possible that the line of discontinuities coincides with a part of ∂G. Then the derivatives $\partial_1 u(x,t)$, $\partial_2 u(x,t)$ are replaced in Eq. (6) by their limit values within domain G. Notably, Eq. (6) is a consequence of Hooke's law and the law of conservation of momentum. Accordingly, the conclusions obtained from equality (6) also follow from these laws.

Let us call Eq. (6) with condition (2) problem (6), (2). Notice that within the problem statement formulated in [11], the presence of variables $\alpha(x)$, $\beta(x)$ is allowed in Eq. (6); however, all conclusions are drawn for constant coefficients.

Construction of composite characteristics emanating from a point in domain G_1

From now on, we are going to repeatedly use the following simple statement for the functions $u(x,t)$ described in problem (6), (2):

Lemma. *The following equalities hold true:*

$$\int_{(PQ)}\alpha(\xi)\partial_2 u(\xi,\tau)d\xi+\beta(\xi)\partial_1 u(\xi,\tau)d\tau= \\ =\gamma_i(u(Q)-u(P)), \\ (PQ)\subset\overline{G_i},(PQ)=\left\{P-\tau\omega_i^+,\tau\in[0,|Q-P|]\right\}, \\ i=1,2; \quad (7)$$

$$\int_{(PQ)}\alpha(\xi)\partial_2 u(\xi,\tau)d\xi+\beta(\xi)\partial_1 u(\xi,\tau)d\tau= \\ =-\gamma_i(u(Q)-u(P)), \\ (PQ)\subset\overline{G_i},(PQ)= \\ =\left\{P+\tau\omega_i^-,\tau\in[0,|Q-P|]\right\}, \\ i=1,2. \quad (8)$$

Proof. Using the following representation in the left-hand side of the formula (7):

$$(PQ)=\left(p_1-s\frac{\sqrt{\beta_i}}{\sqrt{\alpha_i+\beta_i}},p_2-s\frac{\sqrt{\alpha_i}}{\sqrt{\alpha_i+\beta_i}}\right), \\ 0\le s\le|Q-P|,$$

we can then proceed to an ordinary definite integral:

$$\int_{(PQ)}\alpha_i\partial_2 u(\xi,\tau)d\xi+\beta_i\partial_1 u(\xi,\tau)d\tau= \\ =\int_0^{|QP|}\left[\alpha_i\partial_2 u\left(p_1-s\frac{\sqrt{\beta_i}}{\sqrt{\alpha_i+\beta_i}},\right.\right. \\ \left.p_2-s\frac{\sqrt{\alpha_i}}{\sqrt{\alpha_i+\beta_i}}\right)\frac{-\sqrt{\beta_i}}{\sqrt{\alpha_i+\beta_i}}+ \\ +\beta_i\partial_1 u\left(p_1-s\frac{\sqrt{\beta_i}}{\sqrt{\alpha_i+\beta_i}},\right. \\ \left.\left.p_2-s\frac{\sqrt{\alpha_i}}{\sqrt{\alpha_i+\beta_i}}\right)\frac{-\sqrt{\alpha_i}}{\sqrt{\alpha_i+\beta_i}}\right]ds= \\ =\sqrt{\alpha_i\beta_i}\int_0^{|QP|}\frac{d}{ds}\left[u(P-s\omega_i^+)\right]= \\ \gamma_i(u(Q)-u(P)).$$

As a result, the equalities obtained prove formula (7); formula (8) is proved in a similar fashion.

The lemma is proved.

Next, let us construct the following scheme.

Let us draw a segment of the straight line $x=a_1 t$ from the origin until it intersects the line $x=x_0$ at point $P=(x_0,p)$. We then draw a ray lying on line $x_0=a_2(t-p)$ and located in the domain G from point P. The domain bounded from above by the segment and the ray and from below by the semi-axis Ox, $x > 0$ is denoted by G_3.

Let us prove that equality (6) implies another equality:

$$u(x,t)=0,\ (x,t)\in G_3$$

We take an arbitrary point $H=(x_0,h)$ in domain G_3.

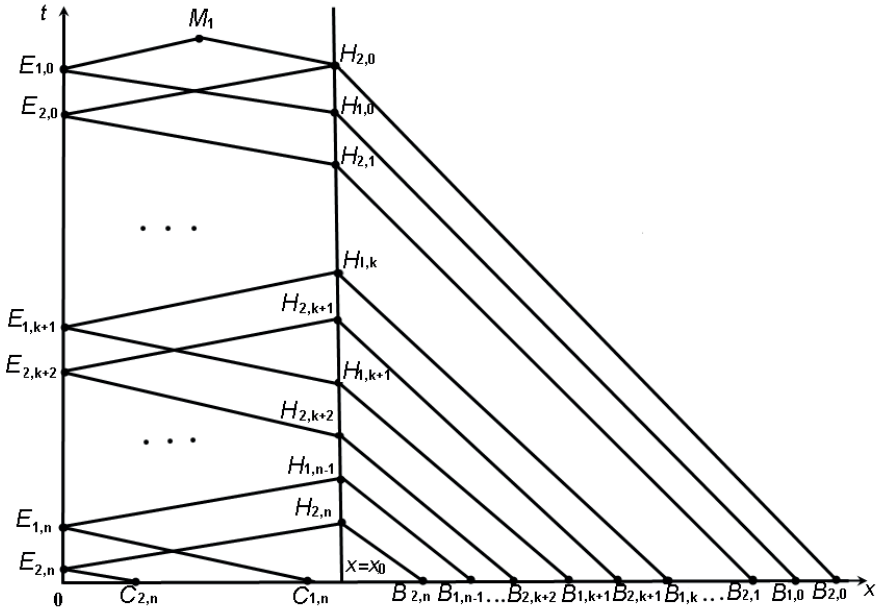

Fig. 1. Illustration to constructing two composite characteristics emanating from point $M_1=(x,t)$, $0 < x < x_0$, $t > a_1x$ on graph of $x(t)$

The straight lines

$$x-x_0=a_1(t-h),\ x-x_0=-a_2(t-h)$$

intersect the semi-axis Ox, $x > 0$ at points C and B, respectively.

We take a triangle $G(H)$ with vertices at points H, B, C as domain G; based on the lemma and formula (6) we obtain:

$$\int_{(PQ)} \alpha_i \partial_2 u(\xi,\tau)d\xi+\beta_i\partial_1 u(\xi,\tau)d\tau =$$
$$\int_{(PQ)} \alpha_i \partial_2 u(\xi,\tau)d\xi+\beta_i\partial_1 u(\xi,\tau)d\tau =$$
$$\int_{(PQ)} \alpha_i \partial_2 u(\xi,\tau)d\xi+\beta_i\partial_1 u(\xi,\tau)d\tau =$$
$$\int_{(PQ)} \alpha_i \partial_2 u(\xi,\tau)d\xi+\beta_i\partial_1 u(\xi,\tau)d\tau =$$
$$\int_{(PQ)} \alpha_i \partial_2 u(\xi,\tau)d\xi+\beta_i\partial_1 u(\xi,\tau)d\tau =$$

Then, in view of equalities

$$u(C) = u(B) = 0$$

we obtain the equality $u(H) = 0$.

Now we take the point

$$M = (x,t) \in G_1 \cap G_3$$

The line $\xi - x = a_1(\tau-t)$ passing through point M intersects the semi-axis Ox, $x>0$ at point C'. Let us now consider a line

$$\xi - x = -a_1(\tau-t)$$

also passing through point M, taking the more complicated of the two possible options when this line crosses the ray (x_0,t), $t > 0$, at point $H=(x_0,h)$ in the domain G_3. Next, we draw through point H a straight line

$$\xi - x_0 = - a_2(\tau-h),$$

intersecting the semi-axis Ox, $x > 0$ at point B'.

Let us consider a quadrangle $G(M)$ with vertices M, C', B', H. We apply formula (6) to the domain $G=G(M)$ and calculate the integrals along the straight sections of its boundary; in view of the equalities

$$u(C') = u(B') = u(H) = 0,$$

we obtain the equality $u(M)=0$.

The reasoning is completely the same for point $M = (x,t) \in G_2 \cap G_3$.

It is known from the theory of differential equations that the characteristics for Eq. (1) are segments of lines

$$x=\pm a_1 t+const$$

in the domain G_1, and segments of lines

$$x=\pm\ a_2 t+const$$

in the domain G_2.

We take the point $M_1 \in G_1 \setminus \overline{G}_3$, i.e.,

$$M_1 = (x,\ t),\ 0 < x < x_0,\ t > a_1x$$

(Fig. 1). We draw two continuous composite characteristics lying in the domain $\overline{G}_1$ from point M; segments of these characteristics passing through

point $P = (p_1, p_2)$ are parts of straight lines

$$\xi - p_1 = \pm a_1(\tau - p_2).$$

These segments have endpoints on the rays.

$$R_1 = (0,t),\ t > 0,$$

$$R_2 = (x_0,t),\ t > 0$$

The points lying on the ray R_1 are denoted as

$$E_{i,k} = (0, e_{i,k}), i = 1,2, k = 0,1,...,$$

and the points on the ray R_2 as $H_{i,k}=(x_0,h_{i,k})$.

In this case, the index i numbers the composite characteristics, and the index k the endpoints.

The first composite characteristic is obtained by the following rule. A straight line

$$\xi - x = a_1(\tau - t)$$

is drawn from point M_1 until it intersects the ray R_1 at point $E_{1,0} = (0, e_{1,0})$. Next, a straight line

$$\xi = - a_1(\tau - e_{1,0})$$

is drawn through the obtained point $E_{1,0}$ until it intersects the ray R_2 at point $H_{1,0} = (x_0,h_{1,0})$. Further construction consists in drawing the lines

$$\xi = - a_1(\tau - e_{1,k})$$

through the obtained points $E_{1,k} = (0, e_{1,k})$ on ray R_1, intersecting ray R_2 at points $H_{1,k} = (x_0, h_{1,k})$. Straight lines

$$\xi - x_0 = a_1(\tau - h_{1,k})$$

are drawn through points $H_{1,k}$.

The formulae for these points have the following form:

$$e_{1,k} = t - \frac{x}{a_1} - 2k\frac{x_0}{a_1},$$

$$h_{1,k} = t - \frac{x}{a_1} - (2k+1)\frac{x_0}{a_1},\ k \ge 0. \qquad (9)$$

Construction continues until the obtained segments of the characteristics have a non-empty intersection with the domain G_1. Thus, we have obtained a set of points $E_{1,k}$, $H_{1,k}$ on rays R_1, R_2 respectively, $0 \le k \le n$. For final construction, we use the straight line

$$\xi = - a_1(\tau - e_{1,n}),$$

intersecting the semi-axis Ox, $x > 0$, at point $C_{1,n}$.

The second composite characteristic emanating from point M_1 is constructed similarly, i.e., a straight line $\xi - x_0 = - a_1(\tau - t)$ is drawn from point M_1 until it intersects ray R_2 at point $H_{2,0}$. The sequence of steps we take then is alternately using the characteristics $\xi = \pm a_1\tau + const$ emanating from the points already obtained; we get a set of endpoints $E_{2,k}$, $0 \le k \le n$, on ray R_1 and $H_{2,k}$, $0 \le k \le n$, on ray R_2 and also point $C_{2,n}$ on the horizontal axis $(0, x_0)$.

The formulae for these points have the following form:

$$e_{2,k} = t - \frac{x_0 - x}{a_1} - (2k+1)\frac{x_0}{a_1},$$

$$h_{2,k} = t - \frac{x_0 - x}{a_1} - 2k\frac{x_0}{a_1}, \qquad (10)$$

$$k \ge 0,\ C_{2,n} = (0, c_{2,n}).$$

Construction of the characteristics used is simpler in the set $\overline{G}_2$: straight lines

$$\xi - x_0 = - a_2(\tau - h_{i,k})$$

are drawn through points $H_{i,k}$, $i = 1, 2$, $k = 0,...,n$, until they intersect the semi-axis Ox, $x > 0$ at points $B_{i,k}$.

Consequences from Eq. (6) for the function $u(x,t)$ in domains G_1, G_2

Let us consider a polygon $G(M_1)$ with vertices at points M_1, $E_{1,0}$, $H_{1,0}$, $B_{1,0}$, $B_{2,0}$, $H_{2,0}$ and apply formula (6) to it for the case $G=G(M_1)$ (see Fig. 1).

Since

$$\partial G(M_1) = (M_1E_{1,0}) \cup (E_{1,0}H_{1,0}) \cup (H_{1,0}B_{1,0}) \cup$$
$$\cup (B_{1,0}B_{2,0}) \cup (B_{2,0}H_{2,0}) \cup (H_{2,0}M_1),$$

we calculate the integral $J(G(M_1))$ using the lemma

$$J(G(M_1)) = \gamma_1(u(E_{1,0}) - u(M_1)) -$$
$$-\gamma_1(u(H_{1,0}) - u(E_{1,0})) - \gamma_2(u(B_{1,0}) -$$
$$-u(H_{1,0})) - \gamma_2(u(H_{2,0}) - u(B_{2,0})) -$$
$$-\gamma_1(u(M_1) - u(H_{2,0})) = 0.$$

It follows then, in view of equalities $u(B_{1,0}) = u(B_{2,0}) = 0$, that

$$u(M_1) = u(E_{1,0}) + \frac{\gamma_2 - \gamma_1}{2\gamma_1} \times$$
$$\times u(H_{1,0}) + \frac{\gamma_1 - \gamma_2}{2\gamma_1} u(H_{2,0}). \qquad (11)$$

To find the expression for $u(H_{2,0})$, let us consider a polygon $G(H_{2,0})$ with vertices at points $H_{2,0}$, $E_{2,0}$, $H_{2,1}$, $B_{2,1}$, $B_{2,0}$. Similar to the calculations we have just performed, using the lemma for the case $G=G(H_{2,0})$, we obtain the following:

$$u(H_{2,0}) = \frac{2\gamma_1}{\gamma_2 + \gamma_1} u(E_{2,0}) + \frac{\gamma_2 - \gamma_1}{\gamma_2 + \gamma_1} u(H_{2,1}).$$

To find the expression for $u(H_{2,1})$, let us consider a polygon $G=G(H_{2,1})$ with vertices

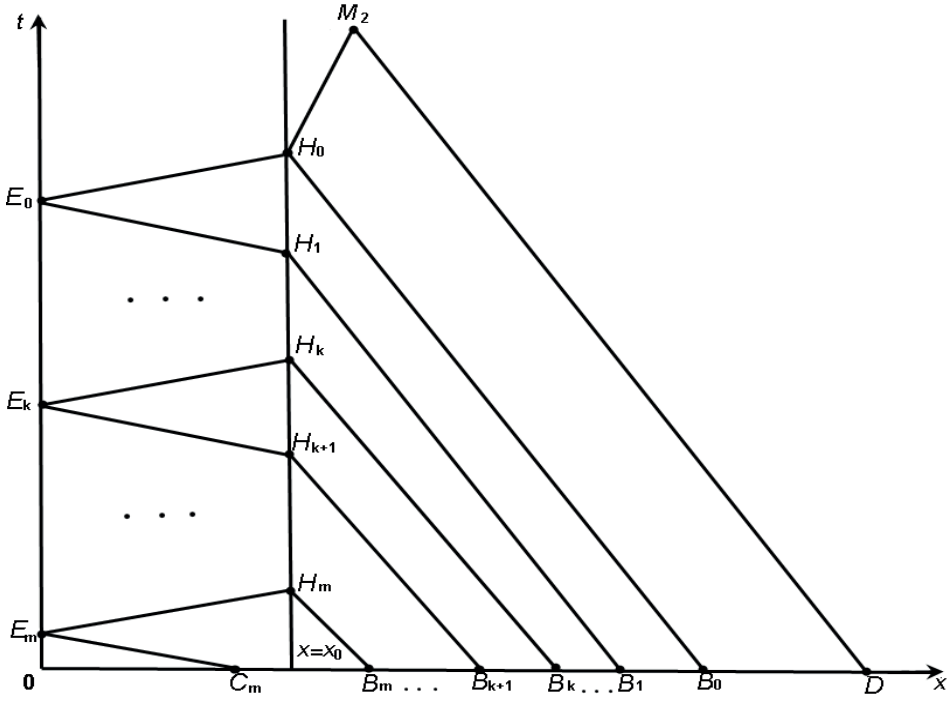

Fig. 2. Illustration to constructing two composite characteristics emanating from point $M_2 \in G_2 \backslash \overline{G}_3$ on graph of $x(t)$

at points $H_{2,1}$, $E_{2,1}$, $H_{2,2}$, $B_{2,2}$, $B_{2,1}$. Using the lemma again and repeating the calculations, we obtain the formula

$$u(H_{2,1}) = \frac{2\gamma_1}{\gamma_2+\gamma_1} u(E_{2,1}) + \frac{\gamma_2-\gamma_1}{\gamma_2+\gamma_1} u(H_{2,2}).$$

In the same way, we can obtain the following general formula:

$$u(H_{2,k}) = \frac{2\gamma_1}{\gamma_2+\gamma_1} u(E_{2,k}) + \frac{\gamma_2-\gamma_1}{\gamma_2+\gamma_1} u(H_{2,k+1}). \quad (12)$$

Using the resulting recurrent formula (12), we obtain:

$$u(H_{1,0}) = \frac{2\gamma_1}{\gamma_2+\gamma_1} \sum_{k=0}^{\infty} \left(\frac{\gamma_2-\gamma_1}{\gamma_2+\gamma_1} \right)^k u(E_{1,k+1}). \quad (13)$$

To find the formulae for $u(H_{1,0})$ in a similar manner but using the elements of the second composite characteristic emanating from point M_1, we obtain the following equality:

$$u(H_{1,0}) = \frac{2\gamma_1}{\gamma_2+\gamma_1} \sum_{k=0}^{\infty} \left(\frac{\gamma_2-\gamma_1}{\gamma_2+\gamma_1} \right)^k u(E_{1,k+1}). \quad (14)$$

Notably, only a finite number of first terms is non-zero in the right-hand sides of equalities (13) and (14), due to condition (3), $\mu(t)=0$, $t \le 0$. Using Eqs. (13), (14) for formula (11), we end up with

$$u(M_1) = u(E_{1,0}) + \sum_{k=0}^{\infty} \left(\frac{\gamma_2-\gamma_1}{\gamma_2+\gamma_1} \right)^{k+1} \times \left(u(E_{1,k+1}) - u(E_{2,k}) \right). \quad (15)$$

Let us now consider a simpler case when an arbitrary point $M_2 = (x,t)$ belongs to the domain $G_2 \backslash \overline{G}_3$. We construct a continuous composite characteristic emanating from this point and ending on the horizontal axis. For this purpose, we once again use the segments of the characteristics lying on the straight lines

$$\xi = \pm a2\ \tau + \text{const}.$$

We denote the endpoints of the individual characteristics obtained on the ray $x=x_0$, $t > 0$, by H_k, $k = 0, 1, ..., m$ and those on the ray $x = 0$, $t > 0$ by E_k, $k = 0, 1..., m$. We denote the endpoints of the individual characteristics on the horizontal axis in ascending order by C_m, B_m, B_{m-1},..., B_0, D (Fig. 2).

By similar reasoning as in the previous case, we obtain the following formulae:

$$u(M_2) = \frac{2\gamma_1}{\gamma_2+\gamma_1} \sum_{k=0}^{\infty} \left(\frac{\gamma_2-\gamma_1}{\gamma_2+\gamma_1} \right)^k u(E_k), \quad (16)$$

$$E_k = \left(0, t - \frac{x}{a_2} + \left(\frac{1}{a_2} - \frac{1}{a_1} \right) x_0 - 2k \frac{x_0}{a_1} \right). \quad (17)$$

Notably, the situation with constructing composite characteristics (see Figs. 1 and 2) does not cover all possible cases, for example, when the last segment of the composite characteristic emanates from point $H_{2,n}$ or H_m and ends on the horizontal axis. We have also analyzed this case, establishing that it does not change the formulae obtained.

Main results

We are going to prove in this section that the formulae obtained above allow solving problem (1), (2).

Theorem. There is a unique solution $u(x,t)$ of problem (1), (2), represented by two equalities: (15) for all $M_1 \in G_1$ and (16) for any point $M_2 \in G_2$.

Proof. Let us carry out the proof in two stages.

1. Existence of the solution. The function $u(x,t)$, $(x,t) \in G_0 \setminus \overline{G}_3$, represented by formulae (15), (16), satisfying Eq. (1) directly follows from the fact that each term in the corresponding series is a solution of this equation. As for set $\overline{G}_3$, it was proved that $u(x,t) = 0$, $(x,t) \in \overline{G}_3$. The remaining task is then to verify whether the rest of the properties we have described in setting the problem are satisfied.

First, notice that if the point M_1 tends to line $\xi = a_1\tau$, then, as follows from formulae (9), (10),

$$\mu(e_{1,k}) \to 0,\ \mu(e_{2,k}) \to 0,$$

which means that $u(x,t)$, $(x,t) \in G_1$ is continuous.

It follows from the same considerations that the first and second-order partial derivatives of the function $u(x,t)$, $(x,t) \in G_1$ are continuous. By similar reasoning, we can easily prove that the requirement for the function $u(x,t)$, $(x,t) \in G_2$ to be smooth is satisfied. It follows from the above that formulae (15), (16) give functions satisfying Eq. (1) everywhere in domain G_0.

Next, we note that that if point $M_1 = (x,t)$ tends to point $(0,t)$, then

$$E_{1,k} \to \left(0, t - 2k\frac{x_0}{a_1}\right),$$

$$E_{2,k} \to \left(0, t - (2k+2)\frac{x_0}{a_1}\right),$$

$$E_{1,0} \to (0,t).$$

It follows then that $|E_{2,k} - E_{1,k+1}| \to 0$. Therefore, the right-hand side of equality (15) tends to $\mu(t)$, which means that the boundary condition $u(0,t)=\mu(t)$ is satisfied. Thus, we proved that conditions (2) are satisfied for the function $u(x,t)$.

Now we have to verify whether the properties of $u(x,t)$ are satisfied with $x \to x_0$. Evidently, the following relation holds true then:

$$E_k, E_{1,k}, E_{2,k} \to \left(0, t - (2k+1)\frac{x_0}{a_1}\right).$$

Consequently, if $x \to x_0$, formula (15) takes the form

$$\begin{aligned} u(x_0,t) &= u(E_0) + \sum_{k=0}^{\infty}\left(\frac{\gamma_2-\gamma_1}{\gamma_2+\gamma_1}\right)^{k+1} \times \\ &\times\left(u(E_{k+1}) - u(E_k)\right) = \frac{2\gamma_1}{\gamma_2+\gamma_1}u(E_0) + \\ &+\sum_{k=1}^{\infty}\left(\left(\frac{\gamma_2-\gamma_1}{\gamma_2+\gamma_1}\right)^{k} - \left(\frac{\gamma_2-\gamma_1}{\gamma_2+\gamma_1}\right)^{k+1}\right)u(E_k) = \\ &= \frac{2\gamma_1}{\gamma_2+\gamma_1}\sum_{k=0}^{\infty}\left(\frac{\gamma_2-\gamma_1}{\gamma_2+\gamma_1}\right)^{k} u(E_k). \end{aligned} \tag{18}$$

The right-hand side of the obtained equality (18) coincides with the right-hand side of equality (16), which proves that the function $u(x,t)$ is continuous for $x \to x_0$.

Let us now prove that conditions (4), (5) are fulfilled. It follows from equality (15) that

$$\frac{\partial u(M_1)}{\partial t} = \mu'(e_{1,0}) + \sum_{k=0}^{\infty}\left(\frac{\gamma_2-\gamma_1}{\gamma_2+\gamma_1}\right)^{k+1} \times$$

$$\times\left(\mu(e_{1,k+1}) - \mu(e_{2,k})\right).$$

From here we obtain:

$$\begin{aligned} \lim_{x\to x_0-0}\frac{\partial u(M_1)}{\partial t} &= \mu'\left(t - \frac{x_0}{a_1}\right) + \\ &+\sum_{k=1}^{\infty}\left(\frac{\gamma_2-\gamma_1}{\gamma_2+\gamma_1}\right)^{k}\left(\mu'\left(t-(2k+1)\frac{x_0}{a_1}\right) - \right. \\ &\left. -\mu'\left(t-(2k-1)\frac{x_0}{a_1}\right)\right). \end{aligned} \tag{19}$$

Next, it follows from equality (16) that

$$\begin{aligned} \lim_{x\to x_0+0}\frac{\partial u(M_2)}{\partial t} &= \frac{2\gamma_1}{\gamma_2+\gamma_1}\sum_{k=0}^{\infty}\left(\frac{\gamma_2-\gamma_1}{\gamma_2+\gamma_1}\right)^{k}\mu'\times \\ &\times\left(t-(2k+1)\frac{x_0}{a_1}\right). \end{aligned} \tag{20}$$

Following the steps similar to those taken to obtain equality (18) for equality (19), we get:

$$\lim_{x\to x_0+0}\frac{\partial u(M_2)}{\partial t} = \lim_{x\to x_0-0}\frac{\partial u(M_1)}{\partial t};$$

and the resulting equality means that condition (4) is fulfilled.

Practically the same steps are taken to verify

whether condition (5) is fulfilled:

$$\lim_{x\to x_0-0}\frac{\partial u(M_1)}{\partial x}=-\frac{1}{a_1}\frac{2\gamma_2}{\gamma_2+\gamma_1}\times$$

$$\times\sum_{k=0}^{\infty}\left(\frac{\gamma_2-\gamma_1}{\gamma_2+\gamma_1}\right)^k\mu'\left(t-(2k+1)\frac{x_0}{a_1}\right);$$

$$\lim_{x\to x_0+0}\frac{\partial u(M_2)}{\partial x}=-\frac{1}{a_2}\frac{2\gamma_1}{\gamma_2+\gamma_1}\times$$

$$\times\sum_{k=0}^{\infty}\left(\frac{\gamma_2-\gamma_1}{\gamma_2+\gamma_1}\right)^k\mu'\left(t-(2k+1)\frac{x_0}{a_1}\right).$$

It follows from the last two equations that

$$\beta_2\lim_{x\to x_0+0}\frac{\partial u(M_2)}{\partial x}=\beta_1\lim_{x\to x_0-0}\frac{\partial u(M_1)}{\partial x},$$

and this means that condition (5) is satisfied.

Thus, we have proved that the solution exists.

2. *Uniqueness of the solution*. To prove this, we take two solutions of problem (1), (2) and denote their difference as $V(x,t)$.

We consider the functions

$$\nu_1(x,t)=\partial_2 V(x,t)+a(x)\partial_1 V(x,t),$$

$$\nu_2(x,t)=\partial_2 V(x,t)-a(x)\partial_1 V(x,t).$$

It is easy to verify that the following equalities hold true:

$$\partial_2\nu_1(x,t)-a(x)\,\partial_1\nu_1(x,t)=0,$$
$$\partial_2\nu_2(x,t)+a(x)\,\partial_1\nu_2(x,t)=0, \quad (21)$$

$$\nu_i(0,t)=0,\ \nu_i(x,0)=0,$$
$$i=1,2,\ (x,t)\in G_0. \quad (22)$$

Let us agree to denote $\nu_1(x,t)$, $\nu_2(x,t)$, $V(x,t)$ in terms of

$$v_1^-(x,t),\ v_2^-(x,t), V^-(x,t),$$

for $0<x<x_0$, and for $x\ge x_0$

$$v_1^+(x,t), v_2^+(x,t), V^+(x,t).$$

Therefore, we obtain the following equation from Eqs. (21) and (22):

$$v_1^-(x,t)=v_2^-(x,t)=0.$$

From here and from conditions (4), (5) the equalities

$$v_1^+(H)=v_2^+(H)=0$$

follow for an arbitrary point H on the ray (x_0,t), $t>0$.

Then, it follows from these equalities and equalities (21), taking into account conditions

$$v_1^+(x,0)=v_2^+(x,0)=0,$$

that

$$v_1^+(x,t)=v_2^+(x,t)=0.$$

Thus, we obtain the equalities

$$v_1(x,t)=v_2(x,t)=0,$$

$$\partial_1 V(x,t)=0,\ \partial_2 V(x,t)=0,$$

$$V(x,t)=\text{const}.$$

Therefore, by virtue of the condition $V(x,t)=0$, we obtain:

$$V(x,t)=0,\ (x,t)\in\overline{\mathbb{R}_2^{++}},$$

which actually means that the solution of the problem is unique.

The theorem is proved.

Conclusion

We have considered a one-dimensional wave equation describing not only the transverse vibrations of an inhomogeneous semi-bounded string but also longitudinal vibrations of an inhomogeneous rod. We have posed a problem of finding the vibration function for a particular case when the process is caused solely by the behavior of the boundary point.

We have proved the theorem that the solution for this problem exists and is unique, and provided simple and explicit formulae for this solution. A compact form for writing the solution is given for the theorem, using convenient auxiliary notations.

More complete formulas containing only the initial data of the problem have the following form:

$$(x,t)\in G_1,\ u(x,t)=\mu\left(t-\frac{x}{a_1}\right)+$$

$$+\sum_{k=0}^{\infty}\left(\frac{\gamma_2-\gamma_1}{\gamma_2+\gamma_1}\right)^{k+1}\left(\mu\left(t-\frac{x}{a_1}-2(k+1)\frac{x_0}{a_1}\right)-\right.$$

$$\left.-\mu\left(t-\frac{x}{a_1}-(2k+1)\frac{x_0}{a_1}\right)\right),$$

$$(x,t)\in G_2,\ u(x,t)=\frac{2\gamma_1}{\gamma_2+\gamma_1}\sum_{k=0}^{\infty}\left(\frac{\gamma_2-\gamma_1}{\gamma_2+\gamma_1}\right)^k\times$$

$$\times\mu\left(t-\frac{x}{a_2}+\left(\frac{1}{a_2}-\frac{1}{a_1}\right)x_0-2k\frac{x_0}{a_1}\right).$$

Importantly, the last of the given formulae allow to easily construct the corresponding numerical algorithm.

REFERENCES

[1] **G. Petrova, B. Popov,** Linear transport equations with discontinuous coefficients, Communications in Partial Differential Equations. 24 (9–10) (1999) 1849–1873.

[2] **F. Bouchut, F. Jame,** One-dimensional transport equations with discontinuous coefficients, Journal Nonlinear Analysis, Theory, Methods and Applications. 32 (7) (1998) 891–933.

[3] **A.G. Kulikovskiy, E.I. Sveshnikova, A.P. Chugaynova,** Matematicheskiye metody izucheniya razryvnykh resheniy nelineynykh giperbolicheskikh sistem uravneniy [Mathematical methods of studies in discontinuous solutions of systems of nonlinear hyperbolic equations], SEC lecture course, Iss. 16 (2010), MIAN, Moscow.

[4] **E. Tadmor,** Local error estimates for discontinuous solutions of nonlinear hyperbolic equations, SIAM J. Numer. Anal. 28 (4) (1991) 891–906.

[5] **N.N. Kalitkin,** Chislennyye metody [Numerical methods], Nauka, Moscow, 1978.

[6] **I.M. Gel'fand,** Some problems of analysis and differential equations, Uspekhi Mat. Nauk. 14 (2(86)) (1959) 87–158.

[7] **A.F. Filippov,** Differentsialnyye uravneniya s razryvnoy pravoy chastyu [Differential equations with a discontinuous right-hand part], Nauka, Moscow, 1985.

[8] **V.A. Il'in,** A d'Alembert-type formula for longitudinal oscillations of an infinite rod consisting of two segments with different densities and elasticities, Doklady Mathematics. 80 (1) (2009) 613–615.

[9] **V.A. Ilin,** A d'Alembert-type formula for transverse oscillations of an infinite rod consisting of two segments with different densities, Doklady Mathematics. 80 (1) (2009) 624–626.

[10] **D.S. Anikonov, D.S. Konovalova,** Direct and inverse problems for a wave equation with discontinuous coefficients, St. Petersburg State Polytechnical University Journal. Physics and Mathematics. 11 (2) (2018) 61–72.

[11] **A.N. Tikhonov, A.A. Samarskiy,** Uravneniya matematicheskoy fiziki [Mathematical physics equations], Nauka, Moscow, 1977.

[12] **G.S. Salekhov,** A generation of formulas of d'Alembert and Poisson, Uspekhi Mat. Nauk. 2 (4(20)) (1947) 175–182.

[13] **A.G. Sveshnikov, A.N. Bogolyubov, V.V. Kravtsov,** Lektsii po matematicheskoy fizike [Lectures on mathematical physics], MSU, Moscow, 2004.

Received 02.11.2018, accepted .12.11.2018.

THE AUTHORS

ANIKONOV Dmitriy S.
Sobolev Institute of Mathematics
4 Acad. Koptyug Ave., Novosibirsk, 630090, Russian Federation
anik@math.nsc.ru

KONOVALOVA Dina S.
Sobolev Institute of Mathematics
4 Acad. Koptyug Ave., Novosibirsk, 630090, Russian Federation
dsk@math.nsc.ru

СПИСОК ЛИТЕРАТУРЫ

1. **Petrova G., Popov B.** Linear transport equations with discontinuous coefficients // Communications in Partial Differential Equations. 1999. Vol. 24. No. 9–10. Pp. 1849–1873.

2. **Bouchut F., Jame F.** One-dimensional transport equations with discontinuous coefficients // Journal of Nonlinear Analysis. Theory, Methods and Applications. 1998. Vol. 32. No. 7. Pp. 891–933.

3.Куликовский А.Г., Свешникова Е.И., Чугайнова А.П. Математические методы изучения разрывных решений нелинейных гиперболических систем уравнений // Лекционные курсы НОЦ. Вып. 16. М.: Изд. Математического института им. В.А. Стеклова РАН, 2010. 122 с.

4. **Tadmor E.** Local error estimates for discontinuous solutions of nonlinear hyperbolic equations // SIAM J. Numer. Anal. 1991. Vol. 28. No. 4. Pp. 891–906.

5. Калиткин Н.Н. Численные методы. М.: Наука, 512 .1978 с.

6. Гельфанд И.М. Некоторые задачи теоᴛ рии квазилинейных уравнений // Успехи ма-

тематических наук. 1959. Т. XIV. Вып. 2 (86). С. 87– 158.

7. Филиппов А.Ф. Дифференциальные уравнения с разрывной правой частью. М.: Наука, 255 .1985 с.

8. Ильин В.А. Формула типа Даламбера для продольных колебаний бесконечного стержня, состоящего из разной плотности и разной упругости // Доклады Академии наук. 2009. Т. 4 № .427. С. 466–468.

9. Ильин В.А. Формула типа Даламбера для поперечных колебаний бесконечного стержня, состоящего из двух участков разной плотности // Доклады Академии наук. 2009. Т. 5 № .427. С. 609–611.

10. Аниконов Д.С., Коновалова Д.С. Прямая и обратная задачи для волнового уравнения с разрывными коэффициентами // Научно-технические ведомости СПбГПУ. Физико-математические науки. 2018. Т. № .11 2. С. 72–61.

11. Тихонов А.Н., Самарский А.А. Уравнеа ния математической физики. М.: Наука, .1977 735 с.

12. Салехов Г.С. Обобщение формул Дая ламбера и Пуассона // Успехи математических наук. 1947. Т. 2. Вып. 40. С. 182–175.

13. Свешников А.Г., Боголюбов А.Н., КравK цов В.В. Лекции по математической физике. М.: Изд-во МГУ, 416 .2004 с.

Статья поступила в редакцию 02.11.2018, принята к публикации 12.12.2018.

СВЕДЕНИЯ ОБ АВТОРАХ

АНИКОНОВ Дмитрий Сергеевич – *доктор физико-математических наук, заведующий лабораторией условно-корректных задач Института математики им. С.Л. Соболева СО РАН.*
630090, Российская Федерация, г. Новосибирск, ул. Коптюга, 4
anik@math.nsc.ru

КОНОВАЛОВА Дина Сергеевна – *кандидат физико-математических наук, старший научный сотрудник лаборатории условно-корректных задач Института математики им. С.Л. Соболева СО РАН.*
630090, Российская Федерация, г. Новосибирск, ул. Коптюга, 4
dsk@math.nsc.ru

DOI: 10.18721/JPM/12105
УДК 621.039.539.7

ULTRACOLD NEUTRON SUPERSOURCE AT THE WWR-M REACTOR: A BIOLOGICAL SHIELDING DESIGN

M.S. Onegin, V.A. Lyamkin, A.P. Serebrov

NRC «Kurchatov Institute» – PNPI,
Gatchina, Leningrad region, Russian Federation

In the paper, the biological shielding at the output of the ultracold neutron (UCN) supersource for the WWR-M reactor based on superfluid helium has been designed. The configuration of a casemate, i.e., a biological protection around the thermal column splitter, was calculated. The flux density, the spectrum and the angular divergence of the neutron beam at the exit of the intercanal part of the UCN source, as well as the materials' geometry and composition inside the casemate were taken into account. The total thickness of the shielding made from steel, polyethylene and lead varied from 85 to 92 cm. The calculated maximum dose rate for neutrons and gammas on the casemate surface did not exceed 1 mrem p.h. Thus, the casemate design of the UCN supersource ensures the safe operation of the facility. The calculation was carried out by the Monte Carlo method within the SCALE-6.2 complex using the MAVRIC program.

Keywords: WWR-M reactor, ultracold neutron source, biological shielding, nuclear safety

Citation: M.S. Onegin, V.A. Lyamkin, A.P. Serebrov, The ultracold neutron supersource at the WWR-M reactor: a biological shielding design, St. Petersburg Polytechnical State University Journal. Physics and Mathematics. 12 (1) (2019) 55–65. DOI: 10.18721/JPM.12105

РАСЧЕТ БИОЛОГИЧЕСКОЙ ЗАЩИТЫ СУПЕРИСТОЧНИКА УЛЬТРАХОЛОДНЫХ НЕЙТРОНОВ ДЛЯ РЕАКТОРА ВВР-М

М.С. Онегин, В.А. Лямкин, А.П. Серебров

НИЦ «Курчатовский институт» – ПИЯФ,
г. Гатчина Ленинградской области, Российская Федерация

В работе выполнены проектирование и расчет биологической защиты на выходе суперисточника ультрахолодных нейтронов (УХН) на сверхтекучем гелии, предназначенной для исследовательского водо-водяного ядерного реактора (ВВР-М). Рассчитана конфигурация каземата – биологической защиты вокруг расщепителя тепловой колонны. В расчете учитывались плотность потока, спектр и угловая расходимость пучка нейтронов на выходе внутриканальной части источника УХН, а также геометрия, химический состав и свойства материалов, находящихся внутри каземата. Для слоистой конструкции, выполненной из стали, полиэтилена и свинца, толщина защиты варьируется от 85 до 92 см. Максимальная расчетная мощность дозы для нейтронов и гамма-квантов на поверхности каземата не превышает 1 мбэр/час, следовательно, конструкция каземата источника УХН обеспечивает безопасную эксплуатацию источника. Расчет проводился методом Монте-Карло в рамках комплекса SCALE-6.2 по программе MAVRIC.

Ключевые слова: реактор ВВР-М, источник ультрахолодных нейтронов, биологическая защита, ядерная безопасность

Ссылка при цитировании: Онегин М.С., Лямкин В.А., Серебров А.П. Расчет биологической защиты суперисточника ультрахолодных нейтронов для реактора ВВР-М // Научно-технические ведомости СПбГПУ. Физико-математические науки. 2019. Т. 12. № 1. С. 61–72. DOI: 10.18721/JPM.12105

Introduction

A source of ultracold neutrons (UCN) allowing to extract not only UCN but also cold and very cold neutrons has been developed using the facilities of the WWR-M reactor (a research pressurized water reactor) located at the Petersburg Nuclear Physics Institute (part of the Kurchatov Institute National Research Centre). The setup is intended for research in fundamental interactions and condensed matter physics [1]. The WWR-M reactor provides a unique opportunity for maintaining conditions of low heat release with a sufficiently high neutron flux (10^{12} $cm^{-2} \cdot s^{-1}$). This task can be achieved in the so-called thermal column (TC), a channel with a large diameter (1 m) adjacent to the reactor core. The project of the UCN source is described in detail in [2, 3].

The new UCN source is supposed to increase the accuracy with which the electric dipole moment (EDM) of the neutron [4] can be measured by two orders of magnitude and check the predictions of supersymmetric theories that are extensions of the Standard Model. According to these theories, the neutron EDM should be in the range accessible for the planned experiments. As supersymmetric theories also predict baryon asymmetry of the Universe at the observable level, this indicates that the given theoretical approach might be valid.

Beside the setup for measuring the neutron EDM, the WWR-M reactor includes two systems for measuring the neutron lifetime: with a magnetic trap [5] and with a large gravitational trap [6]. Precision measurements of the neutron lifetime are important for checking the model describing the evolution of the Universe in its early stages, as well as for finding deviations from the Standard Model. Another setup has been constructed to search for mirror dark matter (n–n') [7]. All of these installations have been designed and constructed at PNPI and are currently tested on UCN beams at the Institut Laue–Langevin (Grenoble, France). These installations are supposed be transferred to a new UCN source at PNPI. Increasing UCN intensity by more than two orders of magnitude should allow to carry out fundamentally different types of studies. Finally, an experiment on searching for neutron–antineutron oscillations (n–c) [8] in order to verify the baryon number violation (one of Sakharov's Conditions for the origin of the Universe) can be discussed for a high-intensity UCN source.

Thus, aside from the crucial experiment on finding the neutron EDM, the UCN source presents opportunities for a whole series of experiments in physics of fundamental interactions.

The program of condensed matter studies on CN beams is designed for five experimental stations, including four finished systems: the reflectometer [9], the polarimeter [10], the powder diffractometer [11] and the spin echo

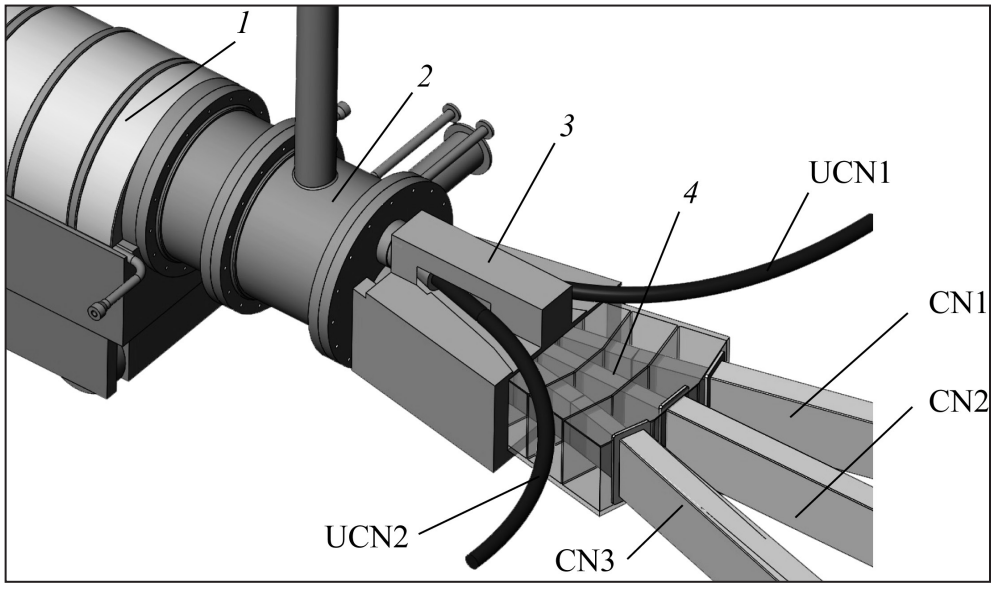

Fig. 1. Model of beam-splitting system at output of in-core thermal column (TC): interchannel section *1* of ultracold (UCN) source, coupling coil *2*, cast-iron collimator *3*, splitter *4*; UCN1, UCN2 are ultracold neutron guides, CN1, CN3 are cold neutron guides; CN2 is a very cold neutron guide

spectrometer [12]. There is an additional option of extracting the auxiliary UCN beam (CN3) for future experiments.

A general schematic of the neutron guides for extracting the UCN, CN and VCN beams is shown in Fig. 1. A vacuum coil with a system of vacuum tubes is directly adjacent to splitter *4*, separating the neutrons transported through the intrachannel section of UCN source (*1*) into three beams (CN1, CN2 and CN3), which direct the CN and VCN beams to the experimental setups. Two UCN neutron guides (UCN1 and UCN2) are located above the spliter. A cast iron collimator *3* intended to protect personnel and the environment from direct neutron beams emanating from the reactor shields the splitter and UCN neutron guides. The central neutron beam is transported by a straight neutron guide that should be designed to include additional biological shielding. The splitter with the collimator should also be surrounded by biological shielding. A general view of the reactor with the adjacent neutron guide system and the intended biological shielding for this system is shown in Fig. 2.

In this study, we have carried out calculations for the so-called casemate for shielding the splitter and the collimator.

Calculation of parameters of TC neutron beam at the edge of the reactor's biological shielding

Calculations of biological shielding of the casemate involve calculating the flux density, spectrum and angular divergence of the neutron beam at the output of the vacuum channel inside the TC.

The neutron spectrum at the output of the TC substantially depends on the operating mode of the UCN source. Fig. 3 shows the spectral brightnesses of the neutron radiation source (brightness depending on the neutron radiation wavelength) for different modes. The neutron radiation spectrum becomes harder in warm mode when there is no liquid deuterium and superfluid helium in the chambers, so the thermal neutron flux is greater than in cold mode by an order of magnitude. Moreover, without deuterium and helium filling the chambers, the flux densities of fast and resonance neutrons at the output of the TC significantly increase. In view of this, the calculations for biological shielding were performed for the warm operating mode of the source when the radiation conditions at the output are the most dangerous.

The mean neutron flux density in the cavity at the edge of the reactor's biological shielding is

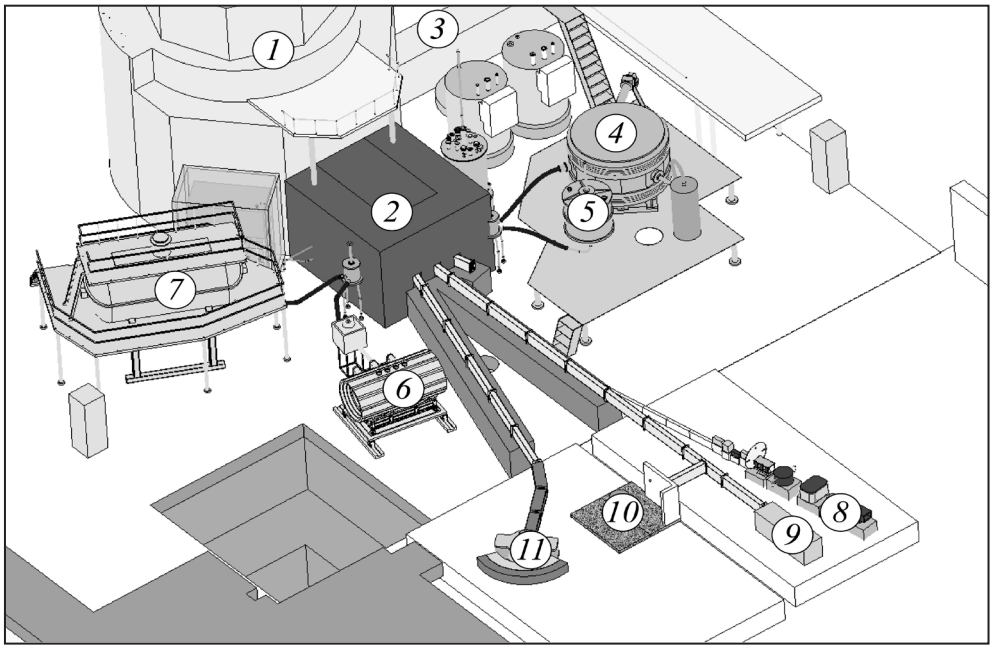

Fig. 2. General view of neutron guide system with shielding:
WWR-M reactor *1*, casemate *2*, cryogenic equipment *3*,
EDM spectrometer *4*,
UCN magnet trap *5*, system *6* for mirror dark matter search,
UCN gravitational trap *7*, reflectometer *8*, polarimeter *9*,
powder diffractometer *10*, spin echo spectrometer *11*

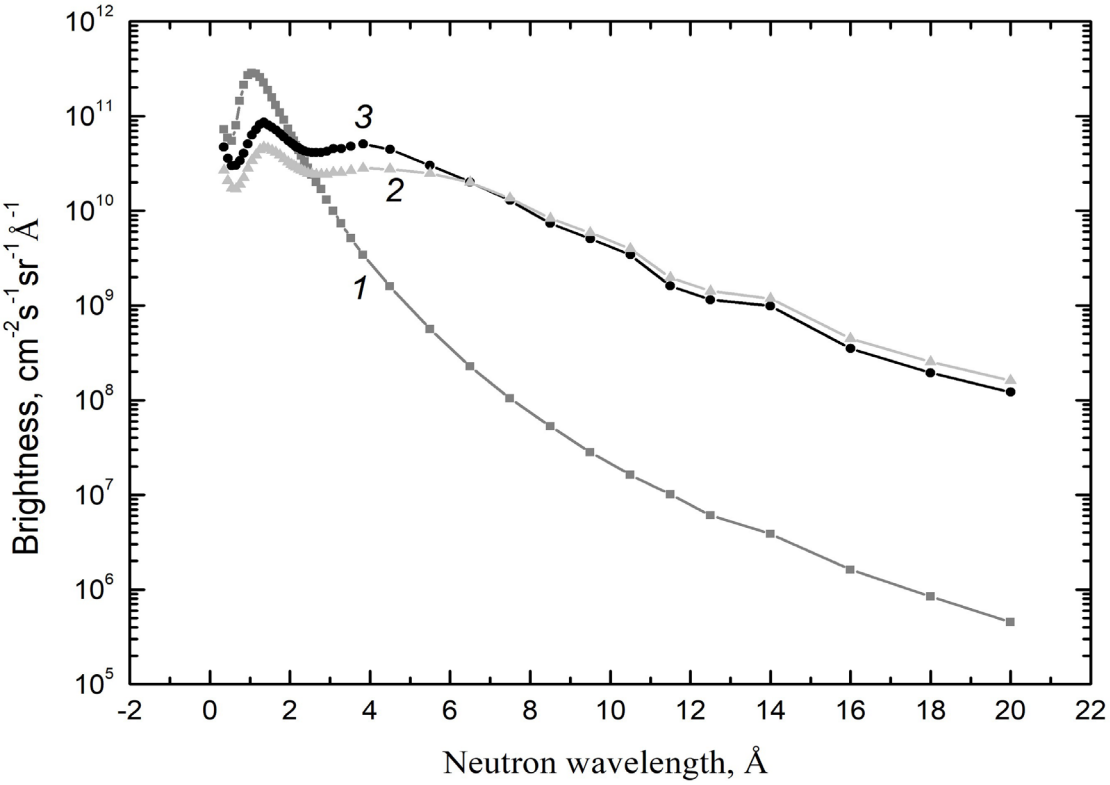

Fig. 3. Spectral brightness of UCN source in different modes of operation: warm *1* (without liquid helium and deuterium), cold *2* (with liquid helium and deiterium), *3* without liquid helium in chamber

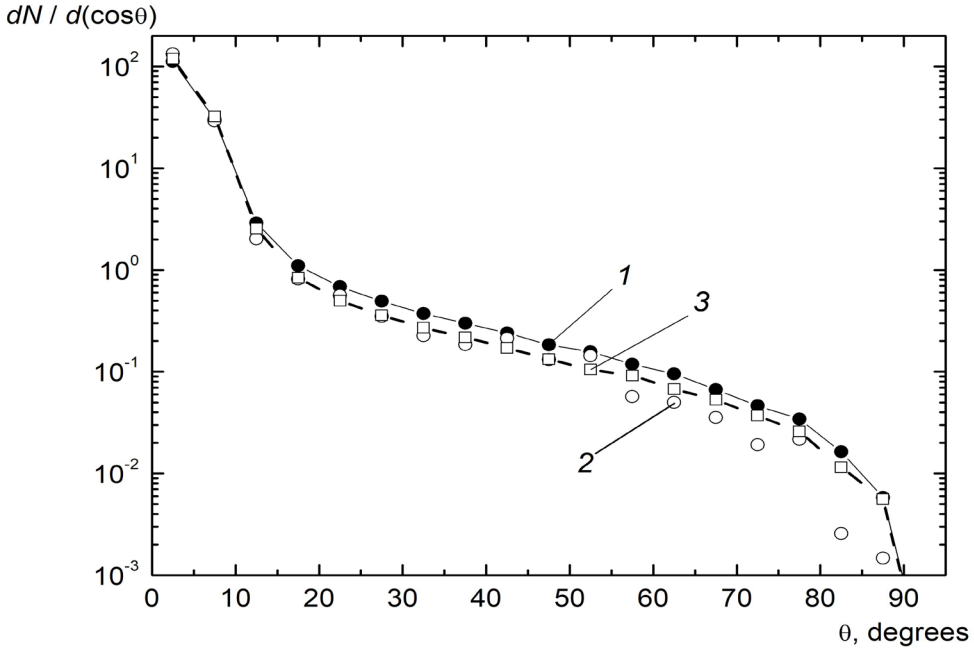

Fig. 4. Calculated angular distribution of neutrons at the edge of biological shielding of TC vacuum channel: for neutrons of all energy groups (*1*); for fast neutrons with energy $E > 0.5$ MeV (*2*); for thermal neutrons with $E < 0.625$ eV (*3*)

$2.15 \cdot 10^{10} cm^{-2} \cdot s^{-1}$. The flux density of fast neutrons (with the energy of more than 0.5 MeV) is $1.3 \cdot 10^{9}$ $cm^{-2} \cdot s^{-1}$. The total intensity of the neutron source is $5.1 \cdot 10^{13}$ s^{-1}. Fig. 4 shows the calculated angular distributions of neutrons (in the range $0° < \theta < 90°$) for different energy groups.

As follows from the calculations, the angular distributions for thermal and fast neutrons coincide with those for neutrons of all energies, up to values of 10°. The main radiation intensity lies within this angle range, so the angular distribution obtained for all energies was used in further calculations of biological shielding, regardless of the neutron energy.

Simulation of neutron splitter geometry

A computer model of the neutron splitter in horizontal cross-section (along the central axis of the WWR-M reactor) is shown in Fig. 5. The vacuum channel inside the TC ends with coupling coil *1*, closed with aluminum flange *2*. The neutron model developed to calculate biological shielding included such elements of the reactor's core as the end section of the TC with an aluminum collimator (not shown in Fig. 5), the coupling coil with the flange and CN beam splitter (*3*) with the system of neutron guides *4* inside. The first stage of the simultion did not take into account the intensity of radiation from neutron guides adjacent to the neutron splitter.

The horizontal cross-section of the neutron splitter has the shape of an isosceles trapezoid. Its height was taken equal to 40 cm and length to 167 cm. The walls of the splitter box are made of aluminum with a thickness of 20 mm. The front face of the splitter is 35 cm wide, the back is 95 cm. Three neutron guides are located inside the splitter. The central one is straight, the other two are bent, respectively, to the right and to left. The neutron guides consist of four links, each 400 mm long. There is vacuum inside the neutron guide. The cross-section of the vacuum channel of each neutron guide has the dimensions of 30 × 200 mm. The vacuum cavity is closed with K8 glass with a Ni^{58} layer, which reflects the cold neutrons, deposited on it. The external cross-section of the neutron guide is 90 × 260 mm. The entire box, with the exception of four steel plates (10 mm thick each) inside the splitter, is filled with polyethylene balls. The first meter of the box is surrounded by a cast-iron collimator (see Fig. 1). Its role is to prevent direct leakage of neutrons from the vacuum cavity of the TC to the front wall of the shield. The collimator reduces the radiation

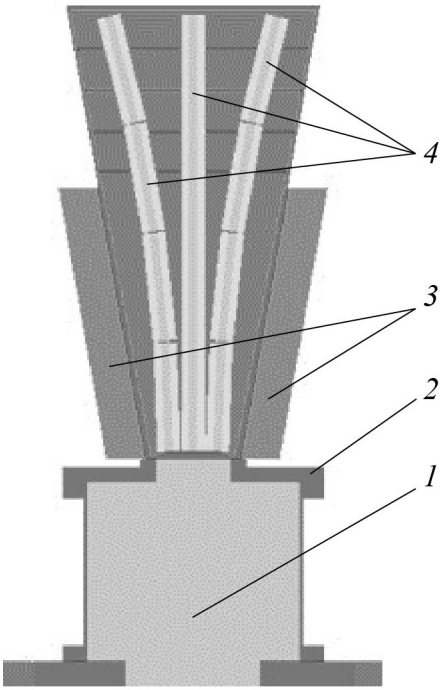

Fig. 5. Computer model of neutron splitter (horizontal cross-section): correcting coil *1*; mating flange *2*; CN beam splitter *3*; CN guide system *4*

load on the front wall of biological shielding by effectively scattering neutrons. Calculations for the biological shielding were carried out using the SCALE-6.2.3 software [13].

Geometry and composition of biological shielding at the output of the TC

The shielding is supposed to be collapsible, consisting of several layers of protective materials first effectively thermalizing and then absorbing the major dose of fast neutrons from the neutron beam incident on the shielding. The steel of the St3sp grade is convenient to use for this purpose, as it contains iron that effectively slows down fast neutrons due to inelastic scattering, transferring them to the energy region lying below the inelastic threshold. This threshold is equal to 0.862 MeV for the ^{56}Fe isotope and to 0.014 MeV for the ^{57}Fe isotope. The inelastic cross-section in the fast region of the neutron spectrum is about 1 barn for these isotopes. Hydrogen is another element that effectively inhibits neutrons due to elastic scattering. The cross-section for elastic scattering of neutrons by hydrogen in the resonance energy region is approximately 20 barn. Two types of

low-density polyethylene (LDPE) containing hydrogen, pure and doped with boron, are used for shielding. However, hydrogen has a fairly large neutron capture cross-section, emitting gamma rays with energies of about 2 MeV. The boron doping (containing the ^{10}B isotope) reduces the generation of captured gammas upon shielding. This property of the ^{10}B isotope is due to its large capture cross-section, so boron-containing materials practically do not emit gamma rays in this type of capture.

Effective shielding can be constructed by alternating layers of steel and polyethylene. The last layer of polyethylene is supposed to contain boron to reduce the generation of gamma radiation. Lead is used as the outer layer to protect against gamma radiation. The first layer of steel in a protective case is to be coated with boron-containing plastic or rubber. The boron carbide in these layers should exceed 50 wt%. Such coating should protect the material from cold and thermal neutrons and reduce its activation upon shielding. The composition of the St3sp steel that we used in the calculations is given in Table 1. It was assumed that LDPE doped with boron contains 3 wt% of boron, while the boron carbide content in plastic was taken to be 50 wt%.

The geometrical scheme of biological shielding of the splitter from the front, sides and top is shown in Fig. 6. The first shielding layer is made of steel coated with borated plastic (rubber), followed by a layer of PVD, then another layer of steel, and another layer of PVD. The outer layer of polyethylene contains boron impurity (3 wt%). The last shielding layer is made of lead. The thicknesses of the layers are given in Table 2. As evident from the data in Table 2, the total thickness of the shielding is 85.5 cm in front of the splitter and 92.5 cm on the sides and on top.

Table 1

Chemical composition of St3sp steel used for biological shielding

Chemical composition, wt%						
C	Si	Mn	Cr	Ni	Cu	Fe
0.3	0.2	0.5	0.3	0.3	0.3	98.1

Note. Steel density is 7.8 g/cm^3

The dose rates for protection against neutrons and gamma rays were calculated separately. Calculation was carried out by the Monte Carlo method within the SCALE-6.2 complex using the MAVRIC program. The Monte Carlo weight method was used to improve the statistics. Solutions for the conjugate function were used as importances for neutrons and gammas.

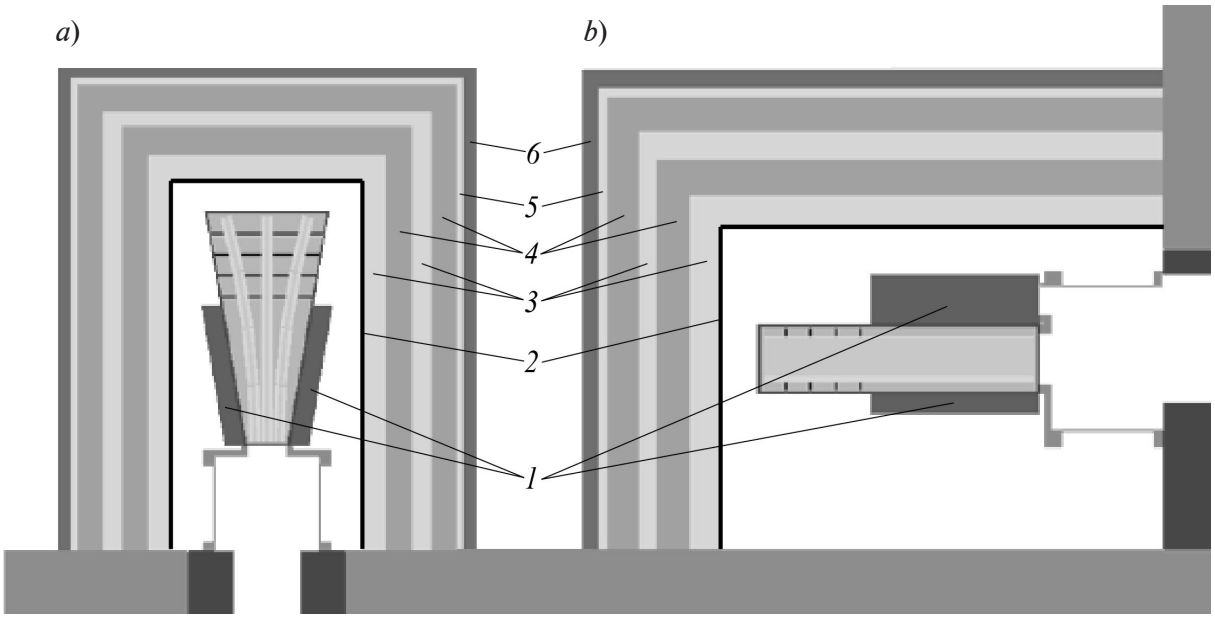

Fig. 6. Horizontal (*a*) and vertical (*b*) cross-sections of neutron splitter (*1*) and its biological shielding including layers of borated rubber (*2*), steel (*3*), low-density polyethylene (LDPE) (*4*) and borated LDPE (*5*). Outer layer is made of lead (*6*)

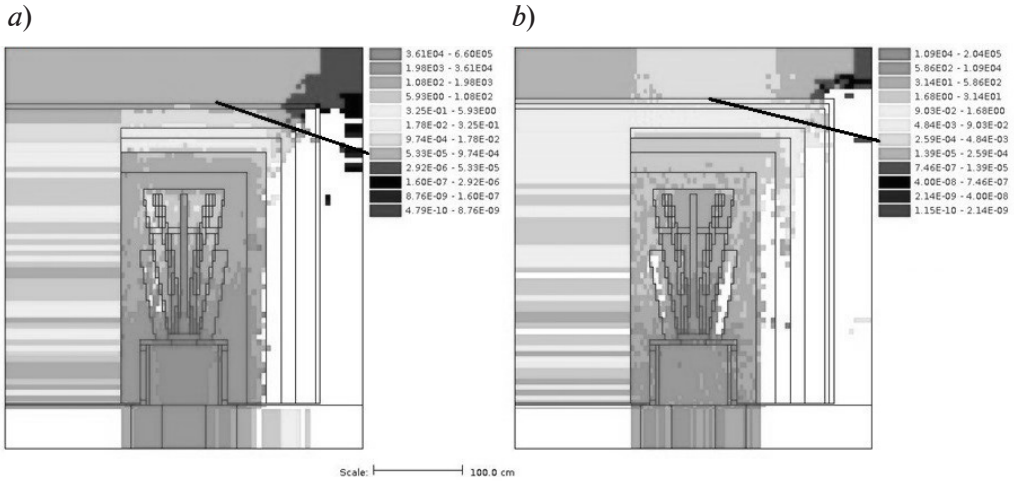

Fig. 7. Estimated dose rate distributions for shielding against neutrons (*a*) and gammas (*b*) for front, rem/h

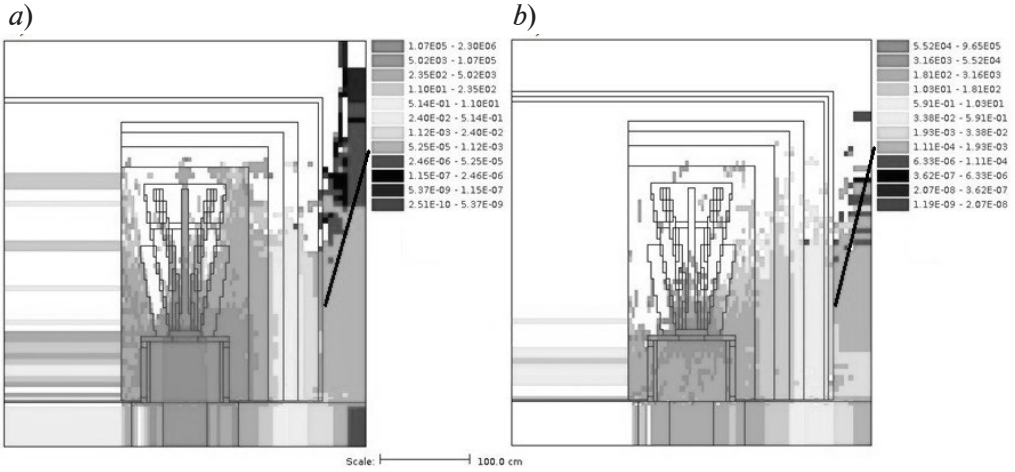

Fig. 8. Same as Fig. 7, for sides

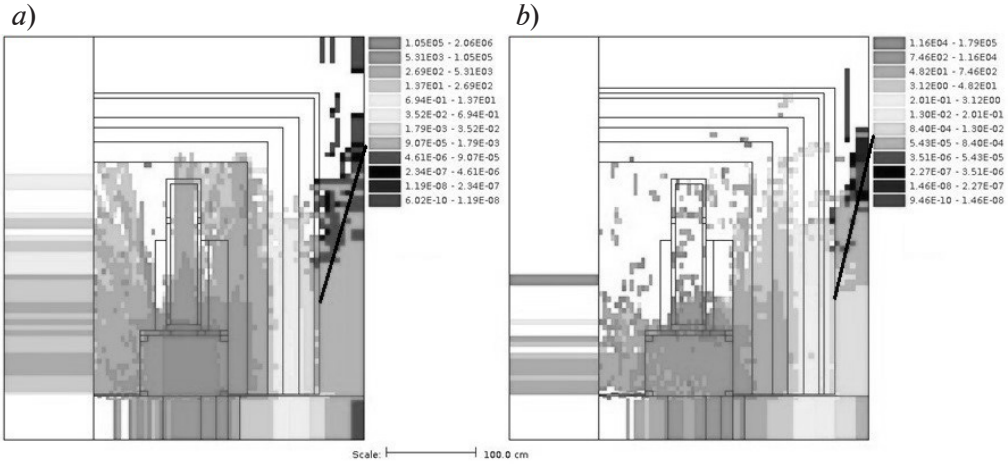

Fig. 9. Same as in Figs. 7 and 8, for top

Table 2

Structure of multilayer coating for biological shielding of neutron splitter

Layer material	Layer thickness, cm		
	Front	Side	Top
Borated plastic (rubber)	0.5	0.5	0.5
St3sp	20	20	20
Low-density polyethylene (LDPE)	20	20	20
St3sp	10	15	15
LDPE	20	20	20
Borated LDPE	5	5	5
Lead (outer layer)	10	12	12
Total shielding thickness, cm	**85.5**	**92.5**	92.5

For this purpose, conjugate functions of the transport equation with the source at the location of point detectors behind the casemate were calculated using the DENOVO software before running the main simulations. Biological shielding was combined in such a way that the total dose rate behind it did not exceed 12 μSv/h (1.2 mrem/h). The calculated dose rate distributions for neutrons and gammas for the front of the shielding are shown in Fig. 7, for the sides in Fig. 8, and for the top in Fig. 9.

Conclusion

This study is dedicated to certain aspects of safe operation of the ultracold neutron source at the WWR-M research reactor. We have designed and calculated biological shielding at the output of the UCN source based on superfluid helium. The interchannel section of the UCN source is supposed to be located in the thermal column of this reactor. Due to the specifics of the UCN source's construction, a large part of the elements required for UCN, CN and VCN beam splitting should be located outside the thermal column of the reactor. For this reason, we have decided to build a protective casemate, that is, multilayer biological shielding around the UCN beam splitter. The shielding should ensure radiation safety in the main chamber of the WWR-M reactor in accordance with the safety requirements for experimental devices of research reactors set out in paragraph 3.5 of NP-033-01 (as amended in 2010).

We have selected the materials and thicknesses of the casemate layers based on the calculations carried out. The first layer of shielding is made of steel coated with borated plastic (rubber), followed by a layer of low-density polyethylene (LDPE), then again a layer of steel and then a layer of the same polyethylene. The outer LDPE layer contains boron impurity (3 wt%). The last layer of shielding is made of lead. The total thickness of shielding in front of the splitter should be equal to 85.5 cm, and to 92.5 cm on the sides and on top.

The maximum calculated dose rate for neutrons and gammas on the surface of the casemate should not exceed 1 mrem/h. With the maximum permissible dose rate for Group A personnel equal to 1.2 mrem/h, the design for the casemate ensures safe operation of the UCN source.

These calculations can be used as a starting point for preparing detailed specifications and documents for the casemate.

The study was carried out at PNPI (the Kurchatov Institute National Research Center) with the financial support of a grant from the Russian Science Foundation (project no. 14-22-00105).

REFERENCES

[1] **A.P. Serebrov, V.A. Mityukhlyaev, A.A. Zakharov,** Project of the ultracold and cold neutron source at the WWR-M reactor with superfluid helium as a moderator, Physics of the Solid State. 52 (5) (2010) 1034–1039.

[2] **A.P. Serebrov, A.K. Fomin, A.G. Kharitonov, et al.,** High-density ultracold neutrons source for the WWR-M reactor for scientific research in fundamental physics, Bulletin of St. Petersburg University, Physics and Chemistry. 2 (1) (2015) 27–41.

[3] **A.P. Serebrov, V.A. Lyamkin, A.K. Fomin, et al.,** High-density ultracold neutrons source for the WWR-M reactor, Nuclear Physics and Engineering. 8 (3) (2017) 235–241.

[4] **A.P. Serebrov, E.A. Kolomenskiy, A.N. Pirozhkov, et al.,** PNPI differential EDM spectrometer and latest results of measurements of the neutron electric dipole moment, Physics of Atomic Nuclei. 78 (14) (2015) 1601–1605.

[5] **V.F. Yezhov, G.B. Krygin, V.L. Ryabov, et al.,** Permanent-magnet trap for ultracold neutron storage, Technical Physics Letters. 27(12) (2001) 1055–1057.

[6] **A.P. Serebrov, A.K. Fomin, A.G. Kharitonov, V.Ye. Varlamov, A.V. Chechkin,** New installation for measuring a neutron lifetime with a big gravitational trap of ultra cold neutrons, Technical Physics. The Russian Journal of Applied Physics. 58 (11) (2013) 1681–1687.

[7] **A.P. Serebrov, O.M. Zherebtsov**, Trap with ultracold neutrons as a detector of dark matter particles with long-range forces, Astronomy Letters. 37 (3) (2011) 181–193.

[8] **A.P. Serebrov, A.K. Fomin, Y.A. Kamyshkov,** Sensitivity of experiment on search for neutron-antineutron oscillations on the projected ultracold neutron source at the WWR-M reactor, Technical Physics Letters. 42 (1) (2016) 99–101.

[9] **N.K. Pleshanov, A.P. Bulkin, V.G. Syromyatnikov,** A new method for improving polarizing neutron coatings, Nuclear Instruments and Methods in Physics. A. Supplement. Proceedings of the International Workshop on Neutron Optics NOP-2010. 634 (1) (2011) S63–S66.

[10] **G.P. Gordeev, V.N. Zabenkin, L.A. Axelrod, et al.,** Investigation of magnetic mesostructure of $(Pd_{0.984}Fe_{0.016})_{0.95}Mn_{0.05}$ alloy by polarized neutrons, Physica B: Condenced Matter, Proceedings of the Sixth International Workshop on Polarised Neutrons in Condensed Matter Investigations (PNCMI 2006). 397 (1–2) (2007) 33–35.

[11] **V.A. Ryzhov, A.V. Lazuta, P.L. Molkanov, et al.,** Comparative study of heterogeneous magnetic state above TC in $La_{0.82}Sr_{0.18}CoO_3$ cobaltite and $La_{0.83}Sr_{0.17}MnO_3$ manganite, Journal of Magnetism and Magnetic Materials. 324 (2012) 3432–3436.

[12] **E.V. Velichko, Y.O. Chetverikov, L.A. Aksel'rod, et al.,** Spin-echo small-angle neutron scattering device: Test experiment using SiO_2 colloidal particles, Journal of Surface Investigation: X-ray, Synchrotron and Neutron Techniques. 7(3) (2013) 401–406.

[13] **B.T. Rearden, M.A. Jessee,** SCALE Code System. Version 6.2.3, Report ORNL/TM-2005/39(2016). https://www.ornl.gov/sites/default/files/SCALE_ 6.2.3. pdf.

Received 13.11.2018, accepted 28.11.2018.

THE AUTHORS

ONEGIN Mikhail S.
NRC «Kurchatov Institute» – PNPI
1, Orlova Roscha microdistrict, Gatchina, 188300, Leningrad Oblast, Russian Federation
onegin_ms@pnpi.nrcki.ru

LYAMKIN Vitaliy A.
NRC «Kurchatov Institute» – PNPI
1, Orlova Roscha microdistrict, Gatchina, 188300, Leningrad Oblast, Russian Federation
lyamkin_va@pnpi.nrcki.ru

SEREBROV Anatolii P.
NRC «Kurchatov Institute» – PNPI
1, Orlova Roscha microdistrict, Gatchina, 188300, Leningrad Oblast, Russian Federation
serebrov_ap@pnpi.nrcki.ru

СПИСОК ЛИТЕРАТУРЫ

1. **Серебров А.П., Митюхляев В.А., Захаров А.А. и др.** Проект источника ультрахолодных и холодных нейтронов на реакторе ВВР-М со сверхтекучим гелием в качестве замедлителя // Физика твердого тела. 2010. Т. 52. Вып. 5. С. 969–973.

2. **Серебров А.П., Фомин А.К., Харитонов А.Г. и др.** Высокоинтенсивный источник ультрахолодных нейтронов на реакторе ВВР-М для научных исследований в области фундаментальной физики // Вестник Санкт-Петербургского университета. Сер. 4. Физика и химия. 2015. Т. 2 (60). № 1. С. 27–41.

3. **Серебров А.П., Лямкин В.А., Фомин А.К. и др.** Суперисточник УХН со сверхтекучим гелием на реакторе ВВР-М // Ядерная физика и инжиниринг. 2017. Т. 8. № 3. С. 235–241.

4. **Серебров А.П., Коломенский Э.А., Пирожков А.Н. и др.** Дифференциальный ЭДМ спектрометр ПИЯФ и последние результаты измерения ЭДМ нейтрона // Ядерная физика и инжиниринг. 2014. Т. 5. № 9–10. С. 795–799.

5. **Ежов В.Ф., Базаров Б.А., Гельтенборт П. и др.** Магнитная ловушка из постоянных магнитов для хранения ультрахолодных нейтронов // Письма в Журнал технической физики. 2001. Т. 27. № 24. С. 64–70.

6. **Серебров А.П., Фомин А.К., Харитонов А.Г., Варламов В.Е., Чечкин А.В.** Новая установка для измерения времени жизни нейтрона с большой гравитационной ловушкой ультрахолодных нейтронов // Журнал технической физики. 2013. Т. 83. № 11. С. 136–141.

7. **Серебров А.П., Жеребцов О.М.** Ловушка с ультрахолодными нейтронами как детектор частиц темной материи с дальнодействующим радиусом сил // Письма в Астрономический журнал. Астрономия и космическая астрофизика. 2011. Т. 37. № 3. С. 204–216.

8. **Серебров А.П., Фомин А.К., Камышков Ю.А.** Чувствительность эксперимента по поиску нейтрон-антинейтронных осцилляций на проектируемом источнике ультрахолодных нейтронов на реакторе ВВР-М // Письма в Журнал технической физики. 2016. № 2. С. 85–90.

9. **Pleshanov N.K., Bulkin A.P., Syromyatnikov V.G.** A new method for improving polarizing neutron coatings // Nuclear Instruments and Methods in Physics. A. 2011. Vol. 634. No. 1. Supplement. Proceedings of the International Workshop on Neutron Optics NOP-2010. Pp. S63–S66.

10. **Gordeev G.P., Zabenkin V.N., Axelrod L.A., et al.** Investigation of magnetic mesostructure of $(Pd_{0.984}Fe_{0.016})_{0.95}$ $Mn_{0.05}$ alloy by polarized neutrons // Physica B. Condenced Matter. 2007. Vol. 397. No. 1–2. Proceedings of the Sixth International Workshop on Polarised Neutrons in Condensed Matter Investigations (PNCMI 2006). Pp. 33–35.

11. **Ryzhov V.A., Lazuta A.V., Molkanov P.L., et al.** Comparative study of heterogeneous magnetic state above TC in $La_{0.82}Sr_{0.18}CoO_3$ cobaltite and $La_{0.83}Sr_{0.17}MnO_3$ manganite // Journal of Magnetism and Magnetic Materials. 2012. Vol. 324. No. 21. Fifth Moscow International Symposium on Magnetism. Pp. 3432–3436.

12. **Величко Е.В., Четвериков Ю.О., Аксельрод Л.А., Забенкин В.Н., Пиядов В.В., Сумбатян А.А., Краан В., Григорьев С.В.** Установка спин-эхо малоуглового рассеяния нейтронов: тестовый эксперимент на коллоидных кристаллах SiO_2 // Поверхность. Рентгеновские, синхротронные и нейтронные исследования. 2013. № 5. С. 3–9.

13. **Rearden B.T., Jessee M.A.** SCALE Code System. Version 6.2.3. Report ORNL/TM-2005/39(2016). https://www.ornl.gov/sites/default/files/SCALE_6.2. 3. pdf.

Статья поступила в редакцию 13.11.2018, принята к публикации 28.11.2018.

СВЕДЕНИЯ ОБ АВТОРАХ

ОНЕГИН Михаил Сергеевич – *кандидат физико-математических наук, старший научный сотрудник* отделения теоретической физики (ОТФ) НИЦ «Курчатовский институт».
188300, Российская Федерация, Ленинградская область, г. Гатчина, мкр. Орлова Роща, д. 1
onegin_ms@pnpi.nrcki.ru

ЛЯМКИН Виталий Александрович – *младший научный сотрудник отделения нейтронной физики (*ОНФ) НИЦ «Курчатовский институт» – *ПИЯФ.*
188300, Российская Федерация, Ленинградская область, г. Гатчина, мкр. Орлова Роща, д. 1
lyamkin_va@pnpi.nrcki.ru

СЕРЕБРОВ Анатолий Павлович – член-корреспондент РАН, *доктор физико-математических наук,* заведующий лабораторией физики нейтрона ОНФ НИЦ «Курчатовский институт» – *ПИЯФ.*
188300, Российская Федерация, Ленинградская область, г. Гатчина, мкр. Орлова Роща, д. 1
serebrov_ap@pnpi.nrcki.ru

DOI: 10.18721/JPM.12106
УДК 536.24

LOW-TEMPERATURE SUB-SYSTEM OF ULTRACOLD NEUTRON SUPERSOURCE AT WWR-M REACTOR: HEAT-HYDRAULIC DESIGN STUDY

A.P. Serebrov, V.A. Lyamkin, A.O. Koptyukhov, M.S. Onegin, D.V. Prudnikov, O.Yu. Samodurov

NRC Kurchatov Institute–PNPI,

Gatchina of Leningrad region, Russian Federation

Heat-hydraulic design studies of the low-temperature sub-system of the ultracold neutron (UCN) supersource at the WWR-M reactor have been presented in the paper. The studies were directed toward selection of the optimal working modes of the aggregate technological complex of this source. According to the calculation data, the Linde TCF-50 standard refrigerator was able to maintain the operating temperature of the thermal screens and the condensation of 50 liters of the deuterium pre-moderator in the chamber. Calculation results for the temperature field of the thermal shield placed in the low-temperature sub-system were used to select the location of the support structures for a superfluid helium vessel. Based on these calculations, an estimate of the total heat penetration at the UCN source chamber was made; it was equal to 35 W. The capacity of the vacuum system for pumping the helium vapor and helium liquefier was established to be sufficient to maintain 35 liters of the superfluid UCN converter.

Keywords: ultracold neutron source, superfluid helium, WWR-M reactor

Citation: A.P. Serebrov, V.A. Lyamkin, A.O. Koptyukhov, M.S. Onegin, D.V. Prudnikov, O.Yu. Samodurov, The low-temperature sub-system of the ultracold neutron supersource at the WWR-M reactor: A heat-hydraulic design study, St. Petersburg State Polytechnical University Journal. Physics and Mathematics, 12(1) (2019) 66-78. DOI: 10.18721/JPM.12106

ТЕПЛОГИДРАВЛИЧЕСКОЙ РАСЧЕТ НИЗКОТЕМПЕРАТУРНОЙ ЧАСТИ ИСТОЧНИКА УЛЬТРАХОЛОДНЫХ НЕЙТРОНОВ ДЛЯ РЕАКТОРА ВВР-М

А.П. Серебров, В.А. Лямкин, А.О. Коптюхов, М.С. Онегин, Д.В. Прудников, О.Ю. Самодуров

НИЦ «Курчатовский институт» – ПИЯФ,

г. Гатчина Ленинградской области, Российская Федерация

Представлены теплогидравлические расчеты низкотемпературной части источника ультрахолодных нейтронов (УХН) на реакторе ВВР-М, направленные на подбор оптимальных режимов работы всего технологического комплекса этого источника. Согласно расчетным данным, штатный рефрижератор Linde TCF-50 способен поддерживать рабочую температуру тепловых экранов и конденсацию 50 л дейтериевого предзамедлителя в камере. Результаты расчетов температурного поля теплового экрана, находящегося в низкотемпературной части источника УХН, были использованы для выбора места установки опорных конструкций для камеры со сверхтекучим гелием. Кроме того, была сделана оценка суммарного теплопритока к камере источника УХН, которая составила 35 Вт. Установлено, что производительность вакуумной системы для откачки паров гелия и гелиевого ожижителя достаточна для поддержания 35 л сверхтекучего конвертора УХН.

Ключевые слова: источник ультрахолодных нейтронов, сверхтекучий гелий, реактор ВВР-М, суммарный теплоприток

Ссылка при цитировании: Серебров А.П., Лямкин В.А., Коптюхов А.О., Онегин М.С., Прудников Д.В., Самодуров О.Ю. Теплогидравлической расчет низкотемпературной части источника ультрахолодных нейтронов для реактора ВВР-М // Научно-технические ведомости СПбГПУ. Физико-математические науки. Т. 12. № 1 62-72. DOI: 10.18721/JPM.12106

Introduction

The history of cold and ultracold neutron sources dates back to the 1970s. Efficient production of low-energy neutrons in a pressurized water reactor (the WWR-M research facility) heavily relies on cryogenic technologies. It was the WWR-M reactor that was used for experiments on transmission of neutrons through low-temperature converters such as cold beryllium [1], liquid hydrogen [2], liquid deuterium [3] and solid deuterium [4], making it possible to obtain UCN flux densities that were rather high for that time. Neutron thermalization in a low-temperature medium allows to increase the fraction of UCNs in the spectrum by tens or even thousands of times.

However, the converter best performs with a moderator temperature of 10^{-3} K, which is unattainable under reactor irradiation. Ultracold neutrons are not formed from thermal ones by additional slowing down but rather as a result of a very rare process, single inelastic collision, which is accompanied by the thermal neutron losing practically all of its energy [5].

Quantitative production of UCNs depends on the intensity of the neutron flux in the reactor and the efficiency of the cryogenic moderator (converter). However, while it is preferable to place the moderator with a cryogenic temperature in a high neutron flux at the reactor, this poses the problem of removing radiative heat; it is the more challenging, the lower the temperature of the moderator.

Bringing up some of the most pressing issues in nuclear research, our study involves highly advanced technologies in its practical implementation, concerning ultra-low temperatures (1.2 K) in a heated reactor. Devices of this type have never been placed inside reactor channels at such low temperatures so far.

The WWR-M reactor provides a unique opportunity for low heat release with a sufficiently high cold neutron flux ($4.8 \cdot 10^{11}$ s^{-1} cm^{-2}). This can be achieved in the so-called thermal column, which is a channel of large diameter (1 m) adjacent to the reactor core [6, 7]. The large diameter of the channel should allow to install a 10 cm thick lead shield to reduce heat release, a liquid deuterium pre-moderator at 20—23 K to produce cold neutrons, and, finally, a 35-L chamber filled with superfluid helium to convert cold neutrons into ultracold ones at 1.2 K.

This configuration should serve to achieve heat input to superfluid helium at a level no higher than 35 W (Fig. 1). A vacuum pumping

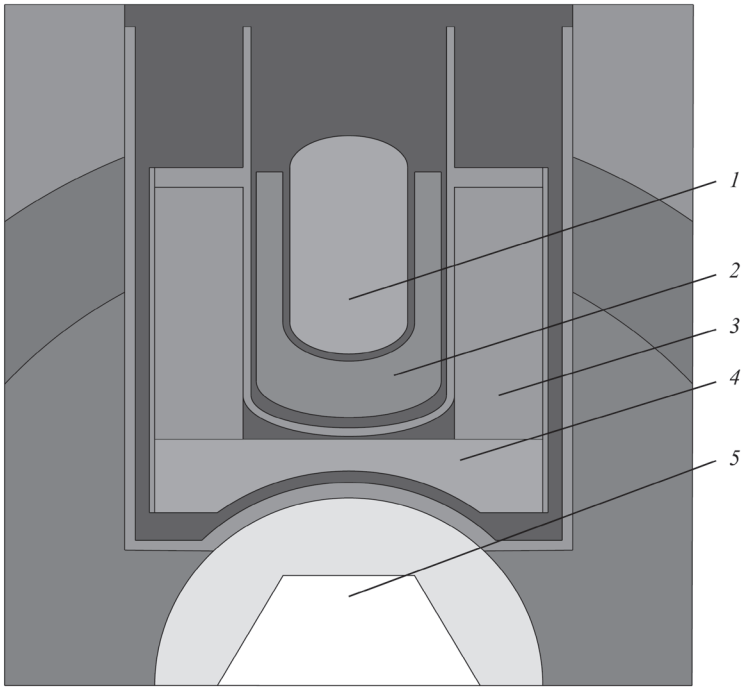

Fig. 1. Location of UCN source in thermal column of WWR-M reactor:
chamber with superfluid helium *1*, chamber with liquid deuterium *2*,
graphite pre-moderator *3*, lead shield *4*,
core *5* of WWR-M reactor
The values of the main parameters of the reactor are given in Table 1 and in the text

system with a capacity sufficient for removing this amount of heat is available at the Petersburg Nuclear Physics Institute (Gatchina, Russia). Combined with the cryogenic facilities from Linde Engineering (Germany), this technological complex can ensure stable operation of the UCN source at the WWR-M reactor. Let us now describe the technical characteristics of the reactor.

Technical characteristics of WWR-M reactor

Power ..... 16 MW
Thermal neutron flux ..... 10^{14} s^{-1} cm^{-2}
Power ..... 16 MW
Cold neutron flux
in superfluid helium ..... $4.8 \cdot 10^{11}$ s^{-1} cm^{-2}
UCN density
in superfluid helium ..... 10^4 cm^{-3}

The specifications for the interchannel section of the UCN source at the WWR-M reactor were developed as part of government contract (no. 1215 of October 20, 2010). However, certain changes were made to the project as design documentation was prepared, since new technical solutions were found, aimed mostly at ensuring safe operation of the UCN source and posing the task to recalculate the low-temperature subsystem. These calculations were carried out based on the design documentation provided.

General description of low-temperature subsystem of UCN source

The component nodes of the low-temperature subsystem (LTS) of the UCN source are made of AMg6 aluminum alloy. The LTS consists of three main parts: deuterium loop, helium loop and thermal shield.

The first loop is a closed system including a working receiver, pipelines and a chamber containing the deuterium pre-moderator. This chamber is enclosed in a shell of helium gas with a temperature of about 20 K. Studies [8] show that the boiling point of equilibrium deuterium is 24.12 K in cold mode with a pressure $P_w = 1.5$ atm in the deuterium loop. At the same time, the most important criterion for the safety of the source is absence of local formations of solid deuterium that can block pipelines and, with increasing heat load on the deuterium chamber, generate pressure sufficient for rupturing the container with the pre-moderator inside the chamber.

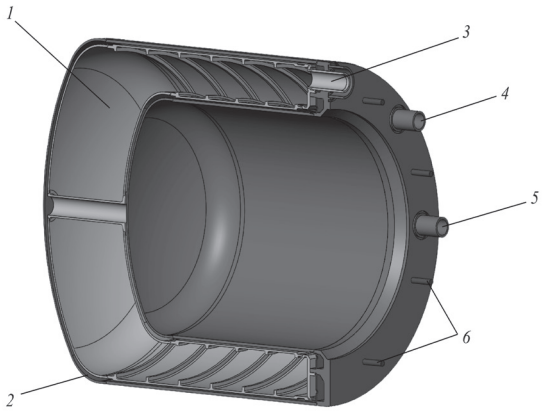

Fig. 2. Deuterium chamber (cross-sectional view): vessel *1* with liquid deuterium; its helium shell *2*; channel *3* supplying and pumping deuterium; channels *4* and *5* supplying and pumping helium, respectively; studs *6* attaching deuterium chamber to thermal shield

Thus, the temperature of deuterium in the deuterium chamber should be carefully maintained in the range of 18.73–24.12 K (18.73 K is the triple point of equilibrium deuterium).

The helium shell serving to condense deuterium simultaneously performs the function of hydrogen safety, preventing a hydrogen–air mixture from forming.

The chamber containing the deuterium pre-moderator (DC) consists of the inner deuterium and outer helium shells (Fig. 2). DC has three nozzles: one welding the deuterium

Table 1

Main physical characteristics of components of interchannel section in UCN source

Parameter	Value			
	Superfluid helium	Liquid deuterium	Graphite pre-moderator	Lead shield
Temperature, K	1.2	20	300	300
Energy release, W	35	287	700	15,000

tube to the helium tube surrounding it and two for two helium tubes cooling the DC. The deuterium tube is located in the upper part of the deuterium chamber so that deuterium can easily evaporate from this chamber when the deuterium loop is switched to "warm" mode. To make sure that the DC is evenly cooled with helium, there is a collector in its rear part, which is an annular gap connected to the rest of the helium cavity of the DC through 16 holes 5 mm in diameter. The collector is installed both in the helium supply area and in the area where helium is pumped from the DC. The deuterium shell of the chamber has an opening in its front part, connecting the helium cavities supplying and removing the cooling helium.

Cooling helium is fed into the deuterium chamber through the nozzle. Then it enters the collector, is evenly distributed in it and moves into the annular gap formed by the inner deuterium and inner helium shells. Next, helium moves to the front of the DC and flows through a hole in the deuterium shell into the gap formed by the outer deuterium and outer helium shells. After that, helium starts moving in the opposite direction and evenly enters the removal collector connected to the outlet nozzle.

A TCF-50 helium refrigerator is used to maintain the temperature of the thermal shield at 20 K and to condense deuterium in the deuterium chamber. Aside from the deuterium loop, the refrigerator should maintain an operating temperature (not more than 20 K) of the thermal shields of the cryostat to produce superfluid helium. For maximum reliability, we chose a

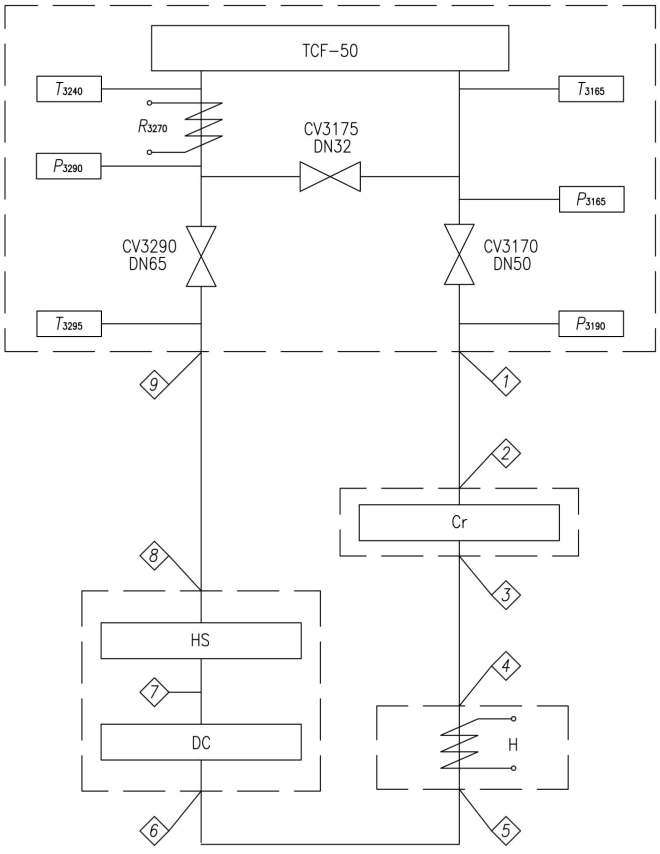

Fig. 3. Circuit diagram of low-temperature cooling loop:
helium refrigerator TCF-50, thermal shield HS, deuterium chamber DC, cryostat Cr, heater H; valves CVkkkk, nominal valve diameter DNkk; *T*kkkk, *P*kkkk denote temperature and pressure, respectively; heater R3270 returns helium; nodal points are numbered in squares

sequential circuit to connect the deuterium loop and the cryostat to the refrigerator (Fig. 3).

Technical characteristics of the TCF-50 refrigerator (obtained experimentally) are given in Table 2.

As a result of two-stage adiabatic expansion, cold helium flow $G = 108$ g/s at temperature $T_{3165} = 10.5$ K and pressure $P_{3165} = 2.5$ atm is generated in the turbo expanders of the refrigerator (see Fig. 3). The pressure P_{3165} is set automatically with the CV-3175 valve. The CV-3170 valve is used to supply helium flow to the LTS. The automated system signals the CV-3290 valve to open when the refrigerator starts operating. The R3270 heater built in the refrigerator serves to return helium at the level $T_{3240} = 21$ K after the experiment. Steady-state operation of the refrigerator is thus established.

After the refrigerator, helium is fed to cool the thermal shields of the cryostat. The system cooling the thermal shield of the cryostat has two parallel-mounted pipelines with a nominal diameter of 14 mm and a length of 6 m each. These shields maintain helium in the lower and drainage tanks of the cryostat at 1.2 K.

After the cryostat, helium enters the heater where it is heated to $T = 20$ K. This temperature is maintained in order to prevent solid deuterium from forming, since this can lead to blockage of the deuterium pipeline and its subsequent rupture.

After the heater, helium enters the UCN source, where it first flows to the deuterium chamber to condense deuterium gas and then to cool the thermal shield of the UCN source.

The geometric characteristics of LTS pipelines are given in Table 3.

Table 2

Specifications of TCF-50 helium refrigerator

Parameter		Value
Helium flow rate, g/s		108
Pressure, atm		
	input	≥ 1.5
	output	2.5
Temperature, K		
	input	≤ 21.0
	output	10.6
Heat load T = 20 K, kW		3

Calculation of heat input to low-temperature subsystem of UCN source

The following requirements are imposed on the low-temperature subsystem (LTS) of the UCN source:

friction factor of all LTS pipelines should be no more than 1 atm;

helium temperature T_{3240} (see Fig. 3) should be no more than 21 K;

deuterium temperature must be above the solidification point but below the condensation point;

heat input to the LTS should be more than 3 kW at temperatures about 20 K.

We used reference book [9] as a source for fundamental equations of hydraulics and heat transfer.

The heat input to low-temperature structures of the UCN source is mainly through three channels: through vacuum insulation, over the thermal bridge, and from reactor radiation.

Heat input through vacuum insulation depends on radiant heat transfer from the "warm" surface of the vacuum jacket to the "cold" surface of the LTS:

$$Q_{rad} = \varepsilon_{ef} C \cdot 10^{-18} (T_1^4 - T_2^4) \cdot S_c$$

where ε_{ef} is the normalized emissivity; C is the blackbody radiation constant ($C = 5.77$ W/(m^2 K); S, m^2, is the area of the outer surface of the "cold" body; T_1, T_2, K, are the temperatures of the "warm" and "cold" surfaces ($T_1 = 300$ K, $T_2 = 20$ K).

The normalized emissivity is calculated by the formula

$$\varepsilon_{red} = \left(\frac{1}{\varepsilon_1} + \frac{1}{\varepsilon_2} - 1 \right)^{-1} = 0{,}028$$

where ε_1, ε_2 are the emissivities of "warm" and "cold" surfaces; in this case, for polished aluminum, $\varepsilon_1 = \varepsilon_2 = 0.055$ [9].

Supporting structures of the low-temperature subsystem, cold helium and deuterium pipelines and the UCN guide act as thermal bridges to the LTS.

To calculate heat input over the thermal bridges, we use the formula

$$Q_{TC} = \frac{\lambda S_b}{L} (T_1 - T_2),$$

where λ, W/(cm K), is the thermal conductivity of the material of the supporting structure ($\lambda = 0.75$ W/(cm K) for the AMg6 aluminum alloy

Table 3

Geometrical characteristics of helium pipelines in LTS

Position in Fig. 3	Pipeline function	Nominal diameter, mm	Length, m
1–2	Supplies helium from refrigerator to cryostat	50	6,000
2–3	Cools thermal shield of cryostat	14	6,000
3–4	Supplies helium from cryostat to heater	50	6,000
4–5	Heats coolant	–	–
5–6	Supplies helium from heater to DC	22	5,000
6–7	Cools deuterium in DC	–	–
7–8	Cools thermal shield of UCN source	22	15,000
8–9	Returns helium from UCN source to refrigerator	50	6,000

Notations: LTS stands for the low-temperature cooling subsystem, UCN stands for ultracold neutrons, DC stands for deuterium chamber.

with T_{av} = 173 K); T_1, T_2, K, are the temperatures of the "warm" and "cold" parts of the bridge (T_1 = 300 K, T_2 = 20 K); S_b, m^2, is the cross-sectional area of the bridge; L, m, is the length of the bridge.

Direct energy release from the reactor in the structural elements of the UCN source is induced by gammas and neutrons. The main source of gamma radiation is the reactor core; gammas are also generated in the process of neutron capture by the nuclei of structural materials. Gamma radiation is generated in the reactor core during nuclear fission; fission fragments also emit gammas.

Neutronics calculations of the WWR-M nuclear reactor with the UCN source were carried out by the Monte Carlo method using the MCNP-4C code [10]. The computational model was optimized in order to obtain the maximum neutron flux density with a wavelength of 9E in superfluid helium. The reactor power was taken to be 16 MW.

The calculated total heat input to the deuterium chamber and the thermal shield are given in Table 4.

The temperature difference of the coolant in the deuterium chamber is found by the formula

$$\Delta T_{DK} = \frac{Q_{\Sigma DC}}{Gc_p} = 1.19 \text{ K}$$

and the temperature difference of the coolant on the thermal shield by the formula

$$\Delta T_{HS} = \frac{Q_{\Sigma HS}}{Gc_p} = 1.74 \text{ K},$$

where G, g/s, is the given mass flow rate of helium (G = 50 g/s); c_p, J·kg^{-1}·K^{-1}, is the specific heat capacity of helium at T_2 = 20 K (c_p = 5.3·10^3 J·kg^{-1}·K^{-1}); $Q_{\Sigma DC}$ and $Q_{\Sigma HS}$, W, are the total heat inputs to the deuterium chamber and the thermal shield, respectively.

Thermohydraulic calculation of low-temperature subsystem of the source

The pressure loss ΔP_{pip} in the pipelines is calculated by the Darcy–Weisbach equation:

$$\Delta P_{pip} = \frac{\lambda_f l w^2 \rho}{2d},$$

where l and d, mm, are the length and the internal diameter of the pipeline; w, m/s, is the

Table 4

Calculated heat input to two LTS nodes

Heat input source	Heat input channel	Heat input, W	
		DC	TS
Through vacuum insulation	Radiant heat transfer	24.00	88.00
Over thermal bridge	Deuterium pipeline	2.45	–
	Tubes for cooling deuterium vapor and thermal shield	–	22.00
	Tubes for pumping helium vapor	–	2.28
	Support trolley with 2 wheels	–	89.23
	2 support beams	–	214.12
	UCN guide	–	26.00
Reactor radiation	To aluminum shell	204.00	20.15
	To liquid deuterium	83.00	–
Total heat input, W		**313.45**	461.78

Notations: DC stands for the deuterium chamber, TS stands for the thermal shield.

flow rate of the gas in the pipeline; λ_f is the friction factor; ρ, kg/m^3, is the density of the gas (helium).

The density ρ is calculated taking into account the absolute pressure and temperature of the gas:

The flow rate of helium in the pipeline is expressed as

$$w = \frac{G}{\rho S},$$

where S, m^2, is the cross-sectional area of the pipeline.

The friction factor λ_f is calculated taking into account its dependence on the Reynolds number.

For the transition range, where

$$20\frac{d}{\Delta} < \mathrm{Re} < 500\frac{d}{\Delta}$$

(Δ, mm, is the absolute roughness of pipes; $\Delta = 0.06$ mm for aluminum), $\lambda_{f\,is}$ calculated by the Altschul formula:

$$\lambda_f = 0.11 \cdot \left(\frac{\Delta}{d} + \frac{68}{\mathrm{Re}}\right)^{0.25}$$

in the range with quadratic law for pressure loss, where $\mathrm{Re} > 500d/\Delta$, $\lambda_{f\,is}$ calculated by the Shifrinson formula:

$$\lambda_f = 0.11 \cdot \left(\frac{\Delta}{d}\right)^{0.25}.$$

The Reynolds number that is the criterion of the flow regime is calculated by the formula

$$\mathrm{Re} = \frac{wd\rho}{\mu}, \qquad (1)$$

where μ, Pa·s, is the dynamic viscosity.

The coefficient μ in Eq. (1) for helium gas can be determined by the Keesom formula [9]:

$$\mu = 5.023\, T^{0.647}.$$

The total pressure loss in the pipelines should also include the pressure loss ΔP_{loc} for local resistance:

$$\Delta P_{loc} = \zeta \frac{\rho w^2}{2}$$

where ζ is the local resistance.

The coefficient ζ for flow deflection at an angle φ is determined by the formula

$$\zeta = \left[0.131 + 0.16 \cdot \left(\frac{d}{R}\right)^{3.5}\right] \cdot \frac{\varphi}{90}.$$

Pressure loss in the cooling loop of the deuterium chamber and the helium heater loop, located in front of the entrance to the deuterium chamber and maintaining a precise temperature for supplying helium for deuterium condensation in the range of 20–24 K, was calculated in COMSOL Multiphysics 5.2a. The calculation results are shown in Fig. 4.

Hydraulic calculations of the low-temperature subsystem of the UCN source at the WWR-M reactor are given in Table

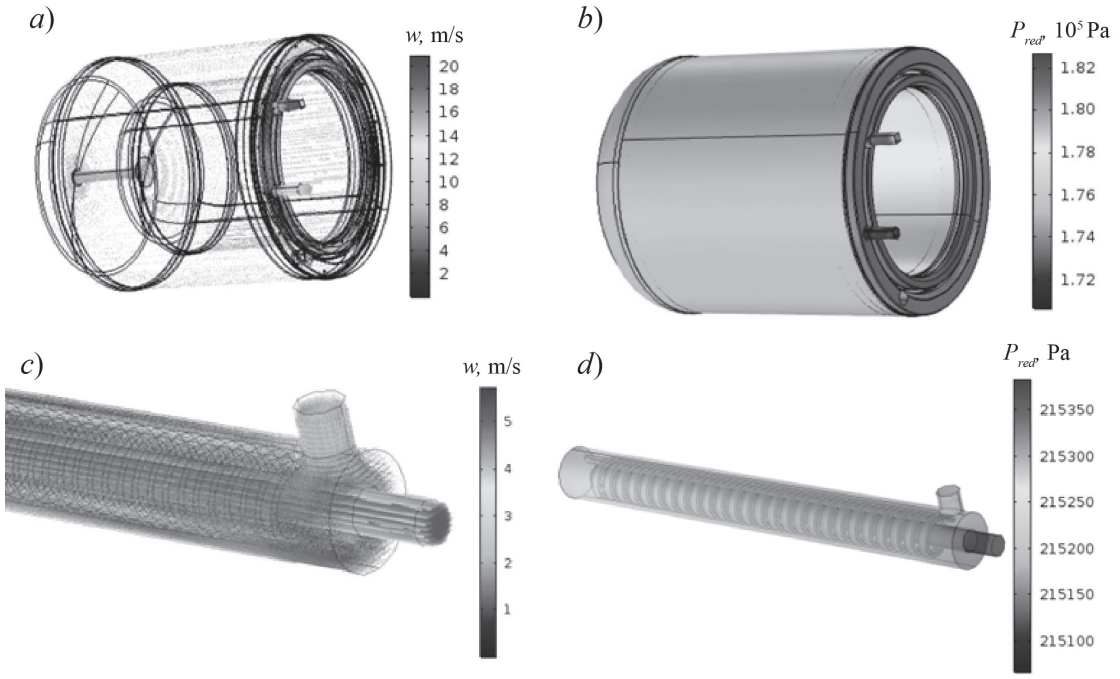

Fig. 4. Calculated velocity fields of coolants (*a*, *c*) and absolute pressure of coolants (*b*, *d*) for cooling loops of deuterium chamber (*a*, *b*) and helium heater (*s*, *d*)

Table 5

Calculated friction factors for low-temperature loop of UCN source

Pipeline function (numbers in Fig. 3)	Helium flow rate in pipeline, m/s	Friction pressure loss, Pa
Returns helium to refrigerator (8–9)	7.92	302
Thermal cooling of LTS shield (7–8)	29.86	37798
Cools deuterium chamber (6–7)	4.54	17288
Supplies helium from heater to deuterium chamber (5–6)	25.21	9676
Heats helium (4–5)	2.47	183
Supplies helium from cryostat to heater (3–4)	2.80	107
Thermal cooling of cryostat shield (2–3)	16.30	11248
Supplies helium from refrigerator to cryostat (1–2)	2.43	94
Total pressure loss, Pa		**76696**

Note. Calculated results are given for the mass flow rate of helium $G = 50$ g/s

5. The pipelines are numbered in accordance with the scheme shown in Fig. 3. The value of the total pressure loss in the LTS loop ΔP_T = 76.7 kPa turned out to be lower than that given in the product specifications for the TCF-50 refrigerator (100 kPa). Thus, the hydraulic calculation has proved that the LTS loop is capable of operating with a mass flow rate of helium G = 50 g/s.

Thermal calculations for the chamber with the liquid deuterium pre-moderator with helium flow rate in the shell G = 50 g/s give the average temperature of the chamber wall equal to 22.83 K (Fig. 5).

Fig. 6 shows the calculated dependence of the maximum deuterium temperature on the mass flow rate of helium. With a helium flow rate G = 50 g/s, the maximum deuterium temperature is 23 K. Since the boiling point of equilibrium deuterium is T = 24.12 K at a pressure of 1.5 atm in the deuterium loop, we can conclude from this calculation that this LTS subsystem can ensure transition of all deuterium in the chamber into the liquid phase.

The thermal field was also calculated for the entire surface of the thermal shield (Fig. 7).

Based on this calculation, we found the points for installing a helium module with superfluid helium in the areas with minimal surface temperature of the thermal shield. The temperature of superfluid helium in the source chamber depends on the magnitude of heat input to the helium chamber, which in turn strongly affects the neutron lifetime. Thus, heat input to superfluid helium directly affects the quality of the UCN source at the WWR-M reactor.

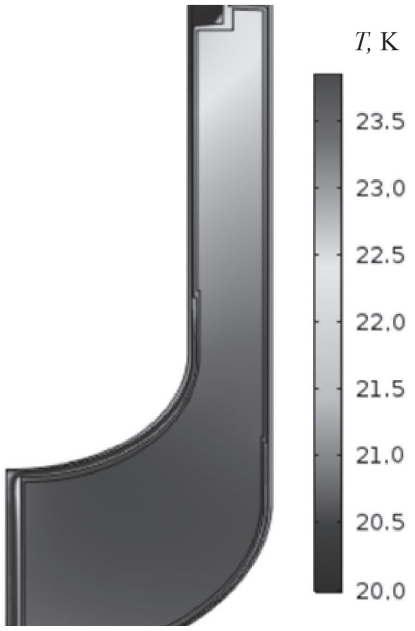

Fig. 5. Calculated temperature distribution of deuterium in deuterium chamber

Our calculations helped establish that the heat input from reactor radiation can be significantly reduced by moving the UCN source away from the core by 25 cm. In particular, the magnitude of heat input to the chamber with superfluid helium was 35.89 W for the UCN source directly adjacent to the reactor core and 22.34 W for the source moved away from the core by 25 cm (Table 6).

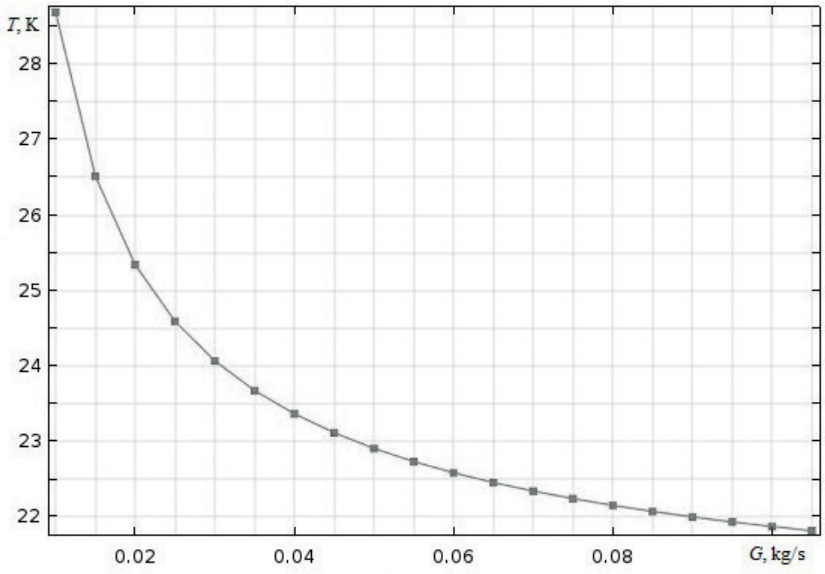

Fig. 6. Calculated dependence of maximum deuterium temperature as function of mass flow rate of helium

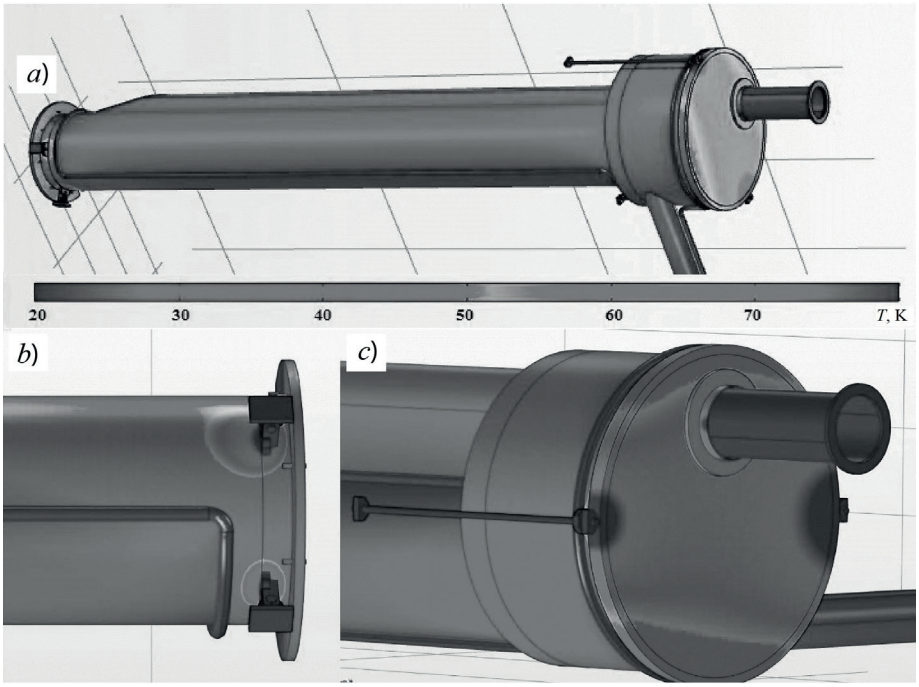

Fig. 7. Calculated temperature distributions over thermal shield of UCN source (*a*) and its fragments: near support trolley (*b*), near support beams and UCN guide (*c*)

Table 6

Heat input to helium chamber depending on its position relative to nuclear reactor

Heat input source	Heat input channel	Heat input, W	
		Initial position	Shift by 25 cm
Through vacuum insulation	Radiant heat transfer	10^{-3}	
Over thermal bridge	Helium chamber supports	0.71	
Reactor radiation	To aluminum shell	17.18	10.28
	To liquid helium	18.00	11.35
Total heat input, W		**35.89**	**22.34**

Conclusion

The paper describes the thermohydraulic calculations of the low-temperature subsystem (LTS) of the ultracold neutron source at the WWR-M reactor. The calculations were based on the design specifications developed earlier. We have obtained the following results.

We have established that the power of 35 W is released in superfluid helium (converting neutrons to UCN) due to the total heat input to LTS, with a reactor power of 16 MW; the thermal load on the low-temperature loop of the LTS is 775 W. The LTS is cooled by the flow of cold helium at a rate $G = 50$ g/s.

The system of LTS pipelines is designed to provide the throughput rate necessary for the given flow of liquid and gaseous helium. We have found that the TCF-50 helium refrigerator is capable of ensuring optimal operation of the UCN source at the WWR-M reactor. According to the calculations that we have carried out, the maximum deuterium temperature in the UCN source is 23 K. With a working pressure $P_w = 1.5$ atm, the deuterium pre-moderator is guaranteed to make a transition to the liquid phase at this temperature.

The calculations performed make it possible to start the construction of the low-temperature subsystem of the UCN source at the WWR-M reactor.

The study was carried out at PNPI (the Kurchatov Institute National Research Center) with the financial support of a grant from the Russian Science Foundation (project no. 14-22-00105).

REFERENCES

[1] **I.S. Altarev, A.I. Egorov, V.F. Ezhov, et al.,** An investigation of the effect of the converter cooling upon the yield of ultracold neutrons and development of a cooled source of ultracold neutrons, Preprint PNPI-246, Gatchina (1976).

[2] **I.S. Altarev, Yu.V. Borisov, A.B. Brandlin, et al.,** A liquid hydrogen source of ultracold neutrons, Physics Letters. A. 80 (5, 6) (1980) 413–416.

[3] **I.S. Altarev, N.V. Borovikova, A.P. Bulkin, et al.,** Universal liquid-hydrogen source of polarized cold and ultracold neutrons at the WWR-M reactor of the Leningrad Institute of Nuclear Physics, JETP Letters. 44 (6) (1986) 344–348.

[4] **A.P. Serebrov, V.A. Mityukhlyaev, A.A. Zakharov, et al.,** Experimental study of solid-deuterium source of ultracold neutrons, JETP Letters. 62 (10) (1995) 785–790.

[5] **A.I. Ahizeer, I.Ya. Pomeranchuk,** On elastic scattering of neutrons with energy of a few Kelvins in liquid helium II, J. Phys. USSR. 9 (1945) 461.

[6] **A.P. Serebrov, A.K. Fomin, A.G. Kharitonov, et al.,** High-density ultracold neutrons source for the WWR-M reactor for scientific research in fundamental physics, Bulletin of St. Petersburg University. Physics and Chemistry. 2 (60) (1) (2015) 27–41.

[7] **A.P. Serebrov**, Supersource of ultracold neutrons at the WWR-M reactor and the program of fundamental research in physics, Crystallography Reports. 56 (7) (2011) 1230–1237.

[8] **S.D. Bondarenko**, Properties of hydrogen isotopes and their compounds on line of vapor-liquid equilibrium. Preprint-PNPI-2471 (2002).

[9] **M.P. Malkov, I.B. Danilov, A.G. Zeldovich, et al.,** Spravochnik po fiziko-tekhnicheskim osnovam kriogeniki [Reference book on physical-technical fundamentals of cryogenics], Energoatomizdat, Moscow (1985).

10. **J.F. Briesmeister,** MCNP™ – A general Monte Carlo *N*-particle transport code. Version 4C, Los Alamos National Laboratory, Los Alamos, New Mexico. (2000) https://permalink.lanl.gov/object/tr?what=info:lanl-repo/lareport/LA-13709-M.

Received 14.11.2018, accepted 28.11.2018.

THE AUTHORS

SEREBROV Anatolii P.
NRC «Kurchatov *Institute*» – *PNPI*
1, Orlova Roscha, Gatchina, 188300, Leningrad Oblast, Russian Federation
serebrov_ap@pnpi.nrcki.ru

LYAMKIN Vitaliy A.
NRC «Kurchatov *Institute*» – *PNPI*
1, Orlova Roscha, Gatchina, 188300, Leningrad Oblast, Russian Federation
lyamkin_va@pnpi.nrcki.ru

KOPTYUHOV Artem O.
NRC «Kurchatov *Institute*» – *PNPI*
1, Orlova Roscha, Gatchina, 188300, Leningrad Oblast, Russian Federation
t44h@yandex.ru

ONEGIN Mikhail S.
NRC «Kurchatov *Institute*» – *PNPI*
1, Orlova Roscha, Gatchina, 188300, Leningrad Oblast, Russian Federation
onegin_ms@pnpi.nrcki.ru
PRUDNIKOV Dmitriy V.
NRC «Kurchatov *Institute*» – *PNPI*
1, Orlova Roscha, Gatchina, 188300, Leningrad Oblast, Russian Federation
dpvbox@mail.ru

SAMODUROV Oleg Yu.
NRC «Kurchatov *Institute*» – *PNPI*
1, Orlova Roscha, Gatchina, 188300, Leningrad Oblast, Russian Federation
samodurov.o@yandex.ru

СПИСОК ЛИТЕРАТУРЫ

1. **Altarev I.S., Egorov A.I., Ezhov V.F., et al.** An investigation of the effect of the converter cooling upon the yield of ultracold neutrons and development of a cooled source of ultracold neutrons. Preprint PNPI-246. Gatchina: PNPI, 1976. 17 p.

2. **Altarev I.S., Borisov Yu.V., Brandlin A.B., et al.** A liquid hydrogen source of ultra-cold neutrons // Physics Letters. A. 1980. Vol. 80. No. 5–6. Pp. 413–416.

3. Алтарев И.С., Боровикова Н.В., Булкин А.П. и др. Универсальный жидководородный источник поляризованных холодных и ультрахолодных нейтронов на реакторе ВВР-М ЛИЯФ // Письма в ЖЭТФ. 1986. Т. 44. Вып. 6. С. 269–272.

4. Серебров А.П., Митюхляев В.А., Захаров А.А., Харитонов А.Г., Несвижевский В.В., Ласаков М.С., Тальдаев **Р.Р.,** Алдущенков А.В., Варламов В.Е., Васильев А.В., Грин Г., Боулс Т. Исследование твердодейтериевого источника ультрахолодных нейтронов // Письма в ЖЭТФ. 1995. Т. 62. Вып. 10. С. 764–769.

5. Ахиезер А.И., Померанчук И.Я. О рассеянии нейтронов с энергией несколько градусов в жидком гелии II // ЖЭТФ. 1946. Т. 16. С. 391.

6. *Серебров А.П., Фомин А.К., Харитонов А.Г., Лямкин В.А., Прудников Д.В., Иванов С.А., Ерыкалов А.Н., Онегин М.С., Митюхляев В.А., Захаров А.А., Гриднев К.А.* Высокоинтенн сивный источник ультрахолодных нейтронов на реакторе ВВР-М для научных исследоваp ний в области фундаментальной физики // Вестник СПбГУ. Физика и химия. 2015. Т. 2 (60). Вып. 1. С. 27–41.

7. **Serebrov A.P.** Supersource of ultracold neutrons at the WWR-M reactor and the program of fundamental research in physics // Crystallography Reports. 2011. Vol. 56. No. 7. Pp. 1230–1237.

8. Бондаренко С.Д. Физические свойства изотопов водорода и их соединений на линии

равновесия жидкость – пар. Препринт ПИЯФ. № 2471. Гатчина: Изд. ПИЯФ, 2002. 39 с.

9. Малков М.П., Данилов И.Б., Зельдович А.Г., Фрадков А.Б. Справочник по физико-техническим основам криогеники. М.: Энергоатомиздат, 1985. 432 с.

10. **Briesmeister J.F.** MCNP™ – A general Monte Carlo *N*-particle transport code. Version 4C // Los Alamos National Laboratory. Los Alamos. New Mexico. 2000. https://permalink.lanl.gov/object/tr?what=info:lanl-repo/lareport/LA-13709-M.

Статья поступила в редакцию 14.11.2018, принята к публикации 28.11.2018.

СВЕДЕНИЯ ОБ АВТОРАХ

СЕРЕБРОВ Анатолий Павлович – член-корреспондент РАН, *доктор физико-математических наук,* заведующий лабораторией физики нейтрона *отделения нейтронной физики (*ОНФ) НИЦ «Курчатовский институт» – *ПИЯФ.*
188300, Российская Федерация, Ленинградская область, г. Гатчина, мкр. Орлова Роща, д.1
serebrov_ap@pnpi.nrcki.ru

ЛЯМКИН Виталий Александрович – *младший научный сотрудник* ОНФ НИЦ «Курчатовский институт» – *ПИЯФ.*
188300, Российская Федерация, Ленинградская область, г. Гатчина, мкр. Орлова Роща, д.1
lyamkin_va@pnpi.nrcki.ru

КОПТЮХОВ Артем Олегович – *стажер-исследователь* ОНФ НИЦ «Курчатовский институт» – *ПИЯФ.*
188300, Российская Федерация, Ленинградская область, г. Гатчина, мкр. Орлова Роща, д.1
t44h@yandex.ru

ОНЕГИН Михаил Сергеевич – *кандидат физико-математических наук, старший научный сотрудник* отделения теоретической физики *(ОТФ)* НИЦ «Курчатовский институт» – *ПИЯФ.*
188300, Российская Федерация, Ленинградская область, г. Гатчина, мкр. Орлова Роща, д.1
onegin_ms@pnpi.nrcki.ru

ПРУДНИКОВ Дмитрий Владимирович – *инженер-технолог* ОНФ НИЦ «Курчатовский институт» – *ПИЯФ.*
188300, Российская Федерация, Ленинградская область, г. Гатчина, мкр. Орлова Роща, д.1
dpvbox@mail.ru

САМОДУРОВ Олег Юрьевич – *инженер-технолог* ОНФ НИЦ «Курчатовский институт» – *ПИЯФК.*
188300, Российская Федерация, Ленинградская область, г. Гатчина, мкр. Орлова Роща, д.1
samodurov.o@yandex.ru

DOI: 10.18721/JPM.12107
УДК 621.391:681.142

HUMAN VISUAL MODEL-BASED TECHNOLOGY: MEASURING THE GEOMETRIC PARAMETERS OF MICROINSTRUMENT

V.N. Savin, V.A. Stepanov, M.V. Shadrin

Ryazan State University named for S.A. Esenin, Ryazan, Russian Federation

In the paper, a scheme of an optical microscope which includes a special bitelecentric optical system for the formation of a diode support and a telecentric objective for capturing the image has been designed and implemented. The use of such system makes it possible to reduce the diffraction effects at the edges of the shadow structure and to measure (using the microscope) the main parameters of a cutting microinstrument: its protrusion and diameter. An algorithm for modeling the two main visual channels of the human eye was developed. It allowed rapid detection of spatial-temporal processes and noise, and provided measuring the cutting edge contour of the instrument with a subpixel error (up to 0.01 pixel) and determining the dimensions of the cutting tool with an error of 0.5 μm.

Keywords: telecentric objective, human visual model, microinstrument, subpixel accuracy

Citation: V.N. Savin, V.A. Stepanov, M.V. Shadrin, Human visual model-based technology: measuring the geometric parameters of microinstrument, St. Petersburg Polytechnical State University Journal. Physics and Mathematics. 12 (1) (2019) 87–95. DOI: 10.18721/JPM.12107

ТЕХНОЛОГИЯ ИЗМЕРЕНИЯ ГЕОМЕТРИЧЕСКИХ ПАРАМЕТРОВ МИКРОИНСТРУМЕНТА НА ОСНОВЕ МОДЕЛИ ЗРЕНИЯ ЧЕЛОВЕКА

В.Н. Савин, В.А. Степанов, М.В. Шадрин

Рязанский государственный университет имени С.А. Есенина

г. Рязань, Российская Федерация

Разработана и реализована схема оптического микроскопа, включающего специальную бителецентрическую оптическую систему для формирования диодной подставки и телецентрического объектива для захвата изображения. Применение указанной системы позволяет снизить влияние дифракционных эффектов на краях теневой картины и измерять с помощью оптического микроскопа основные параметры режущего микроинструмента – его вылет и диаметр. Разработан алгоритм, моделирующий два основных зрительных канала глаза человека и детектирующий быстрые пространственно-временные процессы и шумы. Алгоритм обеспечивает измерение контура режущей кромки инструмента с субпиксельной точностью (до 0,01 пикселя) и позволяет определять физические размеры режущего инструмента с погрешностью 0,5 мкм.

Ключевые слова: телецентрический объектив, модель зрения человека, микроинструмент, субпиксельная точность

Ссылка при цитировании: Савин В.Н., Степанов В.А., Шадрин М.В. Технология измерения геометрических параметров микроинструмента на основе модели зрения человека // Научно-технические ведомости СПбГПУ. Физико-математические науки. 2019. Т. 12. № 1. С.79–86. DOI: 10.18721/JPM.12107

Introduction

Machines and machining centers with CNC (computer numerical control) are the staple of modern metal fabrication (mechanical processing). Such machines can manufacture high-quality products with a given precision. The quality of production depends on a number of factors; some of them are dealt with at the stage of product design. A control program is created, material and tools are selected. However, real tools do not always exactly correspond to the objects designed in the program. While modern systems allow to adjust the operation of the machine to the actual size of the tool, this means that the exact parameters of this tool have to be known.

There are many ways (both optical and mechanical) to estimate and measure the parameters of cutting edges of tools [1]. Presetters based on optical micrometers are the most modern. These devices allow to obtain the necessary data on the geometrical parameters of the cutting tool quickly and in high quality. The accuracy limit is 5 μm for every 100 mm for such devices. There are as yet no modern tools for quick measurements on this scale.

This study is aimed at creating a device with the accompanying software and hardware technology that would make it possible to quickly and accurately measure such parameters of end-cutting and boring microtools as the overhang and diameter of the cutter, drill, tap, etc., before installing them into machine spindles with an accuracy no worse than 1 μm.

The technology is intended for rapid precise non-contact measurement and adjustment of cutting microtools outside the machine in a manufacturing environment.

We have designed and fabricated a device for presetting tools outside the machine (presetter). It is a hardware and software system with an optical micrometer and linear encoders. Special software allows to receive signals from micrometric linear encoders and optical micrometers and calculates the parameters of the tool. The results of the program are displayed on the screen. Interaction with the operator is through the software user interface.

Selection of parameters and development of optical scheme

A distinctive feature of the technology developed is that it is modeled on the human retina and uses bitelecentric optics to form diode backlighting and a telecentric lens to capture images. These tools allow to reduce the effect of diffraction on the edges of the shadow pattern.

Development of the optical scheme is one of the most important stages. The consumer properties of the entire device directly depend on the quality of the scheme. An accurately calculated and constructed high-quality optical system is absolutely necessary no matter how perfect the electronic circuit is. Otherwise, the distorted data received from it after mathematical processing may introduce significant errors in measurement accuracy. This means that special approaches must be taken to developing this system, from the standpoints of both science and design.

To construct optical circuits for an instrumentation system, it is first of all necessary to analyze and use the data on the required range and accuracy of measurements, on methods for calculating and tuning the optical node, on techniques for increasing its resolution and minimizing all kinds of aberrations.

The presetter is based on an optical micrometer (Fig. 1) with a bitelecentric lens and a beam path providing a clear, diffraction-free shadow of the edge of the microtool on an enlarged scale. This shadow is analyzed using an algorithm that finds extreme projection points and uses mathematical interpolation (see the next section) to calculate the coordinates of the points and the values of the radius and height of the microtool (the object of measurement).

The alignment of the lens and the radiation source should be coordinated with high accuracy in the optical scheme of the microscope. The diameter of the bitelecentric lens and the backlight is 16 mm and allows to generate an accurate, nearly diffraction-free shadow in the image plane of the photodetector. The system is designed to work with fixed objects, and the measured cutting edge is strictly coaxial with the spindle of the system.

In case of a telecentric beam path, inaccurate focusing does not affect the scale division of the tool. Lenses with bitelecentric beam paths, free from distortion and characterized by constant linear magnification, seem to be best suited for our purposes [2].

The optical micrometer is the most important part of the developed system; it consists of three main elements, a CMOS (complementary metal-oxide-semiconductor) sensor, a bitelecentric lens and a telecentric illuminator. There are presently two competing companies that are leaders in production of telecentric lenses: Opto Engineering (Italy) and

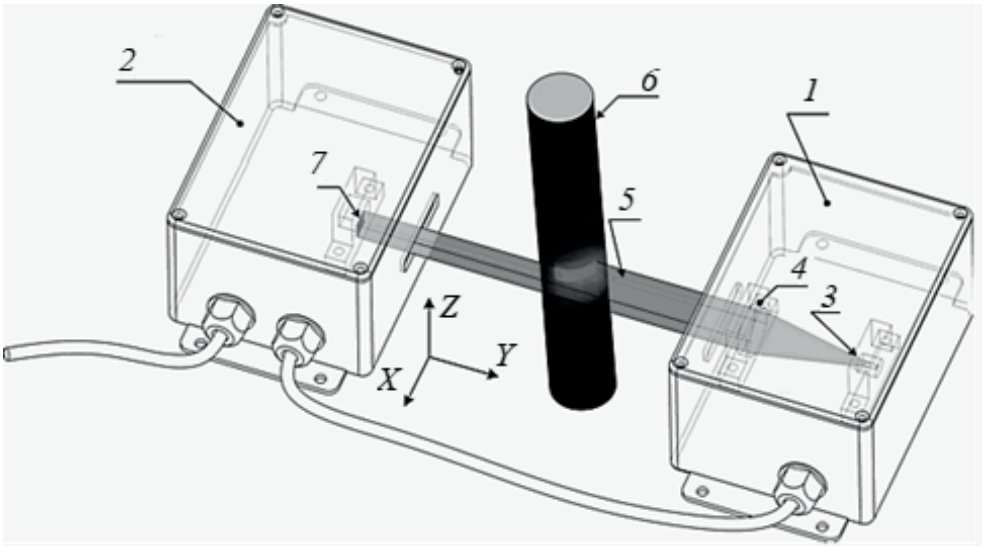

Fig. 1. Functional diagram of optical micrometer:
radiating unit *1*, receiving unit *2* , radiation source *3*, optical scheme *4*, scanning beam *5*, object of measurement *6*, photodetector *7*

SILL Optics (Germany).

The bitelecentric lens is selected in accordance with the requirements imposed on the parameters of the developed system (outlined below).

The bitelelectric lens only captures the beams parallel to its optical axis. Because of this, there is no perspective effect (when distant objects appear smaller than closer objects) and beams falling at an angle and reflected from other surfaces are not captured by the camera. However, the downside of this effect is that the lens only "sees" an area less than or equal to the area of the outer lens. The diameter of the outer lens is 16 mm. Thus, the lens allows to capture an area of approximately 200 mm^2.

The lens should be able to capture an area of at least 8 Ч 6 mm (based on the characteristics of the lens) so that the micrometer can be calibrated and effectively operate.

The second important parameter for finding the maximum focusing point is the depth of field of the lens. It should be no more than 2 mm for adjusting the cutting tool in the given system. This is the only point where the tool's overhang can be measured correctly. Otherwise, the line on which the axis of the tool and its cutting edge lie will not be strictly perpendicular to the optical axis of the micrometer.

The third important parameter is the distance at which the measurement range begins. This distance can be calculated by subtracting the depth of field of the lens from its working distance (the distance at which maximum focus is achieved). This parameter must be taken into account in design of the optical micrometer.

Based on the above requirements, we chose TC 23009, a special bitelecentric lens by Opto Engineering (Italy).

A telecentric illuminator coordinated with the bitelecentric lens is necessary for the lens to operate correctly. The main requirement for the unit is that the diameter of the outer bitelecentric lens should coincide with the diameter of the outer lens of the telecentric illuminator. The LTCLHP023-R illuminator, also by Opto Engineering, fits this requirement.

To obtain correct images of the contours of the measured object, the components of the optical circuit should be arranged as follows:

The backlight module is located opposite the lens, and the axis of the backlight module coincides with the optical axis of the lens. The distance between the lens and the backlight module can range from 120 to 150 mm. We chose a distance of 125 mm (Fig. 2). The measured object should be located at a distance of 62.2 mm from the lens.

The CMOS sensor plays an important role in any optical circuit. As in the case of a three-dimensional triangulation meter with linear illumination, we used an industrial camera from Basler. In our case, there was no need for a high frame rate; the main requirement was that the camera should provide the image of the tool edge without "freezing", i.e., frame delays on the screen were unacceptable. A camera with 25–30 frames per second proved to be sufficient for these purposes.

An industrial CMOS camera, Basler

acA2500-14um, was selected for this purpose. To give a complete picture, let us provide the characteristics of the camera:

Sony IMX264 sensor, 8.4 Ч 7.1 mm;
global shutter;
resolution (L Ч W) 2448 Ч 2048 pixels, pixel size 3.45 Ч 3.45 μm;
maximum frame rate 25 frame/s;
monochrome images;
C-mount;
USB 3.0.

Development and implementation of software interfaces and algorithms

The technology we propose includes a special image-processing algorithm. This algorithm is a spatial and temporal filter that simulates the two main visual channels of the human eye: foveal vision for detailed color vision and peripheral vision for detecting fast processes and events [3].

The retina consists of layers of interconnected cells. To build an algorithmic model of human vision, we selected two main layers of the retina: the outer plexiform and the inner plexiform. Each of the layers is simulated by special filters. The output of the algorithm is simulated by an inner plexiform layer.

Another important feature of the algorithm is that it can remove spatial and temporal noise while simultaneously enhancing image detail. Photoreceptors and perception of information by the brain are simulated in this case; the contrast of the image edges is increased, contours are improved, a logarithmic Gabor filter is implemented. The developed algorithm also makes it possible to increase the accuracy of detecting the contours of objects to subpixels.

Fig. 3 shows images illustrating the changes in sharpness of the object's contour. For example, blurring at the edges of the object is greatly reduced. The differences in intensity are also practically absent in the elements of the object.

We developed a data exchange algorithm making it possible for the optical micrometer to interact with a personal computer. At the physical level, the interaction happens via the USB 3.0 interface. A set of functions is implemented to build the logical level, allowing to connect and control different parameters of the optical micrometer. These parameters include exposure time, gain, range of interest, frame rate. To get real-time images, we used the functionality of the Pylon and OpenCV libraries. The functions for receiving frames and transmitting them for further processing are performed, in accordance with our projects, in separate streams, which allows to achieve high speed at a frame rate of 25 frame/s.

The algorithm also contains functions for detecting (with subpixel accuracy) the contours of the cutting edge of the tool in an image obtained with an optical micrometer.

This image has certain specifics because of telecentric optics used:

diffraction effects at the edges of the tool are minimal;

dimensions of the object image on the matrix of the video camera match the real dimensions of the object.

Thus, knowing the physical size of the pixel on the video camera matrix and the number of pixels occupied by the contour, we can calculate the position of the tool's edges (in micrometers) relative to the optical axis of the camera. With this approach, the positions of the tool's edges can be detected with pixel accuracy. The matrices used in most modern video cameras have a pixel size that

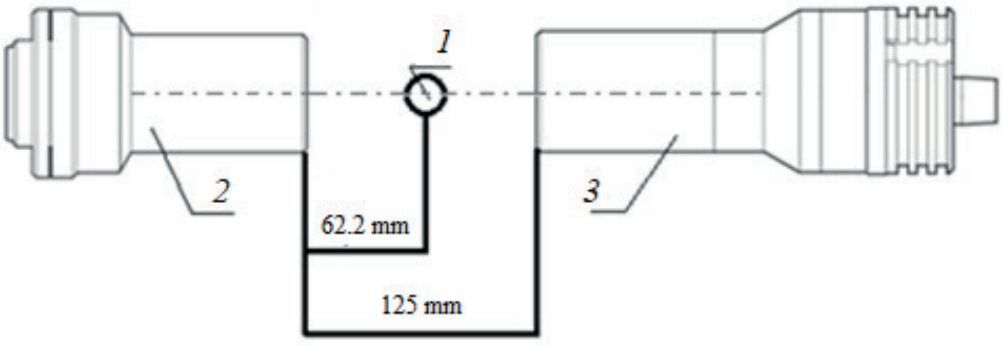

Fig. 2. Layout of components in optical system:
measurement object *1*, bitelecentric lens *2*, backlight module *3*

does not exceed 3–4 μm. This parameter value does not guarantee that the required dimensions are detected with micrometer accuracy.

To detect the edges of the tool more accurately, we have developed an algorithm with subpixel accuracy and used its functionality.

There are three main groups of methods for detecting the contours with sub-pixel accuracy:

approximation methods;

methods based on calculating the image moments;

interpolation methods.

The methods of the first group use continuous functions to fit the image function. The subpixel position of the contour is defined as the inflection point of a continuous function.

The methods of the second group use statistical models.

The methods of the third group provide subpixel accuracy by interpolating image data to obtain a finer grid of pixels [4].

The algorithm that we developed belongs to interpolation methods (third group).

The algorithm consists of the following operations.

Step 1. Gaussian blur is applied to the image.

Step 2. A filter with a Canny kernel is applied separately for rows and columns; results are recorded in the corresponding matrices.

Step 3. The points of the contour are detected with pixel precision.

Step 4. The position of the contours is refined with subpixel accuracy based on the contours obtained in Step *3* and the matrices recorded in Step *2*.

The subpixel coordinates of the contours are calculated by setting the position of each of the points of the contour in its 3×3 neighborhood. Eigenvectors and eigenvalues of the Hessian matrix of a given neighborhood are found next [5]. Because of this, the direction and magnitude of the contour point offset are found relative to the initial ones. Thus, when each point of the contour is shifted by a certain vector, a subpixel value is found for the position of each point of the contour.

The method developed makes it possible to obtain the sought-for values with an accuracy of 0.01 pixels. Such accuracy allows to determine the physical dimensions of the measured tool with an accuracy not less than 0.5 μm.

Geometric parameters, such as overhang and diameter, are calculated as follows. Subpixel coordinates of the contour points are analyzed, with the minimum and maximum points searched by x and y coordinates. The point with the minimum value of the x coordinate corresponds to the tool point most distant from the axis, and the point with the minimum y coordinate to the tool point with the maximum height. The values of the characteristic points are then converted to world coordinates by multiplying the coordinate value by the pixel size in the corresponding direction and by the magnification factor.

Precise image focusing is necessary to obtain the most accurate images. A function calculating the value of the Laplacian of the image (it represents the summed value of second-order derivatives) is used to control focusing. Next, the standard deviation for the Laplacian matrix, i.e., the "focusing" value of the image, is calculated. The degree of focusing of the image is estimated by the value of the parameter obtained. This algorithm includes a threshold value of the parameter, separating the "focusing" values into acceptable (that can be used for measurements) and unacceptable (focusing should be improved if these values are reached) [6].

In addition to the above, we implemented a system for calibration by a given template. The software was developed in the Qt Creator environment using the Qt and OpenCV libraries.

The OpenCV 3.1.0 library intended for image processing was used to develop the functional module of the program. The image received from the camera contains information about the con-

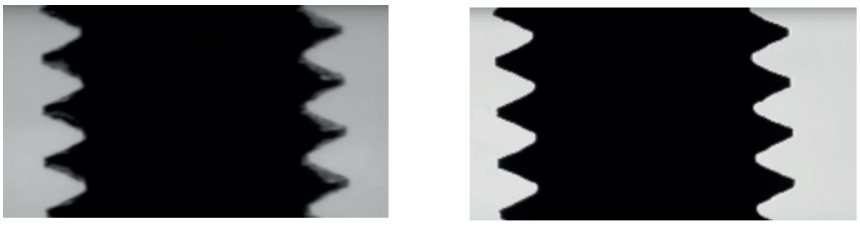

Fig. 3. Comparison of two images of object:
source *a*, processed by algorithm for removing spatial and temporal noise *b*

tours of the object. This image is generated by a telecentric optical scheme allowing to capture images with virtually no diffraction around the edges of the object. This simplifies the task of detecting the contour of an object for further measurement.

In order to increase contrast, we applied an algorithm based on a model of human vision. The object's contours were then detected with subpixel precision. For example, if lens magnification is 1.005, an estimate for the size of the contour on the matrix of the video camera can be made. This size is equal to the number of pixels that the contour occupies, multiplied by the pixel size and magnification factor.

For example, to calculate the size of the contour along the horizontal axis X

$$X = dNp,$$

where d is the lens magnification factor, N is the number of pixels between the edges of the contour, p, μm, is the pixel width.

To calibrate contour size, a template object with known parameters is measured. The position of the rotation axis of the tool in the coordinate system of the camera matrix can be then determined. For example, a cone can be used as a template.

The calibration module allows to determine the position of the point with the maximum value of the Z coordinate (it corresponds to the axis of rotation).The value of the X coordinate corresponding to the axis of rotation is taken to be zero for calibration. In other words, the vertex of the cone serves as the origin of coordinates in the XZ system. The initial value of the Z coordinate is defined as the difference between the obtained value of cone height subtracting the actual cone height (Fig. 4, *a*).

The user interface developed for the measurement mode (Fig. 4, *b*) contains the following areas: image view from the optical micrometer; input of measurement results.

Conclusion

We have carried out a study aimed at creating a device and the accompanying software and hardware technology for quickly and accurately measuring the main parameters of cutting tools. We have obtained the following results.

1. We have developed an optical microscope and an optical scheme for it, including bitelecentric optics for diode illumination and a telecentric lens for image capturing. The lens of the optical microscope has a depth of field less than 1 mm (images are generated without diffraction).

We have established that such an optical scheme allows to reduce the effect of diffraction at the edges of the shadow pattern and measure such parameters of the cutting tool as the overhang and diameter with an optical microscope.

2. We have developed an algorithm detecting fast spatial and temporal processes; it provides measurement of the cutting edge contour of the tool with subpixel accuracy (up to 0.01 pixel) and the physical dimensions of the cutting tool with an accuracy up to 0.5 μm.

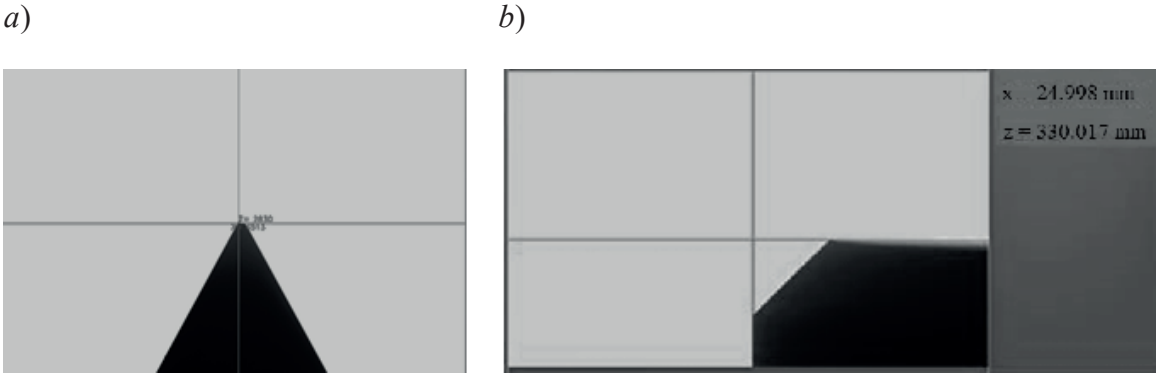

Fig. 4. Example of user interfaces
for calibration (*a*) and measurement (*b*) of size of cutting edge contour;
A cone was used as a template.

REFERENCES

[1] **V.N. Demkin, V.A. Stepanov, M.V. Shadrin,** Rapid phototyping systems with laser scanning, St. Petersburg State Polytechnical University Journal. Physics and Mathematics. (3(177)) (2013) 136–143.

[2] **V.N. Demkin, D.S. Dokov, A.Z. Venediktov,** Measurement of wheel pair parameters of a rolling stock during movement, Proceedings of SPIE. 5066 (International conference "Lasers for measurement and information transfer". St. Petersburg, Russia, 2002) (2003) 48–53.

[3] **A. Benoit, A. Caplier, B. Durette, J. Herault,** Using human visual system modeling for bio-inspired low level image processing, Computer Vision and Image Understanding. 114 (7) (2010) 758–773.

[4] **C. Steger,** An unbiased detector of curvilinear structures, IEEE Transactions on Pattern Analysis and Machine Intelligence. 20 (2) (1998) 113–125.

[5] **F.-J. Shioiu, M.-J. Chen**, Intermittent process hybrid measurement system on the machining center, International Journal of Production Research. 41

(18) (2003) 4403–4427.

[6] **G.B. Garcia, O.D. Suarez, J.L.E. Aranda, et al.** Learning image processing with OpenCV, Packt Publishing, Birmingham (2015) 183–193.

[7] A. **Benoit, A. Caplier,** Fusing bio-inspired vision data for simplified high level scene interpretation: Application to face motion analysis, Computer Vision and Image Understanding. 114 (7) (2010) 774–789.

[8] R. **Grompone, G. Randall,** A sub-pixel edge detector: An implementation of the Canny/ Devernay algorithm, Image Processing on Line. 7 (2017) 347–372.

[9] **H. Spontón, J. Cardelino,** A review of classic edge detectors, Image Processing on Line. 5 (2015) 90–123.

[10] **B. Machilsen, J. Wagemans,** Integration of contour and surface information in shape detection, Vision Research. 51 (1) (2011) 179–186.

Received 20.03.2018, accepted 05.12.2018.

THE AUTHORS

SAVIN Vladislav N.
Ryazan State University named for S.A. Yesenin
46 Svobody St., Ryazan, 390000, Russian Federation
savin-vladislav@mail.ru

STEPANOV Vladimir A.
Ryazan State University named for S.A. Yesenin
46 Svobody St., Ryazan, 390000, Russian Federation
vl.stepanov@365.rsu.edu.ru

SHADRIN Maxim V.
Ryazan State University named for S.A. Yesenin
46 Svobody St., Ryazan, 390000, Russian Federation
m.shadrin@kvantron.com

СПИСОК ЛИТЕРАТУРЫ

1. **Демкин В.Н., Степанов В.А., Шадрин М.В.** Системы быстрого прототипирования с лазерным сканированием // Научно-технические ведомости СПбГПУ. Физико-математические науки. 177) 3 № .2013). С. 136– 143.

2. **Venediktov A.Z., Demkin V.N., Dokov D.S., Tireshkin V.N.** Measurement of wheel pair parameters of a rolling stock during movement // Proceedings of SPIE: The International Society For Optical Engineering. Vol. 05066. The International conference "Lasers for measurement and information transfer. St. Petersburg, Russia (2002)". 2003. Pp. 48–53.

3. **Benoit A., Caplier A., Durette B., Herault J.** Using human visual system modeling for bio-inspired low level image processing // Computer Vision and Image Understanding. 2010. Vol. 114. No. 7. Pp. 758–773.

4. **Steger C.** An unbiased detector of curvilinear

structures // IEEE Transactions on Pattern Analysis and Machine Intelligence. 1998. Vol. 20. No. 2. Pp. 113–125.

5. **Shioiu, F.-J., Chen M.-J.** Intermittent process hybrid measurement system on the machining center // International Journal of Production Research. 2003. Vol. 41. No.18. Pp. 4403–4427.

6. **García G.B., Suarez O.D., Aranda J.L.E., et al.** Learning image processing with OpenCV. Birmingham: Packt Publishing, 2015. 319 p.

7. **Benoit A., Caplier A.** Fusing bio-inspired vision data for simplified high level scene interpretation: Application to face motion analysis // Computer Vision and Image Understanding. 2010. Vol. 114. No. 7. Pp. 774–789.

8. **Grompone R., Randall G.** A sub-pixel edge detector: An implementation of the Canny/Devernay algorithm // Image Processing on Line. 2017. Vol. 7. Pp. 347–372.

9. **Spontón H., Cardelino J.** A review of classic edge detectors // Image Processing on Line. 2015. Vol. 5. Pp. 90–123.

10. **Machilsen B., Wagemans J.** Integration of contour and surface information in shape detection // Vision Research. 2011. Vol. 51. No. 1. Pp. 179–186.

Статья поступила в редакцию 20.03.2018, принята к публикации 05.12.2018.

СВЕДЕНИЯ ОБ АВТОРАХ

САВИН Владислав Николаевич – *инженер кафедры общей и теоретической физики и методики преподавания физики Рязанского государственного университета имени С.А. Есенина, г. Рязань, Российская Федерация.*

390000, Российская Федерация, г. Рязань, ул. Свободы, 46

savin-vladislav@mail.ru

СТЕПАНОВ Владимир Анатольевич – *доктор физико-математических наук, профессор кафедры общей и теоретической физики и методики преподавания физики Рязанского государственного университета имени С.А. Есенина, г. Рязань, Российская Федерация.*

390000, Российская Федерация, г. Рязань, ул. Свободы, 46

vl.stepanov@365.rsu.edu.ru

ШАДРИН Максим Владимирович – *инженер кафедры общей и теоретической физики и методики преподавания физики Рязанского государственного университета имени С.А. Есенина, г. Рязань, Российская Федерация.*

390000, Российская Федерация, г. Рязань, ул. Свободы, 46

m.shadrin@kvantron.com

DOI: 10.18721/JPM.12108
УДК 537.534.3:621.384.8 (075.8)

TWO-ELECTRODE DESIGN FOR ELECTROSTATIC ION TRAP INTEGRABLE IN POLAR COORDINATES

K.V. Solovyev[1,2], *M.V. Vinogradova*[1]

[1] Peter the Great St. Petersburg Polytechnic University, St. Petersburg, Russian Federation

[2]Institute for Analytical Instrumentation of the Russian Academy of Sciences,

St. Petersburg, Russian Federation

An electrostatic field with a square additive dependence on one of coordinates, also providing integrability of charged particle motion equations has been studied in the paper. The conditions of ion-motion finiteness were found for this field and in doing so it was shown the ion trap constructability. Potential parameter values providing a presence of sufficient workspace between two field-defining electrodes were revealed. An algorithm of optimal matching in beam characteristics and electrodes' configuration was synthesized. To test the operability of the designed algorithm, three-dimensional equipotentials and a trajectory inside the ion-trap workspace were constructed. The ion trap designed in our studies can be put to experimental use as a mass spectrometer, extending the class of electrostatic ion traps presented by well-known Orbitrap and Cassini trap.

Keywords: mass spectrometry, ion trap, ideal focusing

Citation: K.V. Solovyev, M.V. Vinogradova, Two-electrode design for electrostatic ion trap integrable in polar coordinates, St. Petersburg Polytechnical State University Journal. Physics and Mathematics. 12 (1) (2019) 87–94. DOI: 10.18721/JPM.12108

ДВУХЭЛЕКТРОДНАЯ РЕАЛИЗАЦИЯ ЭЛЕКТРОСТАТИЧЕСКОЙ ИОННОЙ ЛОВУШКИ, ИНТЕГРИРУЕМОЙ В ПОЛЯРНЫХ КООРДИНАТАХ

К.В. Соловьев[1,2], *М.В. Виноградова*[1]

[1] Санкт-Петербургский политехнический университет Петра Великого,

Санкт-Петербург, Российская Федерация;

[2]Институт аналитического приборостроения Российской академии наук,

Санкт-Петербург, Российская Федерация

В работе исследовано квадратичное (по одной из координат) электростатическое поле, обеспечивающее интегрируемость уравнений движения заряженной частицы. Найдены условия финитности движения иона в этом поле и тем самым показана возможность построения ионной ловушки. Выявлены значения параметра поля, при которых структура эквипотенциалей поля обеспечивает наличие существенного рабочего пространства между двумя полезадающими электродами. Построен алгоритм оптимального согласования характеристик пучка и конфигурации электродов.

Ключевые слова: масс-спектрометрия, ионная ловушка, идеальная фокусировка

Ссылка при цитировании: Соловьев К.В., Виноградова М.В. Двухэлектродная реализация электростатической ионной ловушки, интегрируемой в полярных координатах // Научно-технические ведомости СПбГПУ. Физико-математические науки. 2019. Т. 12. № 1. С. 96–104. DOI: 10.18721/JPM.12108

Introduction

Electrostatic ion traps with perfect space and time focusing (PSTF) of the beam are becoming increasingly popular in mass spectrometry. The principle of perfect focusing of ions in an electrostatic field as a basis for designing mass spectrometry devices was patented by Golikov [1]; Makarov constructed the industrially produced OrbiTrap analyzer (see, for example, [5]) using this principle. The so-called Cassinian traps (also with PSTF) [3, 4–6], first proposed by Golikov and studied by Nikitina [7], have also been the center of much attention. Perfect focusing systems are an important area, with research ongoing in this direction.

This article continues a series of studies [8–11] considering a class of integrable electrostatic traps with PSTF. Perfect focusing along the z direction (for definiteness) in the trap is provided by including an additive term z^2 into the potential structure [8, 9]. We have earlier discussed in detail (see [9–11) the conditions for finite motion in traps that are integrable in parabolic and elliptic coordinates. In this case, we mean the coordinate systems separating the variables in the Hamilton–Jacobi equation after isolating oscillatory motion along z.

We have considered the case of integration in the polar coordinate system that we have briefly touched upon in [8]. Analysis was carried out in dimensionless variables that we have also used earlier [8–11].

Conditions for finite ion motion

An expression for the potential providing separation of variables was obtained in [8]:

$$\varphi(r,\gamma,z) = \\ = z^2 - \frac{r^2}{2} + \mu \ln(r) + \varepsilon \frac{\cos 2\gamma}{r^2}, \qquad (1)$$

where μ, ε are the field parameters; $x = r\cos\gamma$, $y = r\sin\gamma$.

Assuming $\mu \neq 0$, (we are going to confirm below that this condition holds true) and introducing a substitution of variables $r = r_1\sqrt{\mu}$, $r = r_2\sqrt{\mu}$, we obtain the following expression from equality (1)

$$\varphi_1 = z_1^2 - \frac{r_1^2}{2} + \ln r_1 + \varepsilon_1 \frac{\cos 2\gamma}{r^2},$$

where $\varphi_1 = \frac{\varphi}{\mu} - \frac{1}{2}\ln\mu$, $\varepsilon_1 = \frac{\varepsilon}{\mu^2}$.

We can eliminate the parameter μ in expression (1) by means of this scaling, equating this parameter to unity and greatly simplifying further analysis.

The remaining parameter ε considerably affects the topology of field (1), determining both the number of its saddle points in the $z = 0$ plane and the form of equipotentials. The number of saddle points corresponds to the number of real values of the saddle radius r_s in eight pairs (r_s,γ_s) of polar coordinates

$$\left(\sqrt{1\pm\sqrt{1+8\varepsilon}}\Big/\sqrt{2}, \pi/2\right),$$
$$\left(\sqrt{1\pm\sqrt{1+8\varepsilon}}\Big/\sqrt{2}, -\pi/2\right),$$
$$\left(\sqrt{1\pm\sqrt{1-8\varepsilon}}\Big/\sqrt{2}, 0\right),$$
$$\left(\sqrt{1\pm\sqrt{1-8\varepsilon}}\Big/\sqrt{2}, \pi\right)$$

and varies from 2 to 6 as ε in equality (1) takes critical values $\{-1/8,\ 0,\ 1/8\}$. The topology of field (1) is very important for choosing a system of field-defining electrodes bounding the working volume of the trap.

Ion motion in the $r\gamma$ plane orthogonal to the direction of perfect focusing z is determined by the first integrals

$$\frac{\dot r^2}{2} = E - \left(\ln r - \frac{r^2}{2} + \frac{C}{r^2}\right), \qquad (2)$$

$$\frac{r^4\dot\gamma^2}{2} = C - \varepsilon\cos 2\gamma, \qquad (3)$$

where E and C are variable separation constants.

$$E = \frac{\dot r_0^2 + r_0^2\dot\gamma_0^2}{2} + \ln r_0 - \\ - \frac{r_0^2}{2} + \varepsilon\frac{\cos 2\gamma_0}{r_0^2}, \qquad (4)$$
$$C = \frac{r_0^4\dot\gamma_0^2}{2} + \varepsilon\cos 2\gamma_0.$$

As usual, we should now find the conditions for finite motion in the $r\gamma$ plane. Evidently, the nature of ion motion along r is determined by the profile of the effective potential

$$U_{eff}(r) = \ln r - \frac{r^2}{2} + \frac{C}{r^2}$$

and the transverse energy E.

Notice that the potential U_{eff} has a well (Fig. 1) in the range of values $0 < C < 1/8$, while the coordinates of the minimum and maximum of $U_{eff}(r)$ are defined as

$$r_{\min,\max} = \frac{\sqrt{1\mp\sqrt{1-8C}}}{2}, \qquad (5)$$

where the minus sign corresponds to the

minimum radius and the plus sign to the maximum radius.

The minimum and maximum values of the effective potential are expressed as

$$U_{eff\,\min,\max} = \pm\frac{\sqrt{1-8C}}{2} + \ln\frac{1\mp\sqrt{1-8C}}{2}.$$

If $C \to 0$, $U_{eff\,min} \to -\infty$, $U_{eff\,max} \to -1/2$;

if $C = 1/8$, the maximum and minimum of the potential U_{eff} coincide:

$$r_{min} = r_{max} = 1,\ U_{eff\,min} = U_{eff\,max} = -(\ln 2)/2,$$

and the well disappears.

The term that hinders particle motion towards the r singularity disappears in the expression of the effective potential with $C \le 0$ (the same as for $\mu = 0$ in equality (1)); accordingly, the condition $C > 0$ should be satisfied.

To ensure finite motion with $0 < C < 1/8$, the value of the constant E should satisfy the inequalities

$$U_{eff\,min}(C) \le E < U_{eff\,max}(C).$$

On the other hand, there is an interval of values of the parameter C embedded in the interval $]0.1/8[$, which satisfies the condition for finite motion, for any $E < -(\ln 2)/2$. The upper limit of C is found from the condition $U_{eff\,min}(C) = E$, and there is also a lower limit of the interval for $E > -1/2$, calculated from the condition $U_{eff\,max}(C) = E$.

It is convenient to introduce the quantity

$$\Delta E = E - U_{eff\,min}(C),$$

characterizing the kinetic ion energy.

With constant ΔE, finiteness is observed for

$$0 < C < C_{\max} < 1/8,$$

where $C_{\max}$ is found from the solution of the equation

$$U_{eff\,max}(C_{max}) - U_{eff\,min}(C_{max}) = \Delta E.$$

Notably, the condition for radial stability completely coincides with the case of the classical orbitrap here.

Angular motion is determined by the cosine (with amplitude $|\varepsilon|$) profile of the potential γ well and the value of the C constant. As the oscillations are symmetrical with respect to $\gamma = 0$, it is convenient to choose a negative ε ($\varepsilon < 0$).

Further, the quantity $C \in [-|\varepsilon|, |\varepsilon|[$, mathematically sound in terms of constrained angular motion, limits particle motion in the sector

$$-\gamma_b \le \gamma \le \gamma_b,\ \gamma_b = \frac{\arccos(C/|\varepsilon|)}{2}. \qquad (6)$$

Motion along γ is not limited if $C > |\varepsilon|$, the trajectory of the ion (in case of r finiteness) is located in a ring. Conditions for radial confinement are satisfied provided that the inequalities $0 < C < 1/8$ hold true. Accordingly, the range

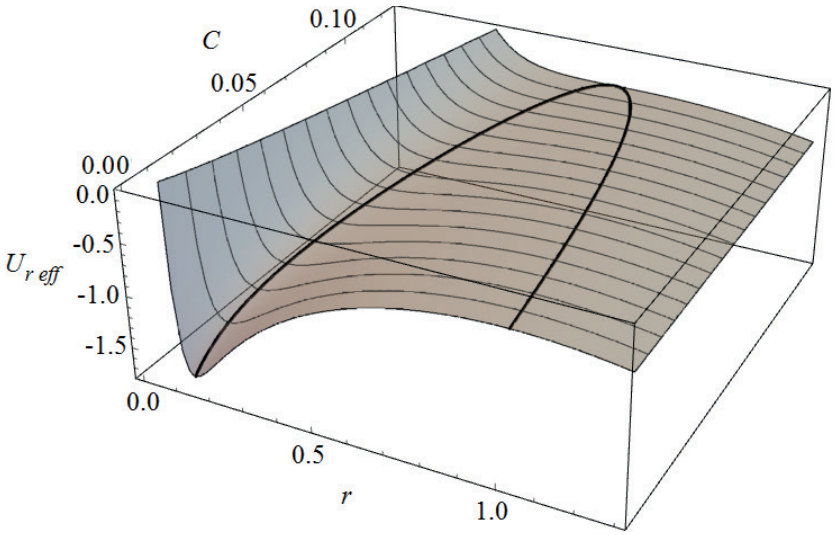

Fig. 1. Graphic representation of function of effective potential $U_{eff}(r, C)$.
Lines indicate the positions of maxima and minima for different C values.

of angular displacements is bounded from below by the segment

$$-\pi/4 \le \gamma \le \pi/4.$$

The range of γ oscillations is also bounded from above with $C < 1/8 < |\varepsilon|$. There are clearly no obstacles to both radial and angular finite motion if the appropriate initial data are chosen for the particle. The trajectory of ion motion in the $r\gamma$ plane lies within the region

$$\Omega = [r1,r2] \times [-\gamma b, \gamma b], \qquad (7)$$

where r_1, r_2 are solutions of the equation $U_{eff}(r, C) = E$.

If $r \to 0$, equipotentials of field (1) have asymptotes $\gamma = \pm\pi/4$ theoretically limiting the angular size of the electrode near the singularity point by $\pi/2$. At the same time, the variation range for angles of γ oscillations of ions cannot be less than $[-\pi/4, \pi/4]$. This calls in question whether a trap using a two-electrode field-defining structure is feasible at all, or in other words, whether particle trajectory (at least with $z = 0$) may lie within the region of a constructively acceptable family of equipotentials. This region (position *1*) is shaded in gray in Fig. 2. This region is bounded by a separatrix passing through a saddle point of the field, asymptotically approaching the z axis at angles $\gamma = \pm\pi/4$. (By "constructively acceptable" we mean that a pair of nested equipotentials (from region *1* in Fig. 2, *b*) of the family (electrodes in an actual device) can bound the working volume, i.e., the region of beam motion (region *5* in Fig. 2, *b*). If it turns out that the beam penetrates through the outer electrode of the given pair at any values of the parameters and initial data, more field-defining fragments are to be included in the device's design, which should be avoided.

To answer the question we have formulated above, let us first consider beams that are infinitely thin with respect to r, formed by trajectories of ions propagating with zero radial velocity along the well of the effective potential $U_{eff}(r)$. Projecting these trajectories onto the $r\gamma$ plane yields arcs symmetrical relative to the angle $\gamma = 0$; the radius of each arc is $r_{\min}(C)$, its angular span is $-2\gamma_b(C)$. The arcs are described by formulae (5), (6) and depend on the parameter C associated with the initial data of the motion. Accordingly, the coordinates of the boundary points of the arcs form the following parametrically defined curves for a set of admissible values of C:

$$x_b(C) = r_{\min}(C)\cos(\gamma_b(C)),$$
$$y_b(C) = \pm r_{\min}(C)\sin(\gamma_b(C)), \qquad (8)$$

whose position (see Fig. 2, curves *3*) relative to the separatrix equipotential is what interests us.

Theoretically, it is possible to create a

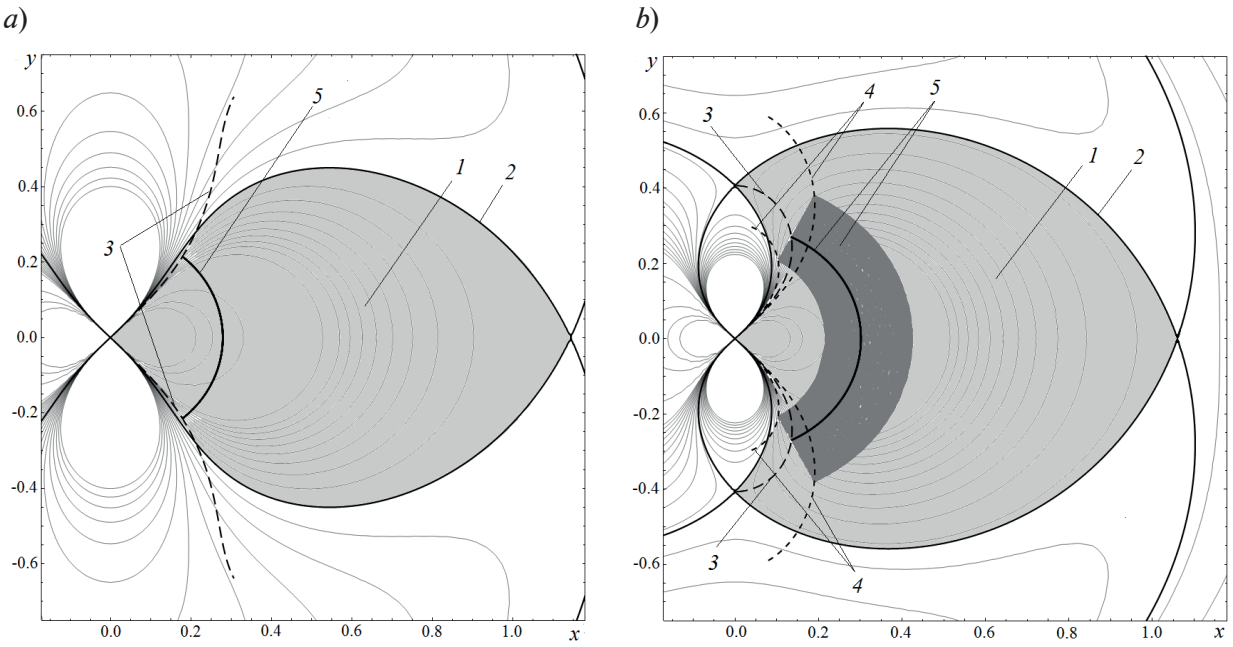

Fig. 2. Ion trajectories and equipotential field structure (1) with $\varepsilon = -0.2$ (*a*) and $\varepsilon = \varepsilon_c$ (*b*):
region *1* of constructively acceptable equipotentials; separatrix equipotential *2*;
parametrically defined curves (8) *3*; boundaries *4* of beam with non-zero radial velocity;
projections *5* of beam trajectories with zero (*a*, *b*) and non-zero (*b*) radial velocities onto plane $r\gamma$

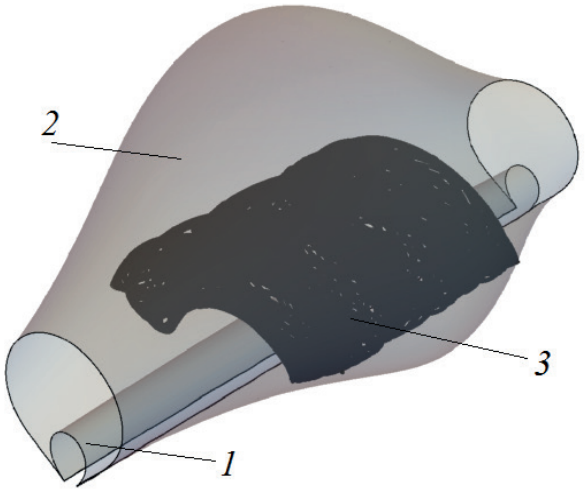

Fig. 3. Example of ion trap based on field (1) with $\varepsilon = \varepsilon_c$. The contours of the inner (*1*) and outer (*2*) electrodes and the ion trajectory (*3*) embedded in the working volume of the trap are shown

two-electrode trap if there is a non-empty interval of C values, such that the points $(x_b(C), y_b(C))$ are located in the region of admissible equipotentials. Notably, non-zero amplitudes of z and r oscillations mean that a gap should exist between the separatrix equipotential and the boundary point of γ oscillations (8). The larger this gap, the greater the phase volume of the ions stored by the trap. Both the position of the separatrix and the form of boundary curve (8) essentially depend on the values of the parameter ε. Equipotential structures with two saddles ($|\varepsilon| > 1/8$) do not allow for sufficient working volume within the separatrix equipotential. For example, the configuration corresponding to

$$\varepsilon = -0.2 < -1/8$$

(see Fig. 2, *a*) is clearly not feasible.

Field configurations with six saddles ($-1/8 < \varepsilon < 0$) offer better options. The range of values $\varepsilon_c < \varepsilon < 0$, where $\varepsilon_c \approx -0.06904$ corresponds to a separatrix that passes simultaneously through the lateral and vertical saddles of field (1), nearest to the center (see Fig. 2, *b*), seems the most attractive. To find ε_c, we use the condition of equal potential (1) at the locations of the given saddle points:

$$\varphi_c = \varphi\left(\sqrt{\frac{1-\sqrt{1+8\varepsilon_c}}{2}}, \frac{\pi}{2}, 0\right) =$$

$$= \varphi\left(\sqrt{\frac{1+\sqrt{1-8\varepsilon_c}}{2}}, 0, 0\right),$$

or

$$\sqrt{1-8\varepsilon_c} + \sqrt{1+8\varepsilon_c} + \ln\frac{1-\sqrt{1+8\varepsilon_c}}{1+\sqrt{1-8\varepsilon_c}} = 0.$$

The actual value of the separatrix potential corresponding to the parameter ε_c is

$$\varphi_c = -\frac{\sqrt{1-8\varepsilon_c}}{2} +$$

$$+\frac{1}{2}\ln\frac{1+\sqrt{1-8\varepsilon_c}}{2} \approx -0.564977.$$

Calculating the dimensions along z of a trap containing ions starting with a nonzero velocity $\dot{z}_0$ from the $z = 0$ plane, we should bear in mind that the three-dimensional equipotential surface of field (1) is pressed against the z axis with distance from the $z = 0$ plane (Fig. 3).

The section of the three-dimensional equipotential

$$f(x, y) + z^2 = d$$

by the plane $z = Z$ has the form

$$f(x, y) = d - Z^2,$$

i.e., it is contained among the equipotentials of the two-dimensional field $f(x,y)$ that is a section of a three-dimensional field by the plane $z = 0$ [8].

Notably, a decrease in the potential with increasing Z corresponds to transition from the separatrix equipotential to internal equipotentials of a region for the given field regions. Accordingly, a cylinder filled with particle trajectories (its base is a region Ω (see formula (7)), and its generator is parallel to the z axis) should be embedded into the surface, which collapses to the z axis with distance from the $z = 0$ plane. Therefore, if we can locate points (8) within a certain equipotential that is internal with respect to the separatrix, we can estimate the admissible dimensions of the beam and the trap along the z coordinate and determine the maximum velocities $\dot{z}_0$ of the ion starting from the symmetry plane. Clearly, taking into account non-zero radial velocities determining the radial size of the region Ω, also requires some space in placing the beam within the interelectrode region.

Notice that if we use trajectories with $\Delta E =$ const, the energy

$$E = \Delta E + U_{eff\ min}(C)$$

turns out to be greater than $U_{eff\ max}(C)$ for a certain C and, therefore, the upper admissible value of C is less than 1/8, since the trajec-

tory leaves the well even before it disappears with decreasing well depth (with increasing C). Meanwhile, the actual position of the boundaries of the region Ω depends on two parameters: C and E (or ΔE). Each C is assigned to two values of $r_{\min}(C)$ instead of one: $r_1(C, \Delta E)$, $r_2(C, \Delta E)$ (see formula (7)). As a result, expressions (8) are replaced by pairs of similar parametrically given boundaries (indicated by a short dashed line in Fig. 2, *b*).

Selecting trap parameters

Let us formulate an algorithm for selecting the parameters of the field of a two-electrode ion trap and the initial conditions for the ions confined in this trap.

Step 1. We select the value of the parameter ε in the interval $\varepsilon_c \le \varepsilon < 0$. We select the value of the parameter C allowing for the beam to be located within the working volume with boundaries (8) with zero radial spread. Let the potential of the separatrix surrounding the working volume be equal to φ_0.

Step 2. We assume that the length of the trap along z is equal to $2Z$; we find the potential

$$\varphi_1 = \varphi_0 - Z^2 - \delta,$$

where δ provides the necessary technological gap between the surface of the electrode and the region where the ions from the beam are concentrated.

Step 3. We solve the problem of embedding the beam in an external equipotential $\varphi(x,y,z) = \varphi_1$. We run a test search for the distance between points with a potential φ_1 along a straight line passing through the origin and point $(x_d(C), y_d(C))$ for each boundary point (8). In this case, we take into account the configuration of equipotentials on the $r\gamma$ plane.

To solve the problem, we construct the field distribution along the given straight line, using expressions (1) and (6):

$$U(r,C) = \varphi(r, \gamma_b(C), 0) = -\frac{r^2}{2} + \mu \ln(r) + \varepsilon \frac{\cos(\arccos(C/\varepsilon))}{r^2} = U_{eff}(r,C).$$

The field distribution along the limiting ray $\gamma = \gamma_b(C)$ coincides with the effective potential, which means that the coordinates of the intersection points of the beam with the equipotential φ_1 and their positions relative to $r_{\min}(C)$ coincide with the coordinates and the positions of the radial boundaries of the beam with the section Ω (7) for the energy $E = \varphi_1$. The critical values of the parameter C limiting the range of its admissible values are determined by the equation

$$\varphi(r_{\min}(C), \gamma_b(C), 0) = \varphi_1,$$

giving the tangent point of the equipotential φ_1 and the limiting ray $\varphi(r_{\min}(C), \gamma_b(C), 0) = \varphi_1$. The beam has an arc trajectory (in projection onto the $r\gamma$ plane) with critical values of C. For other values of C from the interval of admissible values, the motion occurs in the region Ω. The initial data for the motion is found by the values given for the parameters E and C using expressions (4). The beam fits perfectly into the dimensions of the external working equipotential. The relationship of admissible values of C and φ_1 is similar to that of C and E.

We should point out that this consideration only determines the boundary ions of the beam in the configuration space; to reduce the effect of space charge on the operation of the trap, it is advisable to increase the area

$$S_\Omega = 2\pi(r_2^2(C) - r_1^2(C))\gamma_b(C)$$

of the region Ω (see Eq. (7)) by selecting an appropriate C.

Note. Choosing an internal equipotential, it should be borne in mind that its maximum size (maximum radius of distance from the center) lies in the plane $r\gamma$ for $\gamma = 0$. Accordingly, if the internal radius of the beam is equal to r_1, it is sufficient to choose the following equipotential surface as the internal boundary of the system:

$$\varphi(r,\gamma,z) = \varphi_2,$$

where $\varphi_2 = \varphi(r_1 - \delta r, 0, 0)$ (δr is the necessary technological gap, see *Step 2*).

An example of a trap constructed according to this procedure and filled with a characteristic ion trajectory is shown in Fig. 3.

Conclusion

We have considered the nature of ion motion in an integrable electrostatic trap with variable separation in polar coordinates.

We have found the conditions for finite motion, analyzed the field of the trap and confirmed that only one of the parameters of the potential is significant.

We have established the effect of this parameter on field topology, finding the range of parameter values for a potential structure that can be used for designing a viable ion trap.

We have confirmed that the effective volume of the trap can be bounded by just two electrodes, which simplifies the design of the device.

We have formulated a method for selecting

a coordinated configuration of the electrodes and the beam.

The algorithm proposed essentially formulates the constraints for subsequently solving a problem of conditional optimization. The next steps should include maximizing the phase volume of the beam over all phase coordinates and additional one-dimensional optimization of the system with respect to the parameter ε.

A part of this study was carried out within the framework of State Task no. 075-00780-19-00 for the Institute for Analytical Instrumentation of the Russian Academy of Sciences.

REFERENCES

[1] **L.N. Gall, E.E. Pechalina, Yu.K. Golikov,** Ob odnom klasse elecktrostaticheskikh poley s prostranstvenno-vremennoy fokusirovkoy [On one class of electrostatic fields with space-time focusing], Nauchnoe priborostroenie, Elektronno-ionnaya optika, Nauka, Leningrad (1989) 3–7.

[2] **Q. Hu, R. Noll, H. Li, et al.,** The Orbitrap: A new mass spectrometer, J. Mass Spectrom. 40 (4) (2005) 430–443.

[3] **E. Nikolaev, M. Sudakov, G. Vladimirov, et al.,** Multi-electrode harmonized Kingdon traps, J. Am. Soc. Mass Spectrom. 29 (11) (2018) 2173–2181.

[4] **C. Kuster,** The concept of electrostatic non-orbital harmonic ion trapping, Int J. of Mass Spectrometry. 287 (1–3) (2009) 114–118.

[5] **C. Kuster,** Twin trap or hyphenation of a 3D Paul- and Cassinian ion trap, J. Am. Soc. Mass Spectrom. 26 (3) (2015) 390–396.

[6] **B. Raupersa, H. Medhatb., F. Gunzerb, J. Grotemeyer**, Influence of the trap length on the performance of Cassinian ion traps: A simulation study, Int. J. of Mass Spectrometry. 438 (1) (2019) 55–62.

[7] **D.V. Nikitina,** Ionnyye lovushki v dinamicheskoy mass-spektrometrii [Ion traps in dynamical mass spectrometry], PhD Thesis, autoabstract, St. Petersburg, 2006.

[8] **Yu.K. Golikov, N.K. Krasnova, K.V. Solovyev, et al.,** Integrable electrostatic traps, Prikladnaya Fizika (Applied Physics). (5) (2006) 50—57.

[9] **Yu.K. Golikov, K.V. Solov'ev,** Electrostatic ion traps with separation of variables in parabolic coordinates, Tech. Phys. Lett. 36 (4) (2010) 333—336.

[10] **Yu.K. Golikov, K.V. Solov'ev,** Criterion of transverse stability for ion traps with transverse motion integrable in elliptic coordinates, Tech. Phys. Lett. 37 (11) (2011) 1062—1064.

[11] **K.V. Solov'ev, M.V. Vinogradova,** Conditions of ion motion confinement in an electrostatic trap with separation of variables in parabolic coordinates, Tech. Phys. Lett. 44 (7) (2018) 618—621.

Received 21.01.2019, accepted 04.02.2019.

THE AUTHORS

Solovyev Konstantin V.
Peter the Great St. Petersburg Polytechnic University
29 Politechnicheskaya St., St. Petersburg, 195251, Russian Federation
k-solovyev@mail.ru

Vinogradova Maria V.
Peter the Great St. Petersburg Polytechnic University
29 Politechnicheskaya St., St. Petersburg, 195251, Russian Federation vinogradova_39@mail.ru

СПИСОК ЛИТЕРАТУРЫ

1. **Галль Л.Н., Печалина Е.Э., Голиков Ю.К.** Об одном классе электростатических полей с пространственно-временной фокусировкой // Сб. «Научное приборостроение». Электронно-ионная оптика. Ленинград: Наука, 1989. С. 7–3.

2. **Hu Q., Noll R., Li H., Makarov A., Hardman M., Cooks G.** The Orbitrap: a new mass spectrometer // J. Mass Spectrom. 2005. Vol. 40. No. 4. Pp. 430–443.

3. **Nikolaev E., Sudakov M., Vladimirov G., Velбsquez-Garcна L.F., Borisovets P., Fursova A.** Multi-electrode harmonized Kingdon traps // J. Am. Soc. Mass Spectrom. 2018. Vol. 29. No.

11. Pp. 2173–2181.

4. **Köster C.** The concept of electrostatic non-orbital harmonic ion trapping // Int. J. of Mass Spectrometry. 2009. Vol. 287. No. 1–3. Pp. 114–118.

5. **Köster C.** Twin trap or hyphenation of a 3D Paul- and Cassinian ion trap // J. Am. Soc. Mass Spectrom. 2015. Vol. 26. No. 3. Pp. 390–396.

6. **Raupersa B., Medhatb H., Gunzerb F., Grotemeyer J.** Influence of the trap length on the performance of Cassinian ion traps: A simulation study // Int. J. of Mass Spectrometry. 2019. Vol. 438. No. 1. Pp. 55–62.

7. **Никитина Д.В.** Ионные ловушки в динамической масс-спектрометрии. Автореферат дис. ... канд. физ.-мат.наук. СПб. 16 .2006 с.

8. **Голиков Ю.К., Краснова Н.К., Соловьев К.В., Никитина Д.В.** Интегрируемые ионные ловушки // Прикладная физика. 5 № .2006. С. 57–50.

9. **Голиков Ю.К., Соловьев К.В.** Электростатические ионные ловушки с разделением переменных в параболических координатах // Письма в ЖТФ. 2010. Т. 36. Вып. 7. С. 88–82.

10. **Голиков Ю.К., Соловьев К.В.** Критерий поперечной устойчивости в ионных ловушках с интегрируемым в эллиптических координатах движением // Письма в ЖТФ. 2011. Т. 37. Вып. 22. С. 49–43.

11. **Соловьев К.В., Виноградова М.В.** Условия финитности движения иона в электростатической ловушке с разделением переменных в параболических координатах // Письма в ЖТФ. 2018. Т. 44. Вып. 14. С. 34–41.

Статья поступила в редакцию 21.01.2019, принята к публикации 04.02.2019.

СВЕДЕНИЯ ОБ АВТОРАХ

СОЛОВЬЕВ Константин Вячеславович – кандидат физико-математических наук, доцент кафедры физической электроники Санкт-Петербургского политехнического университета Петра Великого, младший научный сотрудник Института аналитического приборостроения РАН.

195251, Российская Федерация, г. Санкт-Петербург, Политехническая ул., 29

k-solovyev@mail.ru

ВИНОГРАДОВА Мария Валерьевна – студентка Института физики, нанотехнологий и телекоммуникаций Санкт-Петербургского политехнического университета Петра Великого.

195251, Российская Федерация, г. Санкт-Петербург, Политехническая ул., 29

vinogradova_39@mail.ru

DOI: 10.18721/JPM.12109
УДК 662.612.3:661.487.1

WATER VAPOR CONVERSION DURING THE INTERACTION BETWEEN AN EVAPORATED HYDROGEN FLUORIDE SOLUTION AND CARBON IN THE FILTRATION COMBUSTION MODE

V.V. Kapustin[1], *D.S. Pashkevich*[1], *D.A. Mukhortov*[2], *V.B. Petrov*[2], *Yu.I. Alexeev*[3]

[1] Peter the Great St. Petersburg Polytechnic University, St. Petersburg, Russian Federation;

[2] FSUE RSC "Applied Chemistry", St. Petersburg, Russian Federation;

[3] «New Chemical Products» Ltd., St. Petersburg, Russian Federation

The results of laboratory studies of the water vapor conversion when an evaporized aqueous solution (EAS) of HF and oxygen is being fed into a stationary layer of granular graphite have been presented. It was established that the characteristic time for the water vapor conversion upon the contact of the EAS of HF with carbon at a temperature of about 1500 K was 10 s. Comparison of the experimental results with the literature data on high-temperature interaction of water vapor and carbon showed that HF had little or no effect on the rate of this interaction at a temperature of about 1500 K. Our method derived from the high-temperature interaction of the EAS of HF with carbon can serve as the basis of an industrial technology for the dehydration of an aqueous solution of HF, including azeotropic one.

Keywords: hydrogen fluoride, hydrofluoric acid, water gas, filtration combustion

Citation: V.V. Kapustin, D.S. Pashkevich, D.A. Mukhortov, V.B. Petrov, Yu.I. Alexeev, The water vapor conversion during the interaction between an evaporated hydrogen fluoride solution and carbon in the filtration combustion mode, St. Petersburg Polytechnical State University Journal. Physics and Mathematics. 12 (1) (2019) 95–106. DOI: 10.18721/JPM.12109

КОНВЕРСИЯ ВОДЯНОГО ПАРА ПРИ ВЗАИМОДЕЙСТВИИ ИСПАРЕННОГО РАСТВОРА ФТОРИДА ВОДОРОДА С УГЛЕРОДОМ В РЕЖИМЕ ФИЛЬТРАЦИОННОГО ГОРЕНИЯ

В.В. Капустин[1], *Д.С. Пашкевич*[1], *Д.А. Мухортов*[2], *В.Б. Петров*[2], *Ю.И. Алексеев*[3]

[1] Санкт-Петербургский политехнический университет Петра Великого, Санкт-Петербург, Российская Федерация;

[2] Российский научный центр «Прикладная химия», Санкт-Петербург, Российская Федерация;

[3] ООО «Новые химические продукты» Санкт-Петербург, Российская Федерация

Приведены результаты лабораторного исследования конверсии водяного пара при подаче испаренного водного раствора (ИВР) фторида водорода HF и кислорода в стационарный слой гранулированного графита. Установлено, что характерное время конверсии водяного пара при контакте ИВР HF и углерода при температуре около 1500 K составляет величину порядка 10 с. Сравнение результатов эксперимента с литературными данными по высокотемпературному взаимодействию водяного пара и углерода показало, что при указанной температуре присутствие HF практически не влияет на скорость взаимодействия водяного пара с углеродом. Метод, базирующийся

на высокотемпературном взаимодействии ИВР HF с углеродом, может служить основой промышленной технологии дегидратации водного раствора HF, в том числе азеотропного.

Ключевые слова: фторид водорода, плавиковая кислота, водяной газ, фильтрационное горение

Ссылка при цитировании: Капустин В.В., Пашкевич Д.С., Мухортов Д.А., Петров В.Б., Алексеев Ю.И. Конверсия водяного пара при взаимодействии испаренного раствора фторида водорода с углеродом в режиме фильтрационного горения // Научно-технические ведомости СПбГПУ. Физико-математические науки. 2019. Т. 12. № 1. С. 105–116. DOI: 10.18721/JPM.12109

Introduction

Aqueous solution of hydrogen fluoride HF (hydrofluoric acid) is produced by a number of industries; for example, in processing of depleted uranium hexafluoride UF_6 by hydrolysis [1, 2].

Anhydrous hydrogen fluoride (aHF) [3, 4] is mainly used in industry as a fluorinating agent; its water content should be no higher than 0.06% [5]. For this reason, developing technologies for producing anhydrous hydrogen fluoride from its aqueous solutions is an important task.

While aHF is typically obtained from its aqueous solution by distillation [5], this solution is azeotropic with a hydrogen fluoride content of about 35–40% [6], so the mixture cannot be separated into individual components by conventional distillation. An azeotrope is one of the components with any composition of the initial mixture subjected to distillation. Thus, it is impossible to completely remove hydrogen fluoride from its aqueous solution by distillation.

Different studies considered dehydration of hydrofluoric acid with sodium fluoride [7] and concentrated sulfuric acid [8]. The first method has no industrial application at present. As for the second method, 75% sulfuric acid in the amount of about 30 kg per 1 kg of aHF is formed as a by-product, so it is difficult to select structural materials for industrial implementations of this method.

Ref. [9] proposed a method for dehydration of an aqueous solution of hydrogen fluoride, including azeotropic, by high-temperature interaction of water vapor with carbon with filtration combustion by the scheme:

$$C^{sol} + O_2^{gas} + HF^{gas} + H_2O^{gas} \rightarrow \rightarrow CO^{gas} + CO_2^{gas} + H_2^{gas} + HF^{gas}, \quad (1)$$

where the superscripts *sol* and *gas* correspond to the solid and gas phase of the substances.

Using thermodynamic calculations and laboratory studies, Ref. [9] confirmed that hydrogen fluoride is the only fluorine-containing substance in the system at temperatures above 1000 K.

Thus, it was established that process (1) is in principle possible if hydrogen fluoride remains inert with respect to other components of the system, and water vapor interacts with carbon to form hydrogen H_2^{gas} and carbon monoxide CO^{gas}.

Interaction of water vapor with carbon is well studied in theory on gasification of solid fuels. In particular, it was found in [10] that the characteristic time of interaction of water vapor with carbon of different grades is several seconds at 1500–1600 K.

However, we have not uncovered any data in literature on the reaction rate for interaction of water vapor with carbon in the presence of hydrogen fluoride. It is known that hydrogen fluoride is a polar substance (its dipole moment is equal to 1.88 D) and, as such, has catalytic and inhibitory effects on many chemical processes [4].

The goal of this study has consisted in determining the depth of conversion of water vapor during high-temperature interaction of vaporized aqueous solution of hydrogen fluoride with a layer of granular graphite when oxygen is fed into the layer.

Characteristics of the initial materials

We used ground artificial graphite GII-A (TU 1916-109-71-2000) with a bulk weight of 840 kg/m^3 and the content of the basic substance no less than 99% for the laboratory experiments; the graphite had ash content of no more than 1%, moisture and sulfur contents not more than 1.0 and 0.05%, respectively. The granulometric composition of the mixture is given in Table 1.

The composition of impurities was detected using ICPE-9000, an inductively coupled plasma emission spectrometer, and FTIR-8400S, a FTIR spectrometer. The results of the study suggest that the main impurities in the initial graphite were calcium and iron silicates.

Table 1

Granulometric composition of original graphite

Sieve mesh size, mm	10	7	5	2.0	1.4	0.40	0.25
Weight content of graphite in mixture,%	0.0	0.8	20.0	63.7	12.6	2.9	0.0

It was found by leaching the graphite with 0.4% sodium hydroxide that the acid component was absent in the initial graphite.

We used aqueous solutions of hydrogen fluoride with the weight contents of hydrogen equal to 40% and 72%, since these solutions are formed in a number of technological processes [1, 2].

Laboratory setup and experimental procedure

We constructed a laboratory setup for experimental studies on high-temperature interaction of water vapor and carbon in the presence of oxygen and hydrogen fluoride. The schematic of the setup is shown in Fig. 1.

The steel cylindrical reactor *1* with a volume of 23 L, a height of 400 mm and an internal diameter of 273 mm is equipped with a cooling jacket and systems for supplying components and removing reaction products. The temperature of the coolant in the cooling jacket was 370 K.

A thick-walled copper nozzle *2* with a diameter of 28 mm and a wall thickness of 8 mm was used to supply oxygen into the layer of granulated carbon and evaporated aqueous solution of hydrogen fluoride. A cooling jacket was installed to cool the nozzle in its upper part; water was supplied into the jacket at a temperature of 370 K. Experiments were carried out with two positions of nozzle *2* in reactor *1*.

In position I (Fig. 2, *a*), the nozzle was installed in the side outlet of the reactor's upper flange at an angle of 45°, with the nozzle shut-off valve located on the vertical axis of the reactor. In position II (Fig. 2, *b*), the nozzle was installed in the central outlet of the upper flange, and the reactor was turned over.

The temperature distribution in the zone where gas flowed out of the nozzle was monitored using chromel-alumel thermocouples T_1-T_4

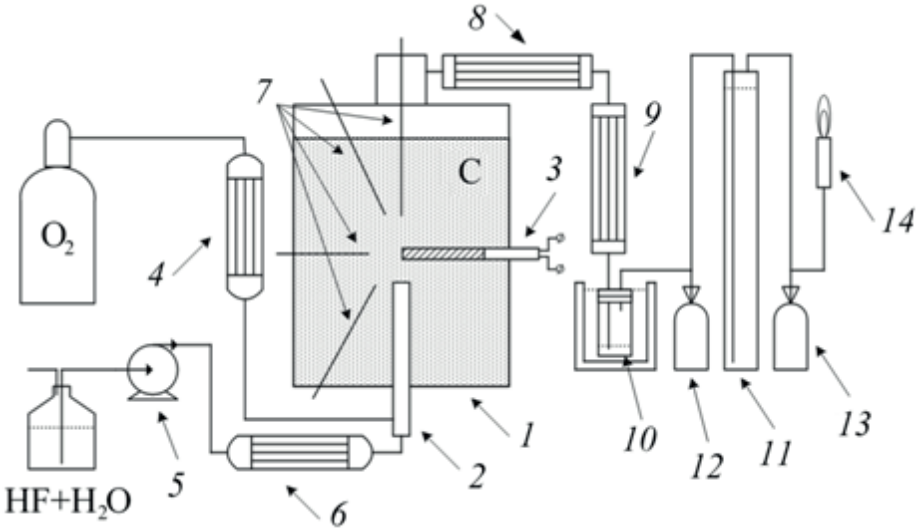

Fig. 1. Layout of laboratory setup:
reactor *1*; two-component nozzle *2*; removable electric heater *3*;
heat exchanger *4* for heating O_2; peristaltic pump *5*;
heat exchanger *6* for evaporating and overheating aqueous solution of HF;
thermocouples *7*; nickel heat exchangers *8*, *9*;
acid collector *10*; alkaline absorber *11*; nickel tubes *12*, *13*;
device *14* for combustion of H_2 and CO in air oxygen

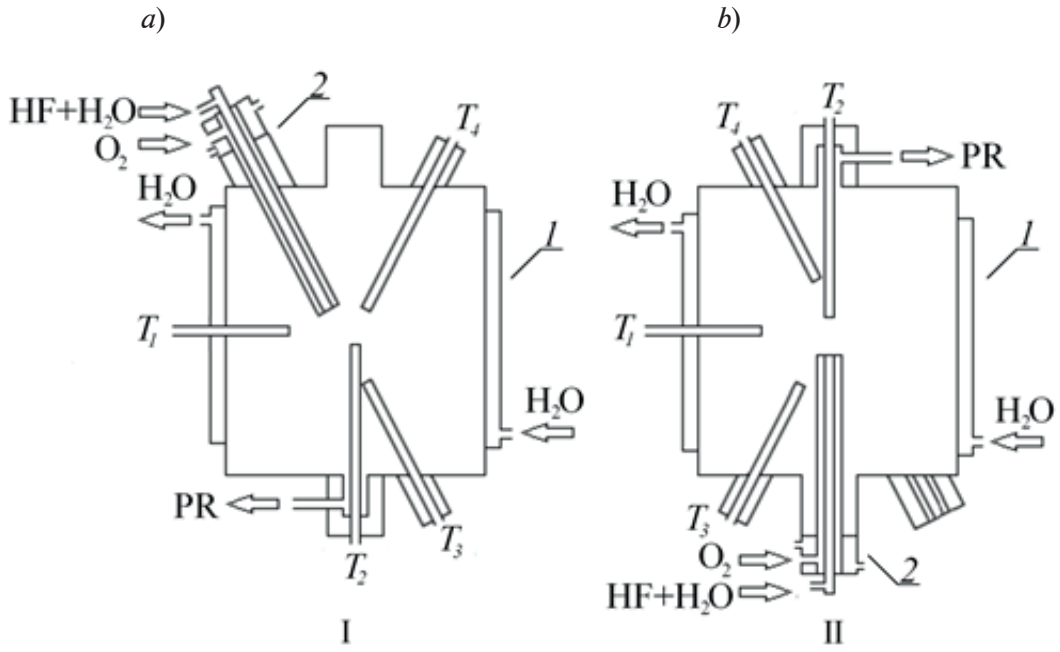

Fig. 2. Schematics for two layouts of nozzle (*2*) and thermocouples (T_1–T_4)in reactor (*1*); *a*, *b* are positions I and II; PR are products of reaction

installed in nickel covers with a diameter of 6 mm and a wall thickness of 1.5 mm.

At the beginning of the experiment, granular graphite was loaded into the reactor up to the level of the upper lid, while the average mass of carbon backfill was 16 kg. Next, the carbon layer was preheated using a removable electric heater *3* (see Fig. 1) installed near the nozzle shut-off valve. After the graphite near the nozzle was heated to a temperature of 900 K, the electric heater was removed from the reactor and oxygen was supplied through the nozzle to further heat the carbon layer and maintain the temperature above 1000 K. In order to prevent condensation of water vapor and hydrogen fluoride on the inner surfaces of the nozzle, oxygen was heated to 500 K in heat exchanger *4* before it was fed into the reactor.

Next, a pre-evaporated aqueous solution of hydrogen fluoride was supplied into the heated carbon layer together with oxygen. The solution was dispensed with peristaltic pump *5* and evaporated in heat exchanger *6* at a temperature of 600 K.

The boundaries and characteristic dimensions of the region in the graphite layer where the temperature exceeded 1000 K were estimated using the theromocouples. Notably, the equilibrium in reaction (1) is shifted to the right at this temperature.

To cool the gas flow of reaction products, nickel heat exchangers *8* and *9* (see Fig. 1) were installed, one after another, at exit from the reactor; the temperatures of 280 K using a cryostat and 220 K using liquid nitrogen, respectively, were maintained in the heat exchangers. The condensed liquid was gathered in collector *10* (lined with fluoroplast-4), where its hydrogen fluoride and water content was measured by titration. The collector was also cooled with liquid nitrogen to a temperature of 220 K.

The gas flow was neutralized in alkaline absorber *11* after the collector. Samples for chromatographic and spectral analysis of gaseous reaction products were collected before and after the absorber into nickel tubes *12* and *13,* respectively (the tubes were passivated with fluorine). Samples for gas analysis were taken from three to five times during one experiment.

Hydrogen and carbon monoxide, formed during high-temperature interaction of carbon and water vapor, were burned in ambient oxygen in device *14* (see Fig. 1).

After the experiment, the reactor was purged with an inert gas, the carbon material was cooled, mixed and a sample was taken. Methods for analyzing carbon and reaction products are described in [9].

Experimental results and discussion

Thermal state of the reactor. The highest possible volume flow rate of oxygen was chosen for the experiments. The requirement imposed on the flow rate was that it would not lead to fluidization of the graphite layer. This flow rate value was 90 cm^3/s.

The change in the flow rate of the evaporated aqueous solution of hydrogen fluoride was in the range of 5–85 mg/s.

Measurements revealed that the graphite temperature in the layer near the exit of gas flows from the nozzle exceeded 1400 K, which is sufficient for the reaction producing water gas. A factor that had to be taken into account was that the nickel tubes where the thermocouples were installed distorted the temperature field due to their thermal characteristics (heat capacity and thermal conductivity); as a result, the measured temperature values were lower than the actual ones.

Fig. 3 shows the experimental temperature distributions recorded by thermocouples for two positions of the nozzle (see Fig. 2).

In position I, an asymmetric high-temperature zone whose shape was close to spherical formed in the reactor. The asymmetry of the high-temperature zone is associated with interaction of forced and natural convection in the gas flow forming through the carbon layer. The gas flow formed by forced convection from the nozzle exit to the reactor exit; it was directed downwards. The gas flow formed by natural convection ($T \approx 1300$ K) moved from the nozzle exit upward, reached the cavity between the upper level of the carbon layer and the upper lid of the reactor ($T \approx 400$ K) and descended along the walls to the exit from the reactor.

The dependence of gas viscosity on temperature also affected the above-described structure of the flow: the viscosity of the gas increased with increasing temperature, and, consequently, the flow resistance of the gas increased in the high-temperature region, causing gas flows to bend around the high temperature region.

In position II, a symmetrical high-temperature region shaped as an ellipsoid stretched along the vertical axis was formed in the reactor. The components of forced and natural convection were collinear and directed towards the exit from the reactor.

The characteristic size of the zone with temperatures above 1000 K was approximately

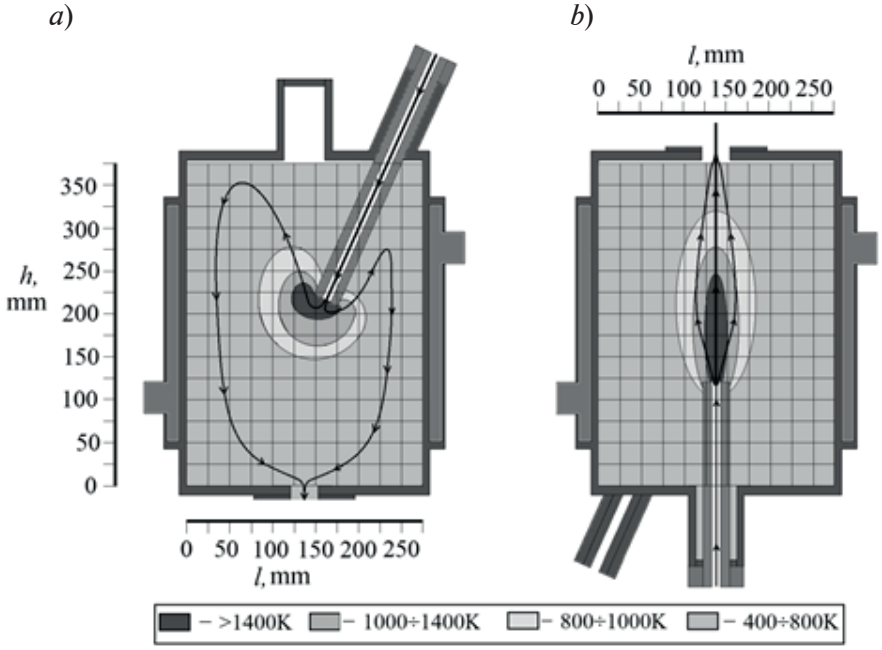

Fig. 3. Experimental temperature distribution in reactor for positions I (*a*) and II (*b*) of nozzle (see Fig. 2); projected flow paths of gas are also shown

7–8 cm in position I, and a region with characteristic heights of 13–15 cm and widths of 5–6 cm was formed in position II.

Water vapor stayed in the high-temperature (T > 1000 K) zone for about 60% longer in position II than in position I with the same flow rate of gaseous components.

Three zones were observed in the high-temperature reaction region. The first was the oxygen zone that occupied the region from the point where the gas flowed from the nozzle to the surface where the oxygen concentration became zero. The second was the zone of interaction between water vapor and carbon that covered the region from the border of the oxygen zone to the surface where the temperature dropped to 940 K.

A highly exothermic reaction of interaction of carbon with oxygen occurred in the oxygen zone [11]. There was virtually no significant change in the water content in the oxygen zone as hydrogen formed by the water interacting with carbon was completely oxidized by oxygen.

We estimated the length of the oxygen zone in accordance with the recommendations given in [12]. The characteristic size of the oxygen zone for oxygen consumption of 90 cm^3/s and particle size distribution of carbon material given in Table 1 was 1.5 cm.

The oxygen zone is followed by the reduction zone where water vapor interacts with carbon, and hydrogen and carbon monoxide form at temperatures above 940 K. In addition, the following endothermic reactions can occur in this zone:

$$H_2O + C^{sol} \rightarrow H_2 + CO \quad (+132\ \text{kJ};\ \Delta G < 0 \text{ with } T > 940\ \text{K}); \tag{2}$$

$$CO_2 + C^{sol} \rightarrow 2CO\ (+172\ \text{kJ};\ \Delta G < 0 \text{ with } T > 1000\ \text{K}); \tag{3}$$

$$H_2O + C^{sol} \rightarrow H_2 + CO \quad (+41\ \text{kJ};\ \Delta G < 0 \text{ with } T > 1330\ \text{K}) \tag{4}$$

Here ΔG is the variation of the Gibbs energy.

To find the region of temperature variation where the equilibrium in reactions (2)–(4) (as well as in reaction (5) below) is shifted to the right, we calculated the Gibbs energy variation depending on temperature.

The temperature is below 940 K in the region where secondary water forms. Under this condition, the reaction of interaction of water vapor with carbon stops but the reverse reaction of interaction of hydrogen with carbon monoxide occurs and secondary water forms:

$$H_2 + CO \rightarrow H_2O + C^{sol} \quad (-132\ \text{kJ};\ \Delta G < 0 \text{ at } T < 940\ \text{K}). \tag{5}$$

Thus, the characteristic size of the oxygen zone is smaller than that of the high-temperature (above 1000 K) zone in the graphite layer by approximately an order of magnitude. It is preferable to maintain the temperature in the reduction zone in the range of 1000–1300 K, at which water vapor interacts with carbon, and reaction (4) is thermodynamically forbidden ($\Delta G < 0$).

Conversion of water vapor depending on the mass flow rate of the evaporated aqueous solution of hydrogen fluoride. One of the parameters that determine the effectiveness of the proposed method for producing hydrogen fluoride is conversion of water vapor during high-temperature contact with carbon.

Conversion of water vapor at a given flow rate of aqueous solution of hydrogen fluoride was measured in two ways: by the composition of gaseous products at the exit of the reactor and by the amount of water gathered in collector *10* (see Fig. 1).

Measuring the composition of the gas phase at the exit from the reactor allows to calculate the conversion of water vapor based on the material balance of oxygen and hydrogen entering the reactor in the form of water vapor and molecular oxygen and leaving the reactor in the form of molecular hydrogen and carbon oxides.

Conversion of water vapor with respect to gaseous reaction products, K_{gas}, was calculated by the following formula:

$$K_{gas} = \frac{W_{O_2}}{W_{H_2O}} \times \frac{c_{H_2}}{\frac{c_{CO} - c_{H_2}}{2} + c_{CO_2} + c_{O_2}} \cdot 100\%, \tag{6}$$

where W, mg/s, is the flow rate of the corresponding components at the inlet of the reactor; c, vol.%, is the concentration of the corresponding substances in gas flow at the exit of the reactor after condensation of water and hydrogen fluoride.

Table 2 shows the typical composition of the gas phase after hydrogen fluoride condenser *10* (see Fig. 1).

The conversion of water vapor with respect to the liquid phase, $K_{flu,}$ was determined as the ratio of the mass of water gathered in collector *10* (see Fig. 1) to the mass of water vapor fed to the reactor as part of aqueous solution of hydrogen fluoride.

Fig. 4 shows the values of water vapor conversion K_{gas} and K_{flu} depending on the flow rate of aqueous solution of hydrogen fluoride for two concentrations of hydrogen fluoride and two positions of the nozzle.

Table 2

Characteristic composition of gaseous reaction products after hydrogen fluoride condenser

Product	*c*, vol.%	Detection method
CF_4	–	Gas chromatography
CO	70	
CO_2	20	
H_2	10	
O_2	0.5	
CH_4	0.1	
$(HF)_n$	0.1 with $n = 4$	Potentiometry
COF_2	–	FTIR

Notes: accuracy for detecting the characteristic concentration *c* was 10^{-2} vol.%; FTIR stands for Fourier-transform infrared spectroscopy

With the flow rate of aqueous solution of hydrogen fluoride varying from 5 to 90 mg/s, conversion of water vapor varies from 10 to 80–90%, passing through a maximum.

Decrease in water vapor conversion with an increasing solution flow rate from 20 to 90 mg/s is associated with a shorter period during which water vapor stays in the high-temperature zone, with the temperature of the carbon layer decreasing as it is cooled by flows of water vapor and hydrogen fluoride, and with the endothermic reaction of water gas formation.

The increase in conversion with the flow rate increasing from 5 to 20 mg/s is probably because the reaction products stay in the zone where secondary water forms for a shorter period of time.

The conversion of water vapor K_{gas} is higher than the conversion of K_{flu} in all experiments, by 14% on average. The likely reason for this is that finely dispersed water droplets are carried away from collector *10*.

The depths of water vapor conversion for experiments with acid containing hydrogen fluoride at concentrations of 40% and 72% are close to each other. The conversion is significantly affected by the position of the nozzle. If the nozzle is installed axisymmetrically (in position II), the conversion of water vapor is higher by about 40%. This is likely because the flow stays in the high-temperature zone for a longer period.

Conversion of water vapor depending on the time it stays in the high-temperature zone. The given time for which the flow stayed in the zone with temperatures above 1000 K was estimated approximately by the flow rate of aqueous solution of hydrogen fluoride and the configuration of the high-temperature zone, taking into account the oxygen flow. We assumed that the reaction forming water gas flows occured outside the oxygen zone. The processed experimental data are given in Fig. 5.

The obtained dependences of the conversion depth on the time of contact of carbon with water vapor in the high-temperature oxygen-free zone allow to conclude that reaction (1) occurs almost completely with a contact time of about 7–10 s and this time does not depend on the initial concentration of hydrofluoric acid.

The obtained values of contact time required for 90% water vapor conversion are in good agreement with the data of [10], considering the interaction of water vapor with different grades of graphite in the absence of hydrogen fluoride. It was additionally established that the concentration of hydrogen fluoride in its initial solution does not affect the value of water vapor conversion.

Based on analysis of the data we have carried out, we can conclude that hydrogen fluoride has practically no effect on the rate of high-temperature interaction of water vapor with graphite at temperatures above 1000 K

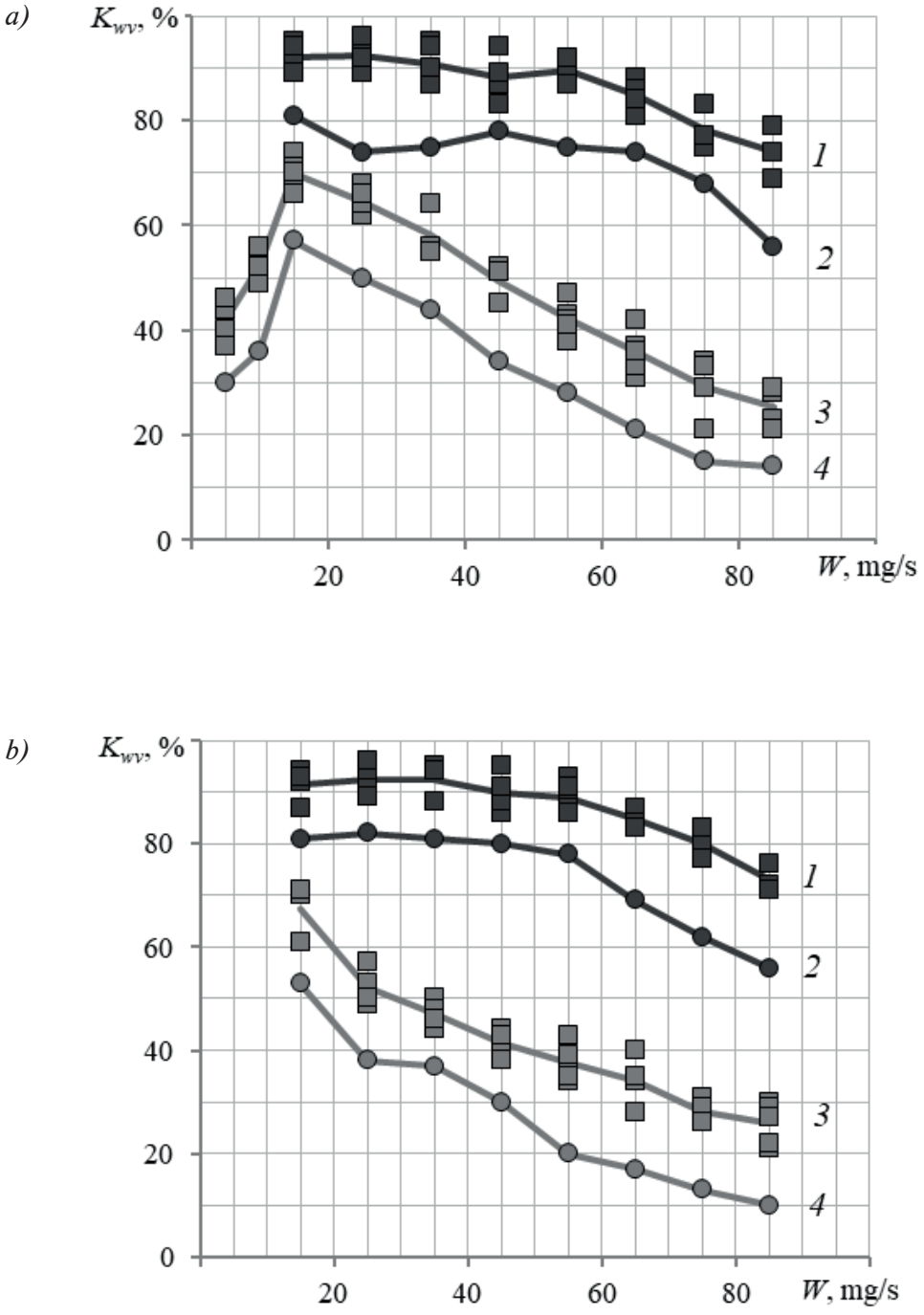

Fig. 4. Dependences for water vapor conversion: K_{wv}, K_{gas} (curves *1*, *3*) and K_{flu} (*2*, *4*) as functions of flow rate of aqueous HF solution upon contact of evaporated solution with high-temperature layer of carbon; HF content in solution was 40% (*a*) and 72% (*b*);
Data are given for positions I (*3*, *4*) and II (*1*, *2*) of the nozzle (see Fig. 2)

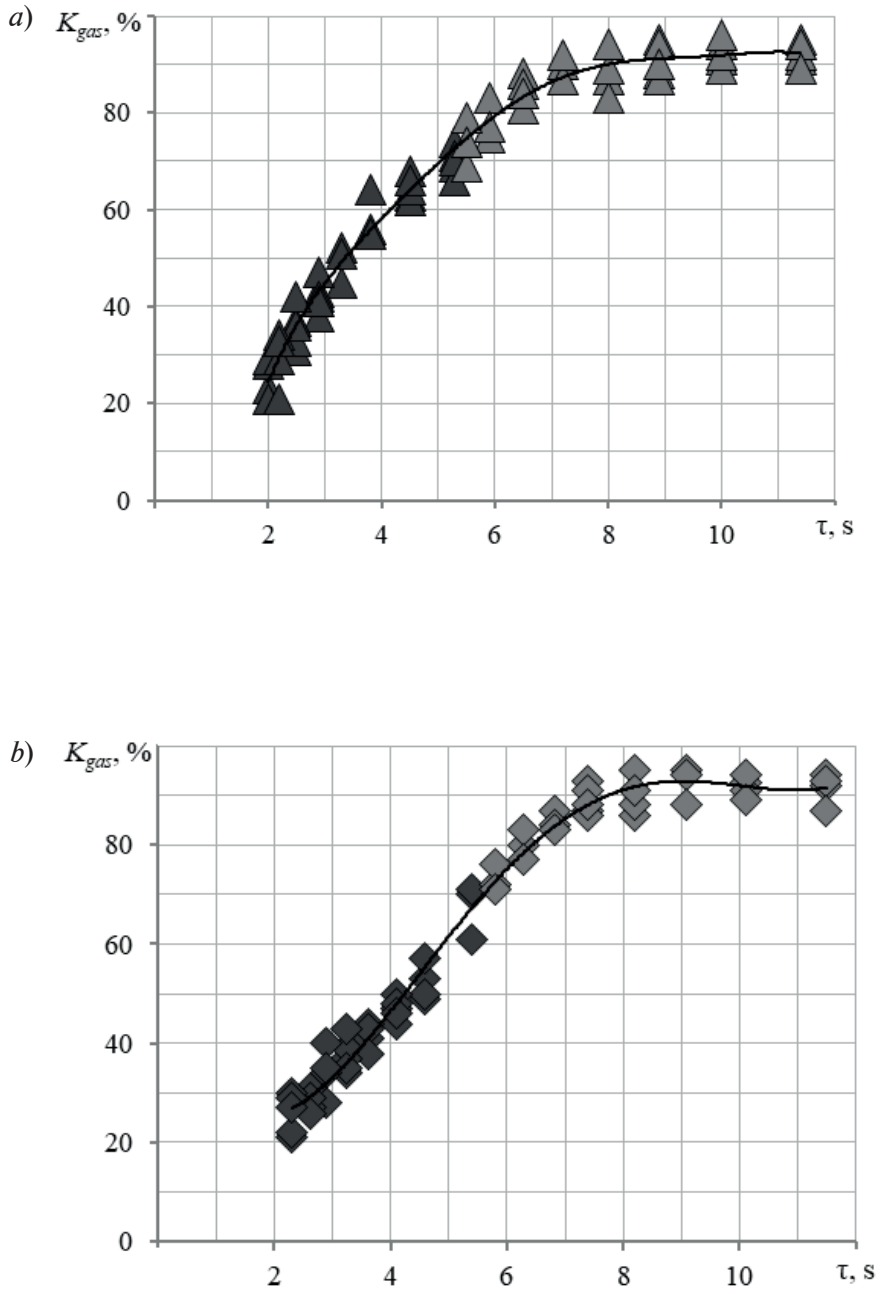

Fig. 5. Dependences K_{gas} for conversion of water vapor (*wv*) with vaporized aqueous HF solution supplied to the high-temperature graphite layer as function of the time that *wv* stays outside the oxygen zone, in the layer with temperatures above 1000 K; HF content in solution was 40% (*a*) and 72% (*b*); data for positions I (black symbols) and II (light gray symbols) of nozzle are given (see Fig. 2)

Conclusion

Based on the laboratory experiments that we have conducted, we have established the following.

The presence of hydrogen fluoride has almost no effect on the rate of reaction for interaction of water vapor with carbon at temperatures above 1000 K.

The characteristic time of contact of water vapor with a fixed graphite layer at temperatures above 1000 K in the presence of hydrogen fluoride with 90% water vapor conversion is about 10 s.

The method of high-temperature interaction of water vapor with carbon can lay the groundwork for industrial technology for dehydration of aqueous solutions of hydrogen fluoride, including azeotropic.

REFERENCES

[1] **J.M. Borgard, F. Herbelet, B. Gwinner,** Recycling hydrofluoric acid in the nuclear industry: The overazeotropic flash process (OVAF), Journal of Fluorine Chemistry. 185 (May) (2016) 17–23.

[2] **B. Morel, B. Duperret,** Uranium and fluorine cycles in the nuclear industry, Journal of Fluorine Chemistry. 130 (1) (2009) 7–10.

[3] **N.S. Turayev, I.I. Zherin,** Khimiya i tekhnologiya urana [Chemistry and technology of uranium], Atominform, Moscow, 2005.

[4] **B.N. Maksimov, V.G. Barabanov, I.L. Serushkin, et al.,** Promyshlennyye ftororganicheskiye produkty [Industrial fluororganic products], Khimiya, Leningrad, 1996.

[5] **V.A. Zaytsev, A.A. Novikov, V.I. Rodin,** Proizvodstvo ftoristykh soyedineniy pri pererabotke fosfatnogo syrya [Production of fluoride compounds in the processing of phosphate raw materials], Khimiya, Moscow, 1982.

[6] **P.P. Korostelev,** Reaktivy dlya tekhnicheskogo analiza [Reagents for technical analysis], Metallurgiya, Moscow, 1988.

[7] **N.V. Troyan, V.A. Ryabin, A.I. Timoshenko, et al.,** Kinetika obrazovaniya biftorida natriya [Sodium bifluoride formation kinetics] Tsvetnyye metally. 8 (1985) 71–73.

[8] **T. Dahlke, O. Ruffiner, R. Cant,** Production of HF from H_2SiF_6, Procedia Engineering. 138 (2016) 231–239.

[9] **D.S. Pashkevich, Yu.I. Alekseyev, V.B. Petrov, et al.,** Stabilnost ftorida vodoroda v vysokotemperaturnoy zone vosstanovleniya vody uglerodom [Stability of hydrogen fluoride in the high-temperature zone of water reduction by carbon], Khimicheskaya promyshlennost. 92 (5) (2015) 211–220.

[10] **S.D. Fedoseyev, A.B. Chernyshev,** Polukoksovaniye i gazifikatsiya tverdogo topliva [Semicoking and gasification of solid fuel], Gostoptekhizdat, Leningrad, 1960.

[11] **B.V. Kantorovich,** Osnovy teorii goreniya i gazifikatsii tverdogo topliva [Fundamentals of the theory of combustion and gasification of solid fuel], SA of the USSR, Moscow, 1958.

[12] **V.P. Mikheyev,** Gazovoye toplivo i yego szhiganiye [Gas fuel and its combustion], Nedra, Leningrad, 1966.

Received 01.10.2018, accepted 29.12.2018.

THE AUTHORS

KAPUSTIN Valentin V.
Peter the Great St. Petersburg Polytechnic University
29 Politechnicheskaya St., St. Petersburg, 195251, Russian Federation
Valentin.Kapustin.2014@yandex.ru

PASHKEVICH Dmitrii S.
Peter the Great St. Petersburg Polytechnic University
29 Politechnicheskaya St., St. Petersburg, 195251, Russian Federation
pashkevich-ds@yandex.ru

MUKHORTOV Dmitrii A.
FSUE RSC "Applied Chemistry"
26A Krylenko St., St. Petersburg, 193232, Russian Federation
dmukhortov@mail.ru

PETROV Valentin B.
FSUE RSC "Applied Chemistry"
26A Krylenko St., St. Petersburg, 193232, Russian Federation
valentinpetrov46@mail.ru

ALEXEEV Yury I.
«New Chemical Products» Ltd.
11 Moyka River Emb., St. Petersburg, 191186, Russian Federation
alexeev-588@yandex.ru

СПИСОК ЛИТЕРАТУРЫ

1. **Borgard J.M., Herbelet F., Gwinner B.** Recycling hydrofluoric acid in the nuclear industry: The overazeotropic flash process (OVAF) // Journal of Fluorine Chemistry. 2016. Vol. 185. May. Pp. 17–23.

2. **Morel B., Duperret B.** Uranium and fluorine cycles in the nuclear industry // Journal of Fluorine Chemistry. 2009. Vol. 130. No. 1. Pp. 7–10.

3. **Тураев Н.С., Жерин И.И.** Химия и технология урана. М.: ЦНИИ Атоминформ, 407 .2005 с.

4. **Максимов Б.Н., Барабанов В.Г., Серушкин И.Л. Зотиков В.С., Семерикова И.А., Степанов В.П., Сагайлакова Н.Г., Каурова Г.И.** Промышленные фторорганические продукты. Ленинград: Химия, 1996. 544 с.

5. **Зайцев В.А., Новиков А.А., Родин В.И.** Производство фтористых соединений при переработке фосфатного сырья. М.: Химия, 248 .1982 с.

6. **Коростелев П.П.** Реактивы для технического анализа. М.: Металлургия, 384 .1988 с.

7. **Троян Н. В., Рябин В. А., Тимошенко А.И., Шубин А.С., Коробицын А.С., Павлович И.В.** Кинетика образования бифторида натрия // Цветные металлы. 1985. № 8. С. 71–73.

8. **Dahlke T., Ruffiner O., Cant R.** Production of HF from H_2SiF_6 // Procedia Engineering. 2016. Vol. 138. Pp. 231–239.

9. **Пашкевич Д.С., Алексеев Ю.И., Петров В.Б., Мухортов Д.А., Камбур П.С., Капустин В.В., Марков С.А., Ласкин Б.М., Макотченко В.Г.** Стабильность фторида водорода в высокотемпературной зоне восстановления воды углеродом // Химическая промышленность. Т. 2015 .5 № .92. С. 211–220.

10. **Федосеев С.Д., Чернышев А.Б.** Полукоксование и газификация твердого топлива. М.: Гостоптехиздат, 327 .1960 с.

11. **Канторович Б.В.** Основы теории горения и газификации твердого топлива. М: Изд-во АН СССР, 601 .1958 с.

12. **Михеев В.П.** Газовое топливо и его сжигание. Ленинград: Недра, 328 .1966 с.

Статья поступила в редакцию 01.10.2018, принята к публикации 29.12.2018.

СВЕДЕНИЯ ОБ АВТОРАХ

КАПУСТИН Валентин Валерьевич – аспирант кафедры гидродинамики, горения и теплообмена Санкт-Петербургского политехнического университета Петра Великого, Санкт-Петербург, Российская Федерация.

195251, Российская Федерация, г. Санкт-Петербург, Политехническая ул., 29
Valentin.Kapustin.2014@yandex.ru

ПАШКЕВИЧ Дмитрий Станиславович – доктор технических наук, профессор кафедры гидродинамики, горения и теплообмена Санкт-Петербургского политехнического университета Петра Великого.

195251, Российская Федерация, г. Санкт-Петербург, Политехническая ул., 29
pashkevich-ds@yandex.ru

МУХОРТОВ Дмитрий Анатольевич – кандидат технических наук, начальник лаборатории Российского научного центра «Прикладная химия».
193232, Российская Федерация, г. Санкт-Петербург, ул. Крыленко, 26А
dmukhortov@mail.ru

ПЕТРОВ Валентин Борисович – старший научный сотрудник Российского научного центра «Прикладная химия».
193232, Российская Федерация, г. Санкт-Петербург, ул. Крыленко, 26А
valentinpetrov46@mail.ru

АЛЕКСЕЕВ Юрий Иванович – кандидат технических наук, главный конструктор ООО «Новые химические продукты».
191186, Российская Федерация, г. Санкт-Петербург, наб. р. Мойки, 11.
alexeev-588@yandex.ru

DOI: 10.18721/JPM
УДК 534.2

RECORDING TYPHOONS' INFRASONIC DISTURBANCES BY LASER STRAINMETERS

V.A. Chupin, G.I. Dolgikh, E.S. Gusev

V.I. Il'ichev Pacific Oceanological Institute, Vladivostok, Russian Federation

In the paper, the field studies of powerful infrasonic disturbances in the range of «voice of the sea» (7–9 Hz) caused by tropical cyclones (typhoons) in the southeastern region of the Far Eastern Federal District (Russia) and the water area of the Sea of Japan have been presented. Event monitoring was carried out using the laser-interference measuring complex located permanently in the south of Primorski Krai. The dynamic spectrograms of the observable events were analyzed and their connection with various meteorological phenomena, such as wind and sea waves, was traced. Using the satellite data, a connection between the distribution of the area of typhoon influence in the region and the observed infrasound excitation was found. The conclusions were drawn regarding the correlation between the exhibition of the «voice of the sea» microseisms and the initiation of primary and secondary microseisms, as well as the one between the «voice of the sea» microseisms' disappearance and the corresponding end of primary microseisms. No dependence of the signal level on the wind speed in the area of the measuring range location was established.

Keywords: infrasonic wave, laser strainmeter, typhoon, voise of sea

Citation: V.A. Chupin, G.I. Dolgikh, E.S. Gusev, Recording typhoons' infrasonic disturbances by laser strainmeters, St. Petersburg Polytechnical State University Journal. Physics and Mathematics. 12 (1) (2019) 107–116. DOI: 10.18721/JPM.12110

РЕГИСТРАЦИЯ ИНФРАЗВУКОВЫХ ВОЗМУЩЕНИЙ ТАЙФУНОВ ЛАЗЕРНЫМИ ДЕФОРМОГРАФАМИ

В.А. Чупин, Г.И. Долгих, Е.С. Гусев

Тихоокеанский океанологический институт им. В.И. Ильичева
Дальневосточного отделения РАН, г. Владивосток, Российская Федерация

В статье приводится описание натурных наблюдений мощных инфразвуковых возмущений в диапазоне «голоса моря» (7 – 9 Гц), вызванных прохождением тропических циклонов (тайфунов) в юго-восточном районе Дальневосточного федерального округа России и акватории Японского моря. Регистрация каждого события выполняется с помощью лазерно-интерференционного измерительного комплекса, стационарно расположенного на юге Приморского края. Проанализированы динамические спектрограммы наблюдаемых событий и прослежена их связь с метеорологическими явлениями, такими как ветер и морские волны. При использовании спутниковых данных найдена взаимосвязь распределения области влияния тайфунов в регионе с наблюдаемым инфразвуковым возбуждением. Сделаны выводы о взаимосвязи проявления микросейсм «голоса моря» с возникновением первичных и вторичных микросейсм, а также хорошей корреляции между исчезновением микросейсм «голоса моря» и соответствующим прекращением первичных микросейсм. Установлено отсутствие зависимости уровня сигнала от скорости ветра в области расположения измерительного полигона.

Ключевые слова: инфразвуковая волна, лазерный деформограф, тайфун, голос моря

Ссылка при цитировании: Чупин В.А., Долгих Г.И., Гусев Е.С. Регистрация инфразвуковых возмущений тайфунов лазерными деформографами // Научно-технические ведомости СПбГПУ. Физико-математические науки. 2018. Т. 12. № 1. С. 117–127. DOI: 10.18721/JPM.12110

Introduction

Cape Shultz is a Marine Experimental Station of the V.I. Il'ichev Pacific Oceanological Institute of the Far Eastern Branch of the Russian Academy of Sciences (POI FEB RAS) that is constantly monitoring a whole range of indicators of the seismo-acoustic and hydrological cycles. The station records variations in the deformation of the Earth's crust (using coastal laser strainmeters), variations in atmospheric pressure (using laser nanobarographs), variations in hydrospheric pressure (using special laser meters) and variations in wind speed (at the meteorological station). Processing of synchronized experimental data for these phenomena revealed low-frequency seismo-acoustic disturbances in the range of 7–9 Hz (the frequency band of the so-called "voice of the sea") in coastal areas of Primorsky Krai.

Excitation of seismic signals in this frequency range is associated with tropical cyclones passing near the measurement site. These natural phenomena significantly affect the life of the Far Eastern Region of the Russian Federation.

The voice of the sea, i.e., high-frequency infrasound (in the range from a few to tens and more Hz) was first hypothesized to exist in [1], suggesting that the mechanism for this phenomenon was wind flowing around large ocean waves. An alternative mechanism by which this infrasound might occur was proposed in [2], where acoustic noise from sea waves crashing on rocky shores was considered. Ref. [3] argued that infrasound was generated by standing surface waves and that the resulting stratification of such properties of the atmosphere as wind speed and temperature affected the given parameters of infrasonic waves. Such standing waves are formed through non-linear interaction between progressive surface waves.

Numerous studies, including [4], recorded primary and secondary microseisms resulting from progressive and standing sea waves acting on the ocean floor. The mechanism of generation of secondary microseisms, i.e., small-amplitude oscillations of the Earth's surface with the period equal to the half-period of progressive sea waves, was described in [5]. Similar acoustic signals in the atmosphere were called microbaroms [6], and the theory describing the conditions in which they occur was developed in [7–9]. Microbaroms and secondary microseisms are formed as a result of non-linear effects from interaction of two progressive counter-propagating sea waves with a double period. Experimental data related to storms were analyzed in [10], suggesting that microbaroms and secondary microseisms have the same source. Deformation disturbances caused by a passing typhoon and lying in the frequency range of the voice of the sea were reported for the first time in [11].

These natural phenomena present a serious threat, which is why comprehensive study of the physics of such processes, as well as study of their dynamic features are very urgent tasks.

Measuring system and experimental data

This paper discusses both our own experimental data and those obtained by Japanese researchers. We collected and studied the following information:

Studies of the Japan Meteorological Agency on movement of tropical cyclones for 2010–2018 [12];

images from the Japanese satellite Himawari-8 [13], which make it possible to visually monitor the region of distribution of the cyclonic vortex with an accuracy up to 1 h;

results of our measurements using a laser strainmeter;

experimental data from our meteorological station.

Variations in the deformation of the Earth's crust were recorded using laser strainmeters from a hardware and software system located at the Cape Schultz site of POI FEB RAS. The system was deployed to study the origin, evolution and transformation of oscillations and waves in sound and infrasound ranges, their interaction with each other and with geospheric inhomogeneities of different scales [14].

Two laser strainmeters were located at Cape Shultz, Sea of Japan. Coordinates of the objects were 42.58°N, 131.157°E. These two devices were positioned so that they represented a two-coordinate laser strainmeter with (almost) mutually perpendicular measuring arms [15]. Each strainmeter was assembled by the unequal-arm Michelson scheme using a frequency-stabilized helium-neon laser. One of the strainmeters had a 52.5 m long measuring arm and was oriented north-south at an angle of 18° (198°); the other was 17.5 m long and was oriented north-south at an angle of 110° (290°). The first one was located at a depth of 3–5 m from the Earth's surface in a hydrothermally isolated room 67 m above sea level,

and the second at a distance of 70 m from the first one at a depth of 3–4 m from the Earth's surface. The angle between the measuring arms of the strainmeters was 92°. The interferometric methods used allow to record the variation in length l of the measuring arm of each strainmeter with an accuracy $\Delta l = 0.01$ nm in the frequency range from 0 (roughly) to 1000 Hz. The sensitivity of the laser strainmeter with an arm length $l = 52.5$ m is $\Delta l/l \approx 0.2 \cdot 10^{-12}$, and that of a laser strainmeter with an arm length $l = 17.5$ m is approximately $0.6 \cdot 10^{-12}$.

Air temperature and humidity, atmospheric pressure, wind speed and direction are measured at the meteorological station. Data on variations of these quantities are recorded with a resolution of 1 Hz.

The readings from laser strainmeters and from the meteorological station are submitted to the laboratory room, where preliminary processing (filtering and downsampling) of the obtained data is performed, the information is then recorded on physical media of the hardware and software system with an experimental data base subsequently organized.

We have initially analyzed the database of typhoons in the northwestern Pacific Ocean that directly affected the Far Eastern region of Russia. We have selected four typhoons as typical examples of these effects. The names of the typhoons and the time intervals for their duration are given in Table. Based on the data of the Japan Meteorological Agency, we have compiled a composite map for the tracks of the given typhoons (Fig. 1), indicating the semi-daily time intervals of their movement in Japan Standard Time (JST), which corresponds to UTC+09, i.e., +9 hours relative to Universal Time Coordinated.

As follows from Fig. 1, the tracks of the given typhoons passed near the measurement site and generated the observed seismo-acoustic disturbances in the range of the "voice of the sea". Images from the Japanese satellite Himawari-8 were used to visually monitor the location of the "eyes" of the typhoons, their leading edges and "tails".Experimental data and analysis

We used data from one laser strainmeter as the most representative, as well as the measured variations in the magnitude of wind speed obtained at the meteorological station. Processing the readings from the strainemeter for the given observation periods, we obtained spectrograms of the "voice of the sea" range were obtained (Fig. 2). Spectrograms of the range of microseisms induced by sea wind waves and ripple acting on the seabed were also obtained (Fig. 3). Fig. 4 shows data on the variation in wind speed in the given observation periods.

Below we have analyzed the data provided for each typhoon in Fig. 1–4 in detail. Images from the Japanese satellite Himawari-8 were also used.

Typhoon Bolaven (B). According to the data from the strainmeter, noise in the range of 1.0–2.5 Hz, as well as narrow-band oscillations with central frequencies around 5.3, 9.1 and 107 Hz occurred at 03:25 UTC on August 28. The "eye" of the typhoon was located in the Yellow Sea and extended to the Korean Peninsula. South/southwest wind at the speed of 1–2 m/s was recorded at Cape Schulz

After noise first appeared, its range gradually expanded to 1.0–4.5 Hz, with an increase in signal levels, and reached its maximum at 2:53 pm (August 28). Amplification of oscillations with central frequencies of 9.1 and 10.7 Hz was observed. The typhoon then tracked over Primorsky Krai (Russia), with its strong tail located in the north of the Yellow Sea; thick tails of the typhoon were located above the Sea of Japan. The wind changed to southeast at Cape Shultz, acquiring a speed of 14–16 m/s.

Table

Time intervals used for processing observation data for typhoons

Notation	Name of typhoon	Period of time
B	Bolaven	28.08. 2012–31.08.2012
S	Sanba	17.09. 2012–31.08.2012
M	Matmo	26.07. 2014–27.07. 2014
Ch	Chan-hom	12.07. 2015–15.07.2015

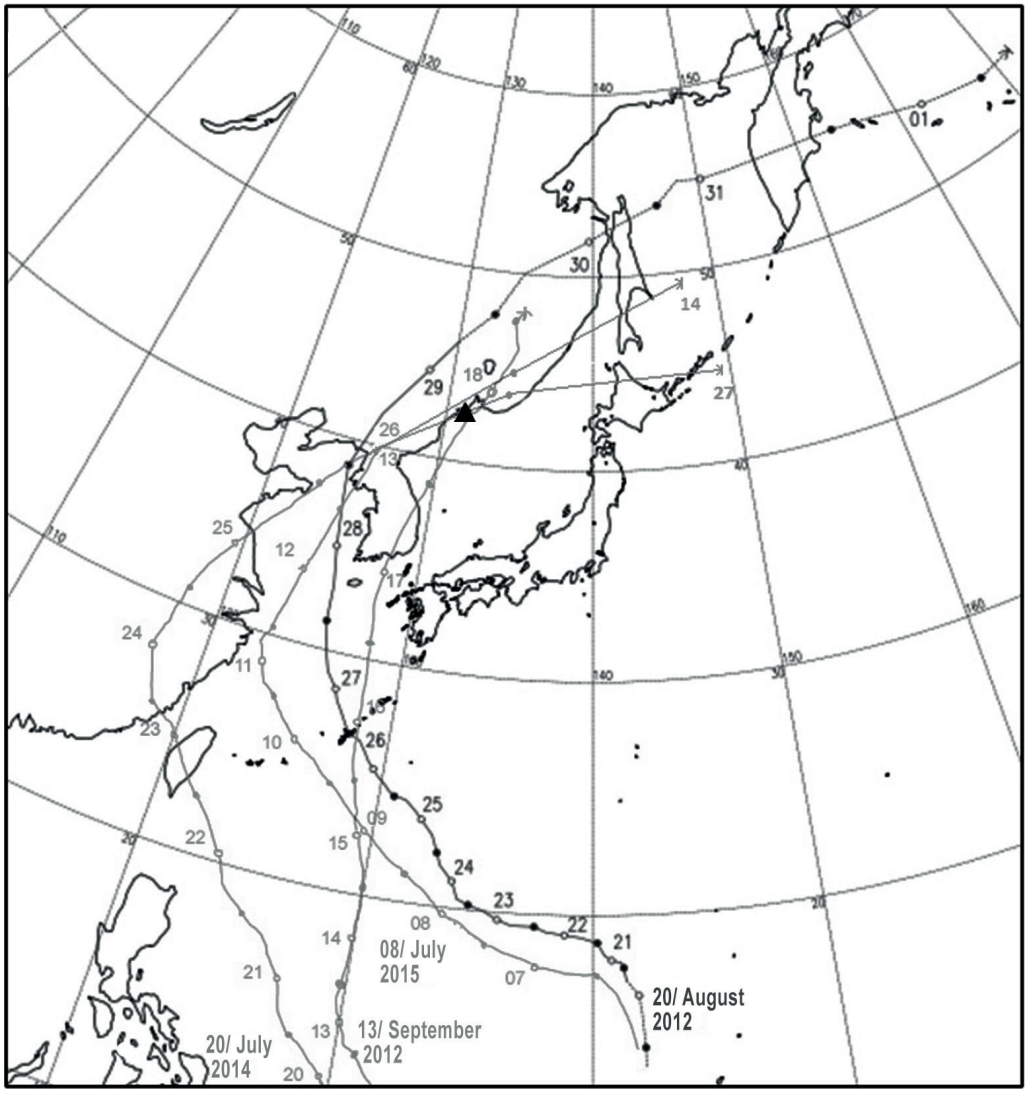

Fig. 1. Composite map of trajectories of given typhoons compiled based on data from Japan Meteorological Agency.
The figure shows the semi-daily time intervals of typhoon movement by Japanese Standard Time (JST), the numbers correspond to the recording dates (see Table and explanations in the text); the triangle indicates the location of the survey site.

The noise level remained constant in the range of 1.0–4.5 Hz until 19:26 on August 28. The intensity of signals with the same central frequencies (9.1 and 10.7 Hz) then either amplified or attenuated periodically. The main, central part of the typhoon nearly left Primorsky Krai, moving to China and Khabarovsk Krai. Only a small tail of the typhoon remained in the south of Primorsky Krai and in the northeast of the Sea of Japan. Southeast wind at a speed of 16–18 m/s was recorded at Cape Schulz.

The noise level kept falling until 22:10 on August 28, its frequency range of 1.0–4.5 Hz narrowed back to 1.0–2.5 Hz. The level of oscillations with central frequencies of 9.1 and 10.7 Hz decreased, however, strong oscillations occurred in the frequency range of 6.5–9.3 Hz with a central frequency of about 8.0 Hz (referred to as the "voice of the sea" microseisms below). The typhoon remained in the north of Primorsky Krai, China and Khabarovsk Krai. Tails of the typhoon tracked to the east and northeast of the Sea of Japan. However, a strong leading edge of another typhoon, whose "eye" was located over Taiwan,

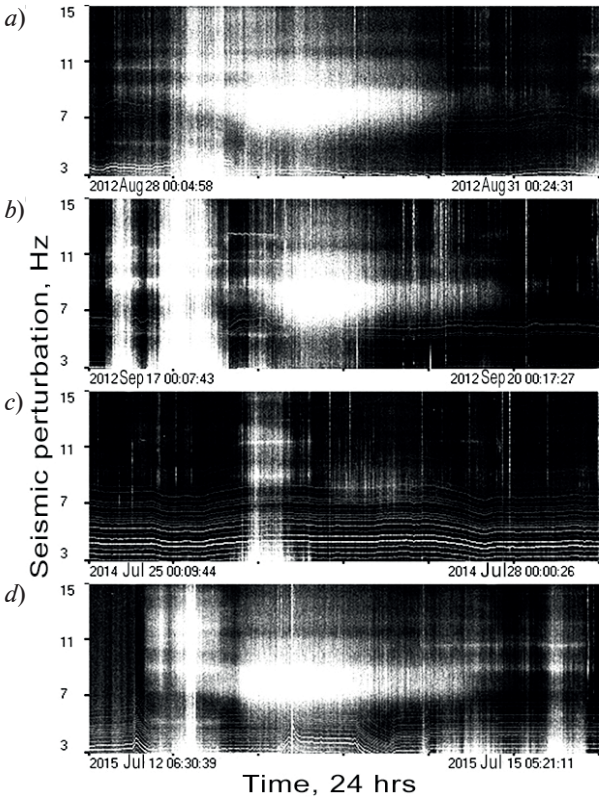

Fig. 2. Spectrograms (dynamics of seismo-acoustic disturbances) for "voice of sea" range, obtained using coastal laser strainmeter, for typhoons B (*a*), S (*b*), M (*c*) and Ch (*d*) (see Table)

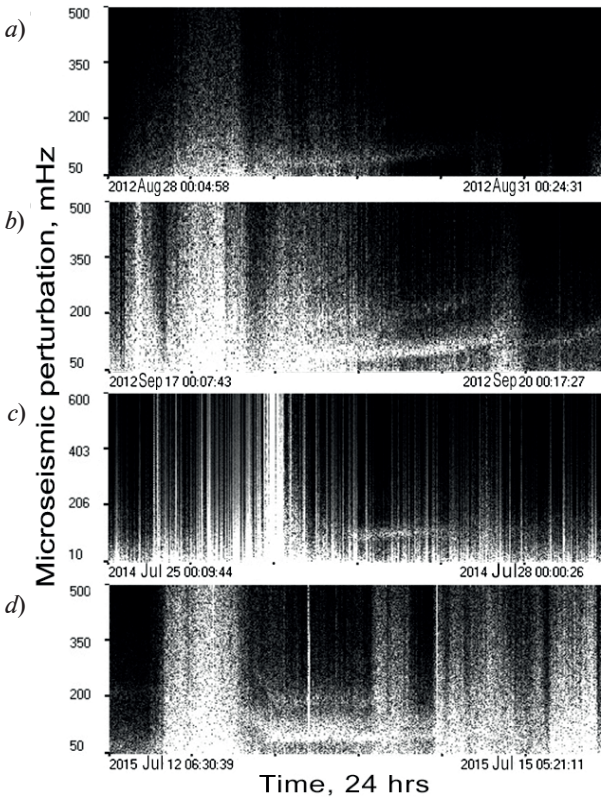

Fig. 3. Spectrograms (dependences of variation in sea disturbance over time) for range of microseisms caused by impact of sea wind waves and ripple, obtained using coastal laser strainmeter, for typhoons B (*a*), S (*b*), M (*c*) and Ch (*d*) (see Table)

penetrated the Sea of Japan from the Korean Peninsula. Southeast wind at a speed of 20–25 m/s was blowing at Cape Schulz.

The widest frequency range of the sea voice microseism was reached at 06:00 on August 29 (6.5–9.5 Hz, white core). At that time, the typhoon raged over China, Mongolia, and the Khabarovsk Krai. Primorsky Krai was almost entirely outside the zone of the typhoon. Small tails were observed off the Japanese coast and in the north of the Sea of Japan. The strongest southeast wind at a speed of 33 m/s was recorded at Cape Schulz.

The main core of the sea voice microseism was not observed at 18:00 on August 29. Both the Primorsky Krai and the Sea of Japan were outside the typhoon zone. The eye of a new typhoon was observed in the south of the Yellow Sea; its leading edge tracked over the Korean Peninsula. West wind with a speed of 8–10 m/s was blowing at Cape Schultz.

Low-frequency noise was not recorded in the range of 1.0–2.5 Hz. The intensity of oscillations in the range of 6.5–9.3 Hz decreased with time, the oscillation frequency range also narrowed to 7.5–8.5 Hz. The given oscillations almost completely attenuated by 23:30 on August 30. The typhoon was located in the Sea of Okhotsk. Northwest wind at a speed of 2–4 m/s was blowing at Cape Schulz.

The laser strainmeter readily recorded the primary and secondary microseisms. Primary microseisms with a period of about 12 s were first recorded by the device at approximately 23:00 on August 28, and their period then gradually decreased to 5 s (20:30 on August 30). Secondary microseisms with a period of about 6 s were readily recorded by the strainmeter at about the same time (11:00 pm on August 28). The period and intensity of secondary microseisms gradually decreased, and they were virtually absent in the recordings from 00:30 on August 30. Up to this point, their period was about 4 s, while the period of primary microseisms was about 8 s.

Thus, the moment when strong oscillations occurred in the frequency range of 6.5–9.3 Hz almost coincided with the time when strong

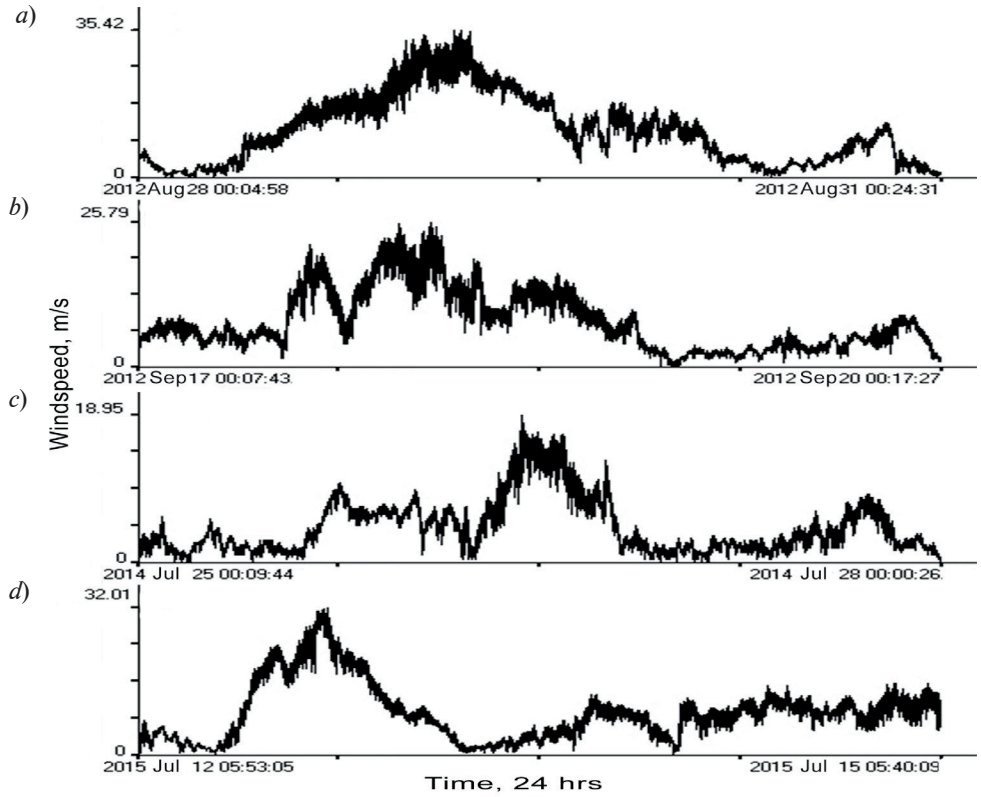

Fig. 4. Variations in wind speed over time.
Experimental data were obtained at meteorological station
for typhoons B (*a*), S (*b*), M (*c*) and Ch (*d*) (see Table)

primary microseisms evolved. The period and intensity of primary microseisms were reduced and barely recorded by the device starting from 20:30 on 30 August. Somewhat later (23:30), practically no oscillations were recorded in the range of 7.5–8.5 Hz. Notably, the speed range of the local wind for the same observation period (August 28, 10:10–August 30, 23:30), i.e., during the period when sea voice microseisms appeared and disappeared, increased from 20–25 to 32–33 m/s, and then gradually dropped to 2–4 m/s. The widest frequency range of sea voice microseisms was observed at 6:00 on August 29. Only typhoon tails were recorded at Cape Schulz during the same period of observations.

Typhoon Sanba (S). Noise increased at 02:20 on September 17, leading to an increase in all spectral components and expanded individual frequency ranges. For example, the range from 1.0–2.5 Hz gradually expanded to 1.0–4.5 Hz. Oscillations were observed in narrow frequency ranges with central frequencies of 9.1, 10.7, and 11.3 Hz. At 11:00 on the same day, the eye of the typhoon tracked to the south of the Korean Peninsula. The leading edge of the typhoon covered the entire Korean peninsula, Primorsky Krai, north and northwest of the Sea of Japan, Sakhalin and Sea of Okhotsk, expanding to Kamchatka. As the noise level reduced, the intensity of these disturbances fell and almost disappeared at 07:15 on September 17. At 07:00 the typhoon's eye tracked to the north of the Korean Peninsula. Northeast wind at a speed of 6–8 m/s was blowing at Cape Schulz (2:20).

Noise with a central frequency of 5.3 Hz appeared at 08:20 on September 17. The eye of the typhoon was localized on the shelf of the Sea of Japan, off the coast of South Korea. The leading edge of the typhoon covered Primorsky Krai, Sakhalin, the Sea of Okhotsk, Kamchatka, the northern and western parts of the Sea of Japan. Northeast wind at a speed of 5–6 m/s was blowing at Cape Schulz.

The main zone of the typhoon moved to Khabarovsk Krai, China, Mongolia, the north and the central part of Primorsky Krai at 20:00 on September 17. The eye of the typhoon left the south of Primorsky Krai. A tail of the typhoon

was observed in the center of the Sea of Japan; only a small tail remained on the shelf of the Korean Peninsula. Northeast wind at a speed of 13–16 m/s was rising at Cape Schultz.

Noise in the range of 1.0–4.5 Hz and oscillations in narrow bands with central frequencies of 5.3, 9.1 and 10.7 Hz appeared at 22:35 on September 17. Oscillations with a central frequency of 11.3 Hz were weak. The typhoon nearly left Primorsky Krai. The eye of the typhoon was located on Sakhalin. A tail at the center of the Sea of Japan and a smaller one off the coast of the Korean Peninsula were observed. Northeast wind at a speed of 20–23 m/s was raging at Cape Schultz.

Microseisms of the voice of the sea appeared about 00:10 on September 18; the frequency range at its maximum was from 6.0 to 9.5 Hz with a central frequency (by intensity) of 8 Hz. Oscillations of the sea voice microseism were strongly attenuated by 18:00 on September 18 and were almost untraceable until 10:00 on September 19 (their central frequency was about 8.5 Hz). The locations of the typhoon's eye and its leading edge were almost unchanged, and its tail was in the center of the Sea of Japan. A weak tail of the typhoon extended along the coast of the Korean Peninsula with access to Cape Schulz. A small atmospheric depression was observed in the Yellow Sea, reaching the south of Primorsky Krai through the north of the Korean Peninsula. Northeast wind at a speed of 18–21 m/s (00:10), then northwest wind at a speed of 6–9 m/s (September 18, 18:00) and then north wind at a speed of 3–4 m/s (September 19, 10:00) was blowing at Cape Schultz.

The central part of the sea voice microseism reduced in intensity at 18:00 on September 18. The tail of the typhoon covered the north of the Korean Peninsula, the southern coasts of Primorsky Krai and the Sea of Japan near Korea; this tail subsequently disintegrated, forming a whirlwind. The front of the new typhoon spread through the island of Hokkaido to the north and then to the island of Sakhalin.

Virtually no sea voice microseisms were detected at 10:00 on September 19.

Strong primary microseisms with a period of about 12 s and secondary microseisms with a period of about 6 s appeared at about 23:30 on September 17. Their period then decreased. Secondary microseisms were barely recorded by the laser strainmeter around 03:50 on September 20. Their period fell to 4.2 s, and the period of primary microseisms at that time was about 8.5 s. The amplitude of primary microseisms recorded by the laser strainmeter at 07:30 on September 19 was greatly decreased. Their period was equal to about 7.5 s.

Thus, the time when the sea voice microseisms occurred (00:10, September 18) nearly coincided with the time when the primary microseisms with a maximum period of 12 s arrived (23:30, September 17). Secondary microseisms had a maximum period of 6 s. The wind speed at Cape Schultz was about 18–21 m/s. Sea voice microseisms greatly attenuated by 18:00 on September 18. The wind speed dropped to 6–9 m/s by this time. The sea voice microseisms attenuated completely by 10:00 on September 19. The wind speed dropped to 2–3 m/s at Cape Schultz. The frequency of primary microseisms decreased to 7.5 Hz and was poorly detectable by 7:30 on September 19. Secondary microseisms were not observed.

Typhoon Matmo (M). The weakest manifestations of the given signals in the low-frequency range could be observed on the spectrograms of infrasound disturbances generated by this typhoon, starting to evolve on July 26, 2014 around 10:00 and having approximately the same intensity during the entire time interval that these signals were observed. The center of the typhoon was in the Sea of Japan near Hokkaido at 45°N during this period. Peak frequency was 7.8 Hz. The disturbances attenuated completely at 23:00 on July 26.

Typhoon Chan-hom (Ch). Noise in the range of 1.0–2.5 Hz appeared at 15:00 on July 11. The eye of the typhoon was located in the south of the Yellow Sea, its front occupied the Korean Peninsula and extended to the south of Primorsky Krai. South wind at a speed of 6–8 m/s was blowing at Cape Schultz.

The noise in the range of 1.0–2.5 Hz amplified and expanded to the range of 1.0–4.5 Hz at 14:00 on July 12. The eye of the typhoon covered the north of the Korean Peninsula, and its leading edge (whirlwind) extended from the north of the Yellow Sea to China, Khabarovsk Krai, Primorsky Krai and the center of the Sea of Japan, passing through the southern islands of Japan to the Pacific Ocean. Southeast wind at a speed of 10–12 m/s was blowing at Cape Schultz.

Noise in the frequency range of 1.0–4.5 Hz continued at 14:30 on July 12. Oscillations with central frequencies of 5.3, 9.1 and 10.7 Hz were observed. Southeast wind increased to a

speed of 15–19 m/s at Cape Schultz.

The eye of the typhoon was in the south of Primorsky Krai at 17:20 on July 12. The typhoon did not affect the Sea of Japan along the coast of the Korean Peninsula. Southeast wind at a speed of 17–20 m/s was raging at Cape Schultz.

Strong sea voice microseisms were observed in the frequency range from 7 to 9 Hz at 02:50 on July 13 (no other oscillations were observed). The frequency range of the sea voice microseism then rapidly expanded to 6–11 Hz (06:00 on July 13). The frequency range of the sea voice microseism narrowed to 7–9 Hz and disappeared at 10:00 on July 14. The eye of the typhoon was located in the north of Primorsky Krai, while the center, south and west of the Sea of Japan were not covered by the typhoon. The tail of the typhoon extended in an arc across the Yellow Sea, the Korean Peninsula, the center of Primorsky Krai, the eastern part of the Sea of Japan and the Japanese Islands and moved south into the Pacific Ocean. Southeast wind at a speed of 9–11 m/s was blowing at Cape Schultz.

Weak signals with center frequencies of 9.1 and 10.7 Hz appeared at 04:20 on July 14. The tail of the typhoon was located in the north of the Primorsky Krai, while the south of the Primorsky Krai was not covered by the typhoon. Northwest wind at a speed of 9–11 m/s was blowing at Cape Schultz.

The weak background of the sea voice microseism completely disappeared at 23:18 on July 14. The typhoon left the Primorsky Krai and the Sea of Japan. A slight atmospheric depression extended in the Sea of Japan along the Korean Peninsula. Northeast wind at a speed of 8–11 m/s was blowing at Cape Schultz.

The signals with the central frequencies of 9.1 and 10.7 Hz disappeared at 03:45 on July 15 but the signals with the central frequencies of 9.1 Hz reappeared from time to time. The atmospheric situation remained virtually unchanged. Northeast wind at a speed of 10–14 m/s was blowing at Cape Schultz.

The strainmeter recorded primary microseisms with a period of about 7.2 s and secondary microseisms with a period of about 3.7 s at about 03:00 on July 13. Their periods gradually increased with time, and reached, respectively, 10.5 and 5.3 s at about 05:30 on July 13. They were readily detected by the strainmeter, and their periods remain unchanged until 8:00 pm on July 13. The secondary microseisms then disappeared in the noise, while the primary ones with a period of about 10 s could be detected until 04:30 on July 14. Their period was slightly reduced to 9.3 s by this time.

Thus, the time when the sea voice microseisms appeared (July 13, 02:50) almost coincides with the time when the primary microseisms with a maximum period of 7.2 seconds arrived (03:00 on July 13). The toric period microseisms are characterized with 3.7.The wind speed at Cape Schultz was about 9–11 m/s. The frequency range of the sea voice microseism then rapidly expanded to 6–11 Hz (06:00 on July 13), which is associated with an increase in the periods of primary and secondary microseisms. The periods of these microseisms reached 10.5 and 5.3 s, respectively, by 05:30 on July 13. Secondary microseisms could not be detected at all around 20:00 on July 13. Primary microseisms were readily detected by the laser strainmeter until 04:30 on July 14. Sea voice microseisms disappeared at about 10:00 on July 14.

Conclusion

Analysis of the data we have obtained for each typhoon, as well as images from the Japanese satellite Himawari-8 allowed us to draw the following conclusions.

The time when sea voice microseisms were recorded with a laser strainmeter almost exactly (taking into account the complexity of visual detection by spectrograms) coincides with the time when primary and secondary microseisms were obtained with the same device.

Disappearance of sea voice microseisms is well correlated with the disappearance of primary microseisms and is poorly correlated with the disappearance of secondary microseisms.

The moment when the wind reaches maximum speed does not always coincide in time with the moment when the maximum microseisms of the sea voice are observed.

The study was carried out with partial financial support from the Russian Foundation for Basic Research (Grant no. 18-05-80011 “Dangerous Phenomena”) and the Program “Far East”.

REFERENCES

[1] **V.V. Shuleykin,** O golose morya [On the voice of the sea], Doklady of the USSR Academy of Sciences. 3 (8) (1935) 259–263.

[2] **M. Garces, J. Aucan, D. Fee, et al.,** Infrasound from large surf, Geophys. Res. Lett. 33 (2006) L05611(1–4).

[3] **V.G. Perepelkin, S.N. Kulichkov, I.P. Chunchuzov, I.A. Repina,** On experience in recording the voice of the sea in the water area of the Black Sea, Izvestiya. Atmospheric and Oceanic Physics. 51 (6) (2015) 716–728.

[4] **G.I. Dolgikh, S.G. Dolgikh, S.N. Kovalev, et al.,** Experimental estimate of a relation between sea wave energies and the Earth's crust microdeformations, Acta Geophysica. 55 (4) (2017) 607–618.

[5] **M.S. Longuet-Higgin,** A theory of the origin of microseism, Phil. Trans. R. Soc. London, Ser. A: Math. Phys. Sci. 243 (857) (1950) 1–35.

[6] **H. Benioff, B. Gutenberg,** Waves and currents recorded by electromagnetic barographs, Bull. Am. Meteorol. Soc. 20(10) (1939) 421–426.

[7] **E.S. Posmentier,** A theory of microbaroms, Geophys. J. R. Astron. Soc. 13 (1967) 487–501.

[8] **L.M. Brekhovskikh, V.V. Goncharov, V.M. Kurtepov, K.A. Naugolnykh,** The radiation of infrasound into the atmosphere by surface waves in the ocean, Izv. Acad. Sci. USSR, Atmos. Oceanic Phys. 9(9) (1973) 899–907.

[9] **R. Waxler, K.E. Gilbert,** The radiation of atmospheric microbaroms by ocean waves, J. Acoust. Soc. Am. 119 (5) (2006) 2651–2664.

[10] **W.L. Donn, B. Naini,** Sea wave origin of microbaroms and microseisms, J. Geophys. Res. 78 (21) (1973) 4482–4488.

[11] **G.I. Dolgikh, E.S. Gusev, V.A. Chupin,** The nature of the "Voice of the sea", Doklady Earth Sciences. 481 (1) (2018) 912–915.

[12] Data of the Japan meteorological agency on the movement of tropical cyclones for 2010–2018, URL: http://www.jma.go.jp/jma/jma-eng/jma-center/rsmc-hp-pub-eg/besttrack_viewer_2010s.html.

[13] Himawari 8 Data Archive, GMS/GOES9/MTSAT Data Archive for Research and Education, URL: http://weather.is.kochi-u.ac.jp/archive-e.html.

[14] **G.I. Dolgikh, V.E. Privalov,** Lazernaya fizika. Fundamentalnyye i prikladnyye issledovaniya [Laser physics. Fundamental and applied research], Dalnauka, Vladivostok (2016).

[15] **G.I. Dolgikh, S.N. Kovalev, I.A. Koren, V.V. Ovcharenko,** A two-coordinate laser strainmeter, Izvestiya, Physics of the Solid Earth. 34 (11) (1998) 946–950.

Received 14.11.2018, accepted 28.11.2018.

THE AUTHORS

Chupin Vladimir A.
V.I. Il'ichev Pacific Oceanological Institute
43 Baltiyskaya St., Vladivostok, 690041, Russian Federation
chupin@poi.dvo.ru

Dolgikh Grigory I.
V.I. Il'ichev Pacific Oceanological Institute
43 Baltiyskaya St., Vladivostok, 690041, Russian Federation
dolgikh@poi.dvo.ru

Gusev Egor S.
V.I. Il'ichev Pacific Oceanological Institute
43 Baltiyskaya St., Vladivostok, 690041, Russian Federation
gusev.e.s.95@gmail.com

СПИСОК ЛИТЕРАТУРЫ

1. **Шулейкин В.В.** О голосе моря // Доклады Академии наук СССР. 1935. Т. 3. № 8. С. 259–263.

2. **Garces M., Aucan J., Fee D., Caron P., Merrifield M., Gibson R., Bhattacharyya J., Shah S.** Infrasound from large surf // Geophys. Res. Lett. 2006. Vol. 33. L05611. P. 1–4.

3. **Перепёлкин В.Г., Куличков С.Н., Чунчузов И.П., Репина И.А.** Об опыте регистрации «голоса моря» в акватории Черного моря // Известия РАН. Физика атмосферы и океана. 2015. Т. .51 6 №. С. 728–716.

4. **Dolgikh G.I., Dolgikh S.G., Kovalev S.N., Ovcharenko V.V., Chupin V.A., Shvets V.A., Yakh ovenko S.V.** Experimental estimate of a relation between sea wave energies and the Earth's crust mit-crodeformations// Acta Geophysica. 2017. Vol. 55. No. 4. Pp. 607–618.

5. **Longuet-Higgin M.S.** A theory of the origin of microseism // Philosophical Transactions of the Royal Society of London. Ser. A. Mathematical and Physical Sciences. 1950. Vol. 243. No. 857. Pp. 1–35.

6. **Benioff H., Gutenberg B.** Waves and currents recorded by electromagnetic barographs // Bull. Am. Meteorol. Soc. 1939. Vol. 20. No. 10. Pp. 421–426.

7. **Posmentier E.S.** A theory of microbaroms // Geophys. J. R. Astron. Soc. 1967. Vol. 13. Pp. 487–501.

8. **Бреховских Л.М., Гончаров** В.В., Куртепов **В.М., Наугольных К.А.** К вопросу об излучении инфразвука в атмосферу поверхностными волнами в океане // Известия АН СССР. Физика атмосферы и океана. 1973. Т. 9. № 9. С. 899–907.

9. **Waxler R., Gilbert K.E.** The radiation of atmospheric microbaroms by ocean waves // J. Acoust. Soc. Am. 2006. Vol. 119. No. 5. Pp. 2651–2664.

10. **Donn W.L., Naini B.** Sea wave origin of microbaroms and microseisms // J. Geophys. Res. 1973. Vol. 78. No. 21. Pp. 4482–4488.

11. **Долгих Г.И., Гусев Е.С., Чупин В.А.** Деформационные проявления «голоса моря» // Доклады Академии наук. 2018. Т. 1 № .148. С. 95–98.

12. Данные Японского метеорологического агентства о движении тропических циклонов за 2010 – 2018. http://www.jma.go.jp/jma/jma-eng/jma-center/rsmc-hp-pub-eg/besttrack_viewjer_2010s.html.

13. Himawari 8. Data Archive. GMS/GOES9/MTSAT Data Archive for Research and Education. http://weather.is.kochi-u.ac.jp/archive-e.html.

14. **Долгих Г.И., Привалов В.Е.** Лазерная физика. Фундаментальные и прикладные исследования. Владивосток: Дальнаука, 2016. 352 с.

15. Долгих Г.И., **Ковалев С.Н., Корень И.А., Овчаренко В.В.** Двухкоординатный лазерный деформограф // Физика Земли. 1998. № 11. С. 76–81.

Статья поступила в редакцию 14.11.2018, принята к публикации 28.11.2018

СВЕДЕНИЯ ОБ АВТОРАХ

ЧУПИН Владимир Александрович – кандидат физико-математических наук, старший научный сотрудник Тихоокеанского океанологического института им. В.И. Ильичёва Дальневосточного отделения Российской академии наук, г. Владивосток, Российская Федерация.

690041, Российская Федерация, г. Владивосток, Балтийская ул., 43

chupin@poi.dvo.ru

ДОЛГИХ Григорий Иванович – доктор физико-математических наук, заведующий отделом Тихоокеанского океанологического института им. В.И. Ильичёва Дальневосточного отделения Российской академии наук, г. Владивосток, Российская Федерация.

690041, Российская Федерация, г. Владивосток, Балтийская ул., 43

dolgikh@poi.dvo.ru

ГУСЕВ Егор Сергеевич – инженер Тихоокеанского океанологического института им. В.И. Ильичёва Дальневосточного отделения Российской академии наук, г. Владивосток, Россий-д ская Федерация.

690041, Российская Федерация, г. Владивосток, Балтийская ул., 43

gusev.e.s.95@gmail.com

DOI: 10.18721/JPM.12111
УДК 519.63

A POSTERIORI ERROR ESTIMATE FOR REISSNER–MINDLIN PLATES: VERIFICATION OF IMPLEMENTATIONS AND NUMERICAL TESTING

K.V. Kiselev[1], *M.E. Frolov*[1], *O.I. Chistiakova*[1]

[1]Peter the Great St. Petersburg Polytechnic University, St. Petersburg, Russian Federation

A posteriori error estimate for accuracy control of approximate solutions for the problem of Reissner—Mindlin plates bending has been analyzed in the paper. The estimate was constructed using the functional approach based on rigorous mathematical grounds, in particular, on methods of functional analysis. It is valid for all conforming approximations of exact solutions, and therefore, it is robust. The estimate is guaranteed in practical implementations due to reliability of the respective inequality. The above-mentioned properties of the method of error control are very desirable for engineering analysis, where some details of computations might be hidden. Our paper investigated two independent implementations of the estimate. Using specially constructed numerical tests, correctness of both implementation algorithms and similarity of the obtained results for all examples were shown. An overestimation of the true error was established to remain acceptable for a wide range of plate thickness values.

Keywords: a posteriori error estimate, finite element method, Reissner – Mindlin plate

Citation: K.V. Kiselev, M.E. Frolov, O.I. Chistiakova, A posteriori error estimate for Reissner – Mindlin plates: verification of implementations and numerical testing, St. Petersburg State Polytechnical University Journal. Physics and Mathematics. 12 (1) (2019) 117—129. DOI: 10.18721/JPM.12111

ВЫЧИСЛИТЕЛЬНЫЙ ЭКСПЕРИМЕНТ И ВЕРИФИКАЦИЯ РЕАЛИЗАЦИЙ АПОСТЕРИОРНОЙ ОЦЕНКИ ДЛЯ ПЛАСТИН РЕЙССНЕРА – МИНДЛИНА

К.В. Киселев[1], *М.Е. Фролов*[1], *О.И. Чистякова*[1]

[1]Санкт-Петербургский политехнический университет Петра Великого, Санкт-Петербург, Российская Федерация

В работе рассматривается апостериорная оценка точности приближенных решений задачи об изгибе пластин Рейсснера – Миндлина. Оценка построена при помощи функционального подхода, основанного на строгих математических методах, в частности методах функционального анализа. Она справедлива для любых конформных аппроксимаций точных решений, что делает ее надежной. Она также является гарантированной, и неравенство не нарушается при практической реализации. Эти свойства делают данный метод контроля точности решений привлекательным для использования в инженерных расчетах, где некоторые вычислительные детали могут быть скрыты. В статье исследованы две независимые реализации оценки. Использование вычислительного эксперимента показало корректность работы алгоритмов и близость полученных результатов. Установлено, что для широкого диапазона значений толщины степень переоценки истинной величины погрешности остается приемлемой.

Ключевые слова: апостериорная оценка погрешности, метод конечных элементов, пластина Рейсснера – Миндлина

Ссылка при цитировании: Киселев К.В., Фролов М.Е., Чистякова О.И. Вычислительный эксперимент и верификация реализаций апостериорной оценки для пластин Рейсснера – Миндлина // Научно-технические ведомости СПбГПУ. Физико-математические науки. 2019. Т. 12. № 1. С. 128—141. DOI: 10.18721/JPM.12111

Introduction

The study is dedicated to a posteriori control of exact solutions in problems of plate theory, often considered in different engineering computations. Whether the results of the computation are close to the experiment depends on how adequately the selected model describes the real physical processes occurring during deformation of the given object.

In this paper, we have investigated the problem of controlling the accuracy of the finite element method (FEM) for a model of linearly elastic deformable Reissner–Mindlin plates [1]. This model is typically used for plates of small and medium thickness. Unlike the classical Kirchhoff–Love model which describes plates with a small ratio of thickness to characteristic size, the Reissner–Mindlin model makes it possible to consider plates of medium thickness by abandoning the assumption that fibers normal to the midplane of the plates preserve this property upon application of loads.

The system of equilibrium equations for the Reissner–Mindlin model has the following form:

$$\begin{cases} -\mathrm{Div}(C\varepsilon(\theta)) = \gamma, \\ -\mathrm{div}\gamma = g, \\ \gamma := \lambda t^2(\nabla u - \theta), \end{cases} \quad \text{in the region } \Omega, \quad (1)$$

where u is the scalar deflection field of the midplane, θ is the vector field of rotations of the normal to the midplane; γ is the vector field corresponding to the pair (u, θ); ε is the strain tensor; t is the plate thickness; gt^3 is the distributed transverse load; C is a fourth-order symmetric tensor; Ω is the plane region occupied by the plate;

$$\lambda = \frac{1}{2} Ek / (1+\nu)$$

(E is Young's modulus, ν is Poisson's ratio, k is the correction coefficient; $k = 5/6$ is taken in many computations).

There are several well-known commercial packages for performing computations within the framework of this model using FEM. Since products of this type, such as ANSYS (a computing package popular among engineers), are closed-source, it proves impossible to understand in full detail how the necessary computations were performed. As a result, it might be difficult to estimate the magnitude of the error if either the corresponding rigorous mathematical model has not been developed or the error estimate obtained using this model has not been formulated. Substantial deviations from experimental data may also be due to such factors as incorrectly chosen model, errors in applying it, and poor quality of computations with a fairly adequate model.

Thus, an important task is to construct and numerically study an a posteriori estimate for the accuracy of an approximate solution that is guaranteed and robust, i.e., would not allow for underestimation of the error in practical implementation and would not depend on hidden details of the computation procedure.

The first version of such estimate was obtained in [2] based on the functional approach and modified in [3]. The recent results concerning its numerical implementation were reviewed in [4]. The evolution of the functional approach from 1996 to the present can be traced from the sources cited in monographs [5–7] and recently published papers [8, 9]. Reviews of other approaches applied to the given problem can be found, for example, in [10, 11] and the citations therein.

Such a posteriori assessments have the following general form:

$$\| u - \tilde{u} \| \leq \leq M(\tilde{u}, D, \tilde{\tilde{y}}_1, \tilde{\tilde{y}}_2, ..., c_1, c_2, ...), \quad (2)$$

where the norm of deviation of the unknown exact solution u from the obtained approximate solution $\tilde{u}$ is considered on the left-hand side; it is selected based on the problem statement; the functional M that is the deviation majorant is on the right-hand side. The approximate solution $\tilde{u}$, the parameters of the problem D and the set of constants $(c_1, c_2, ...)$ are arguments of the functional. Importantly, the values of these constants depend on the properties of the problem but not on the properties of the partition. Finally, $(\tilde{\tilde{y}}_1, \tilde{\tilde{y}}_2, ...)$ is a set of free elements.

The functional M should satisfy a natural condition that it should give a zero value if and only if the approximate solution coincides with the exact solution.

At the same time, it seems no less important and useful to know not only the magnitude of the global error of the approximate solution but also of the local distribution of the error over the partition elements. This allows to select the regions with the greatest deviation of the approximate solution from the exact one. Next, instead of refining the entire mesh, the necessary improvements are introduced only for elements with large error. This approach is called adaptive; it helps reduce the computational resources it takes to obtain a solution of the desired quality.

Thus, the full cycle of computations using the adaptive approach takes the following form:

initial partition of region →
obtain solution →
estimate global error
(exit from computation cycle
when required accuracy
is reached) →
find regions (3)
with the greatest local
errors → refine mesh
in selected regions →
computation on new mesh →
obtain more accurate solution

This cycle can be applied to solving real engineering problems provided that the properties of the given estimate can be confidently predicted and a set of parameters for which robust results are obtained can be determined.

We have previously obtained (first Frolov, and then Chistiakova, see the review in [4]) two independent implementations of the a posteriori estimate for Reissner–Mindlin plates: in the FORTRAN language and in the MATLAB package. We have conducted an initial study assessing the robustness of the results for each of the algorithms giving a numerical value of the estimate. It is now seems necessary to expand the study of behavior of a posteriori estimates by examining more examples in order to assess whether the correctness of the given tool, the robustness of the results, and lay the foundations for further improving the method.

The goal of this study has consisted in comparative analysis of two implementations for computing the a posteriori estimate of the accuracy of an approximate solution to the Reissner–Mindlin plate bending problem. Analysis includes constructing examples with different specifics, computing different thicknesses and comparing the estimated values as well as the accompanying auxiliary parameters.

Mathematical statement of the problem

Let us consider the system of equations describing the Reissner–Mindlin model for linearly elastic plates of thickness t. The problem is formulated in terms of a scalar function $u = u(x)$ describing the deflection of the midplane at the point x and a vector function $\theta = \theta(x)$ describing the angles of rotation of the normal to the midplane. The midplane initially occupies a bounded simply-connected region $\Omega \subset \mathbb{R}^2$ with a Lipschitz-continuous boundary Γ.

Problem statement: *Find the pair* (u,θ) *and the vector field* $\gamma = \gamma(x)$ *corresponding to this pair, which would satisfy system of equations* (*1*).

The solution is sought in a generalized sense. We assume that $g \in \mathbb{L}_2$, the tensor C is symmetric, there is a pair of constants ξ_1 and ξ_2 such that a two-way estimate holds true:

$$\xi_1 |\kappa|^2 \le C\kappa : \kappa \le \xi_2 |\kappa|^2$$

$\forall \kappa \in \mathbb{M}^{2\times 2}_{\text{sym}}$, $|\kappa|^2 = \kappa : \kappa$, where $\mathbb{M}^{2\times 2}_{\text{sym}}$ is a space of symmetric tensors of rank 2 and dimension 2.

While this study examines plates made of homogeneous isotropic material, this is not a fundamental limitation.

Let us consider the boundary Γ of the dos main Ω, and represent it as two components: Γ_D, $\Gamma_D \neq \varnothing$, where the plate is clamped, i.e., the conditions for the displacement $u = 0$ and rotation $\theta = 0$ are given, and $\Gamma_S = \Gamma \backslash \Gamma_D$, where the plate has free boundary conditions (other types of boundary conditions can be considered as well).

Generalized statement of the problem on Reissner–Mindlin plate bending: *find such a set of three elements* $(u,\theta,\gamma) \in U \times \Theta \times Q$, *where*

$$\begin{cases} U = \left\{\omega \in \mathbb{W}_2^1(\Omega) \mid \omega = 0 \text{ on } \Gamma_D\right\}, \\ \Theta = \left\{\varphi \in \mathbb{W}_2^1(\Omega) \times \mathbb{W}_2^1(\Omega) \mid \varphi = 0 \text{ on } \Gamma_D\right\}, \\ Q = \mathbb{L}_2(\Omega) \times \mathbb{L}_2(\Omega), \end{cases}$$

which satisfies the relations

$$\begin{cases} \int\limits_\Omega C\varepsilon(\theta) : \varepsilon(\varphi) d\Omega - \\ -\int\limits_\Omega \gamma \cdot \varphi \, d\Omega = 0, \ \forall \varphi \in \Theta; \\ \int\limits_\Omega \gamma \cdot \nabla\omega \, d\Omega = \\ = \int\limits_\Omega g\omega \, d\Omega, \ \forall \omega \in U; \\ \int\limits_\Omega (\lambda^{-1} t^2 \gamma - (\nabla u - \theta)) \cdot \tau \, d\Omega = 0, \\ \forall \tau \in Q. \end{cases} \quad (4)$$

The energy functional in the problem has the following form:

$$J(u,\theta) = \int\limits_\Omega \left(\frac{1}{2} C\varepsilon(\theta) : \varepsilon(\theta) + \right. \\ \left. + \frac{1}{2} \lambda t^{-2} |\nabla u - \theta|^2 - gu \right) d\Omega. \quad (5)$$

The corresponding minimization problem is set in the space

$$S := U \times \Theta.$$

Let us proceed directly to the type of the given a posteriori estimate. Let there be a pair of conformal approximations $(\tilde{u}, \tilde{\theta})$ of the exact solution of the problem (u,θ) in S, then the vector field

$$\gamma = \lambda t^{-2}(\nabla u - \theta)$$

is approximated in space Q by the element

$$\tilde{\gamma} = \lambda t^{-2}(\nabla \tilde{u} - \tilde{\theta}).$$

Let us introduce three deviations for each of the solution components:

$$e_{\tilde{u}} = u - \tilde{u},$$
$$e_{\tilde{\theta}} = \theta - \tilde{\theta},$$
$$e_{\tilde{\gamma}} = \gamma - \tilde{\gamma}.$$

Let us then introduce the squared error, expressed in terms of the difference between the values of the energy functional:

$$\tilde{\varepsilon}^2 = J(\tilde{u}, \tilde{\theta}) - J(u, \theta).$$

It was proved (see [2]) that for $\forall(\tilde{u}, \tilde{\theta}) \in S$, there is a ratio

$$\tilde{\varepsilon}^2 = \frac{1}{2}\left(||| e_{\tilde{\theta}} |||^2 + \lambda^{-1} t^2 \| e_{\tilde{\gamma}} \|_{\Omega}^2 \right),$$

where

$$||| e_{\tilde{\theta}} |||^2 := \int_{\Omega} C\varepsilon(e_{\tilde{\theta}}) : \varepsilon(e_{\tilde{\theta}})\, d\Omega,$$

$$\| e_{\tilde{\gamma}} \|_{\Omega}^2 := \int_{\Omega} | e_{\tilde{\gamma}} |^2 d\Omega.$$

Next, we introduce the free elements necessary for constructing the a posteriori estimate: the vector field $\tilde{\tilde{y}}$ and the asymmetric tensor $\tilde{\tilde{\kappa}}$ represented as its components $\tilde{\tilde{\kappa}} = [\tilde{\tilde{\kappa}}^1, \tilde{\tilde{\kappa}}^2]$. They are selected such that

$$\tilde{\tilde{y}}, \tilde{\tilde{\kappa}}^1, \tilde{\tilde{\kappa}}^2 \in \mathbb{H}(\Omega, \mathrm{div}) :=$$
$$:= \{ y \in \mathbb{L}_2(\Omega)\, \mathbb{L}_2(\Omega) \mid \mathrm{div} y \in \mathbb{L}_2(\Omega) \}.$$

Upon applying identity transformations and known inequalities (given in [3]), the final inequality takes the form:

$$||| e_{\tilde{\theta}} |||^2 + \lambda^{-1} t^2 \| e_{\tilde{\gamma}} \|_{\Omega}^2 \le \hat{a}^2 + \lambda^{-1} t^2 \hat{b}^2, \qquad (6)$$

where

$$\hat{a} = ||| C^{-1}\mathrm{sym}(\tilde{\tilde{\kappa}}) - \varepsilon(\tilde{\theta}) ||| +$$
$$+ c_1 \| \mathrm{skew}(\tilde{\tilde{\kappa}}) \|_{\Omega} + c_2 c_3 (|\Omega| \| g + \mathrm{div}\tilde{\tilde{y}} \|_{\Omega}^2 +$$
$$+ |\Gamma_S| \| \tilde{\tilde{y}} \cdot n \|_{\Gamma_S}^2)^{1/2} +$$
$$+ c_4 (|\Omega| \| \tilde{\tilde{y}} + [\mathrm{div}\tilde{\tilde{\kappa}}^1, \mathrm{div}\tilde{\tilde{\kappa}}^2] \|_{\Omega}^2 +$$
$$+ |\Gamma_S| \| [\tilde{\tilde{\kappa}}^1 \cdot n, \tilde{\tilde{\kappa}}^2 \cdot n] \|_{\Gamma_S}^2)^{1/2}, \qquad (7)$$
$$\hat{b} = \| \tilde{\tilde{y}} - \tilde{\gamma} \|_{\Omega} +$$
$$+ c_3 (|\Omega| \| g + div\tilde{\tilde{y}} \|_{\Omega}^2 +$$
$$+ |\Gamma_S| \| \tilde{\tilde{y}} \cdot n \|_{\Gamma_S}^2)^{1/2},$$
$$c_1, c_2, c_3, c_4 \in \mathbb{R}.$$

The constants in the last row depend only on the geometry of the domain Ω, the boundary conditions and the properties of the material, and are a consequence of the following inequalities:

$$\| \nabla\varphi \|_{\Omega}^2 \le c_1^2 ||| \varphi |||^2,$$

$$\| \varphi \|_{\Omega}^2 \le c_2^2 ||| \varphi |||^2,$$

$$\frac{1}{|\Omega|} \| \omega \|_{\Omega}^2 + \frac{1}{|\Gamma_S|} \| \omega \|_{\Gamma_S}^2 \le$$
$$\le c_3^2 \| \nabla\omega \|_{\Omega}^2,$$

$$\frac{1}{|\Omega|} \| \varphi \|_{\Omega}^2 + \frac{1}{|\Gamma_S|} \| \varphi \|_{\Gamma_S}^2 \le$$
$$\le c_4^2 ||| \varphi |||^2.$$

Procedure for implementing the computational experiment

Let us consider in detail the steps of adaptive algorithm (3), which is typically used to refine the approximate solution more effectively.

The geometry of the given region, the thickness of the plate and the parameters of the material are set and initial partition is constructed as a first step. Next, the computations are performed in a suitable package, for example, ANSYS.

Once the values of displacements and rotations in the mesh nodes have been obtained, the algorithm moves on to the next step, which involves applying the given a posteriori estimate and finding the global error value. It is defined for the entire solution as the root of the sum of squared local errors for each element, called indicators. If the global error value is unsatisfactory within the framework of the problem set, the distribution of indicators over the partition elements is considered.

If the distribution of local errors has been obtained, it becomes possible to select the regions with the highest error value. There are several strategies for selecting elements (see, for example, [12, 13]); they consist in finding the threshold value of the indicator for which selecting too many or too few elements is not allowed globally.

The final part of each cycle of the adaptive algorithm is refining the mesh (and coarsening it in the general case) in the selected regions. The task is neither trivial nor auxiliary because the quality of the mesh affects the accuracy of the computations. The conformality of the mesh has to be preserved; the mesh angles should lie within a certain range, as too small and too large angles negatively affect the accuracy of the computations; in case of symmetry, it is also highly desirable to preserve its character. Different algorithms that solve this problem for quadrilateral elements are considered, in particular, in [14].

Next, the problem is recomputed for a new partition. This adaptive iterative algorithm implies that the result obtained on a modified mesh can again be assessed for accuracy and distribution of error over the computational domain.

Numerical results and discussion

The comparative analysis in this study was carried out for four computational examples with different specifics: a circular plate, a skew plate, a square plate with a large square hole, a square plate with a small circular hole.

Each of these cases has its own specifics which can be indicators of imperfections in the implementations. For example, a square plate with a large square hole has stress concentration zones near the top of hole. The analytical solution is known for the circular plate. A uniformly distributed load is considered in all examples. Oblique plates are also discussed in studies on a posteriori estimates [15, 4]; we used this type of plate in our study to illustrate the behavior of the error with rigidly clamped boundary conditions only imposed on the upper and lower edges (the two other edges remain free), in contrast to the other examples, considering fully clamped edges.

Let us now describe two examples. Notably, while we had to omit some of the results obtained for brevity's sake, they fully confirm the conclusions we ultimately reached.

We generated the region's geometry, imposed boundary conditions, constructed the mesh and obtained the actual solution using the ANSYS Mechanical (APDL) package. The MATLAB solver was also used for verification.

The effectiveness index I_{eff} is introduced to analyze the effectiveness of the estimate; this characteristic is commonly used in theory of a posteriori accuracy control, defined as the ratio of the majorant to the norm of deviation of the approximate solution from the exact one,

$$I_{eff} = M / \| u - \tilde{u} \|.$$

Thus, I_{eff} indicates the degree of error overestimation. Accordingly, the closer its value approaches unity from the right, the better. If the analytical solution of the problem is unknown, the approximate solution computed on a very fine mesh is taken as the exact solution u. This technique always yields slightly overestimated values of I_{eff}, and the actual estimation produces even better results than what we can verify.

The implementations are compared by the most important parameters. First, the constants c_1, c_2, c_3 and c_4 are considered. To compute c_1, we additionally consider a constant c_k in the Korn inequality. The important role of this constant in a posteriori estimates for problems of elasticity theory of elasticity is discussed, in particular, in monograph [6]. Then,

$$c_1 = c_k \sqrt{12(1+\nu)} / E$$

(for problems where $\Gamma_s = \emptyset$, $c_k = \sqrt{2}$).

Next, we compare the error e that is the square root of the left-hand side of estimate (6); the majorant M that is the square root of the right-hand side of estimate (6) and its components D, S, R, where

$$D = \| C^{-1}\mathrm{sym}(\tilde{\kappa}) - \varepsilon(\tilde{\theta}) \| + \lambda^{-1/2} t \| \tilde{\tilde{y}} - \tilde{\gamma} \|_{\Omega},$$

$$S = c_1 \| \mathrm{skew}(\tilde{\kappa}) \|_{\Omega},$$

$$R = c_2 c_3 \left(|\Omega| \| g + \mathrm{div}\tilde{\tilde{y}} \|_{\Omega}^2 + |\Gamma_S| \| \tilde{\tilde{y}} \cdot n \|_{\Gamma_s}^2 \right)^{1/2} + \lambda^{-1/2} t c_3 \left(|\Omega| \| g + \mathrm{div}\tilde{\tilde{y}} \|_{\Omega}^2 + |\Gamma_S| \| \tilde{\tilde{y}} \cdot n \|_{\Gamma_s}^2 \right)^{1/2} + c_4 \left(|\Omega| \| \tilde{\tilde{y}} + [\mathrm{div}\tilde{\kappa}^1, \mathrm{div}\tilde{\kappa}^2] \|_{\Omega}^2 + |\Gamma_S| \| [\tilde{\kappa}^1 \cdot n, \tilde{\kappa}^2 \cdot n] \|_{\Gamma_s}^2 \right)^{1/2};$$

the last of the compared quantities is the efficiency index I_{eff}.

The degree of refinement of the mesh is denoted as R_i, $i \in \{0, 1, 2, 3, 4, 5\}$, where the zero index corresponds to the initial partition.

To compute the majorant M, constants (7) are first approximately computed once for each example, and the results can then be used to obtain the error distribution on all meshes and thicknesses. The computation of the constants is asymptotic with respect to refinement of the mesh R_i; satisfactory values are obtained even on relatively coarse meshes, which is important for potential practical applications of the method.

The auxiliary second block includes searching for a reference solution on fine meshes and computing the energy functional value based on this solution. This is only done for the purpose of the computational experiment and is not required in real engineering problems, where it is simply replaced by computing the functional a posteriori estimate on the current mesh (this task is far less resource-consuming in terms of computational costs).

The final third block is responsible for directly computing the majorant M, where certain c_1, c_2, c_3, c_4, which are somewhat overestimated to provide robustness, are fed to the input.

Let us consider the comparison results, obtained using the examples of the circular plate and the square plate with a large square hole.

Example 1. Round plate. Let us start with a classic example (see ANSYS Verification Manual), where the analytical value of the deflection in the center of the plate is known.

Fig. 1 shows the deformations of the circular plate of average thickness t, computed in ANSYS on an R_1 mesh. The parameters of the model are given in Table 1.Table 2 contains the values of the computed auxiliary constants and allows to compare the performance of both implementations on different meshes. As mentioned above, mesh convergence of the constant values is observed with decreasing sizes of mesh elements. Due to zero boundary conditions, the exact value of the constant c_k is known and equals $\sqrt{2}$. For further computations, the constants obtained on the R_2 mesh are used, overestimated to provide robustness (see column R_2^*).

Table 3 contains the main computed results for comparison, namely the majorant M and its components. Let us consider the upper section of the table, i.e., the case where $Rad/t = 250$. Evidently, the

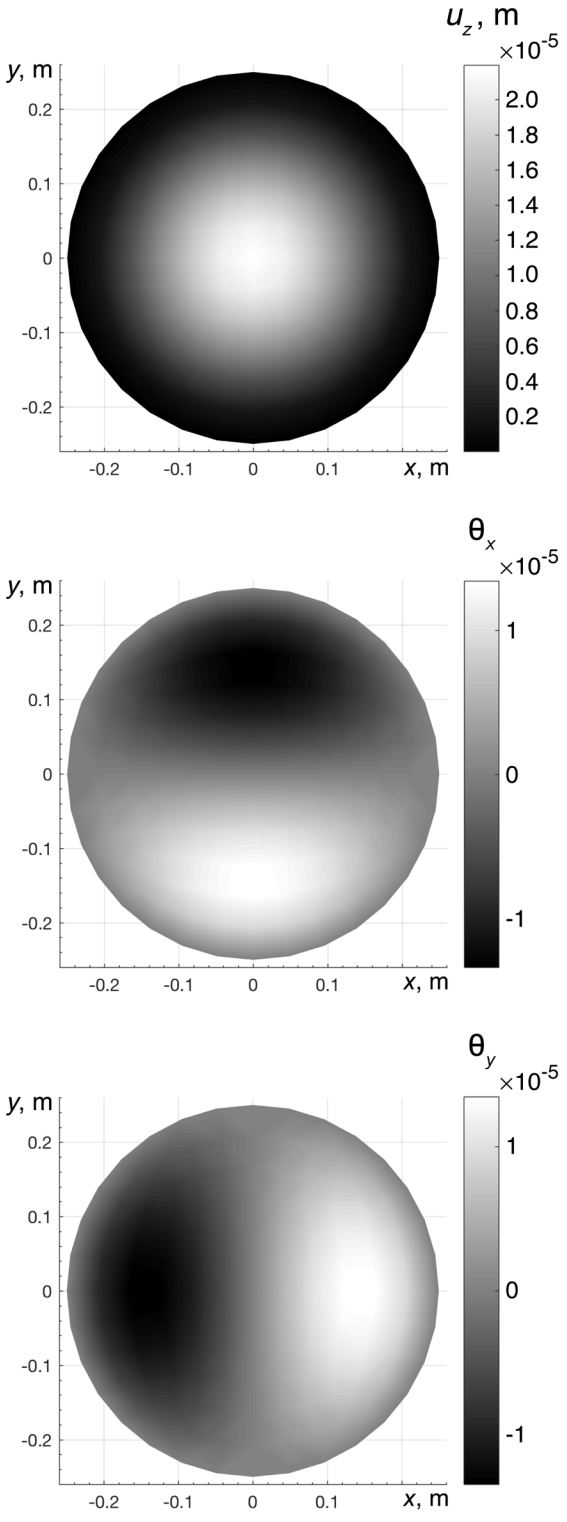

Fig. 1. Computed deformation of circular plate with average thickness in ANSYS on R_1 mesh; u_z is the distribution of the deflection of the midplane; θx, θy are the distributions of the fields of rotation of the normal to the midplane. $Rad/t = 250$ (see the data in Table 1)

Table 1

Model of circular plate

Parameter	Value	Specifics
Young's modulus E, N/m2	2·1011	1. The edge of the plate is fully clamped 2. The mesh constructed in the region has a structure of the general form
Poisson's ratio ν	0.3	
Load, N/m2	6585.175	
Radius Rad, m	0.25	
Thickness t, m	10^{-3}; $5 \cdot 10^{-5}$	

Table 2

Constants for circular plate computed in FORTRAN and MATLAB implementations

Mesh	Number of elements	Constant value				
		c_k	c_1	c_2	c_3	c_4
R_0	32	1.39 1.42	1.23e − 05 1.25e − 05	9.15e − 07 9.01e − 07	0.23	2.09e − 06 2.06e − 06
R_1	128	1.41 1.42	1.25e − 05	9.36e − 07 9.32e − 07		2.12e − 06 2.11e − 06
R_2	512	1.42		9,42e − 07 9.41e − 07		2.13e − 06
R_2^*	512	–	1.30e − 05	9.50e − 07	0.30	2.20e − 06

Notes. 1. The upper numbers in the cells of the table refer to the FORTRAN implementation, the lower to MATLAB; *a single number is given when the data coincide here and below*. 2. The data for the mesh marked with an asterisk correspond to the upper bound, overestimated for reliability. 3. $Rad/t = 250$.

Table 3

Control values of inequality (6) for circular plates of medium and small thickness in two implementations on R_2 mesh

Component of majorant (and majorant)	Control value	
	FORTRAN	MATLAB
$Rad/t = 250$		
e	0.712e + 02	
M	0.114e + 03	
D	0.111e + 03	
S	0.271e + 01	0.272e + 01
R	0.723e + 00	
I_{eff}	1.60	
$Rad/t = 5000$		
e	0.114e + 12	
M	0.162e + 12	
D	0.162e + 12	
S	0.217e + 08	
R	0.568e + 07	
I_{eff}	1.42	

term D plays the determining role, since this component includes the parts of the estimate corresponding to the error terms. The components S and R should be close to zero in the fields close to exact, which is what is observed. The values of I_{eff} given in rows 6 and 12 of the table allow to estimate the degree of overestimation for both implementations. It can be seen that the values computed by the two algorithms (I_{eff} = 1.60 in row 6) coincided, and the value itself is satisfactory, that is, there is no critical overestimation (by an order of magnitude or by several times).

Fig. 2 illustrates the distribution of local error indicators in a region of the circular plate on an R_2 mesh. The indicators are identical and suggest that the error is distributed not only in the zone of maximum plate deflection, but also near the region's

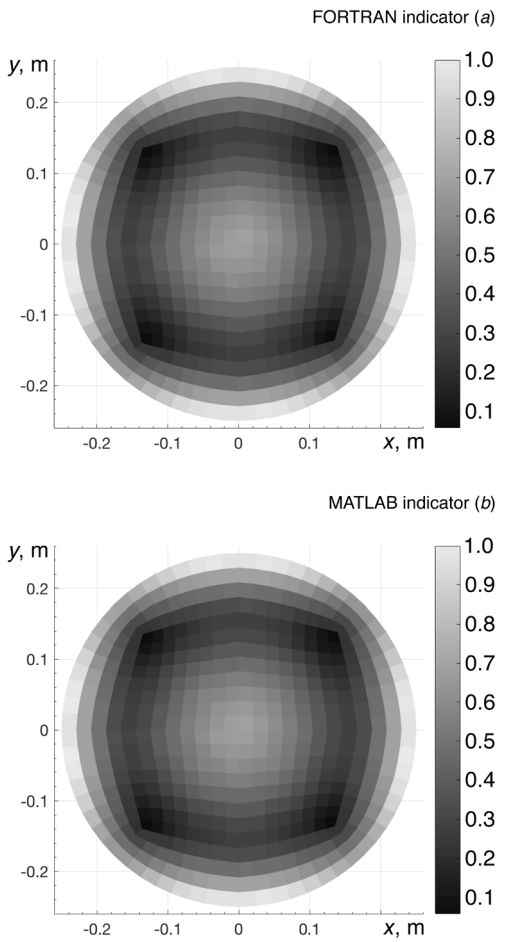

Fig. 2. Computed distributions of local error indicator over elements of region of circular plate in FORTRAN (*a*) and MATLAB (*b*) implementations on R_2 mesh; Rad/t = 250 (see Example 1)

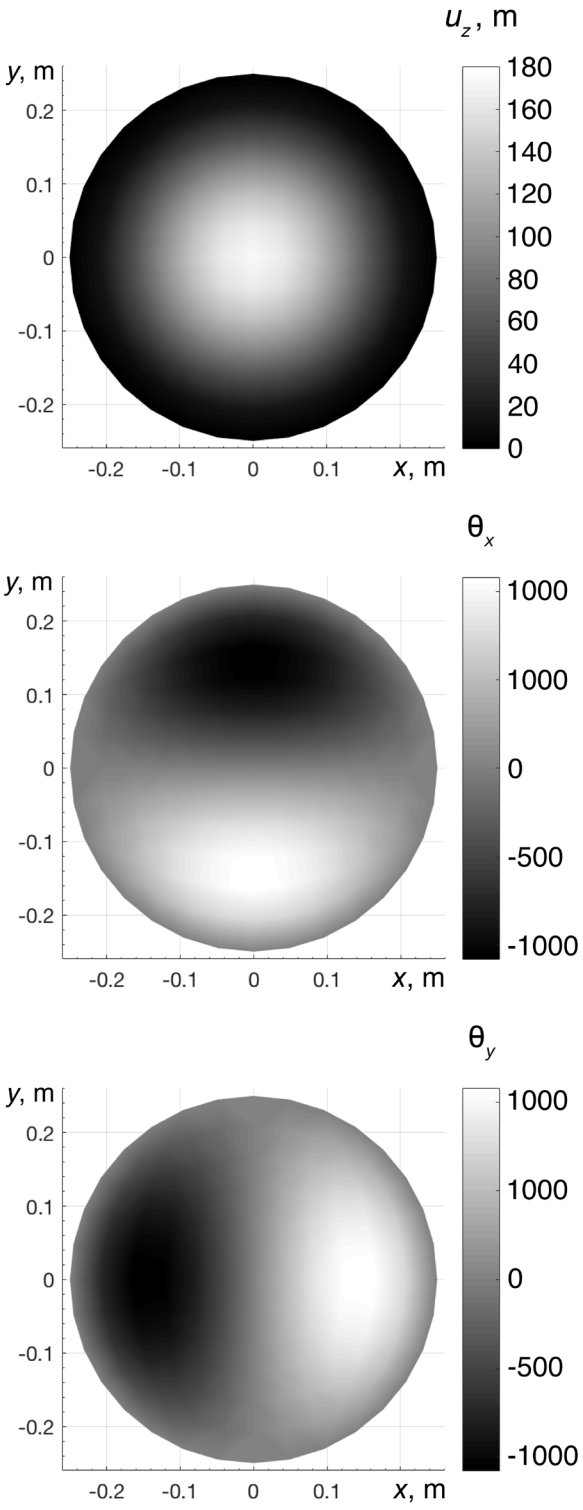

Fig. 3. Computed results similar to Fig. 1 for circular plate with small thickness; Rad/t = 5000 (see Table 1)

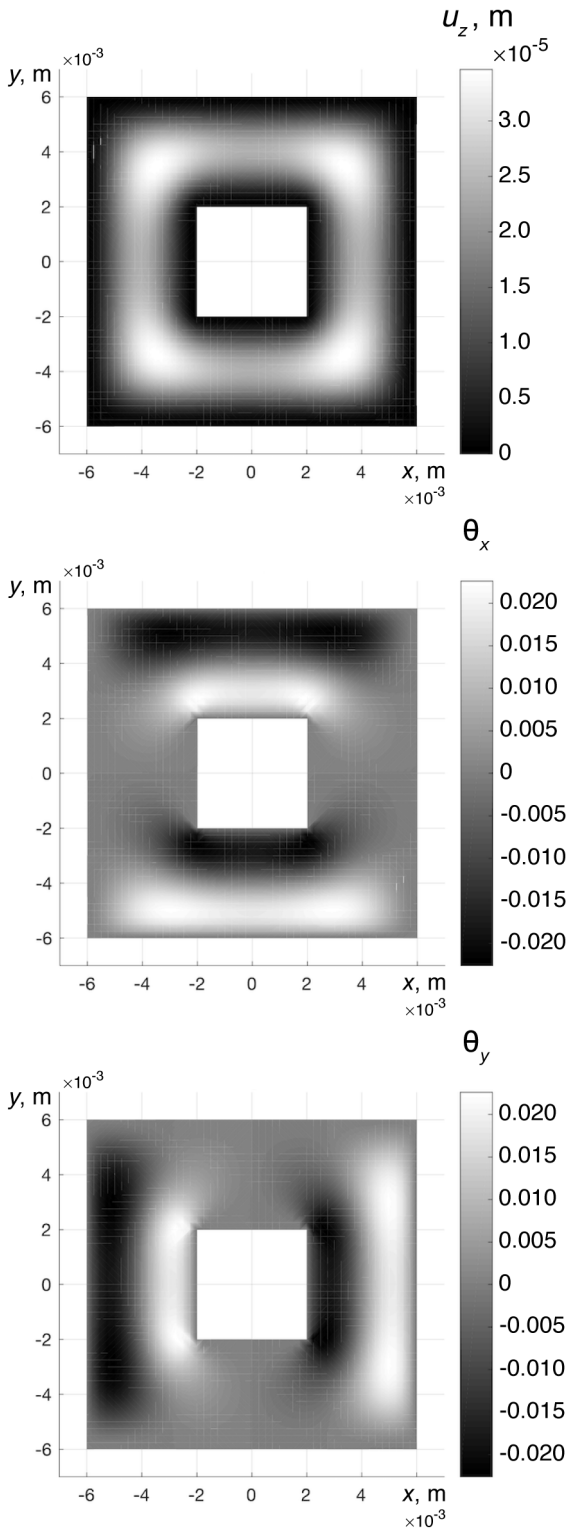

Fig. 4. Computed deformation of square plate with large square hole;
ANSYS was used on R_1 mesh.
Notations for the quantities are the same as in Fig. 1

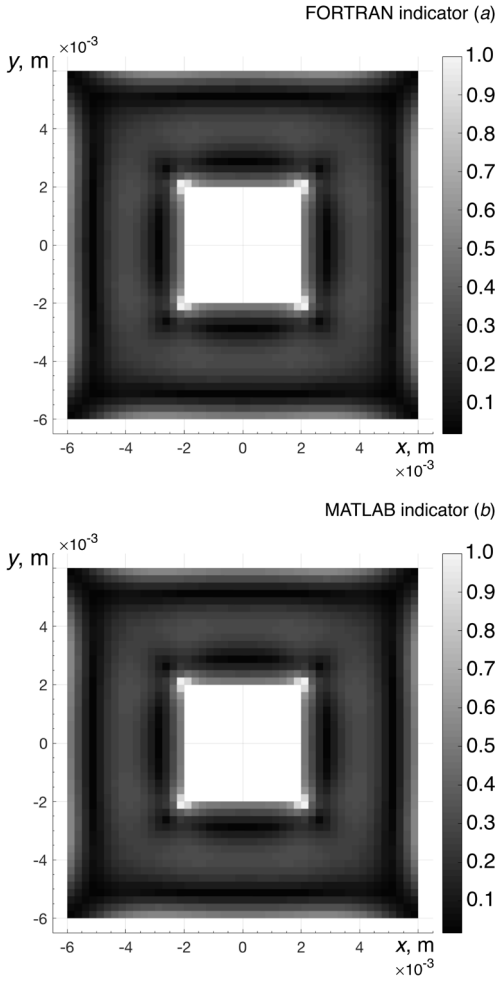

Fig. 5. Computed distributions of local error indicator over elements of region in FORTRAN (*a*) and MATLAB (*b*) implementations on R_2 mesh;
$A/t = 120$ (see Example 2)

boundary. This corresponds to the structure of the energy norm in this problem (this norm is defined in terms of gradients, which are computed with less accuracy at the edge). The lack of complete symmetry is due to the specifics of mesh construction.

Next, let us consider the computed results for a thin round plate with a thickness $t = 0.00005$ m ($Rad/t = 5000$), where the material parameters and the type of boundary conditions remained the same (see Table 1). This allows to assess the effectiveness of the method depending on plate thickness which is the key parameter in this case.

Fig. 3 shows an approximate solution. Evidently, the maximum value of the midplane deflection increased, compared with that in Fig.1. Changing the plate

Table 4

Model of square plate with large square hole

Parameter	Value	Specifics
Young's modulus E, N/m^2	$2 \cdot 10^9$	1. The plate's outer and inner edges are fully clamped 2. Mesh elements are square 3. The solution has stress concentration zones
Poisson's ratio ν	0.3	
Load, N/m^2	6585.175	
Side of square, m outer A inner a	 $12 \cdot 10^{-3}$ $4 \cdot 10^{-3}$	
Thickness t, m	10^{-4}	

Table 5

Computed constants in two implementations for square plate with large square hole

Mesh	Number of elements	Implementation	Constant value				
			c_k	c_1	c_2	c_3	c_4
R_1	512	FORTRAN	1.41	1.25e − 04	1.46e − 07	0.12	1.29e − 05
		MATLAB	1.42				1.28e − 05
R_1^*			−	1.30e − 04	1.50e − 07	0.15	1.30e − 05

Notes. 1. Data for the mesh marked with an asterisk correspond to the upper bound, overestimated for reliability. 2. The geometrical parameter $A/t = 120$.

Table 6

Control values of inequality (6) in two implementations on R_2 mesh for squareplate with large square hole

Component of majorant (and majorant)	Control value	
	FORTRAN	MATLAB
e	0.313e + 04	
M	0.529e + 04	0.534e + 04
D	0.519e + 04	0.515e + 04
S	0.413e + 02	0.348e + 02
R	0.567e + 02	0.161e + 03
I_{eff}	1.69	1.70

thickness does not affect the geometry of the region, and, therefore, the computed values of constants (7). Comparing the values in rows 6 and 12 of Table 3, we can also conclude that the value of the I_{eff} index decreased from 1.60 to 1.42 for a thin plate, i.e., it was close to unity that is the optimal value.

The computed distributions of local error indicators over a region of a circular plate with small thickness t = 0.00005 m (Rad/t = 5000) on an R_2 mesh have the form close to that shown in Fig. 2, so they are not given in this paper. Based on the obtained data, we can conclude that the algorithms work correctly for a fairly wide range of thicknesses, which is confirmed by other studies.

Example 2. Square plate with a large square hole. The following example was considered in order to explore the behavior of the estimate in stress concentration zones. Naturally, similar regions form near the tops of the inner hole with this plate configuration.

Fig. 4 shows the computed deformations of a square plate with a large square hole. The computations were performed in ANSYS on an R_1 mesh. The distributions of the quantities u_z, θ_x and θ_y over a region of the plate are given. As in Example 1, u_z is the midplane deflection; θ_x, θ_y are the distributions of the rotation fields.

Table 5 contains the computed auxiliary constants. For further computations, we used the overestimated values of the constants obtained on the R_1 mesh (data in row R_1^*).

Let us consider the results of the comparison of reference values of the estimate on the R_2 mesh. It can be seen from the data in Table 6 that the values of I_{eff} for the two implementations practically coincide, and no considerable overestimation is observed.

Let us consider the data shown in Fig. 5. The results of the implementations coincide, the distributions of the indicator are almost identical. The zones with the minimum error are located in the corners of the outer edge. Due to boundary conditions, the nodes have minimal displacement in these points. The zones with the maximum error are located in the regions where the stresses exhibit singularities if loads are applied.

Conclusion

In this study, we have compared the results obtained using existing implementations of the algorithms for computing the functional a posteriori estimate for Reissner–Mindlin plates [3]. We have carried out a numerical experiment for plate models with different geometric configurations, thickness values, material parameters and mesh structure.

We have reached the following conclusions based on the results obtained:

1. Both implementations yielded close efficiency indices for all examples where fully clamped edges were given as boundary conditions; the error overestimation had a satisfactory value.

2. The distribution of the error indicator over the computational domain turned out to be almost identical for both implementations, which further confirms that they are correct.

It would be of interest to use this approach in adaptive solutions of applied problems with the help of the resources of the Polytechnic Supercomputer Center in the future.

M.E. Frolov's and O.I. Chistiakova's studies were carried out with the financial support of the grant of the President of the Russian Federation МД-1071.2017.1.

REFERENCES

[1] **R.S. Falk,** Finite elements for the Reissner – Mindlin plate, Mixed finite elements, compatibility conditions, and applications, Springer, Berlin, Heidelberg (2008) 195–232.

[2] **S.I. Repin, M.E. Frolov,** Estimation of deviations from the exact solution for the Reissner – Mindlin plate problem, Journal of Mathematical Sciences. 132 (3) (2006) 331–338.

[3] **M.E. Frolov,** Reliable a posteriori error control for solutions to problems of Reissner – Mindlin plates bending, Proceedings of 10th International Conference Mesh methods for boundary-value problems and applications, Kazan University Publishing House, Kazan, Russia (2014) 610–615.

[4] **M. Frolov, O. Chistiakova,** Adaptive algorithm based on functional-type a posteriori error estimate for Reissner-Mindlin plates // Advanced Finite Element Methods with Applications. Selected papers from the 30th Chemnitz Finite Element Symposium, Lecture Notes in Computational Science and Engineering (LNCSE). 128, Ch. 7 (2019).

[5] **P. Neittaanmäki, S. Repin,** Reliable methods for computer simulation: Error control and a posteriori estimates, Elsevier, Amsterdam, 2004.

[6] **S. Repin,** A posteriori estimates for partial differential equations, de Gruyter, Berlin, 2008.

[7] **O. Mali, P. Neittaanmдki, S. Repin,** Accuracy verification methods: Theory and algorithms, Springer Science+Business Media Dordrecht, 2014.

[8] **U. Langer, S. Repin, T. Samrowski,** A posteriori estimates for a coupled piezoelectric model, Russian Journal of Numerical Analysis and Mathematical Modelling. 32 (4) (2017) 259–266.

[9] **S. Repin, J. Valdman,** Error identities for variational problems with obstacles, ZAMM – Journal of Applied Mathematics and Mechanics. 98 (4) (2018) 635–658.

[10] **P.R. Bцsing, C. Carstensen,** Discontinuous Galerkin with weakly over-penalized techniques for Reissner – Mindlin plates, Journal of Scientific Computing. 64 (2) (2015) 401–424.

[11] **B. Kumar, M. Somireddy, A. Rajagopal,** Adaptive analysis of plates and laminates using natural neighbor Galerkin meshless method, Engineering with Computers. 35 (1) (2018) 201–214.

[12] **W. Dörfler,** A convergent adaptive algorithm for Poisson's equation, SIAM Journal on Numerical Analysis. 33 (3) (1996) 1106–1124.

[13] **R. Verfürth,** A review of a posteriori error estimation and adaptive mesh-refinement techniques. John Wiley & Sons, 1996.

[14] **A.S. Karavaev, S.P. Kopysov,** A refinement of unstructured quadrilateral and mixed meshes, Vestnik Udmurtskogo Universiteta. Matematika. Mekhanika. Komp'yuternye Nauki. (4) (2013) 62–78.

[15] **C. Carstensen, X. Xie, G. Yu, T. Zhou,** A priori and a posteriori analysis for a locking-free low order quadrilateral hybrid finite element for Reissner–Mindlin plates, Computer Methods in Applied Mechanics and Engineering. 200 (9–12) (2011) 1161–1175.

Received 29.12.2018, accepted 02.02.2019 .

THE AUTHORS

KISELEV Kirill V.
Peter the Great St. Petersburg Polytechnic University
29 Politechnicheskaya St., St. Petersburg, 195251, Russian Federation
kvladimirovich10@gmail.com

FROLOV Maxim E.
Peter the Great St. Petersburg Polytechnic University
29 Politechnicheskaya St., St. Petersburg, 195251, Russian Federation
frolov_me@spbstu.ru

CHISTIAKOVA Olga I.
Peter the Great St. Petersburg Polytechnic University
29 Politechnicheskaya St., St. Petersburg, 195251, Russian Federation
Chistiakova.Olga@gmail.com

СПИСОК ЛИТЕРАТУРЫ

1. **Falk R.S.** Finite elements for the Reissner – Mindlin plate // Mixed finite elements, compatibility conditions, and applications. D. Boffi, L. Gastaldi (Eds). Berlin, Heidelberg: Springer, 2008. Pp. 195–232.

2. **Репин С.И., Фролов М.Е.** Об оценке отклонений от точного решения задачи о пластине Рейсснера – Миндлина // Краевые задачи математической физики и смежные вопросы теории функций. Записки научных семинаров ПОМИ. СПб, 2004. Т. 310. С. 145–157.

3. **Фролов М.Е.** Надежный апостериорный контроль точности решений задач об изгибе пластин Рейсснера – Миндлина // Сеточные методы для краевых задач и приложения. Материалы Десятой международной конфеи ренции. Казань, 2014. С. 610–615.

4. **Frolov M., Chistiakova O.** Adaptive algorithm based on functional-type a posteriori error estimate for Reissner-Mindlin plates // Advanced Finite Element Methods with Applications. Selected papers from the 30th Chemnitz Finite Element Symposium, Lecture Notes in Computational Science and Engineering (LNCSE). 2019. Vol. 128. Ch. 7.

5. **Neittaanmдki P., Repin S.** Reliable methods

for computer simulation: Error control and a posteriori estimates. Amsterdam: Elsevier, 2004. 304 p.

6. **Repin S.** A posteriori estimates for partial differential equations. Berlin: de Gruyter, 2008. 316 p.

7. **Mali O., Neittaanmäki P., Repin S.** Accuracy verification methods: Theory and algorithms. Springer Science+Business Media Dordrecht, 2014. XIII+355 p.

8. **Langer U., Repin S., Samrowski T.** A posteriori estimates for a coupled piezoelectric model // Russian Journal of Numerical Analysis and Mathematical Modelling. 2017. Vol. 32. No. 4. Pp. 259–266.

9. **Repin S., Valdman J.** Error identities for variational problems with obstacles // ZAMM – Journal of Applied Mathematics and Mechanics. 2018. Vol. 98. No. 4. Pp. 635–658.

10. **Bösing P.R., Carstensen C.** Discontinuous Galerkin with weakly over-penalized techniques for Reissner – Mindlin plates // Journal of Scientific Computing. 2015. Vol. 64. No. 2. Pp. 401–424.

11. **Kumar B., Somireddy M., Rajagopal A.** Adaptive analysis of plates and laminates using natural neighbor Galerkin meshless method // Engineering with Computers. 2018. Vol. 35. No. 1. Pp. 201–214.

12. **Dörfler W.** A convergent adaptive algorithm for Poisson's equation // SIAM Journal on Numerical Analysis. 1996. Vol. 33. No. 3. Pp. 1106–1124.

13. **Verfürth R.** A review of a posteriori error estimation and adaptive mesh-refinement techniques. John Wiley & Sons, 1996. 127 p.

14. **Караваев А.С., Копысов С.П.** Перестроение неструктурированных четырехугольных и смешанных сеток // Вестник Удмуртского университета. Серия Математика. Механика. Компьютерные науки. 2013. Вып. 4. С. 62–78.

15. **Carstensen C., Xie X., Yu G., Zhou T.** A priori and a posteriori analysis for a locking-free low order quadrilateral hybrid finite element for Reissner –Mindlin plates // Computer Methods in Applied Mechanics and Engineering. 2011. Vol. 200. No. 9–12. Pp. 1161–1175.

Статья поступила в редакцию 29.12.2018, принята к публикации 02.02.2019.

СВЕДЕНИЯ ОБ АВТОРАХ

КИСЕЛЕВ Кирилл Владимирович – *магистрант кафедры прикладной математики Института прикладной математики и механики Санкт-Петербургского политехнического университета Петра Великого.*

195251, Российская Федерация, г. Санкт-Петербург, Политехническая ул., 29
kvladimirovich10@gmail.com

ФРОЛОВ Максим Евгеньевич – *доктор физико-математических наук, директор Института прикладной математики и механики, заведующий кафедрой прикладной математики Санкт-Петербургского политехнического университета Петра Великого.*

195251, Российская Федерация, г. Санкт-Петербург, Политехническая ул., 29
frolov_me@spbstu.ru

ЧИСТЯКОВА Ольга Игоревна – *аспирантка кафедры прикладной математики Института прикладной математики и механики Санкт-Петербургского политехнического университета Петра Великого.*

195251, Российская Федерация, г. Санкт-Петербург, Политехническая ул., 29
Chistiakova.Olga@gmail.com

DOI: 10.18721/JPM.12111
УДК 531.391+681.5.01

THE DAMPING OF THE DISTRIBUTED SYSTEM VIBRATIONS USING PIEZOELECTRIC TRANSDUCERS: SIMULATION

A.V. Fedotov

Institute for Problems of Mechanical Engineering, RAS,

St. Petersburg, Russian Federation

The present paper continues the author's studies where the problem of the control of forced bending vibrations of a metal beam using piezoelectric sensors and actuators has been investigated. In those studies, all the control results were obtained experimentally. However, in order to make the design of the control systems the most effective, it was necessary to develop a numerical model, which would allow one to get the results for different variants of such systems, and that was the objective of the present study. In this study, the main experimental data were reproduced numerically on a basis of the finite element model of the object. In addition, new modal control systems were designed, providing a more efficient reduction of the amplitude of resonance vibrations of a beam compared to the systems considered experimentally.

Keywords: active vibration control, mechatronics, modal control, piezoelectric transducer, finite element model

Citation: A.V. Fedotov, The damping of the distributed system vibrations using piezoelectric transducers: simulation, St. Petersburg Polytechnical State University Journal. Physics and Mathematics. 12 (1) (2019) 130–142. DOI: 10.18721/JPM.12111

ЧИСЛЕННОЕ МОДЕЛИРОВАНИЕ ГАШЕНИЯ КОЛЕБАНИЙ РАСПРЕДЕЛЕННОЙ СИСТЕМЫ С ПОМОЩЬЮ ПЬЕЗОЭЛЕМЕНТОВ

А.В. Федотов

Институт проблем машиноведения РАН, Санкт-Петербург, Российская Федерация

Представленная статья продолжает работы автора, в которых рассматривалась задача об управлении вынужденными изгибными колебаниями металлической балки с помощью пьезоэлектрических сенсоров и актуаторов. При этом все результаты управления были получены экспериментально. Однако для того, чтобы процесс проектирования систем управления был наиболее эффективным, необходима разработка численной модели, позволяющей получать результаты для разных вариантов таких систем, что и является задачей данной работы. В данном исследовании численно на основе конечно-элементной модели объекта воспроизводятся основные экспериментальные результаты, а также проектируются более эффективные модальные системы управления, приводящие к большему снижению амплитуды резонансных колебаний балки, по сравнению с системами, рассмотренными ранее в эксперименте.

Ключевые слова: управление колебаниями, мехатроника, модальное управление, пьезоэлемент, конечно-элементная модель

Ссылка при цитировании: Федотов А.В. Численное моделирование гашения колебаний распределенной системы с помощью пьезоэлементов // Научно-технические ведомости СПбГПУ. Физико-математические науки. 2019. Т. 12. № 1. С. 142–155. DOI: 10.18721/JPM.12111

Introduction

Controlling the vibrations in distributed mechanical systems is complicated because these systems have an infinite number of vibration modes, so they are not fully controllable and observable. In practice, however, dynamics of such systems can be usually analyzed by considering some finite set of the object's normal modes. It was experimentally confirmed in [1] for such cases that modal control, specifically of the forms mainly involved in operation of the given system, had a greater efficiency compared with local control.

The modal approach to vibration control in elastic systems was first formulated in [2] and further developed in [3]. Specific vibration modes of an elastic object can be monitored or controlled via distributed sensors and actuators used as modal filters [4, 5] and arrays of discrete control elements [6–8]. The problem of identifying the control object arises in the latter case, typically solved either by finite element modeling of the object [9–11] or analytically [12, 13]. We have proposed an experimental procedure for identifying an object with the purpose of creating a modal control system in [14]. Piezoelectric sensors and actuators are easy to use and have high performance characteristics, making them widely popular for vibration control in distributed systems.

This paper continues the studies in [1, 14], detailing the experiments on creating control systems that reduce forced vibrations of a cantilevered metal beam. The control systems obtained use a set of discrete piezoelectric sensors and actuators. Both local and modal control systems were constructed as part of the experiment; it was the modal system that proved the most effective one.

The goal of this study has consisted in numerically reproducing the main experimental results and in creating control systems that are more efficient compared with those obtained within the framework of previous experiments.

The first section of the study considers an experimental setup for controlling forced bending vibrations of a beam; the results of finite element modeling of the control object are then described and compared with the results of the experiment. Next, we have outlined the theoretical foundations of modal vibration control in distributed mechanical systems, formulating the stability criteria for a closed-loop system with two feedback loops. The paper is concluded by considering the operation of various control systems that reduce the resonant vibration amplitude of a beam.

Experimental setup

The setup, procedure and results of the experimental study considered in this paper are described in detail in [1, 14].

The schematic for the experimental setup is shown in Fig. 1, *a*. A 70 cm long aluminum beam *1* with a rectangular cross-section of 3 Ч 35 mm, disposed vertically and fixed at one point at a distance of 10 cm from the lower end, was chosen as the control object. This beam experiences forced bending vibrations induced by longitudinal vibration of piezoelectric stack actuator *2*, which is part of the structure connecting the beam to fixed base *3*.

The main purpose of the experimental setup constructed was to perfect the modal approach to control of forced beam vibrations. In order to do this, we designed a control system with two loops including two actuators and two sensors. Piezoelectric actuators *4* and sensors *5* are arranged in pairs on both sides of the beam. Fig. 1, *b* shows a fragment of a finite element model of the beam comprising the fixed stack *2* and one of actuators *4*. In contrast to the simplified scheme given in Fig. 1, *a*, the finite element model includes a complete structure for the beam's fixation used in the experimental setup. The structure includes (in addition to the piezoelectric stack actuator) a steel plate and studs receiving the weight of the beam and thus taking the lateral load off the actuator.

The signals measured by the sensors are converted via discrete controller *6* into control signals supplied to the actuators. The task of the control system is to reduce the amplitude of forced resonant vibrations of the beam with the first and second natural frequencies. Modal control is thus carried out for the first and second modes of the beam's bending vibrations. These modes are shown in Fig. 1, *c*. The quality of suppression of forced vibrations is assessed from the readings of a laser vibrometer measuring the vibration velocity of the beam's upper endpoint. This point has the highest vibration amplitude of all points of the beam for both the first and second modes.

Actuators and sensors are identical rectangular 50 × 30 × 0.5 mm plates made of piezoelectric material, covered with electrodes on both sides and placed inside thin insulation. These piezoelectric elements were considered in [15]. When electric voltage is applied to the actuator electrodes, the piezoelectric layer is either stretched or compressed, resulting in bending deformation of the segment of the beam to which the actuator is glued. Thus, the

impact of the actuator on the beam is equivalent to applying a pair of opposite bending moments to two cross-sections of the beam (end sections of the actuator). The piezoelectric sensor operates by similar principles: as a segment of the beam to which the sensor is attached bends, the sensor material is either stretched or compressed in the longitudinal direction, resulting in potential difference measured as a signal from the sensor appearing on the sensor electrodes. To achieve maximum efficiency in controlling the first and second modes of the beam's bending vibrations, sensors and actuators are located in the points of the beam where these modes have the greatest curvature:

$$110.5 \le x \le 160.5 \text{ mm}$$

for the first sensor/actuator pair and

$$377.5 \le x \le 427.5 \text{ mm}$$

for the second pair (the x coordinate is measured from the lower end of the beam).

In addition to the main elements (see Fig. 1), the control system additionally includes:

an amplifier increasing the amplitude of the control signal by 25 times before it is fed to the actuators;

low-pass filters with a cut-off frequency of 1 kHz smoothing the high-frequency component of the electrical signal and protecting the equipment from high input voltages.

Both the measured signal before it is fed to the controller and the control signal before it is fed to the actuators pass through the filter.

A number of characteristics of the control object should be measured in order to design a control system.

Firstly, we measured the frequency and phase response of the beam upon impact on each of the actuators and as the signal was measured by each sensor.

Secondly, the frequency response and the phase response of the beam were also read upon impact on the stack actuator and as the signal was measured with the vibrometer. Thus, we obtained a total of 9 frequency and phase response curves for each of the 3 cases for external impacts (actuators, piezoelectric stack) and each of the 3 cases for measurements (sensors, vibrometer). All characteristics were measured with filters and amplifiers present.

Thirdly, we analyzed the beam's vibrations in resonant modes (resonant vibrations with the first and second natural frequencies) in order to determine the modal matrices T and F, in accordance with the identification procedure described in [14].

After that, based on the measured characteristics

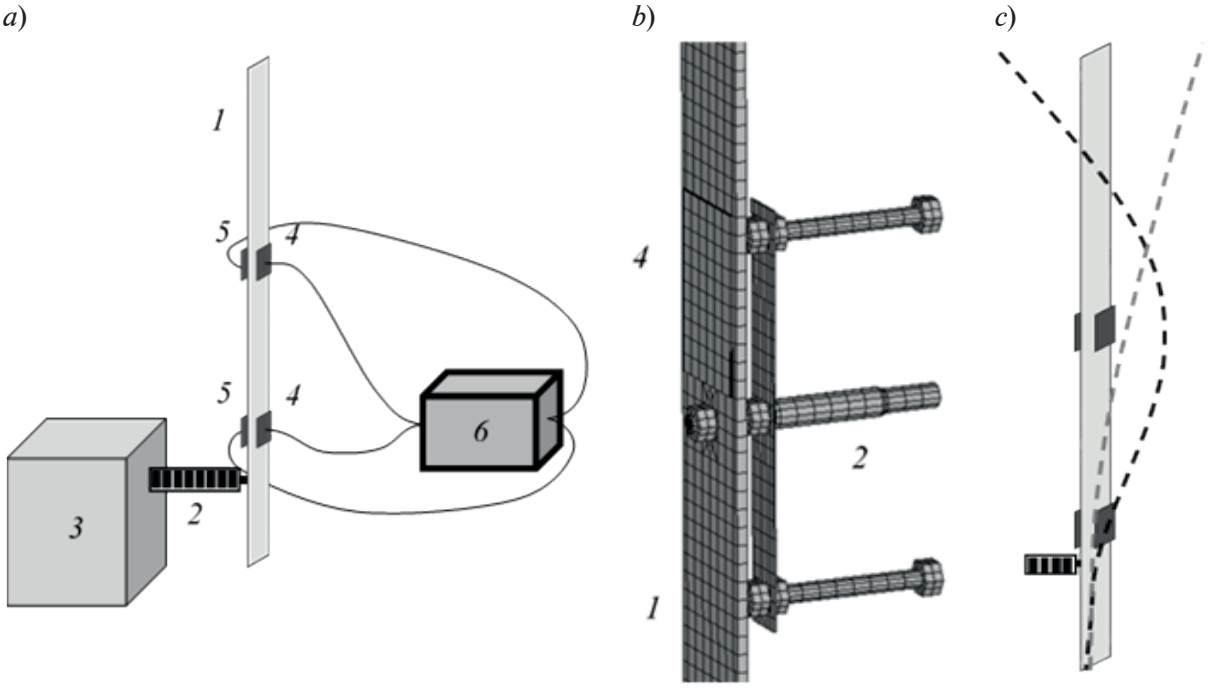

Fig. 1. Schematic of experimental setup (*a*), fragment of finite element model of object (*b*) and two lowest bending vibration modes of beam (*c*)
aluminum beam *1*; piezoelectric stack *2*; fixed base *3*;
actuators *4*; sensors *5*; controller *6*

of the object, we used the method of logarithmic amplitude-frequency characteristics to formulate and then experimentally test the control laws providing the most effective suppression of the beam's forced resonant vibrations.

As a result, we obtained local control systems and a modal control system.

It was the modal system that proved the most effective, allowing to reduce the resonant vibration amplitudes by 83.5% at the first resonance, and by 87.2% at the second. The local control systems we designed yielded good results either at the first (decrease by 78.0%) or at the second (decrease by 88.9%) resonance but it was impossible to obtain a control system that would be simultaneously and equally effective at both resonances within the local approach. The test results for the obtained control systems are described in detail in [1].

Finite-element model of the system

One of the goals of our study was to numerically reproduce the results obtained in the experiment described in the previous section of the paper. For this purpose, we simulated the given system in the ANSYS finite element (FE) package. A fragment of the FE model of the beam with piezoelectric sensors and actuators is shown in Fig. 1, *b*.

The FE model consists of three-dimensional 20-node elements Solid186 (used for common materials: aluminum of the beam, steel of the support structures and insulation of piezoelectric elements) and Solid226 (for piezoelectric materials of sensors, actuators and stacks). The model contains the total of 3534 elements and 21088 nodes. Rigid clamping was given as the mechanical boundary conditions for the points of the support structure which were attached to the fixed base in the experimental setup; electric potentials on the actuator and stack electrodes were given as electrical boundary conditions.

To set the damping factor, we analyzed the experimental results in the CE model of the experimental setup, determining the damping factor ξ from the width of the resonant peak in each of the resonances for all frequency response curves, in accordance with the formula

$$\xi = \frac{\Delta f}{2 f_0}, \qquad (1)$$

where f_0 is the resonant frequency; Δf is the width of the resonant peak, bounded by the frequency values at which the resonant amplitude falls by $\sqrt{2}$ times.

The values of the damping factors obtained this way are given in Table 1 (see the note to Table 1 for notations). As a result, the same damping factor $\xi = 0.0020$ was set for all vibration modes in the FE model.

Harmonic analysis of the system was

Table 1

Damping factors obtained from experimental frequency response at different resonant frequencies f_0

Mode number	f_0, Hz	ξ_1	ξ_2	ξ_3	ξ_4
1	7.125	0.0044	0.0044	0.0055	0.0055
2	42.55	0.0022	0.0021	0.0026	0.0026
3	113.9	0.0031	0.0031	0.0034	0.0034
4	175.2	0.0022	0.0025	0.0031	0.0031
5	249.5	0.0018	0.0019	0.0019	0.0019
6	390.9	0.0010	0.0010	0.0012	0.0010
7	579.4	0.0013	0.0012	0.0016	0.0016
8	790.5	0.0010	0.0009	0.0014	0.0014
9	1073	0.0016	0.0016	0.0018	0.0017
10	1338	0.0015	0.0014	0.0019	0.0019
11	1471	0.0016	0.0017	0.0025	0.0025
12	1763	0.0022	0.0023	0.0034	0.0033

Notations: ξ_1–ξ_4 are the damping factors obtained for different frequency responses: actuator-sensor (ξ_1), actuator-vibrometer (ξ_2), stack-sensor (ξ_3), stack-vibrometer (ξ_4)

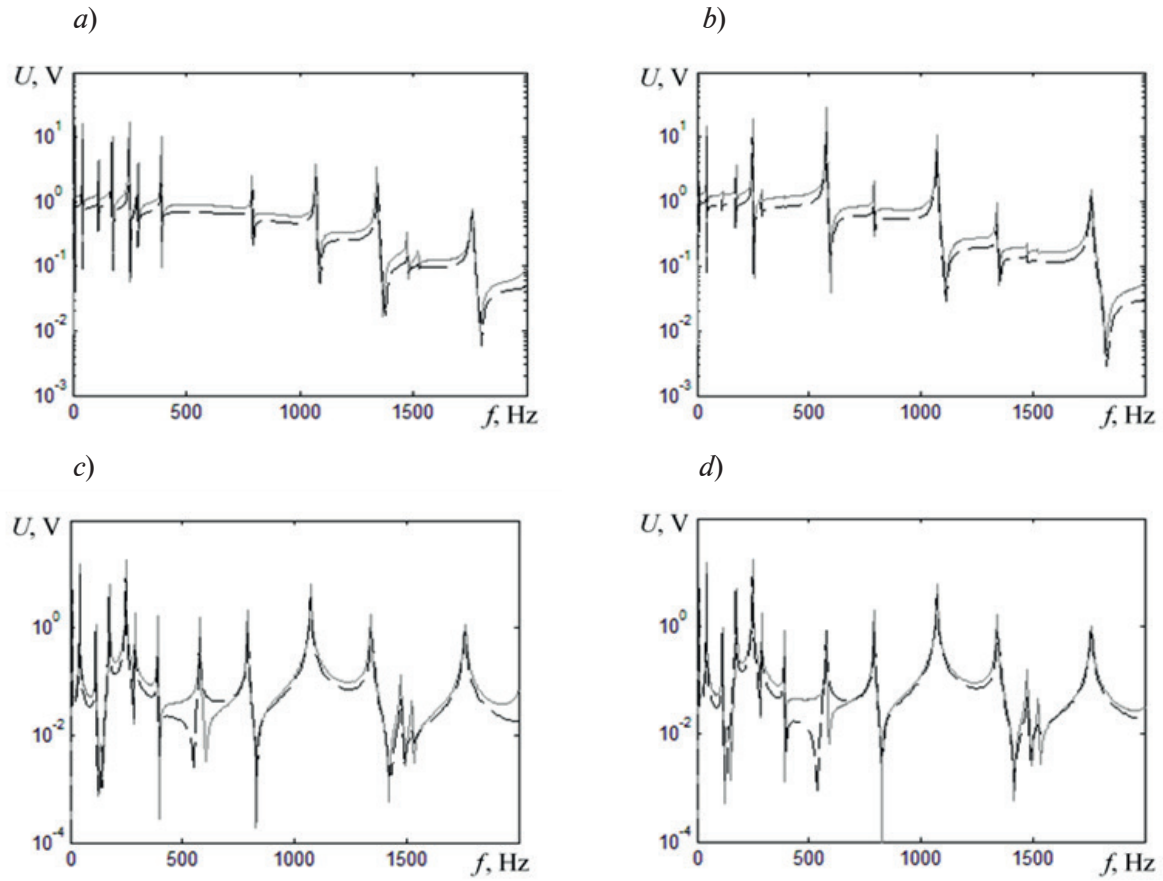

Fig. 2. Comparison of frequency response obtained experimentally (solid lines) and numerically (dashed lines) for impact on actuators *A*1 (*a*, *c*), *A*2 (*b*, *d*) and measurement of signals from sensors *S*1 (*a*, *d*) and *S*2 (*b*, *c*)

performed in the ANSYS package with three variants of action: using each of the two actuators or the piezoelectric stack. Three frequency responses and phase responses were recorded for each variant, corresponding to either signal measurement by one of two sensors, or to transverse displacement of a point at the upper end of the beam. After these characteristics were obtained in ANSYS, they were modified: the characteristics of filters and amplifiers, measured separately as part of the experiment, were added. Thus, the frequency and phase response curves similar to those measured experimentally were obtained.

A comparison of the frequency response obtained numerically and experimentally for each of the two actuators and each of the two sensors is given in Fig. 2. It can be seen that the resonant frequencies in the experiment and in the FE model are in good agreement, but the amplitudes of the experimental curves turn out to be slightly higher than of those obtained by simulation. There is additional disagreement in the magnitudes of the resonant peaks of the curves, since damping is in fact different for different forms of vibrations and differs from the value chosen in the model. However, in general, the data obtained numerically agree well with the experimental results.

Modal control of vibrations in elastic system

Let us consider the operation of a modal system for controlling vibrations in an elastic object, consisting of n sensors and n actuators. The main principle of modal control is that different vibration modes are controlled separately; at the same time, each control loop corresponds to its own vibration mode. Let the control system contain m loops, and control be carried out for m lower vibration modes. It is evident that the number of sensors and actuators used should be no less than the number of independently controlled forms, i.e. $n \geq m$.

Let us assume that the dynamics of a distributed system can be described by using

an expansion of the displacement $u(r,t)$ in terms of the system's normal vibration modes:

$$u(r,t) = \sum_{k=1}^{\infty} w_k(r)\beta_k(t), \qquad (2)$$

where $\beta_k(t)$ are the generalized coordinates, $w_k(r)$ are the vibration modes.

Let the vibration modes be independent of each other; the dynamics of each of the modes is then described by the equation

$$\ddot{\beta}_k(t) + 2\xi_k\lambda_k\dot{\beta}_k(t) + \lambda_k^2\beta_k(t) = f_k + y_k, \qquad (3)$$

where λ_k is the kth normal frequency of the object; ξ_k is the kth damping factor; f_k is the kth generalized external force; y_k is the control action corresponding to the kth mode of the object's vibrations.

The control action is applied to the object using n actuators and is a linear combination of control signals U_i fed to the actuators for each vibration mode:

$$y_k = \sum_{i=1}^{n} \theta_{ki}^a U_i, \qquad (4)$$

where θ_{ki}^a is the coefficient for the impact of an ith actuator on a kth vibration mode.

Separation of the object's first m vibration modes in the control system is provided by the following control structure:

$$U_{n\times 1} = FK_{m\times m}TY_{n\times 1}, \qquad (5)$$

where $K_{m\times m}$ is the diagonal matrix of control laws where each element K_{ii} corresponds to one of the control loops and is a function of the complex variable s; $F_{n\times m}$, $T_{m\times n}$ are modal matrices (synthesizer and analyzer) that perform linear transformation of the vectors of control and measured signals; $Y_{n\times 1}$ is the vector of sensor signals.

The vector $Y_{n\times 1}$ is related to the vector of the first m generalized coordinates $\beta_{m\times 1}$ as follows:

$$Y_{n\times 1} = \theta^s_{n\times m}\beta_{m\times 1} + \tilde{Y}, \qquad (6)$$

where $\theta^s_{n\times m}$ is the weight matrix determining how each of the n sensors reacts to each of the m vibration modes; $\tilde{Y}$ is the term dependent only on the object's higher normal modes which are not controlled.

Substituting expressions (4)–(6) into Eq. (3), we obtain the equation of motion for m first generalized coordinates in the matrix form:

$$\begin{gathered}\ddot{\beta}_{m\times 1} + 2\xi_{m\times m}\Lambda_{m\times m}\dot{\beta}_{m\times 1} + \\ +\Lambda^2_{m\times m}\beta_{m\times 1} = \\ = f_{m\times 1} + \theta^a{}_{m\times n}F_{n\times m}K_{m\times m}\times \\ \times T_{m\times n}\theta^s{}_{n\times m}\beta_{m\times 1} + \Delta_{m\times 1},\end{gathered} \qquad (7)$$

where $\Lambda_{m\times m}$, $\xi_{m\times m}$ are diagonal matrices of natural frequencies and damping factors, respectively; $\Delta_{m\times 1}$ is a vector containing only higher harmonics.

Clearly, for separate control of the object's m lower vibration modes, the diagonal structure of the matrix

$$M = \theta^a FKT\theta^s$$

has to be obtained.

For this purpose, the modal matrices F and T should be defined as follows:

$$\begin{aligned} T_{m\times n} &= (\theta^{sT}_{m\times n}\theta^s_{n\times m})^{-1}\theta^{sT}_{m\times n}, \\ F_{n\times m} &= \theta^{aT}_{n\times m}(\theta^a_{m\times n}\theta^{aT}_{n\times m})^{-1}. \end{aligned} \qquad (8)$$

Thus, the modal matrices F and T should be given first in accordance with formula (8), and the control laws should be chosen next for each loop $K_{ii}(s)$ in order to create a modal control system.

Stability of closed system with two feedback loops

First of all, let us consider the operation of a control system with one feedback loop. Let the disturbance d be fed to the input of the control object with the transfer function $H(s)$, with the object's output signal y converted to the control action u in the feedback loop with the transfer function $R(s)$, which is also fed to the object's input with a minus sign. Thus, the output and control signals are related by the following expressions:

$$\begin{aligned} y &= H(s)\,(d-u), \\ u &= R(s)\,y. \end{aligned} \qquad (9)$$

Let us confine ourselves to considering the transfer functions $H(s)$ and $R(s)$ which do not have poles in the right complex half-plane of the variable s. Thus, the open-loop system is stable. The relationship between the input and output signals of the system is derived from relations (9):

$$y = \frac{H(s)}{1+H(s)R(s)}d = \frac{H(s)}{1+H_0(s)}d. \qquad (10)$$

In order to determine the stability of a closed-loop system, we should analyze the function in the denominator of the obtained fraction. For a closed-loop system to be stable, all zeros of this function should lie in the left half-plane of s. However, in practice it is more convenient to confine the consideration with analysis of the transfer function of an open-loop system

$$H_0(s) = H(s)R(s).$$

According to the Nyquist criterion, provided that an open-loop system is stable, a

closed-loop system is stable if the hodograph of the function $H_0(i\omega)$ does not enclose the point (−1; 0) on the complex plane as the frequency ω changes from 0 to +∞. Now let us obtain a similar criterion for a system with two feedback loops.

Let the control object have two inputs and two outputs, with disturbances d_1 and d_2 fed to the inputs, and the output signals y_1 and y_2 measured by the control system and converted by the transfer functions $R_1(s)$ and $R_2(s)$ to control actions u_1 and u_2, also fed with a minus sign to the object's inputs:

$$\begin{aligned} u_1 &= R_1(s)\, y_1, \\ u_2 &= R_2(s)\, y_2. \end{aligned} \tag{11}$$

To describe the behavior of the object in the given system, we use four transfer functions, $H_{11}(s)$, $H_{12}(s)$, $H_{21}(s)$ and $H_{22}(s)$, each of them corresponding to one of the two inputs and one of the two outputs:

$$\begin{aligned} y_1 &= H_{11}(s)(d_1-u_1)+H_{21}(s)(d_2-u_2), \\ y_2 &= H_{12}(s)(d_1-u_1)+H_{22}(s)(d_2-u_2) \end{aligned} \tag{12}$$

Here we also assume that all transfer functions $H_{ij}(s)$ and $R_i(s)$ do not have poles in the right half-plane of s. The expressions relating input and output signals of the system with closed control loops are obtained from equalities (11) and (12) by simple mathematical transformations:

$$\begin{aligned} y_1 = \Big(\big(H_{11}(s)+\big(H_{11}(s)H_{22}(s)- \\ -H_{12}(s)H_{21}(s)\big)R_2(s)\big)d_1+ \\ +H_{21}(s)d_2\Big)\Big/\Big(\big(1+H_{11}(s)R_1(s)\big)\times \\ \times\big(1+H_{22}(s)R_2(s)\big)- \\ -H_{12}(s)H_{21}(s)R_1(s)R_2(s); \end{aligned} \tag{13}$$

$$\begin{aligned} y_2 = \Big(\big(H_{22}(s)+\big(H_{11}(s)H_{22}(s)- \\ -H_{12}(s)H_{21}(s)\big)R_1(s)\big)d_2+ \\ +H_{12}(s)d_1\Big)\Big/\Big(\big(1+H_{11}(s)R_1(s)\big)\times \\ \times\big(1+H_{22}(s)R_2(s)\big)- \\ -H_{12}(s)H_{21}(s)R_1(s)R_2(s). \end{aligned} \tag{14}$$

The denominator of the obtained fractions (the same for both of them) is analyzed to determine the stability of the system. Notably, this function has no poles in the right half-plane of s. Therefore, the same as in the case of system with one loop, the closed-loop system is stable if all zeros of this function lie in the left complex half-plane of the variable s.

The denominator of fractions (13) and (14) may be rewritten as

$$1 + H_0(s),$$

where the function $H_0(s)$ is defined as follows:

$$\begin{aligned} H_0(s) = H_{11}(s)R_1(s)+ \\ +H_{22}(s)R_2(s)+ \\ +\big(H_{11}(s)H_{22}(s)- \\ -H_{12}(s)H_{21}(s)\big)R_1(s)R_2(s). \end{aligned} \tag{15}$$

Therefore, a criterion similar to the Nyquist criterion can be applied for the given system: for this system to be stable, the hodograph of the function $H_0(i\omega)$ should not enclose the point (−1; 0) on the complex half-plane as the frequency ω changes from 0 to +∞.

Construction of control systems

The first step in constructing a modal control system is defining the modal matrices F (synthesizer) and T (analyzer). The corresponding experimental procedure including studies of resonant modes is given in [14].

The heights of the first and second resonant peaks on the stack-sensor and actuator-vibrometer frequency response curves are analyzed to calculate the modal matrices for numerical solution of the problem. The modal synthesizer F is set so that the first control loop does not induce vibrations of the second mode in the beam and the second loop so that it does not induce vibrations of the first mode. Similarly, the modal analyzer T is set so that the first loop does not react to activation of the second vibration mode, and the second so that it does not react to activation of the first mode.

Analysis of the frequency response revealed that the first and second actuators excite the first mode of the beam's bending vibrations in a ratio of 3.08 : 1.00 and the second form in a ratio of −0.97 : 1.00. The first and second sensors respond to activation of the first mode in a ratio of 3.07 : 1.00, and of the second in a ratio of −0.95 : 1.00. Modal matrices were then obtained from here:

$$\begin{aligned} F &= \begin{bmatrix} 1.01 & -0.49 \\ 0.98 & 1.50 \end{bmatrix}, \\ T &= \begin{bmatrix} 1.01 & 0.96 \\ -0.49 & 1.49 \end{bmatrix}. \end{aligned} \tag{16}$$

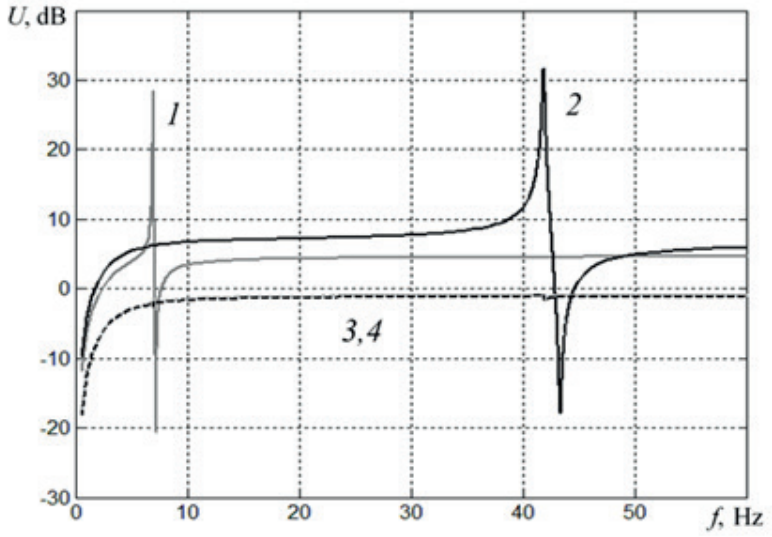

Fig. 3. Frequency response for system corresponding to excitation of vibrations with *i*th modal control loop and measurement with *j*th modal loop; $ij = 11$ (curve *1*), 22 (*2*), 12 (*3*) and 21 (*4*)

These values are sufficiently close to the values of the matrices obtained in the experiment:

$$F^{(\exp)} = \begin{bmatrix} 1.000 & -0.500 \\ 1.035 & 1.525 \end{bmatrix}, \quad T^{(\exp)} = \begin{bmatrix} 1.00 & 1.01 \\ -0.49 & 1.52 \end{bmatrix}. \tag{17}$$

The results of mode separation in modal control loops using the T and F matrices are shown in Fig. 3. The figure also shows the absolute values of the transfer functions H^m_{ij}, corresponding to excitation of vibrations with the *i*th modal control loop and measurement with the *j*th modal loop. These functions are obtained from the transfer functions H_{ij} corresponding to excitation of vibrations with the *i*th actuator and to measurement with the *j*th sensor according to the following formula:

$$H^m_{ij} = \sum_{k=1}^{2}\sum_{l=1}^{2} T_{jl} F_{kl} H_{kl}. \tag{18}$$

As can be seen from the figure, the selected modal matrices provide a good quality of separation of the first and second vibration modes: only the first resonant peak is present on the frequency response curve for H^m_{11} corresponding to the first modal control loop; only the second resonance peak on the frequency response curve for H^m_{22}, with both resonances missing on the cross-coupled frequency response curves for H^m_{12} and H^m_{21}. This means that mutual influence of the control loops is minimal.

Numerical study of the beam's vibrations with control should involve both constructing the control systems and obtaining the results using these systems. The control systems are used to analyze the frequency response curves of the beam, obtained by excitation of vibrations with the stack and by measurement of the vibration amplitude of a point at the upper end of the beam. The effectiveness of the constructed control systems is assessed by comparing the frequency response data near the first and second resonant frequencies of the beam's bending vibrations with the control system turned on and off. The frequency response of the beam with control is obtained from the existing frequency and phase responses of the beam without control in accordance with the mathematical procedure outlined below.

Let three sources of excitation act on the beam, namely, the voltages:

U_d supplied to the stack;

U_1 supplied to the first actuator;

U_2 supplied to the second actuator.

In this case, the transverse displacement y of the point at the upper end of the beam, the voltage Y_1 in the first sensor and Y_2 in the second sensor are measured. The measured values are expressed in terms of the applied

impacts using transfer functions H_d, $H^{(1)}{}_d$, $H^{(2)}{}_d$, $H^{(1)}{}_a$, $H^{(2)}{}_a$, $H^{(11)}{}_{as}$, $H^{(12)}{}_{as}$, $H^{(21)}{}_{as}$, $H^{(22)}{}_{as}$:

$$\begin{cases} y = H_d U_d + H_a^{(1)} U_1 + H_a^{(2)} U_2, \\ Y_1 = H_d^{(1)} U_d + H_{as}^{(11)} U_1 + H_{as}^{(21)} U_2, \\ Y_2 = H_d^{(2)} U_d + H_{as}^{(12)} U_1 + H_{as}^{(22)} U_2. \end{cases} \quad (19)$$

Let the control actions U_1 and U_2 depend on the measured signals Y_1 and $Y_{2\text{ of the}}$ sensors in the following way:

$$\begin{cases} U_1 = -R_{11} Y_1 - R_{12} Y_2, \\ U_2 = -R_{21} Y_1 - R_{22} Y_2. \end{cases} \quad (20)$$

In this case, we can express the displacement y of the point at the upper end of the beam in terms of the voltage U_d applied to the stack by simple mathematical transformations:

$$\begin{cases} y = H_d U_d + H_a^{(1)} U_1 + H_a^{(2)} U_2, \\ U_1 = U_d \left(-R_{21} H_d^{(1)} - R_{22} H_d^{(2)} + \right. \\ + \left(R_{11} R_{22} - R_{12} R_{21} \right) \times \\ \left. \times \left(H_{as}^{(12)} H_d^{(1)} - H_{as}^{(11)} H_d^{(2)} \right) \right) \Big/ \left(1 + \right. \\ + R_{11} H_{as}^{(11)} + R_{12} H_{as}^{(12)} + R_{21} H_{as}^{(21)} + \\ + R_{22} H_{as}^{(22)} + \left(R_{11} R_{22} - R_{12} R_{21} \right) \times \\ \left. \times \left(H_{as}^{(11)} H_{as}^{(22)} - H_{as}^{(12)} H_{as}^{(21)} \right) \right), \\ U_2 = U_d \left(-R_{11} H_d^{(1)} - R_{12} H_d^{(2)} - \right. \\ - \left(R_{11} R_{22} - R_{12} R_{21} \right) \times \\ \left. \times \left(H_{as}^{(22)} H_d^{(1)} - H_{as}^{(21)} H_d^{(2)} \right) \right) \Big/ \left(1 + \right. \\ + R_{11} H_{as}^{(11)} + R_{12} H_{as}^{(12)} + \\ + R_{21} H_{as}^{(21)} + R_{22} H_{as}^{(22)} + \\ + \left(R_{11} R_{22} - R_{12} R_{21} \right) \times \\ \left. \times \left(H_{as}^{(11)} H_{as}^{(22)} - H_{as}^{(12)} H_{as}^{(21)} \right) \right). \end{cases}$$

Thus, based on the known transfer functions of the system without control and the selected control laws, we have calculated the transfer functions of the control system.

Within the framework of this numerical study, we first tested modal control system I, assembled experimentally. Next, we constructed modal control system II, differing from system I by the transfer functions in control loops. The goal in constructing system II was to obtain a control system that would most effectively reduce the amplitude of forced bending vibrations of the beam at the first and second resonances. System I, tested in numerical study, differs from the modal system used in the experiment only by the gains in control loops, which were selected from the condition of the greatest efficiency of the system.

The transfer functions and gains for both loops of control systems I and II are given in Appendix.

Fig. 4, *a* shows the Nyquist diagram for control system I, obtained for both control loops in accordance with formula (15). Fig. 4, *b* shows a segment of this diagram near the point (−1; 0). Since the hodograph does not enclose the point (−1; 0) on the complex plane, this control system is stable. The Nyquist diagram for control system II looks similar.

Fig. 5 shows the frequency response curve of the beam, obtained for impact with the stack and measurement of the vibration amplitude of the point at the upper end of the beam with and without control for control systems I and II. It can be seen that both of the given control systems are sufficiently effective in reducing the vibration amplitude at both the first and the second resonances. Control system I reduces the vibration amplitude by 87.8% at the first resonance and by 89.1% at the second. Control system II reduces the vibration amplitude by 92.4% at the first resonance and by 90.7% at the second. Thus, control system II is somewhat more effective than system I. However, when system II is used, two resonances instead of one appear near the beam's first and second resonant frequencies.

The results of control in experiment and in numerical simulation are given in Table 2. The gains in the first and second loops, K_{p1} and K_{p2} are given for each of the control systems, as well as the ratio of the maximum vibration amplitude of the point at the upper end of the beam with the control turned on to the resonant vibration amplitude of this point without control at the first resonance $y_1/y^{(0)}{}_1$ and at the second resonance $y_2/y^{(0)}{}_2$. As evident from the data in Table 2, the effectiveness of modal control system I in the experiment is close to its effectiveness in numerical study, and the results of system II are better than those of system I, especially for the first resonant frequency.

Conclusion

We have constructed a finite-element model of the experimental setup given in [1, 14], taking into account the piezoelectric effect. This model allowed to numerically obtain the frequency responses for different impacts on the beam and measurements of the output signal. The calculated results were sufficiently close to

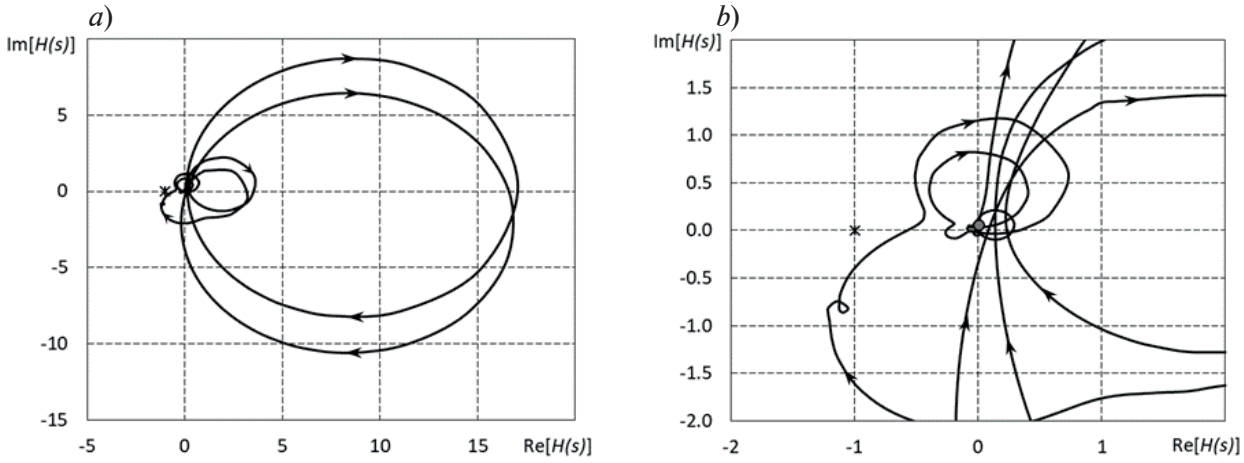

Fig. 4. Nyquist diagrams for both loops of control system I: general view (*a*) and enlarged fragment (*b*)

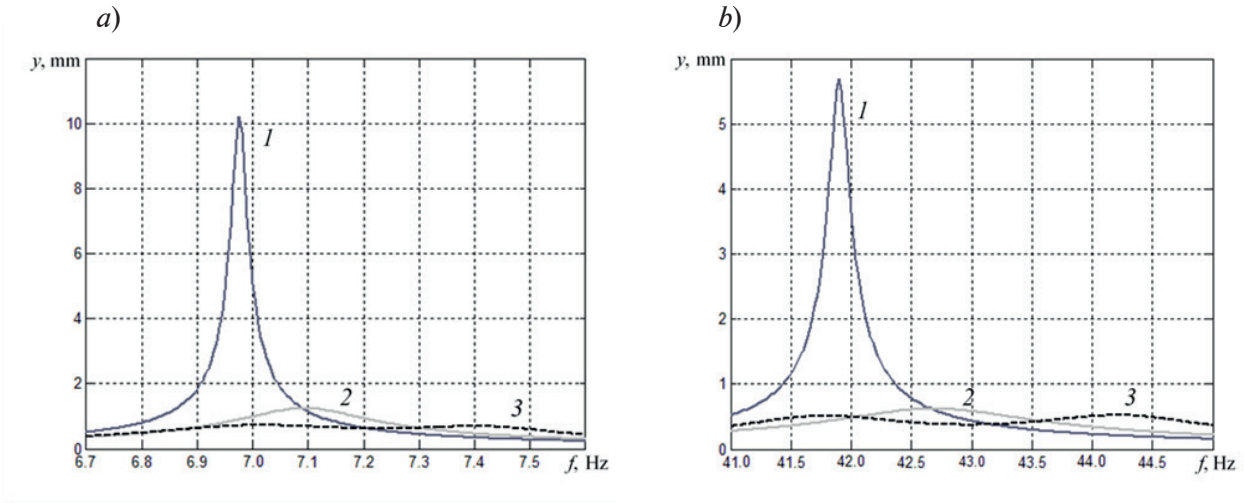

Fig. 5. Frequency response of beam without control (curve *1*) and with control for systems I (*2*) and II (*3*) near the first (*a*) and second (*b*) resonances

Table 2

Performance characteristics of different control system obtained numerically and experimentally

Control system	K_{p1}	K_{p2}	$y_1/y^{(0)}{}_1$, %	$y_2/y^{(0)}$, %
I (experiment)	0.100	0.020	16.5	12.8
I (simulation)	0.170	0.044	12.2	10.9
II (simulation)	0.530	0.650	7.6	9.3

Notations: K_{p1}, K_{p2} are the gains in the first and second loops; $y_1/y^{(0)}{}_1$, $y_2/y^{(0)}{}_2$ are the ratios of the maximum vibration amplitude of a point at the upper end of the beam with the control switched on to the resonant vibration amplitude of this point without control at the first and second resonances, respectively.

the characteristics obtained experimentally. The resonance peaks obtained by simulation and by experiment have different heights because of the difference in the damping factors of the real system and the finite element model.

Based on the frequency and phase response of the system, obtained numerically, we have constructed the solutions to the problem of beam vibrations with modal control for different control laws. The results of numerical simulation of the most effective control system created within the framework of the experiment (with resonant amplitudes at the first and second resonances decreased by 87.8% and 89.1%, respectively) proved closed to the experiment (with a decrease by 83.5% and 87.2%). We have formulated and tested more effective control laws for both loops, resulting in lower resonant amplitudes of the beam's vibrations than the systems considered in the experiment (with resonant amplitudes decreased by 92.4% and 90.7%).

Appendix

Transfer functions of control loops

Transfer function of the first loop of control system I:

$$R_1^{(1)}(s) = \left(44s^6 + 7.2\cdot10^3 s^5 + 1.3\cdot10^8 s^4 + \right.$$
$$+1.4\cdot10^{10} s^3 + 5.5\cdot10^{13} s^2 + 4.8\cdot10^{15} s +$$
$$\left.+1.1\cdot10^{17}\right/\left(s^7 + 668s^6 + 3.1\cdot10^6 s^5 + \right.$$
$$+7.4\cdot10^8 s^4 + 1.3\cdot10^{12} s^3 +$$
$$\left.+1.8\cdot10^{14} s^2 + 7.1\cdot10^{15} s + 6.3\cdot10^{17}\right).$$

Gain $K^{(1)}_{p1} = 0.170$.

Transfer function of the second loop of control system I

$$R_2^{(1)}(s) = \left(1.4\cdot10^5 s^5 + 9.3\cdot10^7 s^4 + 2\cdot10^{11} s^3 + \right.$$
$$+1.1\cdot10^{14} s^2 + 2.9\cdot10^{16} s +$$
$$\left.+1.92\cdot10^{18}\right)\Big/\left(s^7 + 1.1\cdot10^3 s^6 + 2.1\cdot10^6 s^5 + \right.$$
$$+1.8\cdot10^9 s^4 + 1.1\cdot10^{12} s^3 +$$
$$\left.+6\cdot10^{14} s^2 + 1.1\cdot10^{17} s + 4.36\cdot10^{19}\right).$$

Gain $K^{(1)}_{p2} = 0.044$.

Transfer function of the first loop of control system II:

$$R_1^{(2)}(s) = \left(403s^4 + 2.9\cdot10^4 s^3 + \right.$$
$$+9.7\cdot10^8 s^2 + 8.6\cdot10^9 s +$$
$$\left.+1.88\cdot10^{12}\right)\Big/\left(s^5 + 1.1\cdot10^3 s^4 + \right.$$
$$+2.7\cdot10^6 s^3 + 1.5\cdot10^9 s^2 +$$
$$\left.+7.8\cdot10^9 s + 3.54\cdot10^{12}\right).$$

Gain $K^{(2)}_{p1} = 0.530$.

Transfer function of the second loop of control system II:

$$R_2^{(2)}(s) = \left(2.2\cdot10^5 s^4 + 8\cdot10^6 s^3 + \right.$$
$$+2.7\cdot10^{11} s^2 + 4.2\cdot10^{12} s +$$
$$\left.+1.7\cdot10^{16}\right)\Big/\left(s^6 + 372s^5 + \right.$$
$$+1.5\cdot10^6 s^4 + 4.1\cdot10^8 s^3 +$$
$$\left.+4.2\cdot10^{11} s^2 + 3.4\cdot10^{13} s + 2.6\cdot10^{16}\right).$$

Gain $K^{(2)}_{p2} = 0.650$.

REFERENCES

[1] **A.K. Belyaev, A.V. Fedotov, H. Irschik, et al.,** Experimental study of local and modal approaches to active vibration control of elastic systems, Structural Control and Health Monitoring. 25(8) (2017) e2105.

[2] **L.A. Gould, M.A. Murray-Lasso,** On the modal control of distributed parameter systems with distributed feedback, IEEE Transactions on Automatic Control. 11(4) (1966) 729–737.

[3] **L. Meirovitch,** Dynamics and control of structures, John Wiley & Sons, New York, 1990.

[4] **C.-K. Lee, F.C. Moon,** Modal sensors/actuators, ASME Journal of Applied Mechanics. 57(2) (1990) 434–441.

[5] **A. Donoso, J.C. Bellido,** Systematic design of distributed piezoelectric modal sensors/actuators for rectangular plates by optimizing the polarization profile, Structural and Multidisciplinary Optimization. 38(4) (2009) 347–356.

[6] **U. Stoebener, L. Gaul,** Modal vibration control for PVDF coated plates, Journal of Intelligent Material Systems and Structures. 11(4) (2000) 283–293.

[7] **S. Hurlebaus, U. Stoebener, L. Gaul,** Vibration reduction of curved panels by active modal control, Computers and Structures. 86(3–5) (2008) 251–257.

[8] **G. Zenz, W. Berger, J. Gerstmayr, et al.,** Design of piezoelectric transducer arrays for

passive and active modal control of thin plates, Smart Structures and Systems. 12(5) (2013) 547–577.

[9] **F. Braghin, S. Cinquemani, F. Resta,** A new approach to the synthesis of modal control laws in active structural vibration control, Journal of Vibration and Control. 19(2) (2012) 163–182.

[10] **S. Cinquemani, D. Ferrari, I. Bayati,** Reduction of spillover effects on independent modal space control through optimal placement of sensors and actuators, Smart Materials and Structures. 24(8) (2015) 085006.

[11] **G. Canciello, A. Cavallo,** Selective modal control for vibration reduction in flexible structures, Automatica. 75 (January) (2017) 282–287.

[12] **M. Biglar, M. Gromada, F. Stachowicz, T. Trzepiecinski,** Optimal configuration of piezoelectric sensors and actuators for active vibration control of a plate using a genetic algorithm, Acta Mechanica. 226 (10) (2015) 3451–3462.

[13] **Z.-G. Song, F.-M. Li, E. Carrera, P. Hagedorn,** A new method of smart and optimal flutter control for composite laminated panels in supersonic airflow under thermal effects, Journal of Sound and Vibration. 414 (3 February) (2018) 218–232.

[14] **A.K. Belyaev, V.A. Polyanskiy, N.A. Smirnova, A.V. Fedotov,** Identification procedure in the modal control of a distributed elastic system, St. Petersburg Polytechnical University Journal: Physics and Mathematics. 10 (2) (2017) 69–81.

[15] **A. Preumont,** Mechatronics: dynamics of electromechanical and piezoelectric systems, Springer, Dordrecht, 2006.

Received 17.01.2019, accepted 18.02.2019.

THE AUTHOR

FEDOTOV Aleksandr V.
Institute for Problems in Mechanical Engineering, RAS
61 Bolshoi Ave. V.O., St. Petersburg, 199178, Russian Federation
alvafed@yandex.ru

СПИСОК ЛИТЕРАТУРЫ

1. **Belyaev A.K., Fedotov A.V., Irschik H., Nader M., Polyanskiy V.A., Smirnova N.A.** Experimental study of local and modal approaches to active vibration control of elastic systems // Structural Control and Health Monitoring. 2017. Vol. 25. No. 8. P. e2105.

2. **Gould L.A., Murray-Lasso M.A.** On the modal control of distributed parameter systems with distributed feedback // IEEE Transactions on Automatic Control. 1966. Vol. 11. No. 4. Pp. 729–737.

3. **Meirovitch L.** Dynamics and control of structures. New York: John Wiley & Sons, 1990. 425 p.

4. **Lee C.-K., Moon F.C.** Modal sensors/actuators // ASME Journal of Applied Mechanics. 1990. Vol. 57. No. 2. Pp. 434–441.

5. **Donoso A., Bellido J.C.** Systematic design of distributed piezoelectric modal sensors/actuators for rectangular plates by optimizing the polarization profile // Structural and Multidisciplinary Optimization. 2009. Vol. 38. No. 4. Pp. 347–356.

6. **Stoebener U., Gaul L.** Modal vibration control for PVDF coated plates // Journal of Intelligent Material Systems and Structures. 2000. Vol. 11. No. 4. Pp. 283–293.

7. **Hurlebaus S., Stoebener U., Gaul L.** Vibration reduction of curved panels by active modal control // Computers and Structures. 2008. Vol. 86. No. 3–5. Pp. 251–257.

8. **Zenz G., Berger W., Gerstmayr J., Nader M., Krommer M.** Design of piezoelectric transducer arrays for passive and active modal control of thin plates // Smart Structures and Systems. 2013. Vol. 12. No. 5. Pp. 547–577.

9. **Braghin F., Cinquemani S., Resta F.** A new approach to the synthesis of modal control laws in active structural vibration control // Journal of Vibration and Control. 2012. Vol. 19. No. 2. Pp. 163–182.

10. **Cinquemani S., Ferrari D., Bayati I.** Reduction of spillover effects on independent modal space control through optimal placement of sensors and actuators // Smart Materials and Structures. 2015. Vol. 24. No. 8. P. 085006.

11. **Canciello G., Cavallo A.** Selective modal control for vibration reduction in flexible structures // Automatica. 2017. Vol. 75. January. Pp. 282–287.

12. **Biglar M., Gromada M., Stachowicz F.,**

Trzepiecinski T. Optimal configuration of piezoelectric sensors and actuators for active vibration control of a plate using a genetic algorithm // Acta Mechanica. 2015. Vol. 226. No. 10. Pp. 3451–3462.

13. **Song Z.-G., Li F.-M., Carrera E., Hagedorn P.** A new method of smart and optimal flutter control for composite laminated panels in supersonic airflow under thermal effects // Journal of Sound and Vibration. 2018. Vol. 414. 3 Febrary. Pp. 218–232.

14. Беляев А.К., **Полянский В.А., Смирнова Н.А., Федотов А.В.** Процедура идентификации при модальном управлении распределенным упругим объектом // Научно-технические ведомости СПБГПУ. Физико-математические науки. 2017. Т. 10. № 2. С. 69–81.

15. **Preumont A.** Mechatronics: dynamics of electromechanical and piezoelectric systems. Dordrecht: Springer, 2006.

Статья поступила в редакцию 17.01.2019, принята к публикации 18.02.2019.

СВЕДЕНИЯ ОБ АВТОРЕ

ФЕДОТОВ Александр Васильевич – младший научный сотрудник Института проблем машиноведения РАН.

199178, Российская Федерация, г. Санкт-Петербург, Большой проспект В.О., 61.

alvafed@yandex.ru

DOI: 10.18721/JPM.12113
УДК 539.3

A QUASISTATIC APPROACH TO THE THERMOELASTICITY PROBLEM OF ROTATING BODIES

S.V. Polyanskiy[1], *A.K. Belyaev*[1,2]

[1] Institute for Problems in Mechanical Engineering of the RAS,

St. Petersburg, Russian Federation;

[2]Peter the Great St. Petersburg Polytechnic University, St. Petersburg, Russian Federation

The non-stationary problem of thermoelasticity for rotating bodies has been solved through determining the optimal temperature and stress fields in the rolling mills of hot rolling systems, this determination being an issue of the day. The Eulerian approach was applied, it allowed us to reduce the number of independent variables and consider these fields as quasistatic ones. The heavy temperature gradients and stresses bound up with them, as well as the rotating nature of these fields are typical for the processes taking place in the roll core. To solve the problem of simulation of these processes, we proposed to use Fourier series, which allowed us to obtain a solution with a sufficient accuracy for the large number of terms of the series being considered. The peculiarity of the solution obtained is that the stress maximum locates at an insignificant depth beneath the roll surface.

Keywords: temperature stress, mill roll, rotating system, Fourier series

Citation: S.V. Polyanskiy, A.K. Belyaev, A quasistatic approach to the thermoelasticity problem of rotating bodies, St. Petersburg Polytechnical State University Journal. Physics and Mathematics. 12 (1) (2019) 143–152. DOI: 10.18721/JPM.12113

КВАЗИСТАТИЧЕСКИЙ ПОДХОД К РЕШЕНИЮ ЗАДАЧИ ТЕРМОУПРУГОСТИ ВРАЩАЮЩИХСЯ ТЕЛ

С.В. Полянский[1], *А.К. Беляев*[1,2]

[1] Институт проблем машиноведения РАН, Санкт-Петербург, Российская Федерация;

[2]Санкт-Петербургский политехнический университет Петра Великого,

Санкт-Петербург, Российская Федерация

Представлено решение нестационарной задачи термоупругости вращающихся тел на примере определения оптимальных температурных полей и полей напряжений в прокатных валках систем горячего проката, что представляет собой актуальную проблему. Используется пространственное описание, позволяющее уменьшить число независимых переменных и рассматривать поля температуры и напряжений как квазистатические. Для процессов, происходящих в теле валка, характерны большие градиенты температуры и связанные с ними напряжения, а также вращающийся характер полей. Для решения задачи моделирования указанных процессов предлагается использовать ряды Фурье, которые позволяют при довольно большом количестве рассматриваемых членов ряда получать решение с достаточной точностью. Особенностью полученного решения является локализация максимальных напряжений на незначительной глубине от поверхности валка.

Ключевые слова: температурное напряжение, прокатный валок, вращающаяся система, ряд Фурье

Ссылка при цитировании: Полянский С.В., Беляев А.К. Квазистатический подход к решению задачи термоупругости вращающихся тел// Научно-технические ведомости СПбГПУ. Физико-математические науки. 2019. Т. 12. № 1. С. 142–155. DOI: 10.18721/JPM.12113

Introduction

Problems of thermoelasticity in rotating bodies subjected to thermal shocks remain relevant today, with rational solutions obtained for different practical applications.

Simulation of hot rolling of sheet metal, with rotating rolls of the rolling mill operating under heavy mechanical and thermal stress, is a vivid example of such an application. The rolls are affected by a combination of cyclic, mechanical and thermal stresses; characteristic failure of the orange peel type, associated with blister delamination, is observed in the surface layer of the rolls as a result.

The goal of this study has consisted in developing a method for effectively solving thermoelastic problems in rotating bodies exposed to thermal shocks.

The uncoupled thermoelastic problem is considered in several stages. The first stage involves solving a non-stationary boundary problem of thermal conductivity, generating a temperature field that depends on both time and space coordinates. The second stage is aimed at determining the stress-strain state of a rotating body. We have taken a mathematical approach reducing partial differential equations with three independent variables to ordinary differential equations, which makes it possible to obtain a solution in the form of a single series.

The approach we have proposed is universally applicable, as evidenced by a complete solution to the problem of finding thermal stresses in rotating rolls during hot rolling of sheet metal. It was observed that surface fracture of mill rolls in operation has a lamellar structure and cracks form at a relatively small depth (1–2 mm) from the surface rather than on it. The nature of cracks suggests that one of the key factors causing them are non-stationary thermal stresses occurring as a result of sudden changes in temperature. These effects are explained by significant temperature gradients induced by thermal shocks in physics of metals.

The developed approach for analytical calculation of localized temperature fields is preferable to numerical methods, since it does not involve iterative selection of the size of the grids, which is unknown in advance.

The given problem is particularly important for industry, as confirmed by numerous studies considering both temperature fields as a separate issue and temperature fields and mechanical stresses arising during rolling.

Three main approaches are used in study of temperature fields:

direct experimental measurement of surface temperature fields [1];

calculation of temperature fields by the finite element method (FEM) or by the grid method taking into account roll rotation or boundary conditions [2–10];

calculation of temperature fields by the Fourier method in the form of a sum of a series with respect to eigenfunctions [11–14].

A notable group of studies [15–17] developed the theory of harmonic finite elements. In this case, a sequence of one-dimensional FEM problems is solved separately for each harmonic amplitude in a Fourier series and the resulting amplitudes are then multiplied by the corresponding harmonic function and summed.

Study of mechanical stress fields has only been carried out by finite element methods [3, 5, 6, 8–10, 16–18]. The temperature field is taken as the load and the plane problem of elasticity theory is then solved. Practically all solutions, except those given in [17], yield the maximum stresses (by the von Mises criteria) located on the surface of the rolls, in the area of contact with the rolled metal. This result is generally recognized as valid, so in [14], after the temperature was calculated by the Fourier method, the modulus of surface kinematic hardening was calculated, instead of the stresses, using the temperature potential.

However, the nature of failure in rolls indicates that the maximum mechanical stresses are located at small depths within the roll core. The standard FEM approach is inadequate for describing this situation. The same applies to “harmonic” finite elements [15–17]: it was found that these elements cannot be used to calculate stresses, since they yield stresses that are 1.5 times higher than those obtained by the “standard” FEM approach.

In this study, we suggest a spatial approach reducing the non-stationary thermal conductivity problem to a quasistationary one, which makes it possible to develop a mathematical model of thermal conductivity in a rotating elastic body. The temperature distribution field can then be found, and thermal stresses which are particular solutions to the thermoelastic problem are obtained using the thermoelastic potential. The boundary conditions are to be satisfied

via the Airy stress function using the example of trivial loading conditions.

Determining the temperature field in the rolls

Fig. 1 shows the heating and cooling patterns of the mill roll. The roll contacts a hot slab in a narrow contact sector, and then undergoes a complex cooling cycle in different media. In our case, we consider alternate cooling with water and air; other possible schemes involve cooling with a water-vapor mixture, with only water, or only air. The sectors indicate areas with different types of cooling.

Assuming that the temperature field does not depend on the axial coordinate, the non-stationary thermal conductivity equation has the form

$$\lambda \Delta T - \gamma \dot{T} = 0, \qquad (1)$$

where T is the temperature; λ and γ are the thermal conductivity and heat capacity of the roll material, respectively; Δ is the two-dimensional Laplace operator; the dot indicates the material derivative with respect to time.

We have used the spatial (Eulerian) approach, reducing the number of independent variables. Provided that the roll rotates at a constant angular velocity ω, the expression for the material derivative of the temperature field is simplified:

$$\dot{T}(r,\varphi,t) = \frac{\partial T}{\partial t} + \frac{\partial T}{\partial r}\frac{dr}{dt} + \frac{\partial T}{\partial \varphi}\frac{d\varphi}{dt} = \omega \frac{\partial T}{\partial \varphi}, \qquad (2)$$

where r and φ are the radius and the angle in the polar coordinate system.

Since the problem is stationary,

$$\frac{\partial T}{\partial t} = 0, \ \frac{dr}{dt} = 0, \ \frac{d\varphi}{dt} = \omega.$$

As a result, we obtain the equation of stationary thermal conductivity with two independent variables:

$$\lambda\left(\frac{\partial^2 T}{\partial r^2} + \frac{1}{r}\frac{\partial T}{\partial \varphi} + \frac{1}{r^2}\frac{\partial^2 T}{\partial \varphi^2}\right) - \gamma\omega\frac{\partial T}{\partial \varphi} = 0. \qquad (3)$$

The surface temperature of the roll in the narrow zone of direct contact between the roll and the sheet, where $0 \le \varphi \le \varphi_0$ (see Fig. 1) is taken equal to T_c = 600 °C as the average between the temperature of the hot sheet and the temperature of the roll. A boundary condition of the third kind is imposed for the rest of the zone ($\varphi_0 < \varphi \le 2\pi$):

$$r = R, \varphi_0 < \varphi \le 2\pi,$$

$$\lambda\frac{\partial T}{\partial r} + \beta(T - T_m) = 0,$$

where R is the radius of the roll; $T = T_m(\varphi)$ is the temperature of the air/water mixture cooling the surface of the roll.

These two conditions can be written as a single boundary condition of the third kind:

$$r = R, \ \eta\frac{\partial T}{\partial r} + T - T_e = 0, \qquad (4)$$

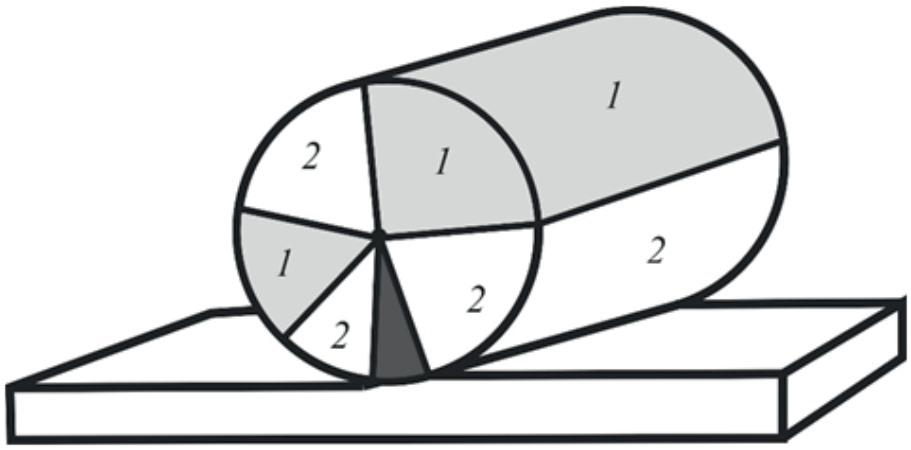

Fig. 1. Rolling pattern (only upper roll is shown) and pattern for cooling roll with water (*1*) and air (*2*); the black sector corresponds to the contact area

where

$$T_e = T_e(\varphi) = \begin{cases} T_c, & 0 \le \varphi \le \varphi_0, \\ T_m(\varphi), & \varphi_0 < \varphi \le 2\pi; \end{cases}$$
$$\eta = \frac{\lambda}{\beta} = \begin{cases} 0, & 0 \le \varphi \le \varphi_0, \\ \eta(\varphi), & \varphi_0 < \varphi \le 2\pi; \end{cases} \quad (5)$$

where the parameters $\lambda(\varphi)$, $\beta(\varphi)$, $T_m(\varphi)$ are piecewise constant functions of the angle φ.

To solve boundary problem (3)–(5), we apply the method of integral transforms:

$$\frac{1}{2\pi}\int_0^{2\pi} T(r,\varphi)e^{-in\varphi}d\varphi = T_n(r),$$

and then seek a solution in the form of a bilateral series:

$$T(r,\varphi) = \sum_{n=-N}^{N} T_n(r)e^{in\varphi}. \quad (6)$$

After integral transformation, Eq. (3) takes the form

$$\frac{d^2T_n}{dr^2} + \frac{1}{r}\frac{dT_n}{dr} + \left(-\frac{n^2}{r^2} - \frac{in\gamma\omega}{\lambda}\right)T_n = 0. \quad (7)$$

The solution of Eq. (7) for $n \neq 0$ is expressed in terms of Bessel functions J_n and Y_n:

$$T_n(r) = A_nJ_n\left(\sqrt{\frac{-in\omega\gamma}{\lambda}}r\right) + B_nY_n\left(\sqrt{\frac{-in\omega\gamma}{\lambda}}r\right). \quad (8)$$

Since $Y_n(0)=\infty$, $B_n=0$ due to limited temperature in the center of the roll. Then,

$$T_n(r) = A_nJ_n\left(\sqrt{\frac{-in\omega\gamma}{\lambda}}r\right) = A_nJ_n\left(-\frac{1-i}{\sqrt{2}}a\sqrt{n}\xi\right), \quad (9)$$

where $a = \sqrt{\frac{\omega\gamma}{\lambda}}R$ and a dimensionless radius $\xi=r/R$, $0 \le \xi \le 1$ is introduced.

Let us consider the case $n = 0$ separately. In this case, Eq. (7) has the form

$$\frac{d^2T_0}{\partial r^2} + \frac{1}{r}\frac{dT_0}{\partial r} = \frac{1}{r}\frac{d}{dr}\left(r\frac{dT_0}{\partial r}\right) = 0.$$

Then, $T_0=C\ln r+A_0$, and it follows that $C = 0$, i.e., $T_0=$ const, from the boundedness condition for $r = 0$.

Now let us carry out integral transformation of boundary condition (4):

$$\frac{1}{2\pi}\int_0^{2\pi}\left[\eta(\varphi)\frac{\partial T}{\partial r} + T - T_e(\varphi)\right]e^{-in\varphi}d\varphi = 0. \quad (10)$$

Representing $\eta(\varphi)$ in the form of a Fourier series, we introduce the following notations:

$$\eta(\varphi) = \sum_{k=0}^{k}\eta_k e^{ik\varphi},$$
$$\eta_k = \frac{1}{2\pi}\int_0^{2\pi}\eta(\varphi)e^{-ik\varphi}d\varphi, \quad (11)$$
$$\tau_n = \frac{1}{2\pi}\int_0^{2\pi}T_e(\varphi)e^{-in\varphi}d\varphi.$$

Let us now separately calculate the first term in Eq. (10):

$$\frac{1}{2\pi}\int_0^{2\pi}\eta(\varphi)\frac{\partial T}{\partial r}e^{-in\varphi}d\varphi = \frac{1}{2\pi}\sum_{k=0}^{k}\eta_k\int_0^{2\pi}\frac{\partial T}{\partial r}e^{-i(n-k)\varphi}d\varphi = \sum_{k=0}^{k}\eta_k\frac{d}{dr}\left(\frac{1}{2\pi}\int_0^{2\pi}Te^{-i(n-k)\varphi}d\varphi\right) = \sum_{k=0}^{k}\eta_k\frac{d}{dr}T_{n-k}(r) = \sum_{k=0}^{k}\eta_kT'_{n-k}.$$

Substituting the explicit expression for T_n and calculating the derivative of the Bessel function by the rule

$$J_n'(z) = J_{n-1}(z) - \frac{n}{z}J_n(z) = 0,$$

we obtain the following formulation for the boundary condition:

$$\begin{cases} A_0 - \tau_0, n = 0; \\ \sum_{k=0}^{K}\left(\frac{\eta_k}{r}A_{n-k}\left[\frac{1-i}{\sqrt{2}}a\sqrt{n-k}J_{n-k-1}(\chi_{n-k}) - (n-k)J_{n-k}(\chi_{n-k})\right] + A_nJ_n(\chi_{n-k})\right) - \tau_n = 0, \ n \neq 0, \end{cases} \quad (12)$$

where $\chi_{n-k} = \frac{1-i}{\sqrt{2}}a\sqrt{n-k}$.

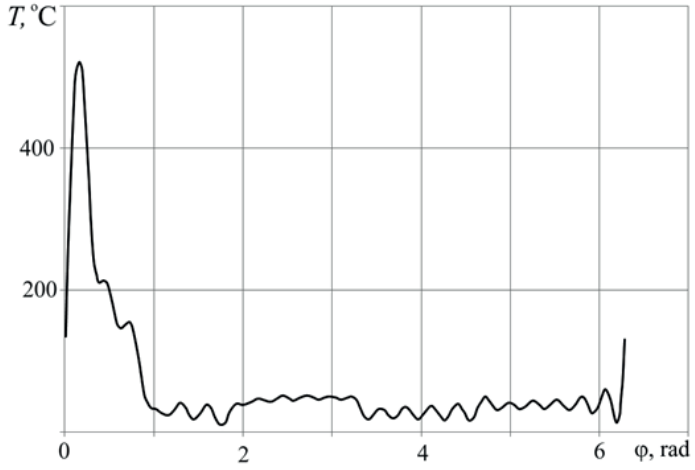

Fig. 2. Calculated temperature on surface of roll as function of angular coordinate ($r = R$); calculation parameters are given in the text

As a result, we obtain a system of n equations with unknown coefficients A_n. To solve it, we use the asymptotic behavior of the Bessel function for large values of the argument:

$$J_n(z) = \sqrt{\frac{2}{\pi z}} \cos\left(z - \frac{n\pi}{2} - \frac{\pi}{4}\right),$$

since the argument of Bessel functions for real parameters of hot rolling ($a = 201.6$) takes the values

$$\left|\frac{1-i}{\sqrt{2}}\right| a\sqrt{n} \approx 201.6\sqrt{n}, \; n = 1,2,\ldots .$$

Substituting these values of the argument, we obtain:

$$J_n(z) = \sqrt{\frac{2}{\pi z}} \cos\left(z - \frac{n\pi}{2} - \frac{\pi}{4}\right) \approx$$
$$\approx \frac{1}{2}\sqrt{\frac{2\sqrt{2}}{\pi(1-i)a\sqrt{n}}} \cdot e^{\frac{a\sqrt{n}}{\sqrt{2}}} \cdot e^{i\left[\frac{a\sqrt{n}}{\sqrt{2}} - \frac{n\pi}{2} - \frac{\pi}{4}\right]}. \quad (13)$$

Thus, by solving the system of equations for the coefficients A_n and substituting them into Eqs. (9) and (6) for $T(r,\varphi)$, we obtain the temperature distribution in the roll.

Since the coefficients in Eq. (12) contain exponential factors, the system's matrix is ill-conditioned. For this reason, we need to estimate the required number of series terms for each function and use a special algorithm for the solution.

The nature of Eqs. (12) allows using an algorithm with choice of the pivot element. If the matrix (η_k) is given asymetrically (see expression (11)), the system matrix becomes triangular, thus allowing to successively calculate all the coefficients A_n. A graph of the temperature field on the surface of the roll as a function of the angular coordinate is given below (Fig. 2) as an example of the calculations for the following numerical values of the system parameters:

1. T_c = 600 °C, φ_0 = 12.68° = 0.2213 rad (in the contact zone);

2. T_e = 25 °C, β = 41700 W/°C m^2 (for water);

T_0 = 25 °C, β = 1500 W/°C m^2 (for air);

3. λ = 31 W/°C m^2, γ = 0.673 kJ/°C kg (for rolls)

Calculating thermal stresses

To calculate the thermal stress field, we use the thermoelastic displacement potential Φ which is introduced by the equality $\underline{u} = \nabla\Phi$. In the problem of plane deformation, The thermoelastic potential Φ is introduced in the problem of plane deformation, satisfying the equation [19]:

$$\Delta\Phi = \frac{1+\nu}{1-\nu}\alpha T. \quad (14)$$

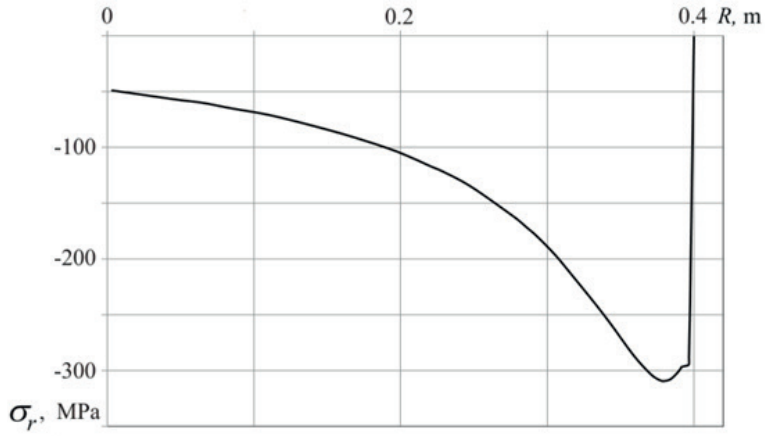

Fig. 3. Radial distribution of stresses σ_r in roll core with $\varphi = 0.1$ rad

Differentiating both sides of this equation over time and substituting *dT/dt* from Eq. (1), we obtain:

$$\frac{d}{dt}\Delta\Phi = \frac{1+\nu}{1-\nu}\alpha\frac{\lambda}{\beta}\Delta T. \qquad (15)$$

Since the thermoelastic potential provides only a partial solution of the thermoelastic equation, the sign of the operator Δ can be omitted in both sides of Eq. (15). As a result, we have:

$$\frac{d}{dt}\Phi = \frac{1+\nu}{1-\nu}\alpha\frac{\lambda}{\beta}T. \qquad (16)$$

The material derivative of the thermoelastic potential in a rotating coordinate system is calculated similarly to calculation by expression (2):

$$\frac{d}{dt}\Phi = \frac{\partial\Phi}{\partial\varphi}\frac{\partial\varphi}{\partial t} = \omega\frac{\partial\Phi}{\partial\varphi} = \frac{1+\nu}{1-\nu}\alpha\frac{\lambda}{\beta}T, \qquad (17)$$

from which we obtain the explicit expression for the thermoelastic potential:

$$\Phi = \frac{1}{\omega}\frac{1+\nu}{1-\nu}\alpha\frac{\lambda}{\beta}\int T d\varphi = \\ = \frac{1}{\omega}\frac{1+\nu}{1-\nu}\alpha\frac{\lambda}{\gamma}\left[\sum_{n=-N}^{N} T_n(r)\frac{1}{in}e^{in\varphi}\right]. \qquad (18)$$

The thermal stresses corresponding to the obtained thermoelastic potential are found by forward differentiation (see [19]):

$$\sigma_r^{\Phi} = -2G\left[\frac{1}{r}\frac{\partial\Phi}{\partial r} + \frac{1}{r^2}\frac{\partial^2\Phi}{\partial\varphi^2}\right],$$
$$\sigma_\varphi^{\Phi} = -2G\frac{\partial^2\Phi}{\partial r^2},$$
$$\tau_{r\varphi}^{\Phi} = 2G\frac{\partial}{\partial r}\left[\frac{1}{r}\frac{\partial\Phi}{\partial\varphi}\right], \qquad (19)$$
$$\sigma_z^{\Phi} = -2G\Delta\Phi = -2G\frac{1+\nu}{1-\nu}\alpha T,$$
$$\tau_{zr}^{\Phi} = \tau_{z\varphi}^{\Phi} = 0.$$

Airy function for satisfying boundary conditions

The given thermal stresses are particular solutions, and in the general case they do not satisfy the boundary conditions. Below we demonstrate how to fulfill trivial force conditions on the entire surface of the roll. To adjust the solution so that it satisfies the trivial boundary conditions, let us introduce the total stresses:

$$\sigma_r = \sigma_r^{\Phi} + \sigma_r^{U},$$
$$\sigma_\varphi = \sigma_\varphi^{\Phi} + \sigma_\varphi^{U},$$
$$\tau_{r\varphi} = \tau_{r\varphi}^{\Phi} + \tau_{r\varphi}^{U}$$

and so on.

The superscript here indicates the stresses determined by the Airy function in the plane

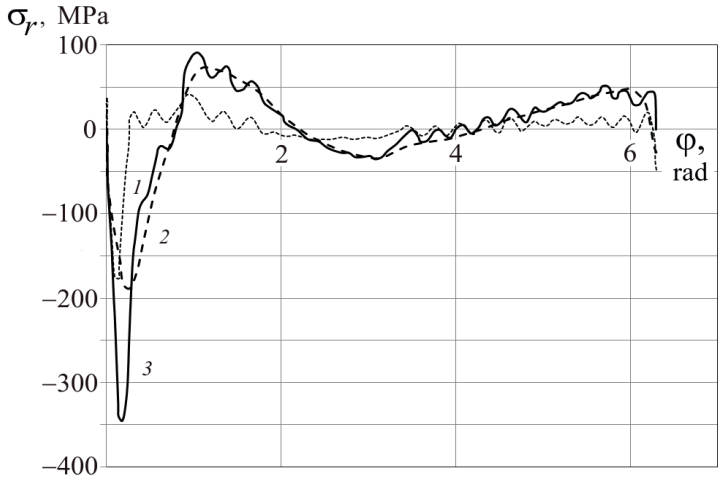

Fig. 4. Radial distribution of stresses σ_r along angular coordinate φ at different depths h, mm, from roll surface: 0.5 (*1*), 4 (*2*), 100 (*3*)

problem $U(r\,\varphi)$.

It satisfies the biharmonic equation $\Delta\Delta U = 0$ and allows to find the stresses:

$$\begin{aligned}
\sigma_r^U &= \frac{1}{r}\frac{\partial U}{\partial r} + \frac{1}{r^2}\frac{\partial U^2}{\partial \varphi^2},\\
\sigma_\varphi^U &= \frac{\partial^2 U}{\partial r^2},\\
\tau_{r\varphi}^U &= -\frac{\partial}{\partial r}\left(\frac{1}{r}\frac{\partial U}{\partial \varphi}\right),\\
\sigma_z^U &= \nu\left(\sigma_r^U + \sigma_\varphi^U\right),\\
\tau_{zr}^U &= \tau_{z\varphi}^U = 0.
\end{aligned} \tag{20}$$

The Airy function as a Fourier series has the following general form (see [19, 20]):

$$\begin{aligned}
U(\xi,\varphi) = &\left[\alpha\xi^3 + \beta\xi^{-1} + \right.\\
&\left. + \lambda\xi + \gamma\xi\ln\xi + \chi\varphi\xi\right]e^{i\varphi} +\\
&+\sum_{n=2}^{\infty}\left(P_n\xi^n + Q_n\xi^{n+2}\right)e^{in\varphi},
\end{aligned} \tag{21}$$

and the coefficients α, β, λ, γ, χ, P_n, Q_n can be found from the no-stress boundary condition imposed for the entire surface of the roll:

$$r = R,\ \sigma_r^\Phi + \sigma_r^U = 0,\ \tau_{r\varphi}^\Phi + \tau_{r\varphi}^U = 0. \tag{22}$$

Fig. 3 shows the stress distribution along the roll radius with the angle $\varphi = 0.1$ rad.

Fig. 4 shows a family of radial stress distributions along the angular coordinate in the roll core with different values of its radius.

Rapid growth of stresses at a small depth from the surface and a smooth decrease towards the center of the roll can be clearly observed from Fig. 3. The stress maximum is reached at a depth *h of* about 4 mm from the surface (see Fig. 4).

Discussion of results

The distribution of radial stresses in the roll core that we have obtained differs considerably from the known results calculated using FEM. The maximum radial stresses of 350 MPa are close to the yield strength, with peculiar drops observed on the curves. The zone of these stresses lies in the roll core at a depth of 2–4 mm from the surface, which explains well blister fatigue failure (with blisters 1–4 mm thick falling off from the roll surface during rolling).

The stress maximum below the surface was obtained in [9] by simulating a multilayer system with different mechanical characteristics near the roll surface.

Sharp drops on the stress curves were obtained in [17] by taking into account contact stresses (in addition to thermal ones) in the rolling zone. Unlike the solution we obtained, the depth of the stress maximum by the von Mises criterion was 5% of the radius, which did not help explain blister delamination. In our case, this depth was about 3 cm.

Thus, the approach we proposed and used made it possible to obtain new results for explaining the experimentally observed blister failure of the surface by "plunging" cyclic radial stresses.

The given problem cannot be solved by the FEM method due to huge radial stress gradi-

ents evolving in the subsurface layer, which is about 0.1% of the roll radius. The stress averaging, which automatically occurs inside finite elements, does not allow to adequately model these gradients.

Notably, the Bessel functions in the Fourier series with asymptotic representation contain factors that are exponents of the form $\exp(\lambda r/R)$, where factors λ have a characteristic value of about 1000. Therefore, there is no sense in taking more than forty terms of the Fourier series, since the coefficients of the Fourier series cannot be determined with a given double precision even if special normalization is applied. The "fluctuations" of all functions, seen on the graphs of angular distributions, are related to this circumstance. Naturally, the numerical FEM solution runs into a similar problem for the case with ill conditions, as discussed in the above-cited studies.

Conclusion

We have introduced a spatial approach to the thermoelastic problem in rotating bodies, which made it possible to reduce the number of independent variables and obtain exact solutions for the temperature and stress fields in the form of a single Fourier series. We have formulated the equations for thermal stresses through the thermoelastic potential that we have then used to calculate thermal stresses on the surface and in the core of the roll. We have confirmed that the Airy function could be tailored to satisfy the boundary conditions on the roll surface. While this approach allows to satisfy any boundary conditions set in advance, we have confined ourselves to the case of trivial force boundary conditions imposed on the entire surface of the roll.

As an example of practical application, we have found a thermal stress field for the mill rolls during hot rolling of sheet metal.

Based on the investigation we have carried out, we were able to conclude that thermal stresses make a significant contribution to the stress state of mill rolls, and the magnitude of the temperature component of the stresses and the cyclic pattern with which they occur indicate that roll surface failure can evolve solely due to thermal "shock" induced by heating and cooling of the roll surface.

The effect of thermal stresses dropping to a small depth beneath the roll surface has been obtained for the first time. Importantly, this effect adequately explains the blister nature of failure in the roll. The object chosen for study appeared to be a good model for describing the processes occurring during operation of rotating systems subjected to complex thermal loading.

Thus, the proposed approach to solving the problem may have other important practical applications for analysis of this type of systems, in particular, in metallurgy and mechanical engineering.

The study was carried out with the financial support of RFBR grants 17-08-00783 and 18-08-00201.

REFERENCES

[1] **R.G. Keanini,** Inverse estimation of surface heat flux distributions during high speed rolling using remote thermal measurements, International Journal of Heat and Mass Transfer. 41 (2) (1998) 275–285.

[2] **O.U. Khan, A. Jamal, G.M. Arshed, et al.,** Thermal analysis of a cold rolling process – A numerical approach, Numerical Heat Transfer, Part A: Applications. 46 (6) (2004) 613–632.

[3] **D. Benasciutti,** On thermal stress and fatigue life evaluation in work rolls of hot rolling mill, The Journal of Strain Analysis for Engineering Design. 47 (5) (2012) 297–312.

[4] **A. Saxena, Y. Sahai,** Modeling of fluid flow and heat transfer in twin-roll casting of aluminum alloys, Materials Transactions. 43 (2) (2002) 206–213.

[5] **W.B. Lai, T.C. Chen, C.I. Weng,** Transient thermal stresses of work roll by coupled thermoelasticity, Computational Mechanics. 9 (1) (1991) 55–71.

[6] **A. Saxena, Y. Sahai,** Modeling of thermo-mechanical stresses in twin-roll casting of aluminum alloys, Materials Transactions. 43 (2) (2002) 214 –221.

[7] **S. Serajzadeh,** Effects of rolling parameters on work-roll temperature distribution in the hot rolling of steels, The International Journal of Advanced Manufacturing Technology. 35 (9–10) (2008) 859–866.

[8] **D. Benasciutti, E. Brusa, G. Bazzaro,** Finite elements prediction of thermal stresses in work roll of hot rolling mills, Procedia Engineering. 2 (1) (2010) 707–716.

[9] **M. Toparli, F. Sen, O. Culha, E. Celic,** Thermal stress analysis of HVOF sprayed WC–Co/NiAl multilayer coatings on stainless steel substrate using finite element methods, Journal

of Materials Processing Technology. 190 (1) (2007) 26–32.

[10] **C. Li, H. Yu, G. Deng, et al.,** Numerical simulation of temperature field and thermal stress field of work roll during hot strip rolling, Journal of Iron and Steel Research, International. 14 (5) (2007) 18–21.

[11] **A. Tudor, C. Radulescu, I. Petre,** Thermal effect of the brake shoes friction on the wheel/rail contact, Tribology in Industry. 25 (1–2) (2003) 27–32.

[12] **R.E. Johnson, R.G. Keanini,** An asymptotic model of work roll heat transfer in strip rolling, International Journal of Heat and Mass Transfer. 41 (6) (1998) 871–879.

[13] **M. Dünckelmeyer, C. Krempaszky, E. Werner, et al.,** Analytical modeling of thermo-mechanically induced residual stresses of work rolls during hot rolling, Steel Research International, Metal Forming. 81 (9) (2010) 697–802.

[14] **D. Benasciutti, F. de Bona, M.G. Munteanu,** A semi-analytical finite element approach in machine design of axisymmetric structures, Intech Open Access Publisher. (2011) 71–96.

[15] **D. Benasciutti, F. de Bona, M.G. Munteanu,** Work roll in hot strip rolling: a semianalytical approach for estimating temperatures and thermal stresses, Proceedings of 9th International Conference on Advanced Manufacturing Systems and Technology (AMST 11) (2011) 395–406.

[16] **D. Benasciutti, F. de Bona, M.G. Munteanu,** An harmonic 1*d*-element for nonlinear analysis of axisymmetric structures: The case of hot rolling, Pan-American Congress on Computational Mechanics – PANACM 2015, In conjunction with the 11th Argentine Congress on Computational Mechanics – MECOM 2015, S. Idelsohn, V. Sonzogni, A. Coutinho, et al. (Eds). (2015) 1–12.

[17] **C.G. Sun, C.S. Yun, J.S. Chung, S.M. Hwang,** Investigation of thermomechanical behavior of a work roll and of roll life in hot strip rolling, Metallurgical and Materials Transactions A. 29 (9) (1998) 2407–2424.

[18] **S.P. Timoshenko, J.N. Goodier,** Theory of elasticity. New-York, Toronto, London, McGraw-Hill Book Comp., Inc. 1951.

[19] **A.I. Lurie,** Theory of elasticity, Springer, 2010.

Received 04.10.2018, accepted 26.12.2018.

THE AUTHORS

POLYANSKIY Sergey V.
Institute for Problems in Mechanical Engineering of the RAS
61 Bolshoi Ave. V.O., St. Petersburg, 199178, Russian Federation
svpolyanskiy@gmail.com

BELYAEV Alexander K.
Institute for Problems in Mechanical Engineering of the RAS
Peter the Great St. Petersburg Polytechnic University
29 Politechnicheskaya St., St. Petersburg, 195251, Russian Federation
vice.ipme@gmail.com

СПИСОК ЛИТЕРАТУРЫ

1. **Keanini R.G.** Inverse estimation of surface heat flux distributions during high speed rolling using remote thermal measurements // International Journal of Heat and Mass Transfer. 1998. Vol. 41. No. 2. Pp. 275–285.

2. **Khan O.U., Jamal A., Arshed G.M., Arif A.F.M., Zubair S.M.** Thermal analysis of a cold rolling process – a numerical approach // Numerical Heat Transfer. Part A: Applications. 2004. Vol. 46. No. 6. Pp. 613–632.

3. **Benasciutti D.** On thermal stress and fatigue life evaluation in work rolls of hot rolling mill //The Journal of Strain Analysis for Engineering Design. 2012. Vol. 47. No. 5. Pp. 297–312.

4. **Saxena A., Sahai Y.** Modeling of fluid flow and heat transfer in twin-roll casting of aluminum alloys // Materials Transactions. 2002. Vol. 43. No. 2. Pp. 206–213.

5. **Lai W.B., Chen T.C., Weng C.I.** Transient thermal stresses of work roll by coupled thermoelasticity // Computational Mechanics.

1991. Vol. 9. No. 1. Pp. 55–71.

6. **Saxena A., Sahai Y.** Modeling of thermo-mechanical stresses in twin-roll casting of aluminum alloys //Materials Transactions. 2002. Vol. 43. No. 2. Pp. 214–221.

7. **Serajzadeh S.** Effects of rolling parameters on work-roll temperature distribution in the hot rolling of steels // The International Journal of Advanced Manufacturing Technology. 2008. Vol. 35. No. 9–10. Pp. 859–866.

8. **Benasciutti D., Brusa E., Bazzaro G.** Finite elements prediction of thermal stresses in work roll of hot rolling mills // Procedia Engineering. 2010. Vol. 2. No. 1. Pp. 707–716.

9. **Toparli M., Sen F., Culha O., Celic E.** Thermal stress analysis of HVOF sprayed WC–Co/NiAl multilayer coatings on stainless steel substrate using finite element methods // Journal of Materials Processing Technology. 2007. Vol. 190. No. 1. Pp. 26–32.

10. **Li C., Yu H., Deng G., Liu X., Wang G.** Numerical simulation of temperature field and thermal stress field of work roll during hot strip rolling // Journal of Iron and Steel Research International. 2007. Vol. 14. No. 5. Pp. 18–21.

11. **Tudor A., Radulescu C., Petre I.** Thermal effect of the brake shoes friction on the wheel/rail contact // Tribology in Industry. 2003. Vol. 25. No. 1–2. Pp. 27–32.

12. **Johnson R.E., Keanini R.G.** An asymptotic model of work roll heat transfer in strip rolling // International Journal of Heat and Mass Transfer. 1998. Vol. 41. No. 6. Pp. 871–879.

13. **Dünckelmeyer M., Krempaszky C., Werner E., Hein G., Schqrkhuber K.** Analytical modeling of thermo-mechanically induced residual stresses of work rolls during hot rolling // Steel Research International. Metal Forming. 2010. Vol. 81. No. 9. Pp. 697–802.

14. **Benasciutti D., de Bona F., Munteanu M.G.** A semi-analytical finite element approach in machine design of axisymmetric structures // Intech Open Access Publisher. 2011. Pp. 71–96.

15. **Benasciutti D., de Bona F., Munteanu M.G.** Work roll in hot strip rolling: A semi-analytical approach for estimating temperatures and thermal stresses // Proceedings of 9th International Conference on Advanced Manufacturing Systems and Technology (AMST 11). 2011. Pp. 395–406.

16. **Benasciutti D., de Bona F., Munteanu M.G.** An harmonic 1*d*-element for nonlinear analysis of axisymmetric structures: The case of hot rolling // Pan-American Congress on Computational Mechanics "PANACM 2015". XI Argentine Congress on Computational Mechanics "MECOM 2015". S. Idelsohn, V. Sonzogni, A. Coutinho, et al. (Eds). 2015. Pp. 1–12.

17. **Sun C.G., Yun C.S., Chung J.S., Hwang S.M.** Investigation of thermomechanical behavior of a work roll and of roll life in hot strip rolling // Metallurgical and Materials Transactions. A. 1998. Vol. 29. No. 9. Pp. 2407–2424.

18. **Тимошенко С.П., Гудьер Дж. Н.** Теория упругости. Пер. с англ. М.: Наука. Гл. ред. физ.-мат. лит-ры, 263 .1975 с.

19. **Лурье А.И.** Теория упругости. М.: Наука, 940 .1970 с.

Статья поступила в редакцию 04.10.2018, принята к публикации 26.12.2018.

СВЕДЕНИЯ ОБ АВТОРАХ

ПОЛЯНСКИЙ Сергей Владимирович – *стажер-исследователь Института проблем машиноведения Российской академии наук.*

199178, Российская Федерация, г. Санкт-Петербург, Большой проспект В.О., 61.

svpolyanskiy@gmail.com

БЕЛЯЕВ Александр Константинович – *доктор физико-математических наук, директор Института проблем машиноведения Российской академии наук; профессор кафедры механики и процессов управления Института прикладной математики и механики Санкт-Петербургского политехнического университета Петра Великого.*

195251, Российская Федерация, г. Санкт-Петербург, Политехническая ул., 29

vice.ipme@gmail.com